VU Research Portal

Structural and spectroscopic in vivo imaging of the human retina with scanning light ophthalmoscopy

Damodaran, M.

2020

document version
Publisher's PDF, also known as Version of record

Link to publication in VU Research Portal

citation for published version (APA)
Damodaran, M. (2020). *Structural and spectroscopic in vivo imaging of the human retina with scanning light ophthalmoscopy*. [PhD-Thesis - Research and graduation internal, Vrije Universiteit Amsterdam].

General rights
Copyright and moral rights for the publications made accessible in the public portal are retained by the authors and/or other copyright owners and it is a condition of accessing publications that users recognise and abide by the legal requirements associated with these rights.

- Users may download and print one copy of any publication from the public portal for the purpose of private study or research.
- You may not further distribute the material or use it for any profit-making activity or commercial gain
- You may freely distribute the URL identifying the publication in the public portal

Take down policy
If you believe that this document breaches copyright please contact us providing details, and we will remove access to the work immediately and investigate your claim.

E-mail address:
vuresearchportal.ub@vu.nl

Download date: 13. Mar. 2024

Structural and spectroscopic *in vivo* imaging of the human retina with scanning light ophthalmoscopy

Mathi Damodaran

2020

This thesis was reviewed by:

Prof. dr. M. L. Groot	Vrije Universiteit Amsterdam
Prof. dr. M. C. G. Aalders	Universiteit van Amsterdam
Prof. dr. ir. R. M. Verdaasdonk	University of Twente
Dr. T. T. J. M. Berendschot	Maastricht University
Dr. D. J. Robinson	Erasmus Medical Centre

© 2020 Mathi Damodaran.
All rights are reserved. Any part of this thesis (including the digital art) may not be reproduced, built upon, text or data mined without prior permission from the author.
Chapters 3 is licensed under the OSA Open Access Publishing Agreement:
© 2020 Optical Society of America. Users may use, reuse, and build upon the article, or use the article for text or data mining, so long as such uses are for non-commercial purposes and appropriate attribution is maintained. All other rights are reserved.
Chapters 4 and 5 were published by SPIE under a Creative Commons Attribution License: Distribution or reproduction of this work in whole or in part requires full attribution of the original publication, including its DOI.

ISBN: 978-94-028-2026-3

Printed in the Netherlands by Ipskamp Drukkers.

Cover art prepared by M. Damodaran and S. K. Vipin using *neural style transfer*.

A digital version of this thesis can be obtained from: *http://dare.ubvu.vu.nl/*

The author acknowledges grant support from Dutch Technology Foundation **STW**, Netherlands Organisation for Health Research and Development **ZonMW**, and **Heidelberg Engineering GmbH**.

VRIJE UNIVERSITEIT

STRUCTURAL AND SPECTROSCOPIC IN VIVO IMAGING OF THE HUMAN RETINA WITH SCANNING LIGHT OPHTHALMOSCOPY

ACADEMISCH PROEFSCHRIFT

ter verkrijging van de graad Doctor aan
de Vrije Universiteit Amsterdam,
op gezag van de rector magnificus
prof.dr. V. Subramaniam,
in het openbaar te verdedigen
ten overstaan van de promotiecommissie
van de Faculteit der Bètawetenschappen
op vrijdag 3 juli 2020 om 11.45 uur
in de aula van de universiteit,
De Boelelaan 1105

door

Mathivanan Damodaran

geboren te Dharmapuri, India

promotor:	prof.dr. J.F. de Boer
copromotor:	prof.dr. A. Amelink

Contents

1 General introduction 1

1.1 Human eye: anatomy and physiology 2

1.1.1 Blood supply to the retina 7

1.1.2 Common retinal pathologies 9

1.2 Retinal imaging techniques 12

1.2.1 Fundus photography 13

1.2.2 Scanning Laser Ophthalmoscope 15

1.2.3 Optical Coherence Tomography 15

1.3 Thesis aim and outline 16

References 18

2 Principles of retinal imaging and retinal oximetry 23

2.1 Retinal imaging by scanning 24

2.1.1 Line scanning 26

2.1.2 Digital micromirror devices 28

2.2 Retinal imaging — optical considerations, laser safety and wavelength ranges 30

2.2.1 Optical considerations 30

2.2.2 Laser Safety considerations in retinal imaging 32

2.2.3 Light sources and signal to noise estimation 36

2.3 Retinal Oximetry 38

2.3.1 Retinal diseases and oxygenation 38

2.3.2 Evolution of retinal oximetry 39

2.3.3 Comparison of oximetry techniques 40

References 44

3 Digital micromirror device based ophthalmoscope 49

3.1 Introduction 50

3.2 Methods 51

3.2.1 Optical system 52

3.2.2 Annular illumination on the pupil plane and retinal resolution 54

3.2.3 Parallel scanning method 55

3.2.4 Confocal image processing using virtual pinholes 56

3.2.5 Model eye measurements to evaluate SNR improvement 57

3.2.6 *In vivo* retinal imaging 60

3.3 Results 60

3.3.1 Model eye measurements to evaluate SNR improvement 60

3.3.2 *In vivo* retinal images . . . 62
3.4 Discussion . . . 66
3.5 Application: Fixational eye motion detection . . . 67
3.6 Conclusion . . . 69
References . . . 71

4 Optimal wavelengths for sub-diffuse scanning laser oximetry . . . 75
4.1 Introduction . . . 76
4.2 Theory of retinal oximetry and identifying optimum wavelengths . . . 79
4.2.1 Theory of retinal oximetry . . . 79
4.3 Experimental validation . . . 93
4.3.1 Scanning Laser Ophthalmoscope - description of the system . . . 93
4.3.2 Measurements in model eye using a retina mimicking phantom . . . 93
4.3.3 Estimating vessel diameter from the images . . . 96
4.3.4 Experimental Results with retinal phantoms . . . 98
4.4 Discussion . . . 101
4.5 Conclusions . . . 105
References . . . 106

5 sub-diffuse scanning laser oximetry of the human retina *in vivo* . . . 111
5.1 Introduction . . . 112
5.2 Methods . . . 113
5.2.1 Wavelength selection for dual wavelength retinal oximetry . . . 113
5.2.2 System design . . . 116
5.2.3 Balanced detection to increase the signal-to-noise ratio . . . 120
5.2.4 Wavelength sweep hyperspectral imaging . . . 121
5.2.5 in vivo human measurements . . . 123
5.2.6 Retinal vessel segmentation and oxygenation map . . . 123
5.3 Results and discussion . . . 124
5.3.1 Technical aspects regarding multispectral SLO with an SC source . . . 124
5.3.2 *in vivo* two wavelength oximetry . . . 128
5.3.3 Wavelength sweep hyperspectral imaging . . . 128
5.4 Conclusion . . . 136
References . . . 138

6 Non-invasive optical measurement of haemoglobin concentration in the posterior eye of adult humans . . . 143
6.1 Introduction . . . 144
6.2 Methods . . . 147
6.3 Results and discussion . . . 151
6.4 Conclusion . . . 153
References . . . 155

7 Discussion and outlook . . . 157
7.1 Background . . . 158
7.2 Digital micromirror based SLO . . . 158
7.3 Quantitative retinal imaging . . . 160
7.3.1 Retinal oximetry . . . 160

7.3.2 Retinal haemoglobin concentration 162
7.4 Future directions 163
7.5 Thesis conclusion 165
References 166

8 Summary 169

9 Curriculum Vitae 177

10 Acknowledgements 181

1

General introduction

Overview

The eye is an organ which gives us the sense of sight and allows us to observe the surrounding world. We use our eyes in almost every activity we perform and hence a disease which affects vision has a negative impact on a person's quality of life. Age-related diseases are a significant public health concern, especially in the western world where there is an increase in the median age of the population [1]. Particularly, retinal diseases can result in visual function impairment, which can lead to reduced social interactions, loss of independence and disability. According to the WHO, about 1.3 billion people live with some visual function impairment, of which 270 million people have moderate to severe vision impairment [2]. About 80 % of all vision impairments globally are considered avoidable. Retinal pathologies and injuries exhibit structural and functional changes in the retina and are assessed using ocular imaging techniques. Retinal imaging is thus vital for our understanding of retinal diseases, and effective clinical evaluation, follow-up and treatment.

Advancements in retinal imaging have drastically improved the quality of eye care in the past two decades. Nevertheless, the current clinical evaluation of retinal diseases relies considerably on subjective visualisation of the retinal anatomy. In many pathological conditions, however, better and more objective imaging and image analysis methods are required. New techniques that can establish a correlation between retinal diseases and optical properties need to be developed. The various optical properties of the retina can be correlated to diagnostic criteria to provide new means for improving clinical care in ophthalmology. For example, a quantitative *in vivo* characterisation of spectral properties of the retina helps in understanding the pathophysiology of various diseases [3]. This thesis focuses on two major approaches to retinal imaging which can improve clinical care in ophthalmology:

1. Structural imaging of the retina using a low-cost, compact, novel **digital micromirror based ophthalmoscope**
2. Quantitative, functional imaging of the retina using a **multispectral scanning laser ophthalmoscope**.

1.1 Human eye: anatomy and physiology

Advancements in retinal imaging have drastically improved the quality of eye care in the past two decades. However, the current clinical evaluation of retinal diseases relies considerably on subjective visualisation of the retinal anatomy. In many pathological conditions, however, better and more objective imaging and image analysis methods are required. New The eye is an essential sensory organ which provides the ability to see in both bright and dim light, focusing on objects both near and far. The eye can detect three primary colours and transmit the information to the brain, which processes and perceives the image in millions of colours. A schematic cross-section of the eye and the retina is shown in Fig.1.1.

Cornea

About one-sixth of the anterior layer of the eye bulges and forms the transparent cornea, the aspherical bulge which serves as the outer transparent window of the eye. The cornea is made up of connective tissue with a thin layer of epithelium on the surface. The cornea contains hardly any cells and blood vessels and is transparent. Light enters the eye through the cornea, and the air-cornea interface does most of the focusing of the light. The cornea transmits about 99 % of visible light [4]. The cornea continues as **sclera**, the opaque portion of the eye. The sclera runs along the circumference of the eye and makes up the remaining posterior five-sixths of the eye's outer layer. The sclera is responsible for the protection of the vital inner layers of the eye and serves to attach the extra-ocular muscles, which aid in eye motion.

Iris, lens and humor

After the cornea, the light passes the anterior part of the eye through the **pupil**. The pupil is the central aperture in the iris and regulates the amount of light entering the eye. The **iris**, a pigmented disc, is visible in most eyes due to the transparency of the cornea. The iris is mostly made up of smooth muscle fibers and connective tissue. As the flux of light entering the eye reduces, the smooth muscles of the iris pull away from the centre, causing the pupil to dilate. On the other hand, if there is a sudden influx of light, the sphincter muscles in the iris pull toward the centre, causing the pupil to contract and allowing less light to reach the retina.

The transparent and crystalline **lens** of the eye is located behind the iris, suspended by ciliary muscles. When viewing an object at infinity, the ciliary muscles pull on the suspension ligaments causing the entire lens to flatten, enabling the lens to focus light from a far-away object. When the eye views an object at a near distance, ciliary muscles contract causing the suspension ligaments to relax. This action causes both lens surfaces to become more convex and enables the eye to focus nearby.

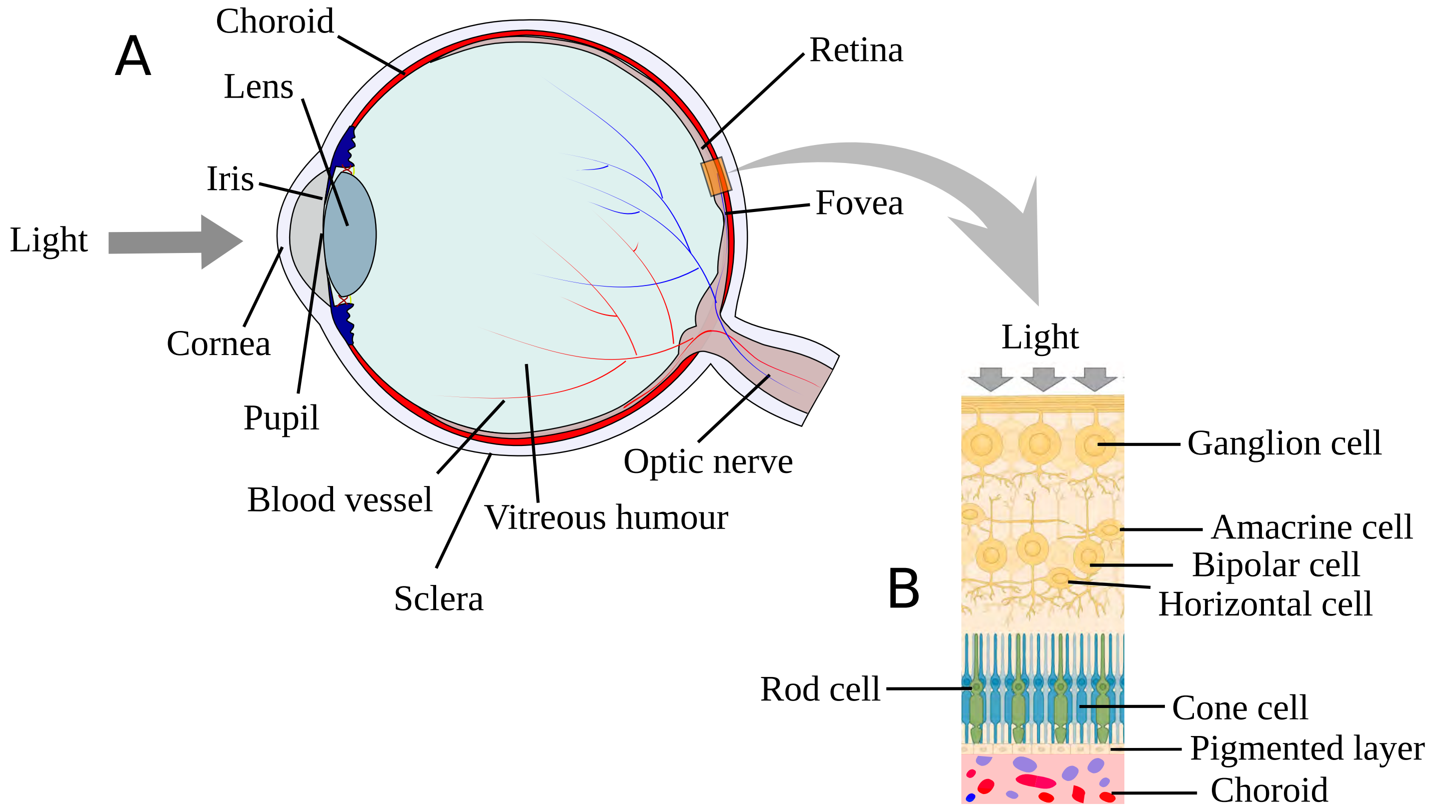
A
Choroid
Lens
Iris
Light
Cornea
Pupil
Blood vessel
Sclera
Vitreous humour
Optic nerve
Fovea
Retina
B
Light
Ganglion cell
Amacrine cell
Bipolar cell
Horizontal cell
Rod cell
Cone cell
Pigmented layer
Choroid

Figure 1.1: A: Cross-section of the human eye and its various constituents — The light enters the eye through the cornea and is focused on the retina by the lens. The blood vessels supply oxygen and nutrients to the retina. B: Cross-section of the retina showing different layers of cells, each performing a special function, [image adapted from Wikipedia]

The **vitreous humor** is a clear, transparent jelly-like substance which occupies the posterior part of the eye. It holds about 80% of the volume of the eyeball. The vitreous keeps the eye structurally intact.

Retina

The retina is a thin multi-layered tissue (Fig.1.1B) with an average thickness of 300 µm, which is responsible for the critical task of receiving light from the external world and transmitting visual stimuli to the brain. Various insults to this delicate structure can thus generate pathological processes and lead to retinal disease(s).

The retina consists of two components: an innermost layer of retinal pigment epithelium (RPE) which is composed of a single layer of melaninated cells, and the neural retina which is a multi-layered structure containing photoreceptors as well as neurons. These two components together are typically called the retina, and it is subdivided into nine recognisable layers: nerve fiber layer (**NFL**), ganglion cell layer (**GCL**), inner plexiform layer (**IPL**), inner nuclear layer (**INL**), outer plexiform layer (**OPL**), outer nuclear layer (**ONL**), external limiting membrane (**ELM**), photoreceptor layer (**PL**), and the retinal pigment epithelium (**RPE**). A histological cross-section of the human retina is shown in Fig. 1.2. The structure and function of each layer of the retina is a fascinating field in itself and is studied by many vision scientists. A brief description of each layer might help the reader in appreciating the complexity of the retina and the vital role it plays in vision.

The **NFL** is formed by the extension of the fibres of the optic nerve. It has the highest thickness near the optic disc and is made up of the support cells of the neural retina. NFL is a sensitive structure, and thus some process can start its spontaneous apoptosis. Any adverse situation can make some damage on NFL such as high intraocular pressure, inflammation, vascular disease and hypoxia [6].

The **IPL** is a region of the retina that is built up of a compact reticulum of fibrils arranged by interlaced dendrites of retinal ganglion cells. A retinal ganglion cell is a variety of neuron found in the **GCL** of the retina of the eye. It collects visual stimuli from photoreceptors through two intermediate cell types, namely bipolar cells and retinal amacrine cells [7].

The **INL** or layer of inner granules of the retina, is made up of several closely arranged cells, namely the bipolar cells, the horizontal cells, and the amacrine cells. The **OPL** is a layer of neuronal synapses in the retina. It consists of a compact network of synapses within dendrites of horizontal cells from the **INL**, and photoreceptor cell inner segments from the **ONL**. It is much thinner than the **IPL**, where amacrine cells synapse with retinal ganglion cells. The **ONL** is typical for verte-

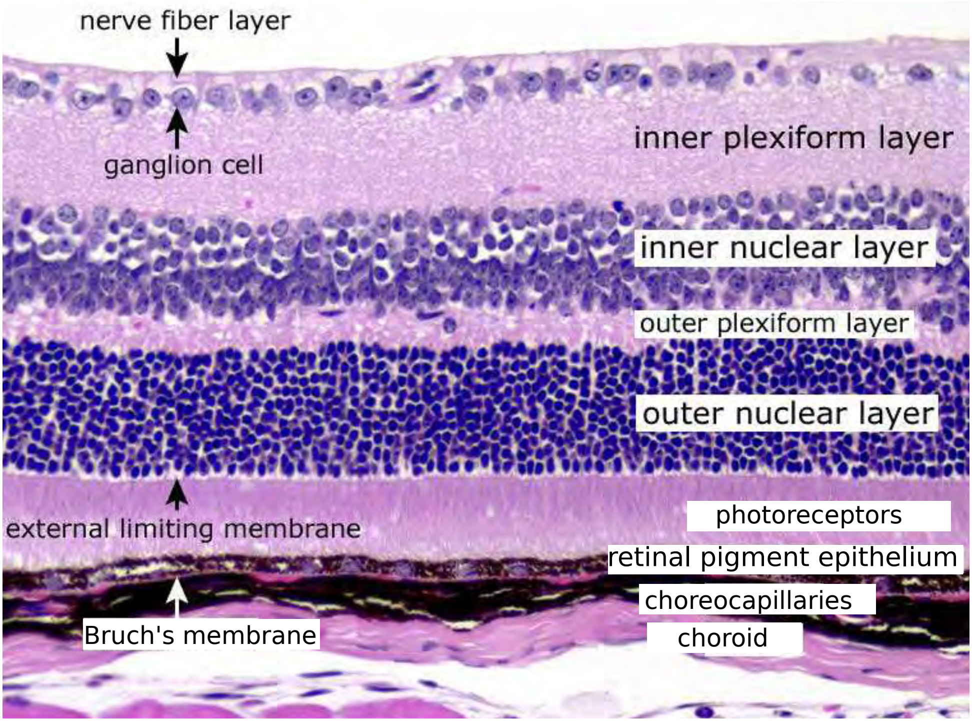
nerve fiber layer
ganglion cell
inner plexiform layer
inner nuclear layer
outer plexiform layer
outer nuclear layer
external limiting membrane
photoreceptors
retinal pigment epithelium
choreocapillaries
Bruch's membrane
choroid

Figure 1.2: Histological cross-section of the posterior eye: retinal layers, choroid and sclera [5].

brate retina and is assumed to be the light-detecting portion of the eye. Like the **INL**, the **ONL** contains several strata of oval nuclear bodies [7].

The **PL** consists of the rod and cone cells. The light must cut across many layers before reaching the rods and cones. Rod cells are cylindrical, while the cone cells have conical outer segments. The rod cells are more receptive to the light stimuli and thus are primarily used in low light levels. The resulting image from the rod cells is monochromatic. The cone cells are sensitive to distinct wavelengths of light and allow the perception of colours and complete visible information. The photoreceptor layer is devoid of any blood capillaries [8].

The outermost layer closest to the choroid is the **RPE** which contains a single sheet of cuboid pigmented cells, with perform the function of absorbing light and thus preventing stray light from reflecting onto the rods and cones. Compact and tight interfaces between the cells in this layer establish the so-called 'blood-retina barrier' to regulate and balance the exchange of molecules from the blood to the retina and vice-versa. The RPE cells play an essential role in nourishing the overlying outer retina. They facilitate the diffusion of nutrients from the choroid. **Bruch's**

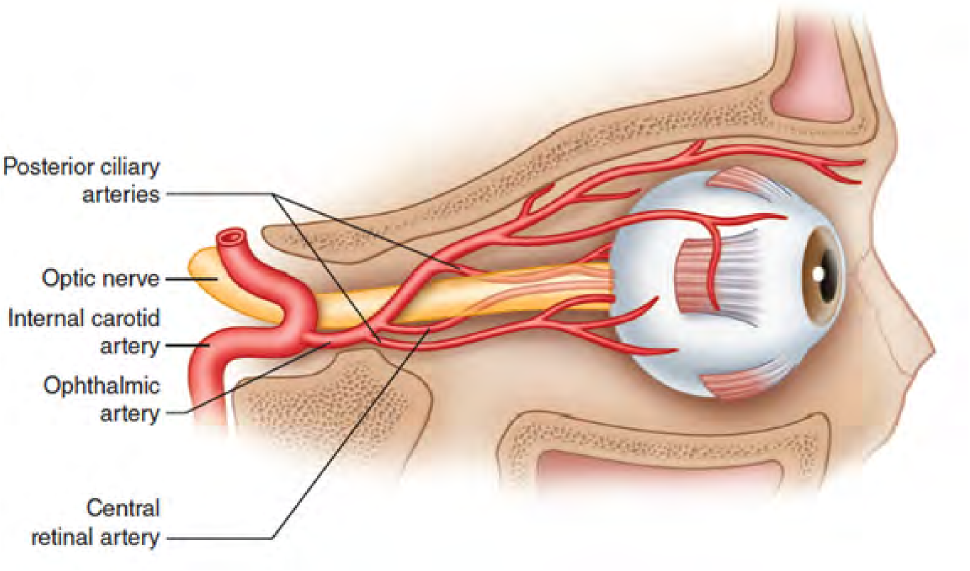

Figure 1.3: Blood supply to the eye: The ophthalmic artery is a branch of the internal carotid artery and divides into the central retinal artery and the posterior ciliary arteries. The former supplies blood to the outer layers of the retina while the later supplies blood to the choroid. Image adapted from Ichsan *et al.* [12].

membrane is the innermost layer of the choroid.

The axons from all the retinal ganglion cells converge and leave the eye through the optic nerve. The point where it exits is the **optic disc** or **optic nerve head (ONH)**. This area is incapable of detecting light, as this point is by definition, a break in the retina. Therefore the ONH creates a blind spot in the lateral visual field. The **fovea** is a small depression in the central portion of the retina. The inner layers of the retina are drastically reduced (or absent) in the fovea. The dominant layer of the fovea is the photoreceptor layer composed exclusively of cone cells. These cells are also slender than they are elsewhere in the retina to accommodate their dense packing. There is a 1:1 ratio of ganglion cells to photoreceptors in the fovea to facilitate excellent discrimination of colours and details. Blood vessels are also absent in the foveal region to allow light to pass unimpeded to the photoreceptors. The fovea is an avascular zone.

1.1.1 Blood supply to the retina

One of the main objectives of the thesis is measuring the blood oxygenation in the retinal vessels. Therefore it is important to understand how the blood is supplied to the retina. The blood supply of the entire eye comes from the ophthalmic artery,

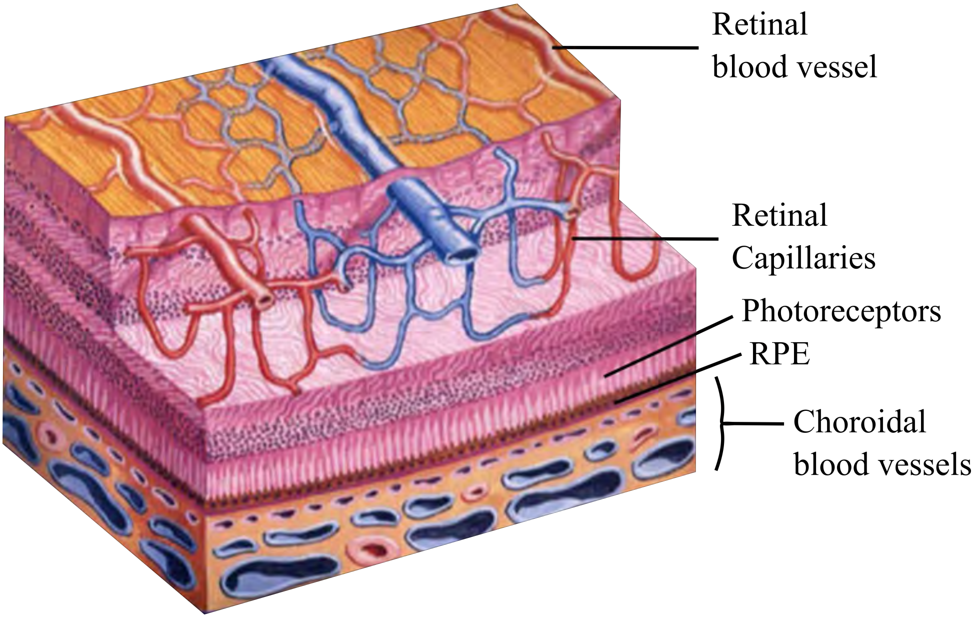

Figure 1.4: Retinal layers and blood vessels: The top layers are supplied oxygen through the retinal vasculature while choroidal vasculture supplies oxygen to the bottom layers (image courtesy of Novartis)

which is a branch of the internal carotid artery, as shown in Fig. 1.3. The retinal circulation originates from the central retinal artery (CRA), which is a branch of the ophthalmic artery [9]. The CRA travels inside the optic nerve and reaches the retina to branch from arteries to arterioles and capillaries into deeper layers, as shown in Fig. 1.4. The capillaries are organised mainly in two different layers, one in the NFL and another in the inner nuclear layer. The retinal capillaries continue to venules, which merge to form the central retinal vein (CRV) and leave the eye through the optic nerve [10, 11].

The choroidal circulation originates from the posterior ciliary arteries. The choroidal vessels can be divided (from outside to inside) into a layer of large arteries; a layer of medium-sized arteries and arterioles ; an innermost layer of choriocapillaris. In healthy eyes, the choroid does not penetrate the retina and does therefore not obscure vision. Oxygen diffuses from the choriocapillaris, through the retinal pigment epithelium to reach the photoreceptors which have high oxygen demand and high metabolic rate. The concentration gradient drives the diffusion of oxygen from the choriocapillaris to the photoreceptors [13].

The retinal and choroidal vasculatures are different in many ways. The retinal vasculature is sparse as a dense network can obscure vision. On the other hand,

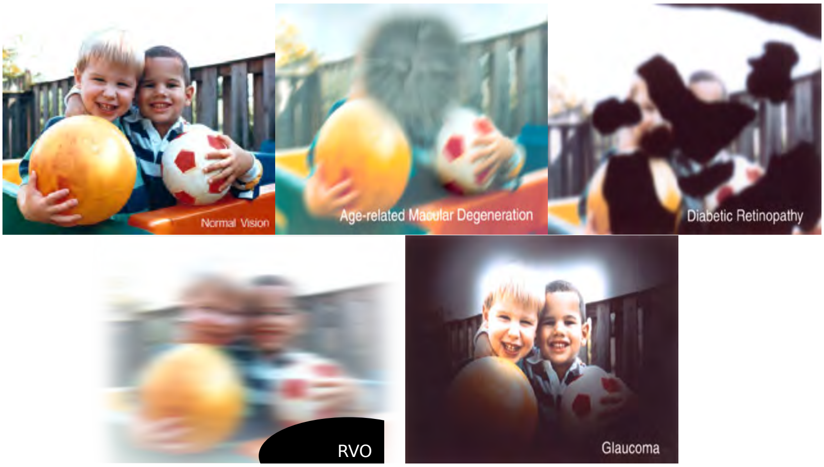

Figure 1.5: Common retinal pathologies and functional changes — Retinal pathology affects vision and reduces the quality of life. The simulated images show the effect of visual impairments [20]

the choroidal vasculature is dense as there is no scope to obscure vision. The retinal circulation penetrates the retinal tissue, and this decreases diffusion distances from capillaries to retinal cells.

1.1.2 Common retinal pathologies

As explained in the previous section, the retina is an incredibly intricate structure, hence is prone to many retinal pathologies due to impairment or injury to one or some of its components. The capacity of the retinal tissue to respond to such damages depends mainly on: the specific cells and tissue involved, type, duration and severity of the injury. The broad range of retinal conditions that may exist is too extensive to review in this brief chapter. Instead, we discuss a few important retinal diseases.

Age related macular degeneration (AMD) is a disease that causes blindness, and is the most common disease that causes blindness in industrialised countries [14]. AMD is also the most common condition whose incidence increases with ageing. The dry form of AMD is identified by drusen and extracellular deposits which accumulate beneath the RPE, and a loss of photoreceptors. In wet AMD, abnormal blood vessels grow under the retina and macula due to a process called choroidal neovascularization. These blood vessels may then leak and bleed, causing the macular region of the retina to bulge, destroying vision in the process. Vision loss due to AMD may be rapid and severe.

Diabetic retinopathy (DR) occurs as small aneurysms or haemorrhages in the retinal tissue. When diabetes is uncontrolled, it damages blood vessels throughout the body. Diabetes results in reduced maintenance of the blood sugar levels, and in the long run, it affects the capillaries throughout the body. A particular example of the location in the body where tiny capillaries are affected is in the retina, resulting in DR.

Retinal vessel occlusions (RVO) is a retinal pathology which disturbs retinal blood flow and oxygenation. Occlusions can be broadly divided into vein occlusions and artery occlusions. Occlusions can be further divided into central occlusions, affecting the central retinal vein or artery, and branch occlusions, affecting branches of the central vessels. The primary symptom of retinal vascular occlusion is a sudden change in vision. This could include blurry vision or a partial or complete loss of sight.

Glaucoma is characterised by degeneration of the NFL and the optic nerve. In cases it is accompanied by loss of vision. Glaucoma has been traditionally linked to high intraocular pressure, although it is not necessarily associate with high pressure and several glaucoma patients have normal or low intraocular pressure [15]. But elevated intraocular pressure is a risk factor for glaucoma and lowering of the intraocular pressure is a widely accepted treatment for glaucoma. Reducing the intraocular pressure generally slows the progression of glaucoma, even in patients with low pressure. However, retinal blood flow does not follow changes in intraocular pressure linearly.

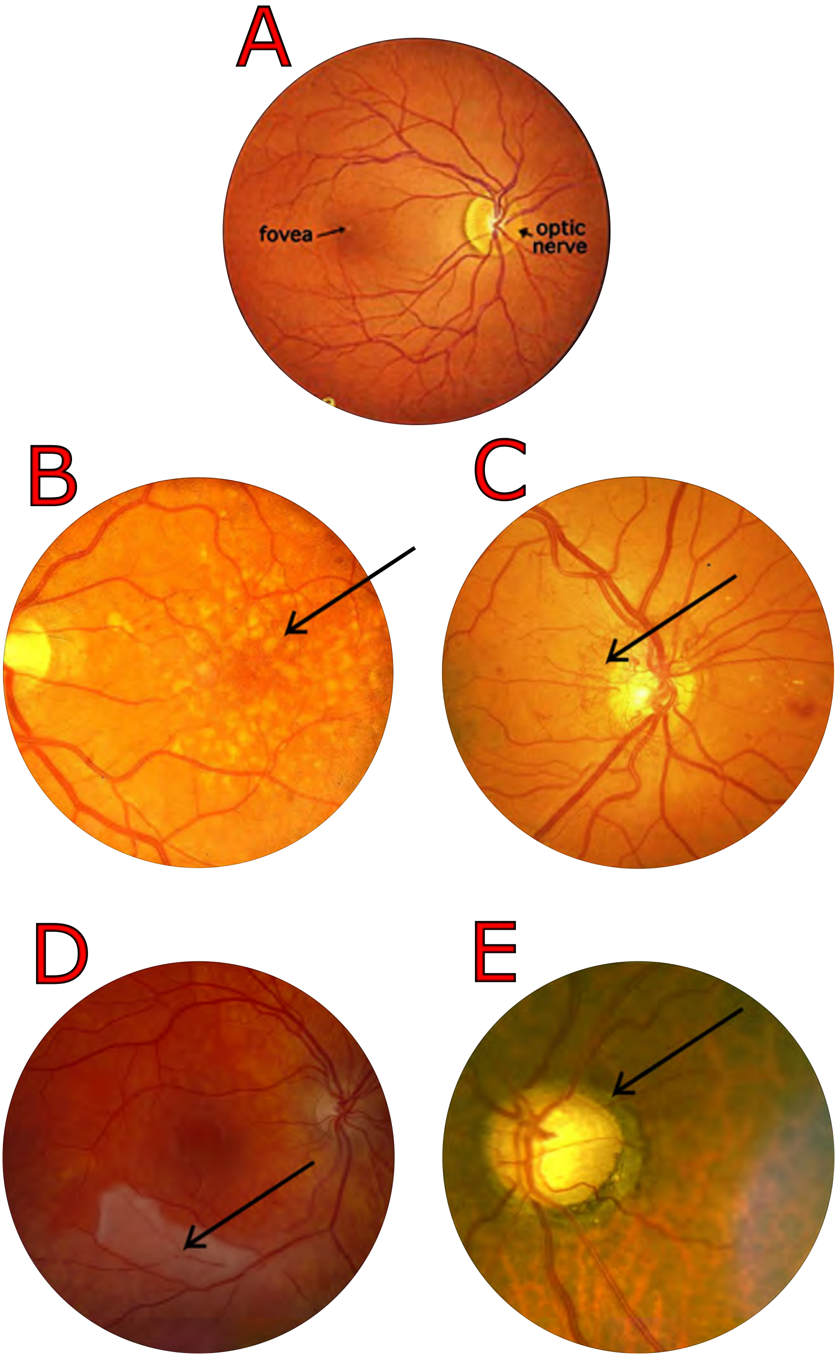

Figure 1.6: Common retinal pathologies and structural changes—A: Fundus image of a normal healthy human retina showing the optic nerve head and the fovea. B: Image of an eye with AMD. The arrow indicates drusen in the fundus [16]. C: Image of an eye with DR [17]. The arrow indicates the abnormal growth of blood vessels. D: image of an eye with RVO with the arrow showing blocked blood vessels in the retina [18]. E: an image of an eye with Glaucoma with the arrow showing the abnormal size of the ONH [19].

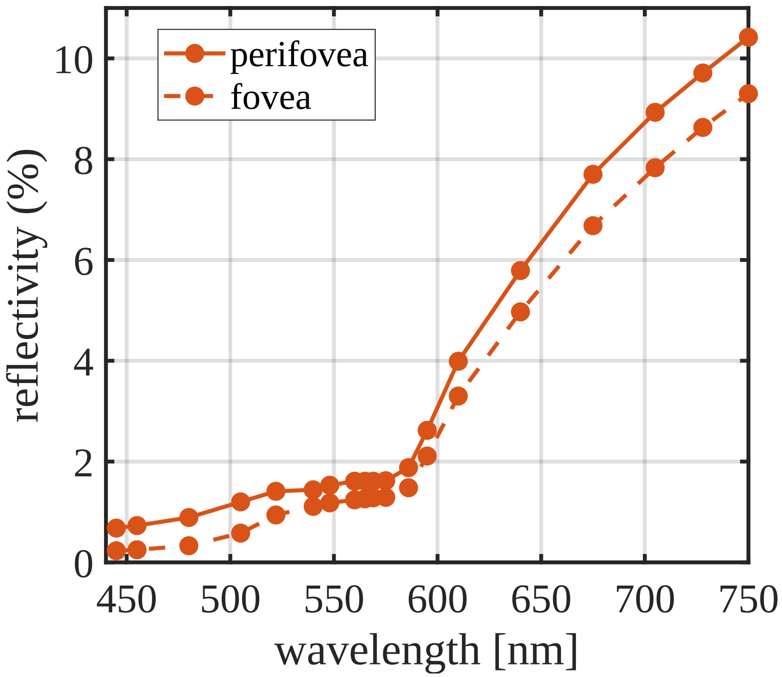

Figure 1.7: Reflection spectrum of the human retina in *perifoveal* and *foveal* region observed from 30 different human subjects. Data taken from Delori *et al.*[22].

1.2 Retinal imaging techniques

Non-invasive imaging of the retina presents some unique challenges because of its location in the posterior eye. The retina must be illuminated and imaged at the same time, a method which requires illumination and detection modules to share a common optical path. The retina is a low reflective [21, 22] (Fig. 1.7) and moderately scattering [23] surface. These attributes result in only a small fraction of the light illuminating the retina to reach the detector. Imaging the retina requires the optics of the eye to be used as a part of the imaging system. The optics of the cornea and the crystalline lens introduce aberrations in an imaging system.

Historical perspective

The invention of the ophthalmoscope by Helmholtz in 1851 [24] was the first breakthrough in modern imaging techniques (1.8A), especially towards the goal of imaging the retina. Helmholtz's design consisted of a partially reflecting mirror that directed light from a source onto the retina. In 1886, Jackman and Webster recorded the first in-vivo human retinal photograph, showing the optic disc and larger blood vessels [25]. In the century that followed, fundus photography to document ophthalmoscopic findings progressed and became a necessary method for the examination and assessment of retinal disease. In 1961, the first successful fluorescein angiography was recorded in humans [26]. Fluorescein angiography has become the main diagnostic tool for the study of retinal flow.

The invention of the scanning laser ophthalmoscope (SLO) in the early 1980s [27–29] thrust the field of fundus imaging into a new era. Instead of capturing the image as a whole, SLO samples the retina point by point in a raster-like fashion with its laser beam. The SLO was combined with confocal optics in 1987 [30]. Despite fundus imaging and fluorescein angiography [31] being gold standards in ophthalmic clinical care, there are limitations of these techniques. These techniques give a macroscopic view of the retina and have a restricted ability for analysing the three-dimensional composition of the tissue. The retina is a three-dimensional structure, and microscopic visualisation of retinal features is possible only with good axial and transverse resolution. With this in mind, various new retinal imaging techniques have emerged to investigate the structure and function of the retina in great detail. For example, ultrasound has been used for eye diagnosis. The optical analogue, called Optical coherence tomography (OCT) was found in 1991 by Huang *et al.* [32] and transformed ophthalmic imaging. OCT uses low-coherence light with interferometry. Low coherence interferometry had been used previously to measure axial distances in the eye [33, 34]. The retina is virtually transparent with extremely low optical backscattering, but the great sensitivity of OCT allows detection of such weak signals. In contrast to conventional microscopy. A brief description of various retinal imaging modalities is given in this chapter, with in-depth working principles described in the next chapter.

1.2.1 Fundus photography

A fundus camera is used to take a snapshot image of the retina and typically has a wide field of view. A simple version of the fundus camera consists of an imaging system, illumination system, and usually also a fixation target. All of these systems must share common optics. Broadband flood illumination is used to illuminate the retina after enlarging the pupil of the eye using mydriating eye drops. The reflected and scattered light is captured by an area sensor such as a CCD camera. Almost every ophthalmic clinic in the world uses a fundus camera for retinal imaging. Fluorescein angiography can also be achieved using fundus camera-based techniques but with an intravenous injection of a fluorescent dye.

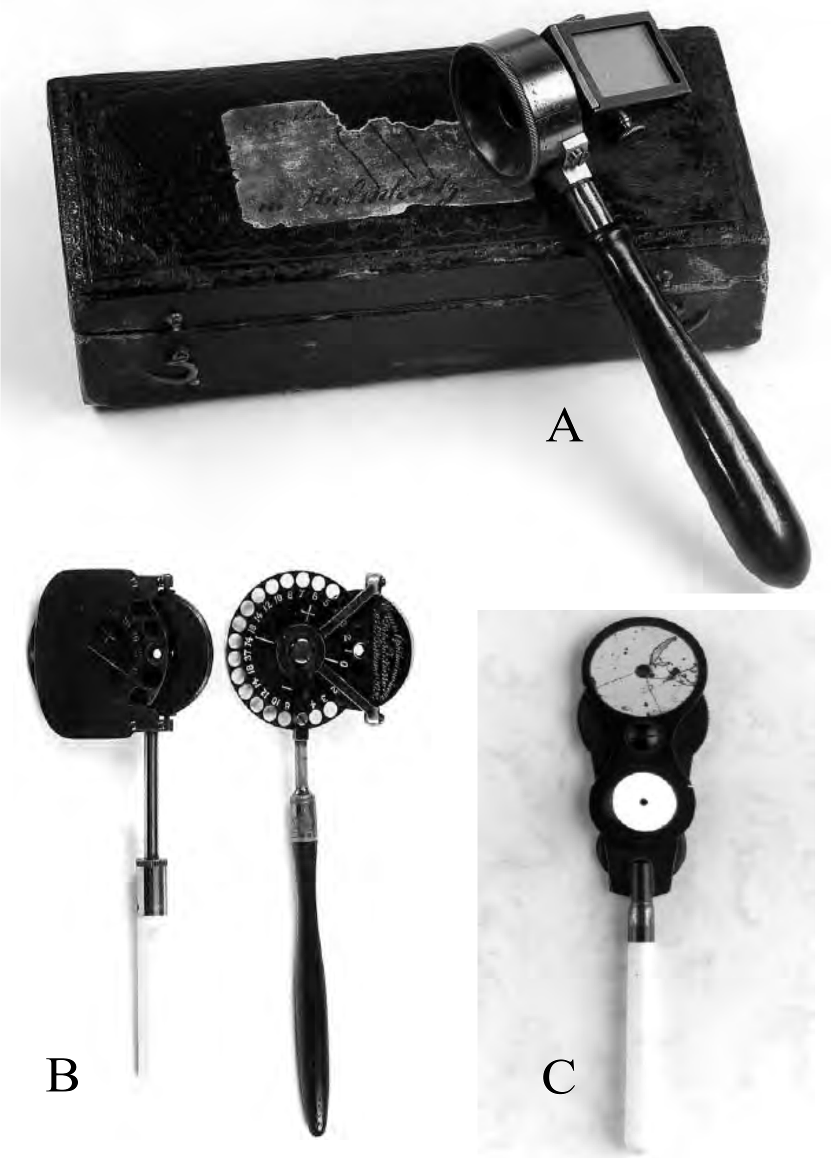

Figure 1.8: A: Early model of the Helmholtz ophthalmoscope (1851). B: John Coupers first ophthalmoscope, with a slide-in Rekoss disc behind a tilting mirror (left), Right: second model. C: Lindsay Johnson ophthalmoscope with two mirrors for direct and indirect ophthalmoscopy.

Fundus photography gives the necessary information to diagnose some retinal disease. The cost of fundus photography continues to be significantly lower than the newer techniques based on retinal scanning. Its main advantages are the easy interpretation, full colour, better detection of haemorrhages etc. Disadvantages include lack of quantitative description and hence inter-observer variability, the need of high photographic quality, and difficult serial comparison because of limited ability to detect subtle changes with a photograph. Another drawback of fundus photography is the need for high light intensity for illumination of the retina, on the order of 10-100 % of the maximum permissible levels [31], typically delivered by a flash.

1.2.2 Scanning Laser Ophthalmoscope

A scanning laser ophthalmoscope (SLO) produces retinal images by scanning a laser spot (line) and detecting backscattered light using a point (line) detector. High contrast images are achieved if a confocal pinhole [30] is used as it enables suppression of the scattered light, and thereby minimising the optical cross-talk outside a volume surrounding the focal point on the retina. SLO systems are used in clinics throughout the world and have been modified for different clinical applications. The diagnostic applications of SLO include detection of the structural biomarkers of AMD, Glaucoma, RVO and DR [35, 36]. SLOs have been combined with optical coherence tomography-based techniques (which are explained below) for eye motion tracking [37–40] as well as for optimal classification of diseases [41–44]. Furthermore, adaptive optics has been implemented in an SLO system with the help of a wavefront detection sensor, and this has enabled visualisation of rod and cone cells in the photoreceptor layer of the retina [45–47]. A detailed description of the working of an SLO is given in chapter 2.

1.2.3 Optical Coherence Tomography

As explained in section 1.1, the complicated structure of the retina demands precise visualization of pathology. OCT enables non-invasive, high-resolution imaging of the retina *in vivo*. OCT's axial resolution surpasses that of ultrasound or confocal SLO and resembles that of conventional histology[48, 49]. In OCT, the axial resolution is mainly determined by the bandwidth and wavelength of the optical source and therefore, the retina of the human eye can be imaged with at least 100 times better axial resolution [50]. Advancements in the field of OCT have led to the development of spectral-domain OCT [51–53]. In principle, an OCT operates as a low coherence Michelson interferometer. Interference occurs when the optical path difference between the sample and reference arms is within the coherence length of the source. As the source becomes less coherent, the coherence length shrinks, making the maximum optical path difference between reference and sample arms needed for the interference to occur smaller.

1.3 Thesis aim and outline

Ophthalmic imaging has been an active area of clinical investigation that has been expanding steadily, providing scientists and doctors with valuable information. New diagnostic and therapeutic methods have been established in this field, driven by an overall need to advance clinical care in ophthalmology. New scanning and imaging technologies have had a significant impact on ophthalmology. Structural imaging techniques help in visualising the retina in great detail and helps in assessing retinal health. However, the structure does not always provide information on the tissue health, and thus techniques which can provide a quantitative, functional aspect of living tissue is required in many cases. The work presented in this thesis aims to develop new devices and techniques which can perform imaging of the retina and to apply them for non-invasive imaging of structure and function in the *in vivo* human retina.

In order to extract structural and functional information from the retina using an SLO, it is essential to understand it's design, construction, and working. For this purpose, **chapter 2** of this thesis discusses the principle of scanning based ophthalmic imaging systems, gives a brief explanation of various design considerations for constructing an SLO, and introduces the retinal oximetry and its importance in diagnosing various retinal diseases. Laser safety considerations for intentional exposure of the retina to the laser light is also described in detail. The knowledge from this chapter forms the basis of the scientific work presented in chapters 3 to 6.

In **Chapter 3**, a novel digital micromirror device (DMD) based SLO is presented. Concentric circle patterns were implemented as a scanning scheme to image the retina and provide fixation at the same time. The DMD was used *in lieu* of traditional scanning mirrors and offered flexibility in terms of speed and confocality. The concentric circles improved the fixation and reduced motion artefacts compared to previously implemented parallel line scanning design. An annulus was used to reduce the corneal reflections from the retina and thereby to increase the signal to noise ratio. *in vivo* imaging was demonstrated by performing non-mydriatic imaging on two subjects at a speed of 7 frames per second with a maximum 20° (diameter) field of view. The images were shot noise limited and clearly show various anatomical features of the retina with high contrast. The images were comparable to images from a commercial SLOs but at a fraction of the cost.

Chapter 4 describes a detailed analysis of the error propagation of measurement noise in retinal oximetry, to identify optimal wavelengths which will yield the lowest uncertainty in saturation estimation for a given measurement noise level. The effect of haemoglobin packing in discrete blood vessels (pigment packing) is also introduced in this chapter. Pigment packing may result in a non-negligible bias in saturation estimation if unaccounted for under specific geometrical conditions, such as sub-diffuse sampling of smaller blood vessels located deeper within the retina. To validate the analysis, an SLO was developed to produce high contrast images. Confocal reflectance measurements were then conducted on a tissue-mimicking scattering phantom with optical properties similar to retinal tissue, including narrow channels filled with absorbing dyes to mimic blood vessels. By imaging at three optimal wavelengths, the ′saturation′ of the dye combination was calculated.

In **Chapter 5**, construction of an SLO based on a double-clad fibre coupler and a supercontinuum source is described in detail. Implementation of a balanced detection scheme to suppress the relative intensity noise of the supercontinuum source is also described with experiments validating the improvements in the signal to noise ratio with the use of balanced detection. The optimum wavelengths for accurate *in vivo* oximetry estimation using two wavelengths are established with an *in silico* analysis. The SLO produced dual-wavelength, high-quality images at 10 frames / second with a 20° imaging field of view. The blood oxygen saturation in retinal blood vessels was mapped from the images.

The eye provides a unique location in the human body with visual access to blood vessels. The blood vessels in the eye are regarded as highly superficial and thus is a desirable access point for Hb concentration estimation due to the lack of thick overlying tissues present elsewhere in the body. In **Chapter 6**, a non-invasive spectrophotometric method to image the retina simultaneously at two isosbestic wavelength to extract the haemoglobin concentration values from the two images is described.

Finally, in **Chapter 7**, the discussion on the results obtained from the scientific work in chapters 3-6 is presented with an outlook for future research. The concluding remarks of the thesis are also given in this chapter. This chapter marks the end of the scientific content of the thesis.

References

[1] World Population Ageing: 1950-2050, United Nations Population Division. https://www.un.org/esa/population/publications/worldageing19502050/

[2] R. R. A. Bourne, S. R. Flaxman, T. Braithwaite, M. V. Cicinelli, A. Das, J. B. Jonas, J. Keeffe, J. Kempen, J. Leasher, H. Limburg, K. Naidoo, K. Pesudovs, S. Resnikoff, A. Silvester, G. A. Stevens, N. Tahhan, T. Wong, H. R. Taylor, P. Ackland *et al.* , "Magnitude, temporal trends, and projections of the global prevalence of blindness and distance and near vision impairment: a systematic review and meta-analysis," Lancet Glob. Heal. **5**, (2017).

[3] A. E. Elsner, A. H. Jalkh, and J. J. Weiter, “New devices in retinal imaging and functional evaluation,” *Practical Atlas of Retinal Disease and Therapy*, W. Freeman, ed. pp. 19-35, Raven Press, New York (1993).

[4] H. F. Edelhouser, J. L. Ubels, and C. Hejny, "The cornea and the sclera," in Adlers physiology of the eye 10th ed., P. L. Kaufman and A. Alm, eds. (Mosby, Inc., 2003), pp. 47-114.

[5] H. A. Kadkhodaeian, T. Tiraihi, N. Daftarian, H. Ahmadieh, H. Ziaei, and T. Taheri, "Histological and electrophysiological changes in the retinal pigment epithelium after injection of sodium iodate in the orbital venus plexus of pigmented rats," J. Ophthalmic Vis. Res. 11, 7077 (2016).

[6] Text in the public domain —from page 1015 of the 20th edition of Gray’s Anatomy (1918).

[7] Text in the public domain —from page 1016 of the 20th edition of Gray’s Anatomy (1918).

[8] Text in the public domain —from page 1017 of the 20th edition of Gray’s Anatomy (1918).

[9] S. S. Hayreh, "Acute retinal arterial occlusive disorders," Prog. Retin. Eye Res. **30**, 359-394 (2011).

[10] S. Pi, A. Camino, X. Wei, J. Simonett, W. Cepurna, D. Huang, J. C. Morrison, and Y. Jia, "Rodent retinal circulation organization and oxygen metabolism revealed by visible-light optical coherence tomography," **9**, 58515862 (2018).

[11] J. P. Campbell, M. Zhang, T. S. Hwang, S. T. Bailey, D. J. Wilson, Y. Jia, and D. Huang, "Detailed Vascular Anatomy of the Human Retina by Projection-Resolved Optical Coherence Tomography Angiography," Sci. Rep. **7**, 111 (2017).

[12] A. M. Ichsan, L. M. Herawati, A. Vanny, J. Vimala Jaury, H. S. Muhiddin, and Budu, "Central Retinal Artery Occlusion and Partial Ophthalmoplegia Caused by Hyaluronic Acid Injection Filler Cosmetic," Ann. Clin. Lab. Res. **06**, 14 (2018).

[13] R. A. Linsenmeier, "Effects of light and darkness on oxygen distribution and consumption in the cat retina.," J. Gen. Physiol. **88**, 521-42 (1986).

[14] http://www.who.int/blindness/causes/en/

[15] H. A. Quigley, "Glaucoma," Lancet **377**, 1367-1377 (2011).

[16] N. F. Mokwa, T. Ristau, P. A. Keane, B. Kirchhof, S. R. Sadda, and S. Liakopoulos, "Grading of age-related macular degeneration: Comparison between color fundus photography, fluorescein angiography, and spectral domain optical coherence tomography," J. Ophthalmol. 2013, (2013).

[17] J. K. H. Goh, C. Y. Cheung, S. S. Sim, P. C. Tan, G. S. W. Tan, and T. Y. Wong, "Retinal Imaging

Techniques for Diabetic Retinopathy Screening," J. Diabetes Sci. Technol. **10**, 282294 (2016).

[18] Branch retinal artery occlusion "Https://emedicine.medscape.com/article/1223362-overview"

[19] Institute of vision and optics, http://www.ivo.gr/en/patient/glaucoma/glaucoma.html

[20] Retinal diseases simulation, National eye institute, https://nei.nih.gov/health/examples

[21] M. Hammer and D. Schweitzer, "Quantitative reflection spectroscopy at the human ocular fundus," Phys.Med.Biol. **47**, 179-191 (2002).

[22] F. C. Delori and K. P. Pflibsen, "Spectral reflectance of the human ocular fundus," **28**, 1061-1077 (1989).

[23] N. Bosschaart, G. J. Edelman, M. C. G. Aalders, T. G. van Leeuwen, and D. J. Faber, "A literature review and novel theoretical approach on the optical properties of whole blood," Lasers Med. Sci. **29**, 453-479 (2014).

[24] H. L. F. von Helmholtz, Beschreibung eines AugenSpiegels. Berlin, Germany(1851).

[25] W. Jackman, and J. Webster, "Photographing the retina of the living human eye". Photogr News. **23**, 340-341 (1886).

[26] H. Novothy and D. Alvis, "A method of photogrphing fluorescence in circulating blood in the human retina," Circulation **24**, 82-86 (1961).

[27] R. H. Webb, G. W. Hughes, and O. Pomerantzeff, "Flying spot TV ophthalmoscope," Appl. Opt. **19**, 2991-2997 (1980).

[28] R. H. Webb and G. W. Hughes, "Scanning Laser Ophthalmoscope," IEEE Transactions on Biomedical Engineering, vol. BME-**28**, 488-492, (1981).

[29] R. H. Webb, "Manipulating Laser Light for Ophthalmology," IEEE Engineering in Medicine and Biology Magazine **4**, 12-16, (1985).

[30] R. H. Webb, G. W. Hughes, and F. C. Delori, "Confocal scanning laser ophthalmoscope.," Appl. Opt. **26**, 1492-1499 (1987).

[31] F. C. Delori, J. S. Parker, and M. A. Mainster, "Light levels in fundus photography and fluorescein angiography," Vision Res. 20, 10991104 (1980).

[32] D. Huang, E. A. Swanson, C. P. Lin, J. S. Schuman, W. G. Stinson, W. Chang, M. R. Hee, T. Flotte, K. Gregory, C. A. Puliafito, and J. G. Fujimoto, "Optical Coherence Tomography HHS Public Access," Science **22**, 1178-1181 (1991).

[33] A. F. Fercher, K. Mengedoht, and W. Werner, "Eye-length measurement by interferometry with partially coherent light," Opt. Lett. **13**, 186 (1988).

[34] C. K. Hirzenberger, "Optical Measurement of the Axial Eye Length by Laser Doppler Interferometry," Invest. Ophthalmol. **32**, 616624 (1991).

[35] M. Kernt and M. W. Ulbig, "Wide-Field Scanning Laser Ophthalmoscope Imaging and Angiography of Central Retinal Vein Occlusion," Circulation **121**, 14591460 (2010).

[36] L. S. Lim, P. Mitchell, J. M.Seddon, F. G. Holz, T. Y. Wong, "Age-related macular degeneration", Lancet. **379**, 1728-38 (2012).

[37] B. Braaf, K. V. Vienola, C. K. Sheehy, Q. Yang, K. A. Vermeer, P. Tiruveedhula, D. W. Arathorn, A. Roorda, and J. F. de Boer, "Real-time eye motion correction in phase-resolved OCT angiography with tracking SLO," Biomed. Opt. Express **4**, 51 (2013).

[38] K. V. Vienola, M. Damodaran, B. Braaf, K. A. Vermeer, and J. F. De Boer, "In vivo retinal imaging for fixational eye motion detection using a high-speed digital micromirror device (DMD)-based ophthalmoscope," Biomed. Opt. Express **9**, 591602 (2018).

[39] C. K. Sheehy, Q. Yang, D. W. Arathorn, P. Tiruveedhula, J. F. de Boer, and A. Roorda, "High-speed, image-based eye tracking with a scanning laser ophthalmoscope," Biomed. Opt. Express **3**, 2611 (2012).

[40] K. V. Vienola, B. Braaf, C. K. Sheehy, Q. Yang, P. Tiruveedhula, D. W. Arathorn, J. F. de Boer, and A.

Roorda, "Real-time eye motion compensation for OCT imaging with tracking SLO," Biomed. Opt. Express **3**, 2950 (2012).

[41] C. K. S. Leung, A. C. K. Cheng, K. K. L. Chong, S. L. King, S. Mohamed, C. S. L. Lau, C. Y. L. Cheung, G. C. H. Chu, R. Y. K. Lai, C. C. P. Pang, and D. S. C. Lam, "Optic disc measurements in myopia with optical coherence tomography and confocal scanning laser ophthalmoscopy," Investig. Ophthalmol. Vis. Sci. **48**, 3178-3183 (2007).

[42] J. E. DeLeon Ortega, L. M. Sakata, B. Kakati, G. McGwin, B. E. Monheit, S. N. Arthur, and C. A. Girkin, "Effect of glaucomatous damage on the repeatability of confocal scanning laser ophthalmoscope, scanning laser polarimetry, and optical coherence tomography," Investig. Ophthalmol. Vis. Sci. **48**, 1156-1163 (2007).

[43] J. I. W. Morgan and E. N. Pugh, "Scanning laser ophthalmoscope measurement of local fundus reflectance and autofluorescence changes arising from rhodopsin bleaching and regeneration," Investig. Ophthalmol. Vis. Sci. **54**, 2048-2059 (2013).

[44] J. V. Kristjansdottir, S. H. Hardarson, G. H. Halldorsson, R. A. Karlsson, T. S. Eliasdottir, and E. Stefánsson, "Retinal oximetry with a scanning laser ophthalmoscope," Investig. Ophthalmol. Vis. Sci. **55**, 3120-3126 (2014).

[45] B. Zhang, N. Li, J. Kang, Y. He, and X. Chen, "Adaptive optics scanning laser ophthalmoscopy in fundus imaging, a review and update," Int. J. Ophthalmol. **10**, 1751-1758 (2017).

[46] S. Marcos, J. S. Werner, S. A. Burns, SA, W. H. Merigan, P. Artal, D. A. Atchison, K. M. Hampson, R. Legras, L. Lundstrom, G. Yoon, J. Carroll, S. S. Choi, N. Doble, A. M. Dubis, A. Dubra, A. Elsner, R. Jonnal, M. Paques, Y. Zhang, M. Campbell, J. Hunter, A. Metha, G. Palczewska, J. Schallek, and L. C. Sincich, "Vision science and adaptive optics, the state of the field.," Vision Res. **132**, 3-33 (2017).

[47] Y. Kaizu, S. Nakao, I. Wada, M. Yamaguchi, K. Fujiwara, S. Yoshida, T. Hisatomi, Y. Ikeda, T. Hayami, T. Ishibashi, and K. Sonoda, "Imaging of Retinal Vascular Layers: Adaptive Optics Scanning Laser Ophthalmoscopy Versus Optical Coherence Tomography Angiography," Transl. Vis. Sci. Technol. **6**, 2 (2017).

[48] W. Drexler and J. G. Fujimoto, "State-of-the-art retinal optical coherence tomography," Prog. Retin. Eye Res. **27**, 45-88 (2008).

[49] A. G. Podoleanu and R. B. Rosen, "Combinations of techniques in imaging the retina with high resolution," Prog. Retin. Eye Res. **27**, 464499 (2008).

[50] A. G. Podoleanu, "Optical coherence tomography," J. Microsc. **247**, 209-219 (2012).

[51] S. H. Yun, G. J. Tearney, B. E. Bouma, B. H. Park, and J. F. De Boer, "High-speed spectral-domain optical coherence tomography at 1.3 μm wavelength," Opt. Express **11**, 35983604 (2003).

[52] T. C. Chen, A. Zeng, W. Sun, M. Mujat, and J. F. De Boer, "Spectral-domain optical coherence tomography and glaucoma," Int. Ophthalmol. Clin. **48**, 2945 (2008).

[53] J. F. de Boer, B. Cense, B. H. Park, M. C. Pierce, G. J. Tearney, and B. E. Bouma, "Improved signal-to-noise ratio in spectral-domain compared with time-domain optical coherence tomography," Opt. Lett. **28**, 2067 (2003).

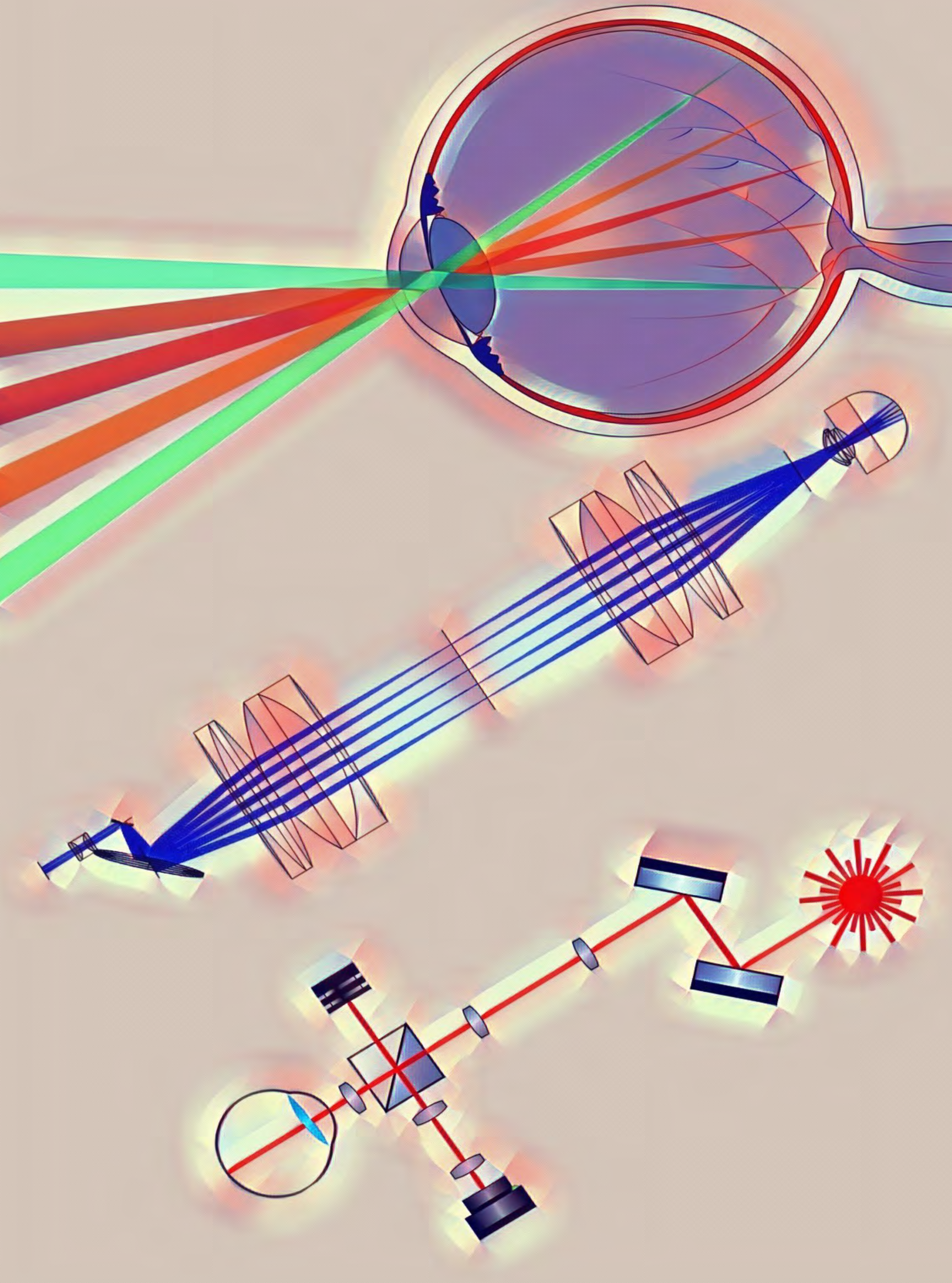

2

Principles of retinal imaging and retinal oximetry

Overview

Modern retinal imaging systems produce dynamic, high-resolution images at low irradiation at a high frame rate. Continuous acquisition of high-contrast images of the retina and other structures in the ocular fundus is possible. An excellent example of a system which benefits from this versatility is a Scanning Laser Ophthalmoscope (SLO). The SLO is a tool that has expanded the therapeutic and diagnostic abilities of retinal imaging not only through qualitative imaging but also through added techniques such as perimetry and angiography. The SLO is comparable in its scope of application and utility to Optical Coherence Tomography (OCT), and both these imaging techniques complement each other perfectly. In this chapter, we outline the principles of scanning-based retinal imaging by using a digital micromirror device (DMD) or a pair of scanning mirrors to produce high contrast images of the human retina. As an important application of retinal imaging, measuring oxygen saturation from the retina is introduced in this chapter in detail as well.

2.1 Retinal imaging by scanning

The first effort to introduce an ophthalmic imaging technique which would not suffer from the limitations of fundus photography was the SLO [1–6]. In the SLO, a narrow beam of 2-4 mm diameter is focused by the cornea and lens to a single point of $\sim$10 µm in the retina. An image is produced by scanning the beam over the retina usually in a raster pattern and detecting the reflected light from each scan point, to produce a digital image. Beam deflection is typically achieved by a combination of two galvanometer scanners, one slow scanner and one fast scanner, to provide scanning in both horizontal and vertical directions. A basic design of an SLO is given in Fig. 2.1.

Widefield imaging systems such as the fundus camera (see section 1.2.1) suffer from corneal back reflections. To avoid these strong reflections, typical fundus camera employs annular illumination where the annulus is imaged on to the pupil. The reflected light from the retina is collected only through a small central spot of the pupil. In contrast, the SLO illuminates a narrow beam through a central portion of the pupil and the reflected light is collected over the entire pupil. This results in increased light collection efficiency, and with a confocal arrangement consisting of illumination and detection pinholes to reject out-of-focus light, the confocal SLO (cSLO) rejects corneal reflections and further increases resolution and contrast through confocality. A pair of scanners are used to construct a two-dimensional scan [7]. The generalised design is described in Fig. 2.1. A Common optical path-

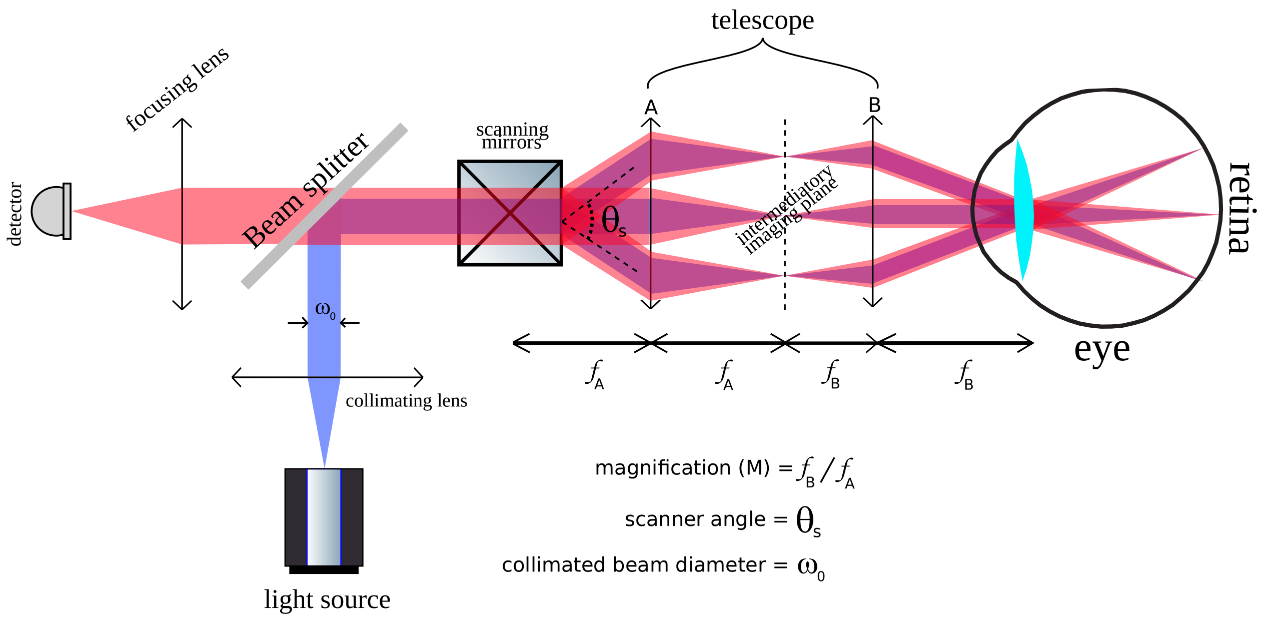
telescope
focusing lens
detector
Beam splitter
scanning mirrors
A
B
θ_s
intermediatory imaging plane
retina
eye
ω_0
collimating lens
light source
f_A
f_A
f_B
f_B
magnification (M) = f_B / f_A
scanner angle = θ_s
collimated beam diameter = ω_0

Figure 2.1: Simplified illustration of a scanning laser ophthalmoscope. Light from the light source is collimated using a collimating lens, and a portion of the light (based on the splitting ratio of the beam splitter) is used for illumination. Scanning mirror is then used to scan the retina continuously. The scanning mirrors can be a simple galvo-scanner which is used for slow scanning (typically: 5-60 Hz, maximum 1 kHz) or a resonant scanner which can scan up to 20 kHz. The mirrors can be placed as close as physically possible or in some implementations; a relay is used to image one mirror on to another. A telescope made up of lenses A and B is used to relay the pivotal point of the scanning mirrors on to the pupil plane. The reflected light from the retina follows the same path and is collected by the detector. The magnification of the telescope is M, the scan angle of the scanner is θ_s, and the collimated beam diameter is ω_0.

way (relay telescope) for illuminating and collecting reflected light from the retina is split into separate paths near the source and the detector. The relay telescope can be made of either lens or curved, and the beam diameter and the focal length of these focusing elements (A and B in Fig. 2.1) determine the magnification and the size of the beam on the pupil plane. For a magnification (M), the size of the beam in the pupil plane is given by M$\times\omega_0$, where ω_0 is the size of the collimated beam from the source. The diffraction-limited spot size (d_{spot}) on the retina considering an aberration-free eye lens of focal length f_{eye} is then,

$$d_{spot} = \frac{2 \cdot \lambda_{ill} \cdot f_{eye}}{\pi \cdot (M \times \omega_0)} \tag{2.1}$$

where λ_{ill} is the illumination wavelength. The combined optical power of both the cornea and the crystalline lens focuses the light onto the retina. The power of this simplified eye model is 60 D and has a corresponding focal length f$_{eye}$ of 16.7 mm in air. The critical design parameters of the SLO design are the Field-of-view (FOV) and frame rate (frames/s).

In retinal imaging, the diameter of the pupil, d$_{pupil}$ is usually the limiting aperture limiting the amount of light entering the eye. Under normal conditions, d$_{pupil}$ remains at around 2-3 mm and reaches 6-7 mm with dark adaptation or with the application of pupil dilating eye drops such as tropicamide. The number of frames per second or the imaging frame rate is given by the ratio of the fast scanning frequency to the number of lines per each recorded frame. i.e.,

$$frames/s = \frac{2 \times resonant frequency}{lines/frame} \tag{2.2}$$

One disadvantage of using a resonant scanning mirror in the SLO is that it introduces distortion into the recorded image due to the non-constant scan velocity of the scanning mirrors. With a resonant mirror, the position of the laser changes with a sinusoidal motion of the mirrors. As a result, the image obtained is stretched progressively towards the edges. The image should be corrected for this sinusoidal distortion, as illustrated in Fig. 2.2.

2.1.1 Line scanning

Line scanning SLO (LSLO) [3, 6] uses an anamorphic optical element such as a cylindrical lens to create a line illumination on the retina in one dimension. Only one scanning mirror is needed to scan the beam in the other dimension. A slit

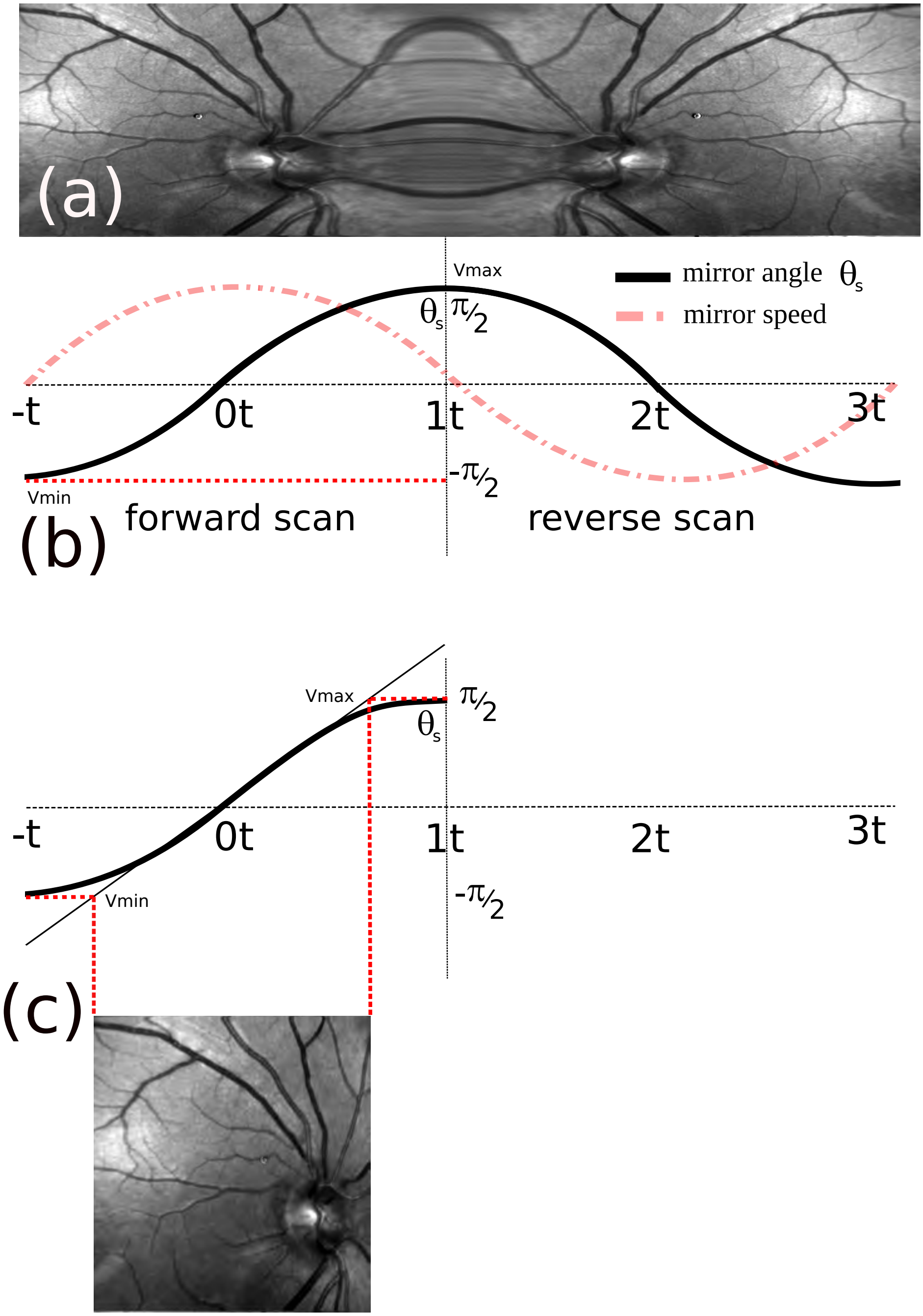
(a)
Vmax
mirror angle θ_s
mirror speed
θ_s
$\pi/2$
-t
0t
1t
2t
3t
$-\pi/2$
Vmin
(b)
forward scan
reverse scan
Vmax
$\pi/2$
θ_s
-t
0t
1t
2t
3t
Vmin
$-\pi/2$
(c)

Figure 2.2: Image correction for resonant scanners — (a): Half-height, double-width images collected by a fixed frequency pixel clock. The mirrored-image is collected by the forward and reverse scan of the resonant mirror. (b): The relationship between the mirror angle θ_s and the mirror velocity during the forward and the reverse scan (c): the correction factor is determined by the ratio of the actual mirror motion and the predicted linear motion. The pixels are then reassigned as shown in the corrected image.

aperture instead is placed of the circular aperture in the conjugate plane; a line detector is used in place of a point detector. With the LSLO, the scattered light is rejected in only one dimension, and thus there is reduced confocality compared to the confocal SLO. However, the imaging speed of the LSLO is significantly higher compared to the confocal SLO. The improvement in the imaging speed scales with the square root of the same FOV since the scanning is only in one dimension for the LSLO. Further, for line projection onto the retina, the maximum permissible exposure is higher compared to conventional SLO. For a detailed description of the principle and construction of an LSLO, the readers are pointed towards Hammer *et al.* [3].

2.1.2 Digital micromirror devices

To reduce the cost and complexity of an SLO, Digital micromirror devices (DMDs) are used as an alternative to galvo scanners. DMDs are based on microscopically small mirrors that are controlled by applying a voltage or current between the two electrodes around the mirror arrays. The DMD is both a micro-electronic mechanical system (MEMS) and a spatial light modulator (SLM). It is a MEMS because it consists of hundreds of thousands of moving micromirrors that are controlled by underlying CMOS electronics, as shown in Fig. 2.3. The spatial light modulator technology pioneered by Texas instruments evolved into the invention of the DMD by Dr Larry Hornbeck in 1986 [8]. The number of mirrors corresponds to the resolution of the projected image. These mirrors can be repositioned rapidly to reflect light either into the desired direction or onto a light dump. To produce greyscales, the mirror is toggled on and off very quickly, and the ratio of on-time to off-time determines the shade produced (binary pulse-width modulation). Liquid crystal devices (LCDs) are also widely-used as SLMs in either transmission or reflection but do not have the speed, precision, or broadband capability that makes the DMD so attractive for many applications.

DMDs have been used for retinal imaging by projecting a series of scan patterns [5, 6, 9, 10] without using conventional scanning mirrors. The DMD provides temporal and spatial flexibility for illumination, which can have several advantages, such as optimising the system for speed and confocality.

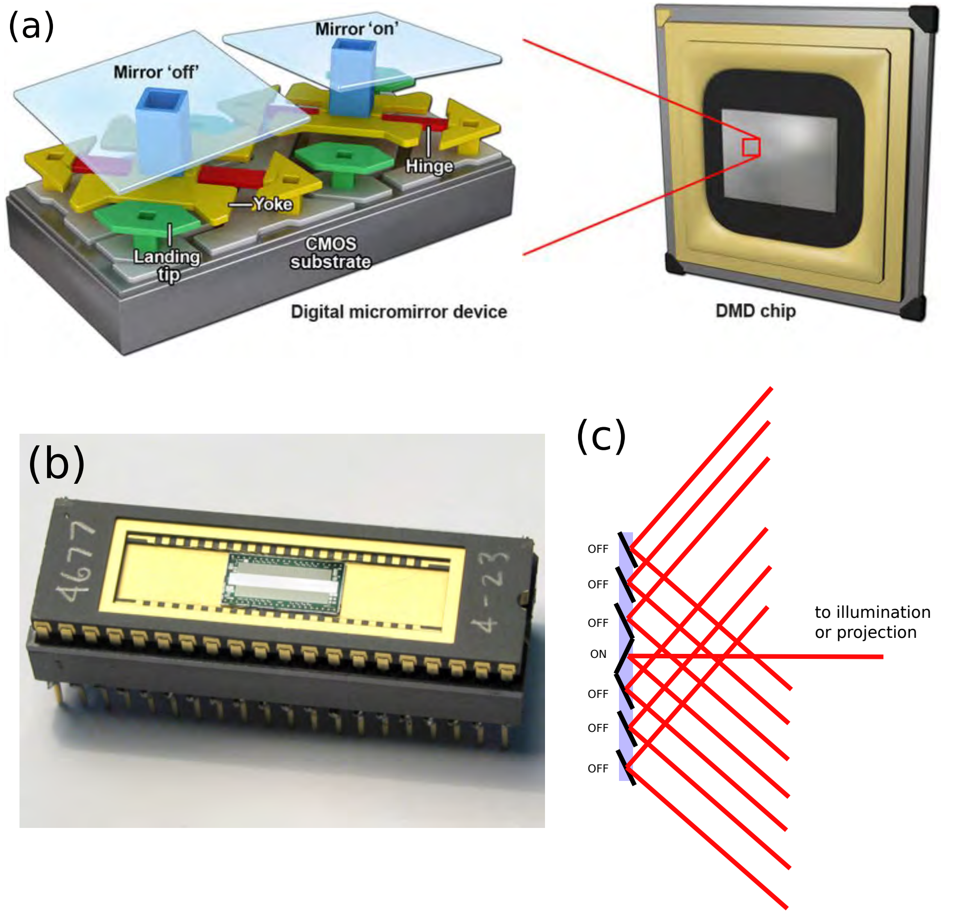
(a)
Mirror 'on'
Mirror 'off'
Hinge
Yoke
Landing tip
CMOS substrate
Digital micromirror device
DMD chip
(b)
4677
4-23
(c)
OFF
OFF
OFF
ON
OFF
OFF
OFF
to illumination or projection

Figure 2.3: (a): DMD construction — a pair of micromirrors are zoomed in from a DMD chip showing the 'ON' and 'OFF' state of the DMD with the corresponding directions of flipping. Each micromirror is attached to a yoke and is connected to the CMOS substrate (image courtesy of [11]). (b): one of the earliest prototypes of the DMD chip. The descendants of this chips can be found in many applications today (image courtesy of *ti.com*). (c): Simplified working of the DMD showing the light from the 'ON' mirrors are directed towards an axis which can be used for projection or illumination while the light from the 'OFF' mirrors are deflected away.

2.2 Retinal imaging — optical considerations, laser safety and wavelength ranges

2.2.1 Optical considerations

Aberrations in the eye

The human eye is a simple optical device with only two elements: the cornea and the crystalline lens. However, there is no good model of the optics of an individual eye due to large interpersonal variations and changes in the optical quality and characteristics with age. The optical quality of the focusing structures in the eye affects the imaging quality. The optical aberrations in the eye affect the resolution [13], and any optical opacity in the crystalline lens or the cornea for the imaging wavelength is detrimental to the imaging quality. The defocus error in most SLOs, including the SLOs in this thesis were corrected by translating the ophthalmic lens (last lens before the cornea) to achieve sharp images. For multispectral imaging of the retina (as described in **Chapter 5 and 6**) the significant chromatic dispersion of the optics of the eye [14] had to be considered for the design of the optics. This chromatic dispersion leads to longitudinal chromatic aberration (LCA) and transverse chromatic aberration (TCA). The magnitude of LCA is about 2.5 D for visible wavelengths between 400 and 700 nm [15] while between 700 and 900 nm, the value of LCA was $\sim$ 0.4 D [16]. LCA also shows less interpersonal variation and is considered to be independent of age [17, 18]. TCA can be corrected (partially) by post-processing techniques by warping the images of different colours to match. Powell [19] suggested the idea of correcting LCA with a lens having opposite dispersion of the eye. Zawadzki *et al.* [20] used such an achromatising lens or dispersion compensating lens (DCL) for Ultrahigh-resolution OCT. Various other groups have used these lenses for OCT and SLO applications [21–23]. In our multi-colour SLO, sharp images at multiple wavelengths were required; therefore, we implemented LCA correction. The simulation of such a DCL in the common path of the SLO is shown in Fig. 2.4.

Optical properties of the retina

The fundamental optical properties of biological tissues such as the retina can be used for the diagnosis of various diseases. A clear understanding of optical properties is thus critical for understanding the quantitative changes in the retina. The optical properties influence the propagation of light in the retinal tissues and vasculature. Thanks to the transparency of the anterior ocular media, ophthalmologists can

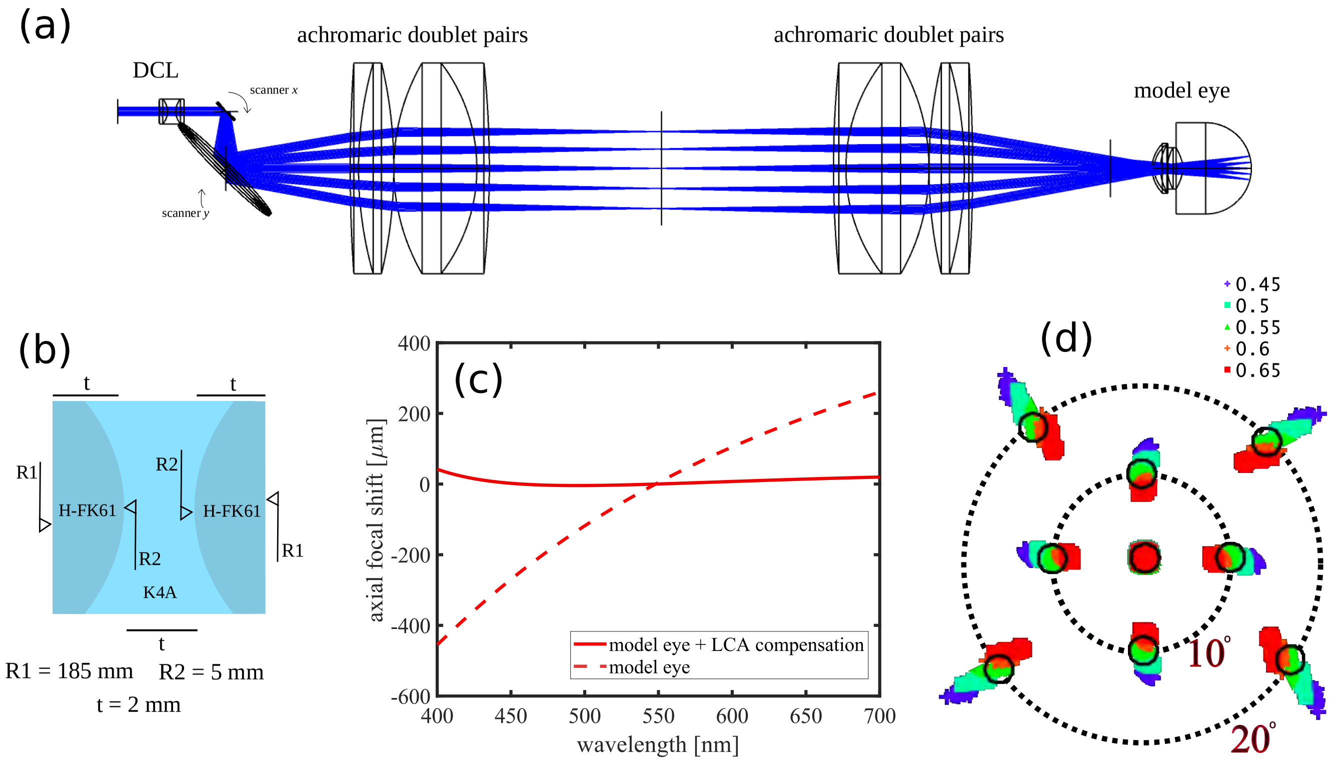

Figure 2.4: (a): Zemax simulation of SLO common path — a zero power dispersion-compensating lens (DCL) was placed in the collimated portion of the beam before the scanners. A telescope comprising of two achromatic doublet pairs was used to image the pivotal point in between the scanners on to the pupil plane. A model eye matching the physical parameters of a healthy human eye was used in the simulation [24]. (b): Design of the DCL with relevant radii and thicknesses. The materials used were H-FK61, and K4A (CDGM catalogue, Universal photonics inc., USA) (c): focal shift at the surface of the retina of the eye model from 400 to 700 nm after passing through optics shown in (a) is shown by the red dashed line. After correction with the DCL (shown by a red line), the focal shift is corrected between the colours. The maximum focal shift range is 40 μm and 0.62 mm for the system with and without correction, respectively. (d): The TCA between different wavelengths from 450 nm to 650 nm show as spot diagrams. The black circle represents the diffraction limit. TCA can be compensated partially by performing an image transform to match the different colours at the same spatial location.

have a direct look into the posterior non-transparent part of the eye. Optical analysis of the emitted light from the fundus has been used to investigate the metabolism and pathology of the retina [25]. Inhomogeneities in the retina arising from the cell components cause scattering [26], while pigments such as haemoglobin and melanin cause absorption. The corresponding wavelength-dependent optical parameters are the scattering coefficient of μ_s [mm^{-1}]. the scattering anisotropy g [-], and absorption coefficient μ_a [mm^{-1}].

Melanin, a dark-brown pigment present in the RPE of the retina, is the primary component for light scattering and absorption in the fundus. Blood is confined to the retinal vasculature and scatters light. However, the most prominent optical characteristic of blood is the absorption as can be readily seen in Fig. 2.5.

Haemoglobin light absorbance

The light is absorbed and scattered in blood by the discoid-shaped erythrocytes. This optical behaviour is a result of the highly concentrated haemoglobin (Hb) content of the cell. Haemoglobin (Hb) is the most vital component in human blood and is responsible for transporting oxygen. Haemoglobin is composed of four heme groups. Each of these four heme groups contains one Fe^{2+} ion, which can bind one oxygen molecule. Haemoglobin shows distinct absorption peaks in the visible range based on the oxygenation of the Haemoglobin molecule, as shown in Fig. 2.5(b). There are many types of Hb, but Hb-A is the most abundant in healthy adult humans [27]. During inhalation of normal atmospheric air, around 9 mmol/L of oxygen is bound to haemoglobin [28]. Oxygen saturation (S) is defined as the proportion (or more often, percentage) of Hb that is bound to oxygen.

$$S = \frac{[HbO_2]}{[Hb] + [HbO_2]} \tag{2.3}$$

where $[HbO_2]$ and $[Hb]$ are the concentration of the oxy- and deoxy-Hb, respectively. Oxy- and deoxy- Hb has different colours and thus, different absorption, as shown in Fig. 2.5(a). This difference in absorption spectrum can be used to determine the oxygenation of blood by spectroscopy, an aim of this thesis. However, at certain wavelengths, the absorption is the same, and these points are called as 'isosbestic' wavelengths (Fig. 2.5(b)).

2.2.2 Laser Safety considerations in retinal imaging

Intentional exposure of light radiation on the eye for retinal imaging is a major safety concern and strict safety standards are in place to ensure safety during imag-

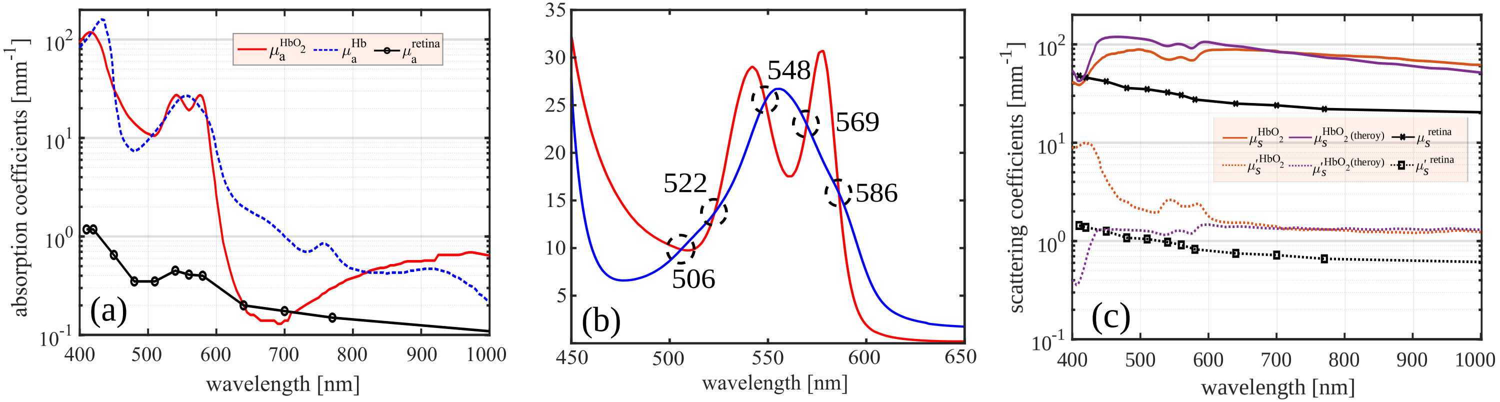

Figure 2.5: (a): Absorption spectrum of oxy- and deoxyhaemoglobin from 400 nm to 1000 nm assuming a concentration of 150 mg of haemoglobin in 1 mL of blood [29]. The absorption spectrum of neural retina measured *in vitro* by Hammer *et al.* [26] is shown for comparison. (b): The absorption spectrum from 450 nm to 650 nm on a linear scale. The absorption of these two types of haemoglobin is different for most wavelengths except for the isosbestic points (denoted by black dashed circles: 506 nm, 522 nm, 548 nm, 569 nm, and 586 nm) where the absorption depends on factors other than the 'oxygen saturation'. (c): The theoretical and experimental scattering coefficient of whole blood from Bosschaart *et al.* [30] in the 400 nm to 1000 nm regime showing a strong scattering of blood. The scattering, reduced scattering coefficient of retina [26] is shown for comparison.

ing. Damage to retina due to light exposure is caused by two mechanisms namely thermal damage and photochemical damage [31]. *Thermal damage* occurs due to temperature increase caused by melanin absorption in the RPE causing denaturation of proteins [32, 33]. The *photochemical damage* occurs in the wavelengths between 400 and 600 nm for duration longer than a second due to photo-oxidation in the photoreceptors and lipofuscin pigments [34, 35].The biological effects of laser radiation on the eye is given in Table 2.1.

Table 2.1: Biological effects of laser radiation on the eye [31]

UV-A (315-400 nm)	Photo-chemical damage, Cataract
Visible (400-780 nm)	Photo-chemical and thermal retinal injury, Colour and night vision degradation
Infrared A (780-1400 nm)	Retinal burns, Cataract
Infrared B (1400-3000 nm)	Corneal burn, aqueous flare, IR Cataract

Calculations for the maximum permissible exposure (MPE) on the retina were performed using the latest laser safety standard IEC 60825-1 published in 2014 [36]. The most conservative estimate of the maximum permissible exposure (MPE) can be obtained by assuming a collimated, static beam entering the eye. A limiting aperture (LA) to determine MPE for the eye was taken to be 7 mm (diameter). A 7 mm LA equals an area of 3.85 × 10^5 m^2 [m^2]. The accessible emission limit (AEL) was then calculated as,

$$AEL = MPE \times LA \tag{2.4}$$

From the IEC standard, the AEL expressed as irradiance or radiant exposure for a wavelength range from 450 nm to 1150 nm for a collimated beam (the correction factors for AEL calculation : C_6 = 1, C_7 = 1) with exposure time of 10 seconds or longer is given by,

$$AEL = \begin{cases} 10^{0.02\cdot(\lambda-450)}[Wm^{-2}] \times 3.85 \times 10^{-5}[m^2] & 450 \leq \lambda \leq 500 \\ 10[Wm^{-2}] \times 3.85 \times 10^{-5}[m^2] & 500 \leq \lambda \leq 700 \\ 10 \cdot 10^{0.002\cdot(\lambda-700)}[Wm^{-2}] \times 3.85 \times 10^{-5}[m^2] & 700 \leq \lambda \leq 1150 \end{cases}$$

The calculated AEL based on the standard is shown in Fig. 2.6. In chapter 3, we used concentric circle illumination on the retina, which extends to the whole field of view. The most conservative estimate of the AEL can be obtained by assuming a collimated static beam entering the eye. For the limiting aperture, a pupil size

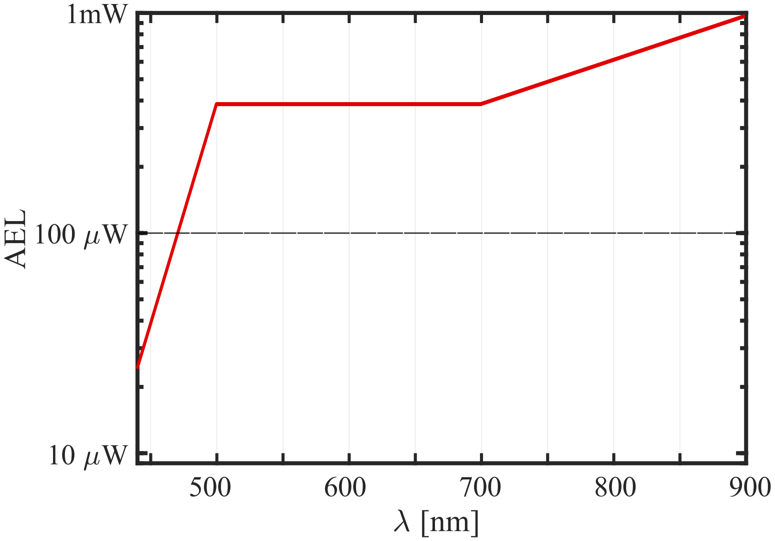

Figure 2.6: The accessible emission limit for different wavelengths for 8 hrs 20 min (30000 seconds) continuous, single point exposure— based on IEC 60825-1.

of 7 mm was used. Thus, based on Fig. 2.6, a limiting AEL of 630 µW was used. However, concentric circles are projected within the whole FOV, and the power is distributed amongst all of the circles. If the illumination of the retina is assumed to be what the standard calls extended view, the MPE limit will be more than an order of magnitude higher.

In chapters 4-6, scanners were used to scan multiple wavelengths in the whole FOV. In this case, the following criterion was used to ensure safety:

$$\frac{P(\lambda_1)}{AEL(\lambda_1)} + \frac{P(\lambda_2)}{AEL(\lambda_2)} + \frac{P(\lambda_3)}{AEL(\lambda_3)} + ... \leq 1 \tag{2.5}$$

Where the P(λ) is the applied power per wavelength divided by the corresponding AEL(λ) value, based on the AEL and the detector sensitivity, the ratio of P(λ) and AEL(λ) was chosen suitably for optimum image quality.

Significant increase in AEL can be obtained by considering a line or area illumination in the retina instead of a spot illumination. In chapter 3, we describe a DMD based ophthalmoscope to scan multiple concentric circles on the retina. In chapters 5 and 6, we use an SLO with a resonant scanner and a galvo scanner, where the fast scan can be considered as a line projection on to the retina. Figure 2.7 shows the AEL for line projection in the retina, where it can be observed that the AEL is significantly higher compared to Fig. 2.6. However, in the *in vivo* experiments in

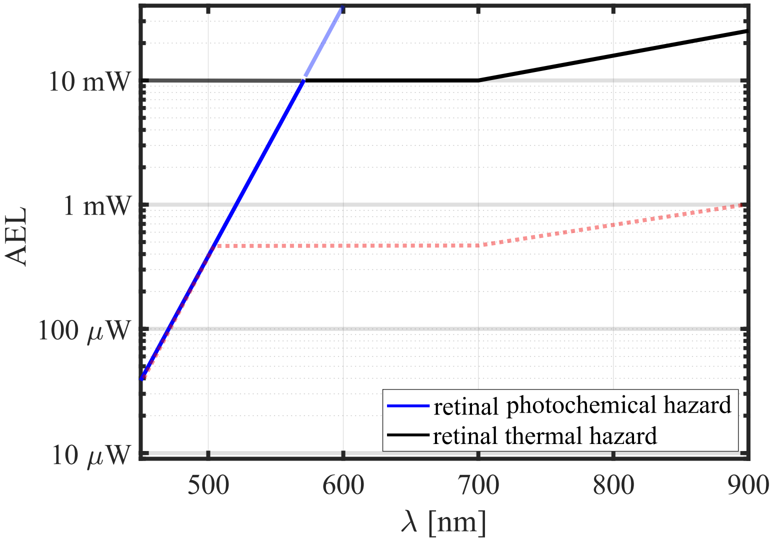

Figure 2.7: The accessible emission limit for a line projection at different wavelengths based on IEC 60825-1. The following parameters were used to arrive at this graph : α_{min} = 1.5 mrad, α_{max} = 100 mrad (see IEC 60825-1). The dotted red line corresponds to single point exposure for 8 hrs 20 mins (Fig. 2.6).

chapters 5 and 6, conservative AEL based on Fig. 2.6 was used.

2.2.3 Light sources and signal to noise estimation

Ophthalmic imaging, like any tissue imaging, requires a suitable wavelength of light based on the tissues which light has to traverse. Different types of tissues affect image quality and information as they absorb and scatter differently. In retinal imaging, light has to travel through a 25 mm column of vitreous humour before reaching the retina. The vitreous is 99% water, and hence highly absorbs ultra-violet (UV) and infra-red (IR) light. As a result, wavelengths roughly shorter than 400 nm and longer than 1100 nm are not usually chosen for retinal imaging. There are other essential factors to consider the wavelength choice based on the application (which is described in **Chapter 4**), and safety, as explained in section 2.2.2.

A simplified model of how a pixel grey value is created is shown in the Figure 2.8. The number of photons (mean = μ_p, variance = σ_p^2) hitting the sensor during the exposure time t_{exp} are converted to electrons (mean = μ_e, variance = σ_e^2) with a wavelength dependent quantum efficiency $\eta(\lambda)$. The number of electrons fluctuates statistically with a *Poissonian distribution* whose mean and standard deviation are the same. Thus,

$$\mu_e = \sigma_e^2 \tag{2.6}$$

The noise arising due to particle nature of electrons and photons is called *shot noise*

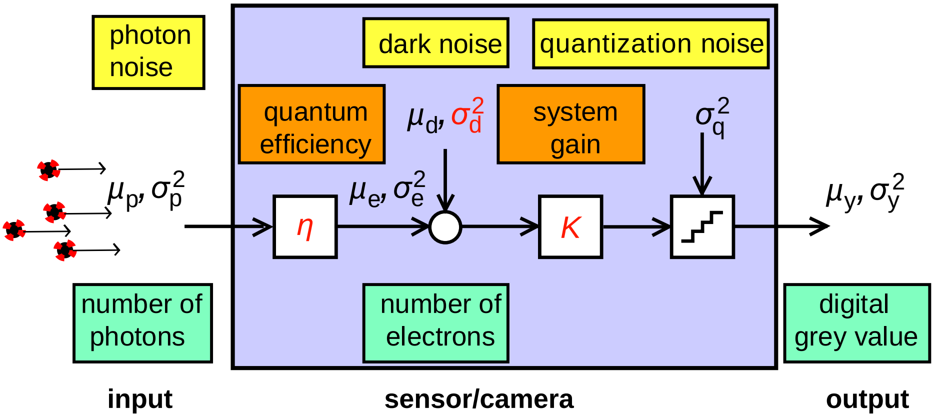
photon noise
dark noise
quantization noise
quantum efficiency
μ_d, σ_d^2
system gain
σ_q^2
μ_p, σ_p^2
μ_e, σ_e^2
η
K
μ_y, σ_y^2
number of photons
number of electrons
digital grey value
input
sensor/camera
output

Figure 2.8: Noise model of a detector sensor or camera adapted from EMVA standard [37] showing how a grey value is generated. The mean values are represented as $\mu_{(\cdot)}$, and the variance as $\sigma^2_{(\cdot)}$ respectively. K is the system gain and η is the quantum efficiency. The intrinsic detector parameters are in red.

and the performance of all imaging systems is limited by shot noise. All noise sources related to the detector read-out and amplifier can be described by a signal independent, normal distributed noise source called *thermal noise* with variance σ_d^2. The mean electrons are digitised to a grey value (mean = μ_y, variance = σ_y^2) with a overall gain of K and this process suffers from *quantization noise* (variance = σ_q^2). The noise adds up in an linear fashion and we can write

$$\sigma_y^2 = K^2 \cdot (\sigma_d^2 + \sigma_e^2) + \sigma_q^2 \tag{2.7}$$

This equation is central to a noise-figure estimation of any imaging system. The signal to noise ratio (SNR) can then be defined in terms of grey values as

$$SNR = \frac{\mu_y - \mu_{dark}}{\sigma_y} \tag{2.8}$$

or in terms of number of photons as

$$SNR(\mu_p) = \frac{\eta \cdot \mu_p}{\sqrt{\sigma_d^2 + \sigma_q^2/K + \eta(\lambda) \cdot \mu_p}} \tag{2.9}$$

This means that the SNR increases linearly at low irradiation when dark and quantisation noise dominate shot noise to a slower square root increase at high irradiation when shot noise dominates dark noise and quantisation noise. In this thesis, there are two types of light sources used for retinal imaging namely a LED at 810 nm (**Chapter 3**) and a supercontinuum light source for visible wavelengths (**Chapter 4-6**).

2.3 Retinal Oximetry

As was mentioned in **Chapter 1**, one of the main focuses of this thesis is measuring blood components such as oxygenation in retinal blood vessels. Blood flow within the retinal vasculature supplies oxygen and nutrients to the retinal layers and helps to dispose of waste products [38]. Maintenance of normal retinal function depends on a continuous supply of oxygen and on the capability to detect and respond rapidly to local oxygen deficiency or hypoxia. Retinal hypoxia can cause retinal dysfunction and degeneration that lead directly to vision loss. In this section, the role of retinal oximetry in retinal pathologies and the overall technological progress in measuring retinal oximetry is presented.

2.3.1 Retinal diseases and oxygenation

Most major retinal pathologies mentioned in section 1.1.2 cause alteration in the retinal oxygenation. For example, both retinal vessel occlusions (RVO) and diabetic retinopathy (DR) cause hypoxia [39]. Several changes are induced in the retina during hypoxia, most prominent being the vascular endothelial growth factor or VEGF. There are reports about the increase in VEGF in DR by various investigators [40, 41]. Another change which happens as a result of hypoxia in the retina is overexpression of Hypoxia ineducable factor 1 or HIF1 [42, 43].

Retinal vessel occlusions result in a decrease in blood flow in the retina and thus affects oxygenation staring from capillary level [44] and can be seen with a fundus camera when the occlusion reaches artery or vein level. However, it is difficult to reliably and accurately measure oxygen saturation in small vessels with a fundus camera. SLOs are expected to perform better for diagnosis and follow-ups on vessel occlusions in small capillaries due to increased resolution. Retinal oxygen saturation is considered as an independent risk factor for the severity of diabetic retinopathy [45]. DR causes damage to the retinal capillaries and micro-aneurysms, causing reduced blood flow and hypoxia. The major result of hypoxia in the retina is neovascularisation. The retina tries to grow new vessels in response to hypoxia. The new vessels pose a risk of haemorrhage due to their fragility.

Glaucoma is another disease where oxygen metabolism is affected. Glaucoma causes an increase in intraocular pressure (IOP), which in turn affects the blood flow [46]. Vandewalle *et al.* [47] reported that the arterio-venule (A-V) difference in oxygen saturation decreased as the rim area and the nerve fiber layer decreased in glaucomatous patients. Since Glaucoma treatment alters the blood flow and IOP, oximetry measurements before and after glaucoma treatment may help to understand the role of blood flow and oxygen saturation in glaucoma [48]. For example, it is very valuable to investigate whether a glaucoma patient receives enough blood flow and oxygenation after treatment. Age-related macular degeneration (AMD) is the leading cause of irreversible blindness throughout the world. Ageing and age-associated degenerative diseases, such as AMD, are intimately associated with decreased levels of tissue oxygenation and hypoxia that may induce accumulation of detrimental RPE-associated deposits, inflammation and neovascularisation processes in the retina.

2.3.2 Evolution of retinal oximetry

There has been a need for better instruments for oxygen measurements in the retina over the past few decades.The earliest attempts at *in vivo* retinal oximetry started in the 1960's based on work by Hickam *et al.* [49, 50]. Significant developments in the field came when François Delori developed a 3 wavelength retinal oximetry method that could operate continuously [51]. Delori determined oxygen saturation by scanning a focused point of light across the vessel, allowing both the vessel diameter and the optical density of the blood to be calculated from the profile of the reflected light. Vessel tracking was used to minimise the effects of eye movements during scanning.

Smith *et al.* [52] developed a prototype eye oximeter (Fig. **??**(a)) to study the effect of blood loss on retinal venous oxygen saturation, with a goal to apply their technique to monitoring trauma patients [52]. Two diode lasers emitting at 670 nm and 803 nm were initially used in the eye oximeter (EOX) to produce a line scan of a retinal vessel. A photodiode was used to measure the reflected light from the retina and blood vessel. An imaging ophthalmic-spectrometer was developed by Schweitzer *et al.* to analyse the spectral reflection of pigments such as melanin, and xanthophyll in the fundus. The reflectance spectrum in the range from 450 nm to 700 nm with a spectral resolution of 2 nm was acquired from a small area using a spectrograph. The measurement of the oxygen saturation in retinal vessels involved extensive analysis of the properties of fundus reflectance and the multiple light pathways in the retina [53]. The mean oxygen saturation was found to be 92.2±4.1 % for arterial blood and 57.9±9.9 % for venous blood. Beach *et al.* [54] attempted two-wavelength oximetry using an isosbestic wavelength and oxygen-sensitive wavelength in a fundus camera. They also attempted to calibrate the oxygen saturation values based on vessel diameters and pigmentation in the fundus.

In the past decade two commercially available retinal oximetry systems— the Oxymap retinal oximeter (Oxymap ehf, Iceland) [55] and the Imedos retinal oximeter (Imedos Systems UG, Germany) [56] (Fig. 2.9) have been used for various clinical studies to measure oxygenation under different retinal pathologies.

A critical factor for clinically relevant retinal oximetry is to be able to determine blood oxygen saturation in small retinal vessels — capillaries, venules and arterioles. It is in these microvessels that the oxygen saturation is expected to decrease in response to increased metabolic demand or decreased oxygen delivery capacity. The larger retinal vessels ($>$100 µm) are expected to be less sensitive to changes in tissue metabolic demand or microvascular dysfunction and are therefore not ideal as early hypoxia markers.

Spectral Domain optical coherence tomography (SD-OCT) based on visible wavelengths [22, 23, 59] has been used to measure oxygenation in retinal blood vessels. Recent intense and broadband supercontinuum light sources have made it possible to perform OCT in the visible wavelength regime. Visible light OCT enables oxygen saturation mapping and has a higher axial resolution for a given wavelength bandwidth compared to 800 nm or 1000 nm OCT. Higher absorption and scattering of the retina at visible wavelengths limit penetration depths. Further, Supercontinuum light source used in visible OCT systems introduces significant amounts of relative intensity noise.

Various groups have also undertaken hyperspectral imaging [60–63] approaches towards in vivo retinal oximetry. However, acquiring images with sufficient SNR from multiple wavelengths at high spatial resolution remains a challenge in hyperspectral imaging.

2.3.3 Comparison of oximetry techniques

SLO based oximetry systems have advantages over other techniques based on fundus camera based multispectral or hyperspectral imaging. As mentioned in section 2.2, SLOs are capable of producing high contrast, confocal images due to scanning and use of a confocal pinhole. SLOs also typically use lasers to create monochromatic images at multiple wavelengths, and minimise unnecessary exposure of light

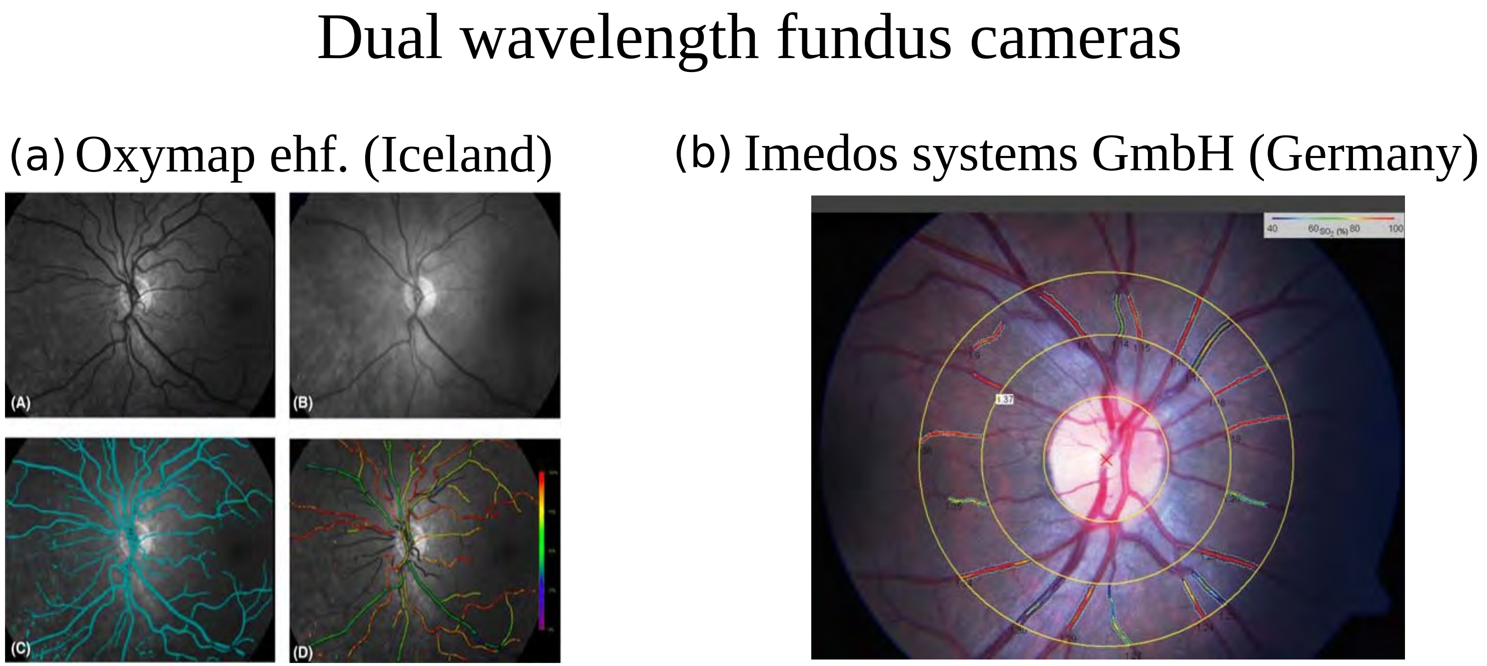
Dual wavelength fundus cameras
(a) Oxymap ehf. (Iceland)
(b) Imedos systems GmbH (Germany)
(A)
(B)
(C)
(D)
40
60 SO₂ (%) 80
100
1.37

Figure 2.9: (a): the Oxymap retinal oximeter (Reykjavik, Iceland) using 570 nm and 600 nm wavelengths to map the oxygen saturation values (b):Retinal oxygen saturation measurement by Imedos UG, Jena, Germany. (images taken from Rilven *et. al*.[57] and Man *et al.* [58])

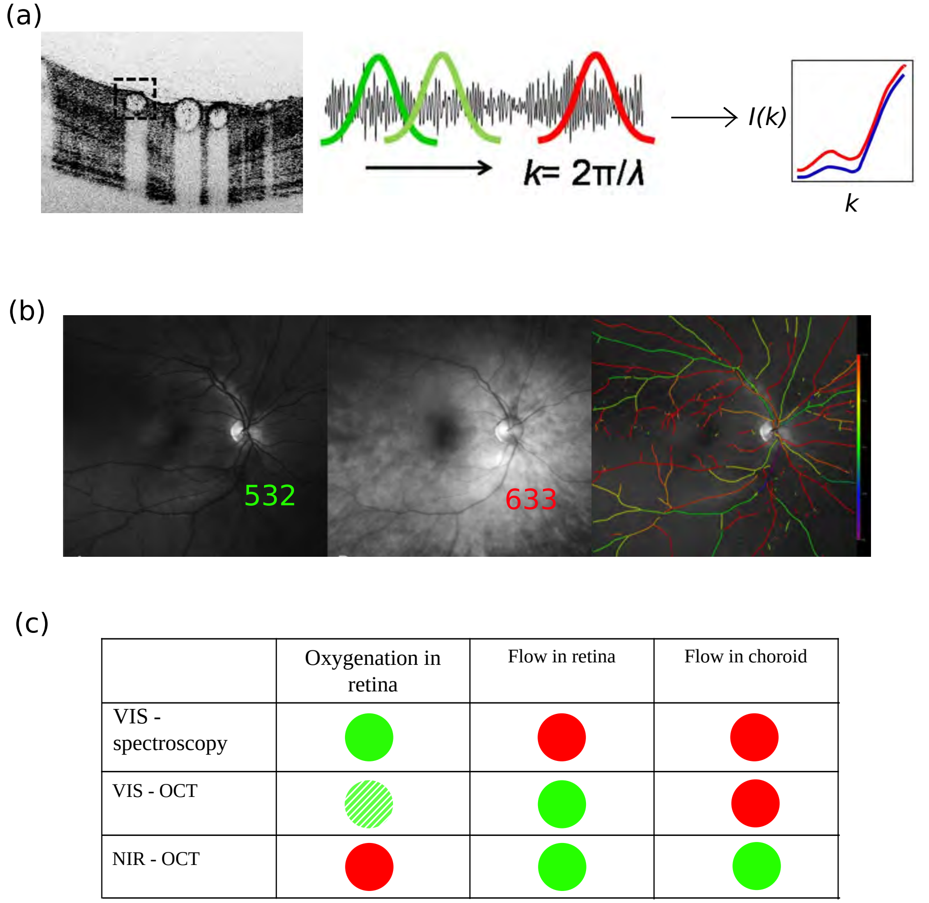

	Oxygenation in retina	Flow in retina	Flow in choroid
VIS - spectroscopy	🟢	🔴	🔴
VIS - OCT	▨	🟢	🔴
NIR - OCT	🔴	🟢	🟢

Figure 2.10: (a): Illustration of visible light OCT retinal oximetry showing a OCT b-scan. A Fourier transform is used to convert the intensity in the bottom of the blood vessel into spectral information, which is then fit per wave number (k) to extract the oxygen saturation measurement— illustration was adapted from Yi *et al.*[59]. (b):Retinal oxygen saturation measurement by Optomap 200Tx using 532 nm and 633 nm wavelengths. The images are then analysed using oximetry algorithm to extract oxygen saturation values (images from Kristjansdottir *et al.* [64]). (c) Table showing the potential of spectroscopic and OCT based techniques for retinal oxygenation and flow measurements; green and red circles represent technological possibility and impossibility respectively.

to the fundus, unlike the fundus camera-based oximeters were broadband light is typically used and spectral filtering is performed in the detection. With suitable optics, wide-field scanning of almost the entire fundus is possible with an SLO (Fig. 2.10(b)), whereas conventional fundus cameras are limited to relatively narrow images of the posterior pole [64]. A major drawback of SLO based oximetry is the lack of available lasers at optimum wavelengths which have been addressed in chapter 5 of this thesis.

Visible light OCT offers the prospect of functional retinal imaging, as most retinal chromophores possess distinct absorption signatures at visible wavelengths. An illustration of visible light OCT retinal oximetry is shown in Fig. 2.10(a). Quantifying oxygen saturation using visible OCT is considered more advantageous than using Near infrared (NIR) OCT due to the high absorption of blood in the visible range compared to 800 nm or 1050 nm. Visible OCT can measure the flow in the retina [22], but the penetration of visible light into the retina is limited, and visible OCT is incapable of measuring choroidal flow.

Further, OCT being a coherent detection scheme suffers from speckles, and a significant amount of averaging has to be performed to reduce the speckle contrast. The spectral bands (Fig. 2.10) extracted from the OCT signal of the blood vessels should be wide enough to ensure good signal-to-noise ratio of individual spectral bands to get a good fit of the absorption spectrum. However, the absorption of Hb in the visible range is a fast-changing function of wavelength (Fig. 2.5(b)), and smaller bands are thus required to get an accurate fit. All current OCT systems are based on supercontinuum sources which suffer from excess noise or RIN noise [22]. These factors make SLOs attractive for retinal oximetry. Another significant advantage is that SLOs with two or more wavelengths can be easily integrated with the NIR OCT modules operating at 1050 nm to get the overall oxygen metabolism of the retina and the blood flow in the choroid. Substantially higher amounts of light can be used for OCT imaging at longer wavelengths (as explained in section 2.2.2) compared to visible wavelengths, which make the combination of visible SLO and NIR OCT more viable.

References

[1] R. H. Webb, G. W. Hughes, and F. C. Delori, "Confocal scanning laser ophthalmoscope.," Appl. Opt. **26**, 14921499 (1987).

[2] M. Rajadhyaksha, R. R. Anderson, and R. H. Webb, "Video-rate confocal scanning laser microscope for imaging human tissues in vivo.," Appl. Opt. **38**, 21052115 (1999).

[3] D. X. Hammer, R. D. Ferguson, T. E. Ustun, C. E. Bigelow, N. V Iftimia, and R. H. Webb, "Line-scanning laser ophthalmoscope.," J. Biomed. Opt. **11**, 041126 (2014).

[4] A. E. Elsner, S. A. Burns, G. W. Hughes, and R. H. Webb, "Reflectometry with a scanning laser ophthalmoscope," Appl. Opt. **31**, 36973710 (1992).

[5] M. Damodaran, K. V. Vienola, B. Braaf, K. A. Vermeer, and J. F. de Boer, "Digital micromirror device based ophthalmoscope with concentric circle scanning," Biomed. Opt. Express **8**, (2017).

[6] K. Vienola, M. Damodaran, B. Braaf, K. Vermeer, and J. F. J. de Boer, "Parallel line scanning ophthalmoscope for retinal imaging," Opt. Lett. **40**, 53355338 (2015).

[7] S. Stephen, Optical systems for laser scanners, in Handbook of Optical and Laser Scanning, 2nd ed., pp. 69132, CRC Press, Boca Raton, FL (2011).

[8] Spatial light modulator and method, US patent no. 4566935 (1986).

[9] M. S. Muller, J. J. Green, K. Baskaran, A. W. Ingling, J. L. Clendenon, T. J. Gast, and A. E. Elsner, “Non-mydriatic confocal retinal imaging using a digital light projector,” Proc. SPIE. **9376**, 93760E (2015).

[10] B. Lochocki, A. Gambin, S. Manzanera, E. Irles, E. Tajahuerce, J. Lancis, and P. Artal, “Single pixel camera ophthalmoscope,” Optica **3**(10), 1056-1059 (2016).

[11] M. A. Davis, "Hardware triggering: maximising speed and efficiency for live cell imaging," Nat. Methods **14**, iii (2017).

[12] T. Garcia, DLP5531-Q1 Chipset Video Processing for Light Control Applications (2018).

[13] J. Tabernero, A. Benito, E. Alcón, and P. Artal, "Mechanism of compensation of aberrations in the human eye.," J. Opt. Soc. Am. A. Opt. Image Sci. Vis. **24**, 3274-83 (2007).

[14] E. J. Fernández, A. Unterhuber, B. Povaay, B. Hermann, P. Artal, and W. Drexler, "Chromatic aberration correction of the human eye for retinal imaging in the near infrared," Opt. Express **14**, 6213 (2006).

[15] L. N. Thibos, A. Bradley, and X. Zhang, The effect of ocular chromatic aberration on monocular visual performance, Optom. Vision Sci. **68**, 599-607 (1991).

[16] D. A. Atchinson and G. Smith, Chromatic dispersions of the ocular media of human eyes, J. Opt. Soc. Am. A **22**, 29-36 (2005).

[17] P. A. Howarth, X. X. Zhang, A. Bradley, D. L. Still, and L. N. Thibos, Does the chromatic aberration of the eye vary with age?, J. Opt. Soc. Am. A **5**, 2087-2092 (1988).

[18] C. Ware, Human axial chromatic aberration found not to decline with age, A. Graefes Arch. Klin. Exper. Ophthalmol. **218**, 39-41 (1982).

[19] I. Powell, "Lenses for correcting chromatic aberration of the eye," Appl. Opt. **20**, 2-5 (1981).

[20] R. J. Zawadzki, B. Cense, Y. Zhang, S. S. Choi, D. T. Miller, and J. S. Werner, "Ultrahigh-resolution optical coherence tomography with monochromatic and chromatic aberration correction," Opt. Express **16**, 1734-1746 (2008).

[21] F. LaRocca, D. Nankivil, S. Farsiu, and J. A. Izatt, "True color scanning laser ophthalmoscopy and optical coherence tomography handheld probe," Biomed. Opt. Express **5**, 3204 (2014).

[22] S. P. Chong, M. Bernucci, H. Radhakrishnan, and V. J. Srinivasan, "Structural and functional human retinal imaging with a fiber-based visible light OCT ophthalmoscope," Biomed. Opt. Express **8**, 323 (2017).

[23] S. P. Chong, T. Zhang, A. Kho, M. T. Bernucci, A. Dubra, and V. J. Srinivasan, "Ultrahigh resolution retinal imaging by visible light OCT with longitudinal achromatization," Biomed. Opt. Express **9**, 1477 (2018).

[24] J. A. Díaz, C. Pizarro, and J. Arasa, "Single dispersive gradient-index profile for the aging human lens," J. Opt. Soc. Am. A **25**, 25061 (2008).

[25] F. C. Delori, and K. P. Pflibsen, "Spectral reflectance of the human ocular fundus" Appl. Opt. **28** 1061-77 (1989).

[26] M. Hammer, A. Roggan, D. Schweitzer, G. Müller, and G. Muller, "Optical properties of ocular fundus tissues–an in vitro study using the double-integrating-sphere technique and inverse Monte Carlo simulation.," Phys. Med. Biol. **40**, 963-78 (1995).

[27] A. N. Schechter, Hemoglobin research and the origins of molecular medicine, blood, **112**(10), 3927-3938 (2008).

[28] M. Friebel and M. Meinke, Determination of the complex refractive index of highly concentrated hemoglobin solutions using transmittance and reflectance measurements, J. Biomed. Opt. **10**, 640-19 (2005).

[29] A. Amelink, T. Christiaanse, and H. J. C. M. Sterenborg, "Effect of hemoglobin extinction spectra on optical spectroscopic measurements of blood oxygen saturation," Opt. Lett. **34**, 15251527 (2009).

[30] N. Bosschaart, G. J. Edelman, M. C. G. Aalders, T. G. van Leeuwen, and D. J. Faber, "A literature review and novel theoretical approach on the optical properties of whole blood," Lasers Med. Sci. **29**, 453479 (2014).

[31] F. C. Delori, R. H. Webb, and D. H. Sliney, "Maximum permissible exposures for ocular safety (ANSI 2000), with emphasis on ophthalmic devices," J. Opt. Soc. Am. A **24**, 1250 (2007).

[32] D. H. Sliney, Retinal injury from laser radiation, Nonlinear Opt. **21**, 117 (1999).

[33] D. J. Lund, Action spectrum for retinal thermal damage, in Measurements of Optical Radiation Hazards, R. Matthes and D. Sliney, eds. (International Commission on NonIonizing Optical Radiation, 1998), pp. 209228.

[34] W. T. J. Ham and H. A. Mueller, The photopathology and nature of the blue light and near-UV retinal lesions produced by lasers and other optical sources, in Laser Applications in Medicine and Biology, M. L. Wolbarsht, ed. (Plenum, 1989), pp. 191246.

[35] B. E. Stuck, The retina and action spectrum for pnotoretintis, in Measurements of Optical Radiation Hazards, R. Matthes and D. Sliney, eds. (International Commission on Non-Ionizing Optical Radiation, 1998), pp. 193208.

[36] International Electrotechnical Commission, Safety of Laser Products Part 1: Equipment Classification and Requirements, (Geneva, Switzerland), IEC-60825-1 (2014).

[37] European Machine Vision Association, "EMVA Standard 1288 - 3.0: Standard for characterisation of Image Sensors and Cameras," **82** (2012).

[38] J. H. Parsons, The Ocular Circulation Bale and Danielsson (1903).

[39] O. Arjamaa and M. Nikinmaa, "Oxygen-dependent diseases in the retina: role of hypoxia-inducible

factors,". Exp Eye Res, **83**(3), 473-483.(2006).

[40] H. Noma, H. Funatsu, T. Mimura, M. Tatsugawa, K. Shimada, and S. Eguchi, "Vitreous Inflammatory Factors and Serous Macular Detachment in Branch Retinal Vein Occlusion," Retina, **32**(1), 86-91. (2012).

[41] L. P. Aiello, R. L. Avery, P. G. Arrigg, B. A. Keyt, H. D. Jampel, S. T. Shah, L. R. Pasquale, H. Thieme, M. A. Iwamoto, J. E. Park, "Vascular endothelial growth factor in ocular fluid of patients with diabetic retinopathy and other retinal disorders,". N Engl. J. Med., 331(22), 1480-1487 (1994).

[42] C. A. K. Lange and J. W. B. Bainbridge, "Oxygen sensing in retinal health and disease," Ophthalmologica **227**00, 115131 (2012).

[43] O. Arjamaa, M. Nikinmaa, A. Salminen, and K. Kaarniranta, "Regulatory role of HIF-1ALPHA in the pathogenesis of age-related macular degeneration (AMD)," Ageing Res. Rev. **8**, 349358 (2009).

[44] S. Yoneya, T. Saito, Y. Nishiyama, T. Deguchi, M. Takasu, T. Gil, and E. Horn, "Retinal oxygen saturation levels in patients with central retinal vein occlusion," Ophthalmology, **109**(8), 1521-1526 (2002).

[45] T. Bek, E. Stefansson, and S. H. Hardarson, "Retinal oxygen saturation is an independent contributor to the severity of retinopathy in diabetic patients," Br. J. Ophthalmol. (2018).

[46] D. Schmidl, G. Garhofer, and L. Schmetterer, "The complex interaction between ocular perfusion pressure and ocular blood flow - Relevance for glaucoma". Exp Eye Res, 93(2), 141-155. (2011).

[47] E. Vandewalle, L. A. Pinto, O. B. Olafsdottir, E. De Clerck, P. Stalmans, J. Van Calster, T. Zeyen, E. Stefánsson, and I. Stalmans, "Oximetry in glaucoma: Correlation of metabolic change with structural and functional damage," Acta Ophthalmol. **92**, 105-110 (2014).

[48] S. Traustason, S. H. Hardarson, M. S. Gottfredsdottir, T. Eysteinsson, R. A. Karlsson, E. Stefánsson, and A. Harris, "Dorzolamide-timolol combination and retinal vessel oxygen saturation in patients with glaucoma or ocular hypertension," Br. J. Ophthalmol. **93**, 10641067 (2009).

[49] J. B. Hickam, H. O. Sieker, and R. Frayser, "Studies of retinal circulation and A-V oxygen difference in man.," Trans. Am. Clin. Climatol. Assoc. **71**, 3444 (1959).

[50] J. B. Hickam, R. Frayser, and J. C. Ross, "A study of retinal venous blood oxygen saturation in human subjects by photographic means," Circulation **27** 37585 (1963).

[51] F. C. Delori, "Noninvasive technique for oximetry of blood in retinal vessels.," Appl. Opt. **27**, 1113-1125 (1988).

[52] M. H. Smith, K. R. Denninghoff, L. W. Hillman, and R. A. Chipman, "Oxygen saturation measurements of blood in retinal vessels during blood loss," J. Biomed. Opt. **3**, 296-303 (1998).

[53] D. Schweitzer, M. Hammer, J. Kraft, E. Thamm, E. Königsdörffer, and J. Strobel, "In vivo measurement of the oxygen saturation of retinal vessels in healthy volunteers.," IEEE Trans. Biomed. Eng. **46**, 1454-1465 (1999).

[54] J. M. Beach, K. J. Schwenzer, S. Srinivas, D. Kim, and J. S. Tiedeman, "Oximetry of retinal vessels by dual-wavelength imaging: calibration and influence of pigmentation," J. Appl. Physiol. **86** 748-58 (1999).

[55] S. H. Hardarson, A. Harris, R. A. Karlsson, G. H. Halldorsson, L. Kagemann, E. Rechtman, G. M. Zoega, T. Eysteinsson, J. A. Benediktsson, A. Thorsteinsson, P. K. Jensen, J. Beach, and E. Stefánsson, "Automatic retinal oximetry," Investig. Ophthalmol. Vis. Sci. **47**, 5011-5016 (2006).

[56] M. Hammer, W. Vilser, T. Riemer, A. Mandecka, D. Schweitzer, U. Kühn, J. Dawczynski, F. Liemt, and J. Strobel, "Diabetic patients with retinopathy show **inc**reased retinal venous oxygen saturation," Graefes Arch. Clin. Exp. Ophthalmol. **247** 1025-1030 (2009).

[57] S. Rilven, T. L. Torp, and J. Grauslund, "Retinal oximetry in patients with ischaemic retinal diseases," Acta Ophthalmol. **95**, 119-127 (2017).

[58] R. E. Man, R. Kawasaki, Z. Wu, C. D. Luu, J. J. Wang, T. Y. Wong, and E. L. Lamoureux, "Reliability

and reproducibility of retinal oxygen saturation measurements using a predefined peri-papillary annulus," Acta Ophthalmol **91**, 590-594 (2013).

[59] J. Yi, Q. Wei, W. Liu, V. Backman, and H. F. Zhang, "Visible-light optical coherence tomography for retinal oximetry," Opt. Lett. **38**, 1796-1798 (2013).

[60] J. C. Ramella-Roman, S. a Mathews, H. Kandimalla, A. Nabili, D. D. Duncan, S. a DAnna, S. M. Shah, and Q. D. Nguyen, "Measurement of oxygen saturation in the retina with a spectroscopic sensitive multi aperture camera.," Opt. Express **16**, 6170-6182 (2008).

[61] W. R. Johnson, D. W. Wilson, W. Fink, M. Humayun, and G. Bearman, "Snapshot hyperspectral imaging in ophthalmology.," J. Biomed. Opt. **12**, 01403-6 (2014).

[62] B. Khoobehi, J. M. Beach, and H. Kawano, "Hyperspectral Imaging for Measurement of Oxygen Saturation in the Optic Nerve Head," Invest. Ophthalmol. Vis. Sci. **45**, 1464-72 (2004).

[63] J. Beach, J. Ning, and B. Khoobehi, "Oxygen saturation in optic nerve head structures by hyperspectral image analysis.," Curr. Eye Res. **32**, 161-170 (2007).

[64] J. V. Kristjansdottir, S. H. Hardarson, G. H. Halldorsson, R. A. Karlsson, T. S. Eliasdottir, and E. Stefánsson, "Retinal oximetry with a scanning laser ophthalmoscope," Investig. Ophthalmol. Vis. Sci. **55**, 3120-3126 (2014).

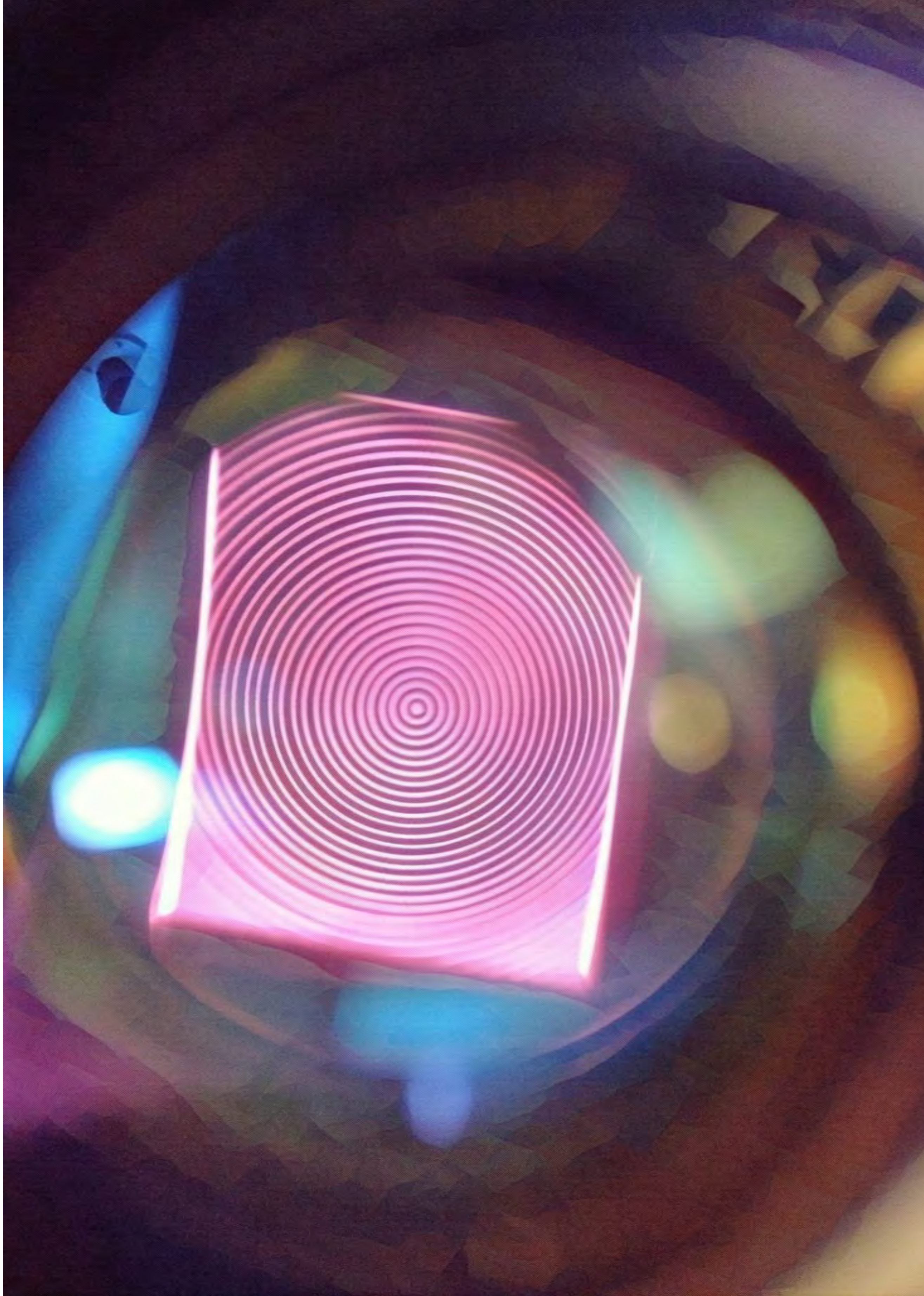

3

Digital micromirror device based ophthalmoscope

based on :

M. Damodaran, K. V. Vienola, B. Braaf, K. A. Vermeer, and J. F. de Boer, "Digital micromirror device based ophthalmoscope with concentric circle scanning," Biomed. Opt. Express 8, 2766-2780 (2017).

partly based on:

K. V. Vienola, **M. Damodaran**, B. Braaf, K. A. Vermeer, and J. F. de Boer, "In vivo retinal imaging for fixational eye motion detection using a high-speed digital micromirror device (DMD)-based ophthalmoscope," Biomed. Opt. Express 9, 591-602 (2018). [section 3.5]

Abstract

Retinal imaging is demonstrated using a novel scanning light ophthalmoscope based on a digital micromirror device with 810 nm illumination. Concentric circles were used as scan patterns, which facilitated fixation by a human subject for imaging. An annular illumination was implemented in the system to reduce the background caused by corneal reflections and thereby to enhance the signal-to-noise ratio. A 1.9-fold increase in the signal-to-noise ratio was found by using an annular illumination aperture compared to a circular illumination aperture, resulting in a 5-fold increase in imaging speed and a better signal-to-noise ratio compared to our previous system. We tested the imaging performance of our system by performing non-mydriatic imaging on two subjects at a speed of 7 Hz with a maximum 20° (diameter) field of view. The images were shot noise limited and clearly show various anatomical features of the retina with high contrast.

3.1 Introduction

Retinal imaging is an indispensable tool for diagnosing pathologies associated with the retina. Most retinal pathologies exhibit structural and functional changes in the ocular fundus [1]. Novel methods of observing and monitoring these changes have attracted much attention. The ocular fundus is located in the posterior part of the eye is minimally reflective and moderately scattering [2–4] making imaging challenging.

Traditional fundus photography uses so-called flood illumination where a homogeneous broadband light illuminates the whole field-of-view (FOV) [5]. In this type of imaging, both the in-focus and out-of-focus light reflected from the retina is collected by the camera, where the latter reduces the image contrast. To reject the out-of-focus light, pinholes can be implemented to make the system confocal. The confocal arrangement requires scanning using a spot or a line and produces higher contrast images by rejecting out-of-focus light [6–10].

Scanning laser/light ophthalmoscopy (SLO) is used widely in clinical settings for investigation and monitoring of the retina. In a conventional confocal SLO [10–12], a single spot is used to scan the retina continuously over two dimensions using scanning mirrors. Significant improvement in speed can be achieved by eliminating one scan dimension and using a line illumination in ophthalmoscopes[13–16] at the cost of a reduced confocality.

Spatial light modulators such as a digital micromirror device (DMD) have been used for retinal imaging by projecting a series of scan patterns [17–19] without using conventional scanning mirrors. The DMD provides temporal and spatial flexibility for illumination which can have several advantages such as optimising the system for speed and confocality. To date, retinal imaging systems based on DMDs either employ a single-line scanning method combined with a camera operating in rolling shutter mode [19] or use a large number of parallel lines with a global shutter camera as reported in our prior work [17]. Muller *et al.* reported acquiring confocal images with a 38° FOV at 14.3 Hz and the registering and averaging 50 frames into a single high-quality image. Our first-generation parallel line scanning ophthalmoscope (PLSO) produced high-quality images with a $10^\circ \times 10^\circ$ FOV at an imaging speed of 1.4 Hz although without averaging. At these speeds, image quality can suffer from motion artefacts, and a larger FOV is desirable.

In this paper, we present a parallel and circle SLO which uses a DMD to produce concentric circle illumination to fixate the eye and reduce eye motion during imaging. The signal-to-noise ratio (SNR) is improved by eliminating back reflections from the cornea. Corneal back reflections typically have higher intensities compared to the intensity reflected from the retina and reduce the image quality by forming a de-focussed background in the image. An annulus is placed conjugate to the pupil plane to create an annular illumination, and the reflected light from the retina is collected through the un-illuminated portion in the centre [20]. A circular aperture in the detection arm blocked most of the corneal reflections but passed the signal from the retina to the camera. The resulting improvement in SNR enabled faster imaging speeds without reducing the image quality.

A model eye was developed to study the SNR improvement obtained with the annulus and a circular aperture with the same outer diameter. Imaging two healthy volunteers demonstrated the capability of the system for *in vivo* retinal imaging.

3.2 Methods

The study obeyed the principles of the Declaration of Helsinki and was approved by the Institutional Review Board for human use at the VU University medical centre, Amsterdam. A written, informed consent was obtained from each subject. The optical power used for measuring human subjects was in agreement with the maximum permissible exposure limit prescribed by the latest IEC standard 60825-1 [21].

3.2.1 Optical system

The optical layout of the system is shown in Fig. 5.3A. A light-emitting diode (LED) with a bandwidth of 30 nm and a centre wavelength of 810 nm (SFH 4780S, OSRAM GmbH, Munich, Germany) was used for illumination. The half-angle divergence of the LED was ±10° with a maximum radiant intensity of 2900 mW/sr. The use of a LED with low spectral coherence reduced the speckle noise in the final retinal images. The light from the LED was homogenised using a tapered light pipe homogenising rod (Edmund Optics Inc., Barrington, USA) with a square entrance aperture (4 mm × 4 mm). The lenses L1 (f = 40 mm) and L2 (f = 50 mm) relayed the exit aperture (8 mm × 8 mm) of the light pipe onto the DMD.

The SLO used a DMD with a 0.7-inch diagonal micromirror array containing 1024 × 768 micromirror elements with a pitch of 13.6 ţm. The Vialux™ DLP©V-module V4100 board (Vialux GmbH, Chemnitz, Germany) provided control logic and power for the DMD. Each micromirror can be individually programmed to be in an 'ON' or 'OFF' state. A total internal reflection (TIR) prism [22] was used to guide the reflected light from the micromirrors in a perpendicular direction. The 4f system consisting of the lens pairs L3 (f = 37.5 mm), L4 (f = 42.9 mm), the ophthalmic lens L5 (f = 30 mm) and the eye (f = 60 D or 16.7 mm for a typical eye) relayed the light reflected from the DMD 'ON' mirrors onto conjugate positions on the retina. The DMD was magnified by a factor of 0.64 and illuminated the retina with a FOV of 30° × 21°. The scattered and reflected light from the retina was imaged on the CMOS camera (ace2040-180kmNIR, Basler, Germany) using lens L6 (f = 40 mm) and the camera objective lens L7 (f = 16 mm). The retinal image was magnified by a factor of 0.72 on the camera, forming an image of approximately 1150 × 850 pixels. However, due to the aberrations and field curvature induced by the optics, the maximum area where the retina was in sharp focus corresponded to a FOV of 20° diameter. Overall, the DMD was magnified by a factor of 0.45 onto the camera plane. Individually, each DMD mirror element was mapped to 1.1 pixels in the camera.

To minimise the stray reflections from the optical elements in the system, we used polarizers P1 and P2 in cross-polarized states in combination with the polarizing beam splitter (PBS) and the quarter-wave plate (QWP). The light from the DMD was linearly polarised to the transmission state of the PBS after passing through P1 and was then circularly polarised after passing through the QWP. The reflection from the retina (and the cornea) again passed through the QWP in the return path, which converted the reflected light to a linear polarisation state aligned with the reflection state of the PBS and passed through P2. In this configuration, the stray

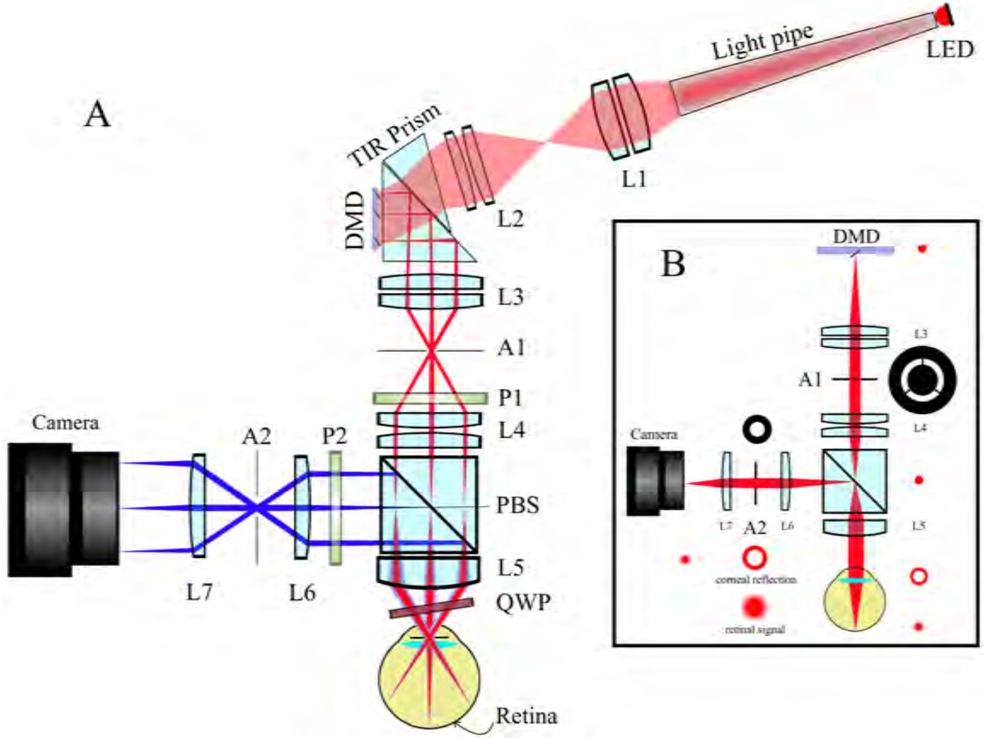
A
LED
Light pipe
L1
TIR Prism
DMD
L2
L3
A1
P1
L4
PBS
L5
QWP
Retina
Camera
A2
P2
L7
L6
B
DMD
L3
A1
L4
L5
Camera
L7
A2
L6
corneal reflection
retinal signal

Figure 3.1: A: Schematic of the optical setup showing both the illumination path (red) and the reflection path (blue). L1-L7: Lenses; P1, P2: Polarisers; A1: Annulus; A2: Circular aperture; PBS: Polarizing Beam Splitter; QWP: Quarter Wave Plate. B: The optical paths and beam shapes at different positions in the setup to block the corneal reflections - A point source in the DMD was relayed to a point in the retina using a $4f$ system consisting of lenses L3-L5 and the eye lens. An annulus was placed at the conjugate pupil plane between lenses L3 and L4 and was imaged onto the cornea using L4 and L5. The reflection from the retina was relayed to the camera using another $4f$ system consisting of the eye lens and the lenses L5-L7. The reflection from the cornea formed an image again at the conjugate pupil plane in the detection arm and was blocked by the circular aperture, while the retinal signal passed through the circular aperture.

reflections by components in the system between the two cross polarisers were rejected.

The camera sensor contained 2048 × 2048 pixels on a 5.5 µm pitch and operated in a global shutter mode. The maximum frame rate at full resolution was 180 frames/second (with 8-bit encoding). The full well charge of each pixel was 11800 electrons (e). A frame grabber (NI PCIe-1473R, National Instruments Inc., USA) was used to acquire and save images. The DMD control board sent the trigger signals to the camera to capture a frame for each pattern. There was a live preview of the image acquired by the camera to make sure that the retina is in focus in the camera.

3.2.2 Annular illumination on the pupil plane and retinal resolution

The diameter of a un-dilated pupil varies according to factors such as age and the luminance of the light used for imaging. The system was designed for a 3 mm pupil diameter as it corresponds to the diameter of an undilated pupil reported in the literature [23]. An annulus with an outer diameter of 4 mm and an inner diameter of 3 mm was made by laser cutting a 1 mm thick sheet of metal. The central obstruction is connected to the outer obstruction by thin metal bridges, as shown in Fig. 5.3B. The annulus was placed conjugate to the pupil plane (A1 in Fig. 5.3B) between L3 and L4 to create an annular illumination on the cornea with an outer diameter of 2.8 mm and an inner diameter of 2.1 mm. The image of the annular corneal reflections is focussed at the conjugate plane in the detection arm at location A2 in Fig. 5.3B and has an outer diameter of 3.7 mm and an inner diameter of 2.8 mm. We used a 2.8 mm circular aperture in the detection arm to block the corneal reflections and allow imaging the retina through the central un-illuminated portion of the pupil [20]. Thus, we rejected most of the corneal reflections and reduced the background, thereby improving the SNR. Having a circular aperture of 2.8 mm diameter in the detection arm translates to a 2.1 mm circular aperture on the cornea. From the Rayleigh criterion, this corresponds to a resolution of 7.9 µm on the retina and 5.6 µm in the camera plane. Since the camera pixel size was 5.5 µm, the resolution was not limited by the camera. In practice, the resolution in the retina is worse because of ocular aberrations. For the measurements on the model eye with an aperture, the annulus was replaced by a circular aperture with a diameter of 3 mm.

3.2.3 Parallel scanning method

The DMD can be used to create a large variety of parallel scanning patterns, as shown in Fig. 3.2. The illumination pattern is produced by programming sequential binary patterns which are displaced relative to each other by a constant distance. The parallel scanning strategy has already been showed to provide high-quality confocal images in fluorescence microscopy [24, 25]. The parallel line scanning ophthalmoscope (PLSO) [17] has been used to produce *in vivo* retinal images.

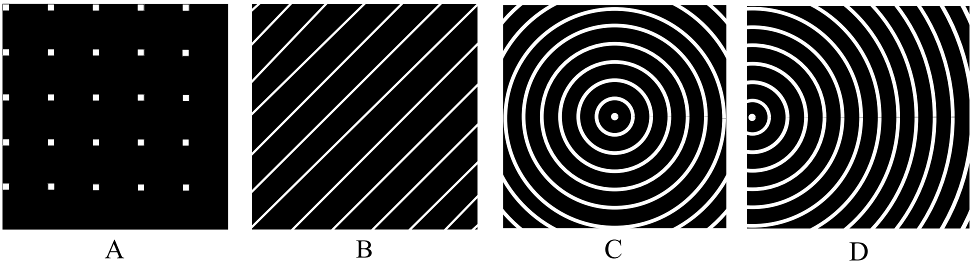

Figure 3.2: Illustrations of the parallel scanning methods used - A: Spots have been used in fluorescence microscopy for imaging stationary biological samples [24]. B: Parallel lines used in our prior work (PLSO) [17]. C: Concentric circles used in our system for scanning with the centres of the circles in the middle of the frame. D: Concentric circle scanning with the centre of the circles at the edge of the frame

However, there is a natural tendency for the human eye to follow motion, in this case, the moving spot (Fig. 3.2A) or line (Fig. 3.2B) patterns which are projected typically at 100 Hz to 200Hz. This eye movement caused by the subjects inclination to follow the scan patterns leads to motion artefacts in the final images. However, a pattern of concentric circles that shrink provides an illusion of depth where the subject tends to fixate on the centre of the concentric circles where each circle seems to disappear. When the circles are centred in the middle of the DMD (Fig. 3.2C), the fovea is in the middle of the FOV. When the centre of the circles is shifted to different regions on the DMD, *e.g.* the edge of the DMD (Fig. 3.2D), the subject fixates on the centre of these circles bringing different areas around the fovea in the FOV, including the optic nerve head (ONH). Thus, an area around the fovea can be imaged with a scan pattern that at the same time, provides a fixation target to the subject.

Each mirror in the DMD can be programmed individually to be turned ‘ON’, thereby reflecting the light along the optic axis or turned ‘OFF’ thus not contributing to the illumination on the retina. Let s be the number of ‘ON’ mirrors per scanning pattern and p be the total number of DMD mirrors used for illumination. The fill-factor (Γ) for scanning the retina is then defined as

$$\Gamma = \frac{s}{p}. \tag{3.1}$$

$N = 1/\Gamma$ then gives the total number of patterns required for scanning the FOV. At the end of N measurements, we have an image stack of N frames. By summing all the frames into a single image, we obtain a wide-field image.

3.2.4 Confocal image processing using virtual pinholes

True confocality occurs in an ophthalmoscope which has an illumination pinhole to produce a diffraction-limited spot in the retina and a detection pinhole which suppresses the out-of-focus scattered light. Line scanning achieves quasi confocality, not all out of focus light is rejected. Some of the scattered light from adjacent illuminated spots along the line dimension can lead to cross talk in the image. This is also true for parallel illumination schemes such as multiple lines or concentric circles. To create a confocal image, pinholes should be implemented in the detection arm. These pinholes should be precisely position matched with the illumination pattern to extract just the signal reflected from the sample and reject the out-of-focus light. These detection pinholes are tough to implement as real physical pinholes, and hence these pinholes ought to be created in the digital domain using post-processing techniques.

To reduce the scattered light from the retina and suppress the corneal reflections for each pattern in the sequence, we used a post-processing method first presented by Heintzmann *et al.* [26]. The Heintzmann method determines the maximum and minimum greyscale values for every image pixel overall acquired pattern frames (I). The maximum value corresponds to the signal in focus, while the minimum value is a measure of the background signal. The values in between the maximum and minimum relate to different amounts of out-of-focus signal and are therefore excluded from the analysis. The confocal image $I_{conf}(x, y)$ is then calculated as the difference between the maximum and the minimum pixel values as:

$$I_{conf}(x, y) = \max_{i=1..N}[I(x, y; i)] - \min_{i=1..N}[I(x, y; i)]. \tag{3.2}$$

In this study, the five lowest values per pixel were averaged to obtain a better estimate of the background value for each pixel, and this value was subtracted from the maximum value of that pixel.

3.2.5 Model eye measurements to evaluate SNR improvement

In this section, we describe the SNR model and the experiments done in the model eye to evaluate the SNR improvement with an annulus compared to a circular aperture for different fill-factors. These experiments demonstrate the SNR in the transitional regime between point scanning and full-field illumination and form the rationale behind the increase in imaging speed with the annulus without compromising the SNR. A model eye was developed to characterise the imaging performance and to study the SNR improvement when using a circular aperture or an annulus. An uncoated N-BK7 0.5-inch plano-convex lens with a 15 mm focal length (LA1540, Thorlabs GmbH, Germany) and a 7.7 mm radius of curvature was used in the model eye. This radius of curvature matched well to the human cornea anterior radius of curvature of approximately 7.6 mm [27]. The near-identical radius of curvature in the model eye ensured that the corneal reflections for the model eye followed the same ray paths as can be expected for the human eye. Besides, the model eye was filled with water to mimic the optical properties of the human eye, which increased the focal length to 20 mm. A uniformly scattering layer of titanium dioxide (TiO_2) of 300 µm thickness and scattering coefficient (μ_s) of 10 mm^{-1} was used as an artificial retina. The amount of power incident on the DMD remained constant as a function of fill-factor but varied between two values for the annulus and aperture measurement such that the power incident on the cornea was the same for annulus and aperture with the same fill-factor. As a result, the amount of optical power incident on the cornea (180 µW at $\Gamma = 0.05$) varied with the fill-factor Γ only for both the annulus and aperture measurements.

We determined the readout and dark noise variance for the camera by taking dark frames. The dark plus read-out noise power ($\sigma^2_{dark+readout}$) was approximately 350 e^2. We further determined the step size of the A/D conversion by illuminating the sensor with different power levels, establishing the gain factor according to the European Machine Vision Association (EMVA) standard [28] as shown in Fig. 3, which gave a step size of 46 electrons per digital number (DN). The quantization noise then becomes $(46)^2/12 = 176$ e^2. The total measured noise of 350 e^2 minus the quantization noise of 176 e^2 results in a dark noise power of 174 e^2. Therefore, the shot noise limited regime is reached above 350 detected photoelectrons or a digital number DN = 7.5. Our retinal measurements were performed at detection levels of 2500 photoelectrons (DN = 54).

We took the following definition of SNR according to the European Machine Vision Association standard [28]:

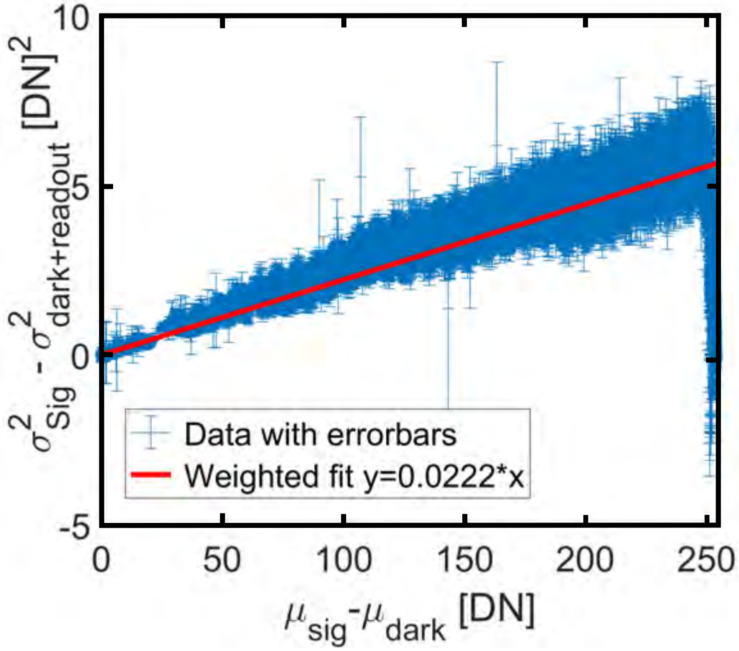

Figure 3.3: The measured variance $\sigma^2_{sig} - \sigma^2_{dark+readout}$ against the mean gray value $\mu_{sig} - \mu_{dark}$ and the linear regression line used to determine the overall system gain K. σ^2_{sig} is the variance in signal and μ_{sig} is the mean signal. The graph indicated that the gain of the system is 46 electrons/ DN (1/ slope of the fitted line) according to the method described in the EMVA standard [28].

$$SNR(\mu_p) = \frac{\eta\mu_p}{\sqrt{\sigma_d^2 + \sigma_q^2/K^2 + \eta\mu_p}} \tag{3.3}$$

where η is the wavelength-dependent quantum efficiency of the camera sensor, μ_p is the mean photon count, K is the overall system gain and σ_d and σ_q are the dark noise and quantization noise respectively. In our system, dark noise and quantum noise were negligible for the signal levels we obtain on the camera and hence Eq. (3.3) becomes,

$$SNR_s = \frac{\eta\mu_p}{\sqrt{\eta\mu_p}} = \frac{\mu_e}{\sqrt{\mu_e}} \tag{3.4}$$

where μ_e is the mean number of electrons. Based on the encoding, the number of electrons is converted to a grey value by the camera. These values have contributions both from the light reflected from the retina (retinal signal) and the light reflected from cornea and other surfaces. If $\mu_{e,background}$ is the background and $\mu_{e,signal}$ is the total signal on the camera, the light reflected exclusively from the

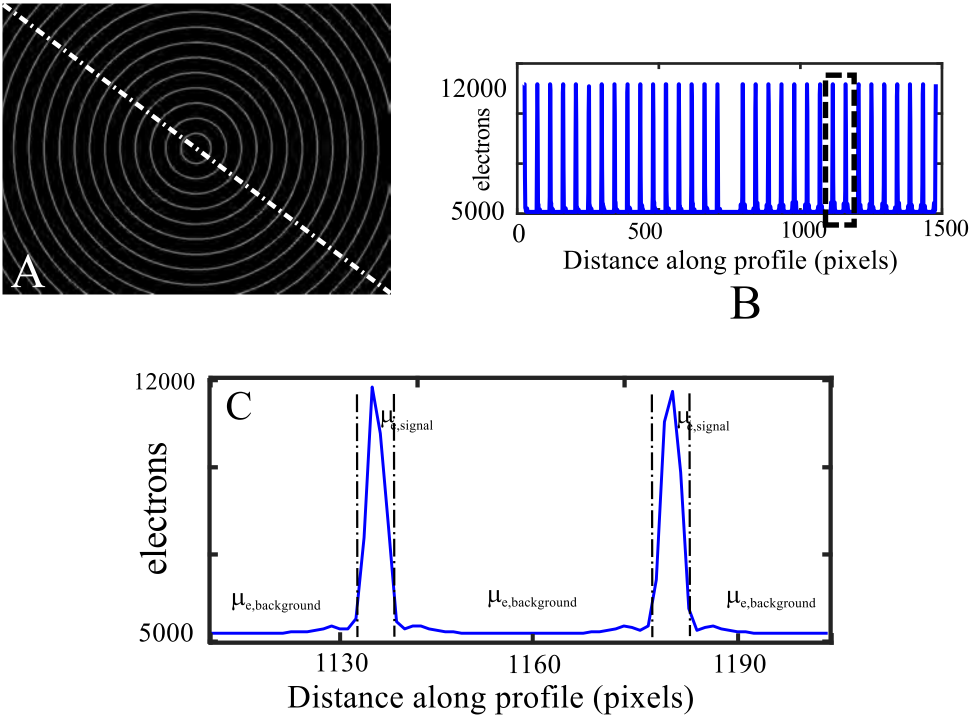

Figure 3.4: Calculating the SNR - illustration : A single frame from the stack of images (Γ = 0.05 illustrated here) is taken and a line profile is plotted (shown as white line). B: The line profile along the white line showing peaks along the signal. C: Each peak is examined to estimate $\mu_{e,signal}$ and $\mu_{e,background}$. This is repeated for several line profiles and the averages of $\mu_{e,signal}$ and $\mu_{e,background}$ is recorded.

retina is given by $\mu_{e,signal} - \mu_{e,background}$. Then the SNR for the retinal signal alone (SNR_s) can be rewritten as [17]

$$SNR_s = \frac{\mu_{e,signal} - \mu_{e,background}}{\sqrt{\mu_{e,signal}}} \tag{3.5}$$

The retinal signal per pixel remains constant for all values of Γ. However, the total background varies linearly with Γ. Eq. (3.5) can then be written as:

$$SNR_s(\Gamma) = \frac{\alpha}{\sqrt{\alpha + \beta \cdot \Gamma}} \tag{3.6}$$

with α the retinal signal ($\mu_{e,signal} - \mu_{e,background}$) per pixel and β the background per pixel. Equation (3.6) was used as a model to fit the experimental SNR$_s$ data. The SNR$_s$ for the annulus and the circular aperture as described in section 3.2.2 was measured for different Γ. When a circular aperture was used, the corneal reflections saturated the camera. Reducing the source power below the saturation threshold gave a very poor signal with the annulus. Hence a neutral density (ND) filter (OD = 0.6, 35% transmission at 810 nm) was placed in front of the camera when measuring with the circular aperture to prevent saturation. The mean electron count was corrected for this attenuation.

The SNR_s was estimated for different Γ with the DMD projecting patterns at 140 Hz. For each Γ, one frame (Fig. 3.4A) was taken, and the signal profile was plotted along different lines, as illustrated in Fig. 3.4B. The mean signal was estimated within a $1/e^2$ width of the signal peak and the mean background was measured elsewhere from this profile as shown in the Fig. 3.4C. The same procedure was repeated several times and averaged.

3.2.6 *In vivo* retinal imaging

To demonstrate the imaging capabilities of our system, we imaged the right eye of two healthy volunteers. Subject 1 was 32 years old with a refractive error > -1 D and subject 2 was 27 years old with a refractive error > -1.75 D and astigmatism of -2.25 D. Imaging was performed in a dimly lit room with un-dilated pupils ($\sim$ 3 mm in diameter) and with an incident power at the cornea of 180 ţW. The maximum permissible radiant power for a collimated static beam at 810 nm wavelength is 639 ţW [21]. Laser safety calculations are detailed in the Appendix.

The DMD was used to project concentric circular pattern at 140 Hz with a $\Gamma = 0.05$ ($N = 20$) resulting in an imaging speed of 7 Hz. An annulus with dimensions as described in section 2.2 was used to minimise the corneal reflections. The circular pattern stimulated the subject to fixate on the centre of the circular design. The ophthalmic lens could be translated along the optic axis to bring the retina in focus. The measurements were done for 7.2 seconds (1000 frames). Confocal videos were created by updating the image stack with every newly acquired pattern frame and recalculation of the confocal image. As such out of a single dataset, a confocal video with 981 video frames could be obtained.

3.3 Results

3.3.1 Model eye measurements to evaluate SNR improvement

Figure 3.5A shows the mean signal (retinal signal + background) and mean background plotted for different values of Γ for both the circular aperture and the annulus. When the Γ increases, so do the background and the low signal. The offset between these two is the retinal signal which remains constant with both illumination methods.

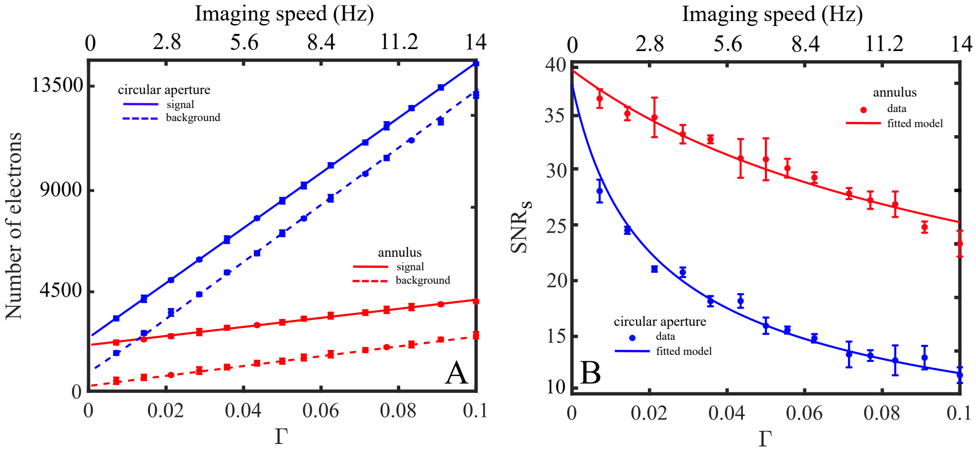

Figure 3.5: A: The signal and background obtained in the model eye for different imaging speeds. Blue and red lines and points are for the circular aperture and annulus, respectively. B: SNR comparison obtained in the model eye with the annulus and aperture for different imaging speeds. The imaging speed indicated in the top horizontal axis is for a DMD pattern speed of 140 Hz.

As explained in section 3.2.2, the corneal reflections which form as a background in the image are substantially reduced with the annulus. The SNR$_s$ model (Eq. (3.6)) was used to fit the SNR$_s$ data for different values of Γ. For the circular aperture, the model fit gave α = 1499 e and β = 134645 e. For the annulus, the model fit gave α = 1531 e and β = 20344 e. These values are in agreement with the argument that the retinal signal α remains fairly constant for both circular aperture and the annulus for the same power level on the cornea. At the same time, there is a 6.6-fold decrease in the background when an annulus is used. This effect translates to increase in SNR$_s$ as shown in Fig. 3.5B.

When the Γ is as small as possible (for example only one mirror on at a time), the performance of the system falls in line with a conventional single spot scanning SLO. Then the SNR$_s$ should be the same with or without annulus, as the corneal reflections would be minimal also in circular illumination case. This effect is already seen in Fig. 3.5B as the curves start to converge for small values of Γ. However, for Γ>0.4, the benefit of using an annulus is pronounced as there is almost a two-fold increase (1.9 at Γ=0.05) in the SNR$_s$. It is also evident from Fig. 3.5B that a given SNR$_s$ can be achieved for a higher fill-factor Γ in the case of an annulus compared to a circular aperture thereby making higher imaging speeds feasible in terms of SNR.

There was still some background when the annulus was used for imaging. This residual background can be attributed to light scattering in the retina, which contributes to the background and some small portion of the corneal reflection which reaches the camera. Further, the image formed by a single DMD mirror projected on the retina through an annulus is convolved with the system optics point spread function of the circular aperture in the detection arm to form a slightly blurred spot on the camera. Also, when the corneal reflections are defocused at the circular aperture in the detection arm, they do not get blocked completely.

3.3.2 *In vivo* retinal images

Figure 3.6 shows the results of in vivo imaging of the foveal region and various peri- and parafoveal regions around the retina of subject 1. Figure 3.6A is a fundus photograph (Canon CR-2, Canon Europa N.V, The Netherlands) with the coloured circles highlighting the different peri- and parafoveal regions with the fovea in the centre (blue dashed circle). Since we used polarization optics in our system, the macular bow-tie structure is noticeable in Fig. 3.6D. This structure occurs around the fovea due to a meridional variation in birefringence exhibited by Henle's fibres surrounding the fovea [29]. The different regions (Figs. 3.6B-3.6G) were imaged with a 18° FOV (diameter) by shifting the centre of the concentric circles to different places in the DMD.

Figure 3.7 shows the comparison of a *in vivo* image with a Spectralis (Heidelberg Engineering GmbH, Heidelberg, Germany) confocal SLO image of the inferior region of the retina of subject 1. Figure 3.7A is the non-confocal image produced by adding all the individual frames. This image suffers from multiple scattered and out-of-focus light resulting in poor quality with features that are not discernible. The virtual pinholes method was applied to this image in Fig. 3.7B, which shows the resulting high contrast confocal image. Figure 3.7C shows the average of 5 confocal frames after median filtering with a kernel of 3×3. Figure 3.7D and Figure 3.7E show the single frame and 20 frame average from a Spectralis SLO using the infrared (IR) channel. Figure 3.7F shows the line profiles through the same blood vessels (indicated by numbers 1 through 5 in Fig. 3.7B) from the images shown in Figs. 3.7A-3.7E. Arrows indicate the location of 5 blood vessels. The single-frame Spectralis SLO shows a marginally better Michelson contrast ([max-min/max+min]) for blood vessel 5 compared to the single frame DMD based SLO (0.52 vs 0.47), while the contrast for the blood vessel 2 (smallest) is better with the DMD based SLO (0.31 vs 0.25).

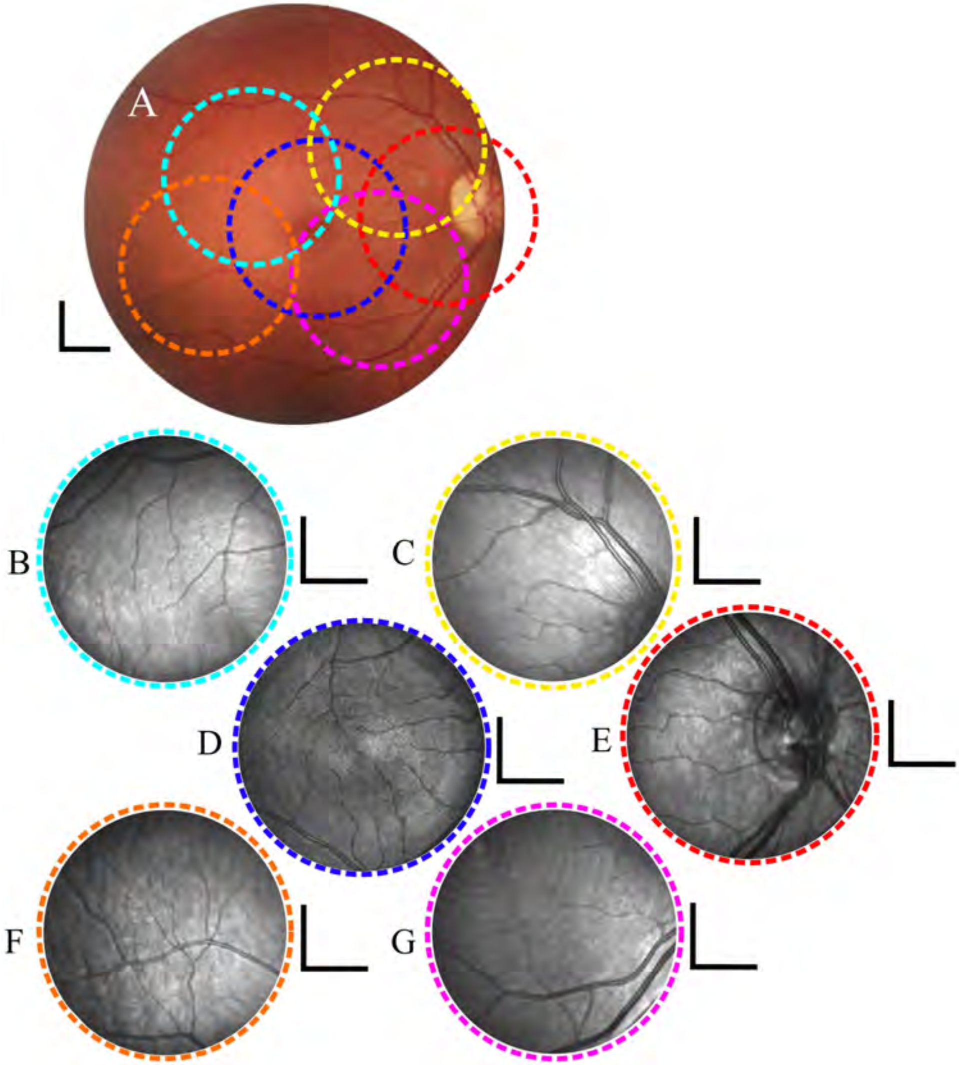

Figure 3.6: A: Fundus photograph of subject 1 coloured dashed circles showing the area imaged with our system. B-G: confocal images of the corresponding region showing the fovea and various peri- and parafoveal regions. Scale bar is 2° in the retina.

Figure 3.8 shows the *in vivo* results of different regions of the retina of subject 2 by projecting concentric circles with centres at two different locations in the DMD. Figure 3.8A shows the fundus photograph (Topcon TRC 50-DX Type 1A, Topcon Europe Medical B.V., The Netherlands) of subject 2 with a 50° FOV with the regions imaged with our system denoted by dashed circles. Figure 3.8B shows the macular region with fovea in the centre (red arrow) with a 20 degree FOV. Figure 3.8C shows the image of the optic nerve head.

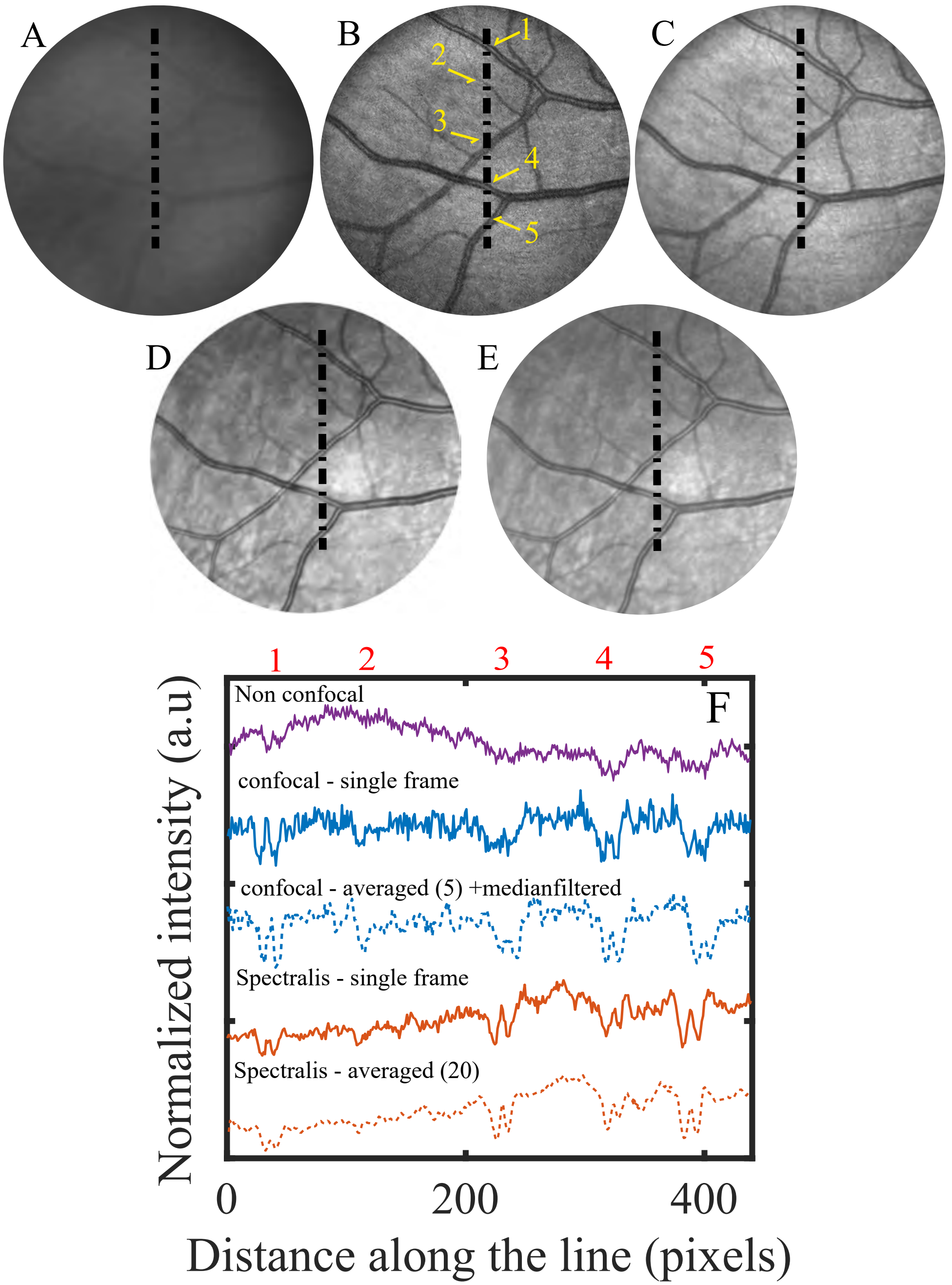
A
B
1
2
3
4
5
C
D
E
1
2
3
4
5
F
Non confocal
confocal - single frame
confocal - averaged (5) +medianfiltered
Spectralis - single frame
Spectralis - averaged (20)
Normalized intensity (a.u)
0
200
400
Distance along the line (pixels)

Figure 3.7: Comparison of the DMD based SLO with a Spectralis SLO - A: Non-confocal image of the inferior region of subject 1. B: Single confocal frame from the DMD based SLO. C: 5 frame average and median filtered image from the DMD based SLO. D and E: Single frame and 20 frames averaged images from the Spectralis SLO. F: Line profiles through the line indicated in A-E crossing through five blood vessels 1-5. The location of the blood vessels is indicated in the top axis. All in-vivo images have a 16.5° FOV.

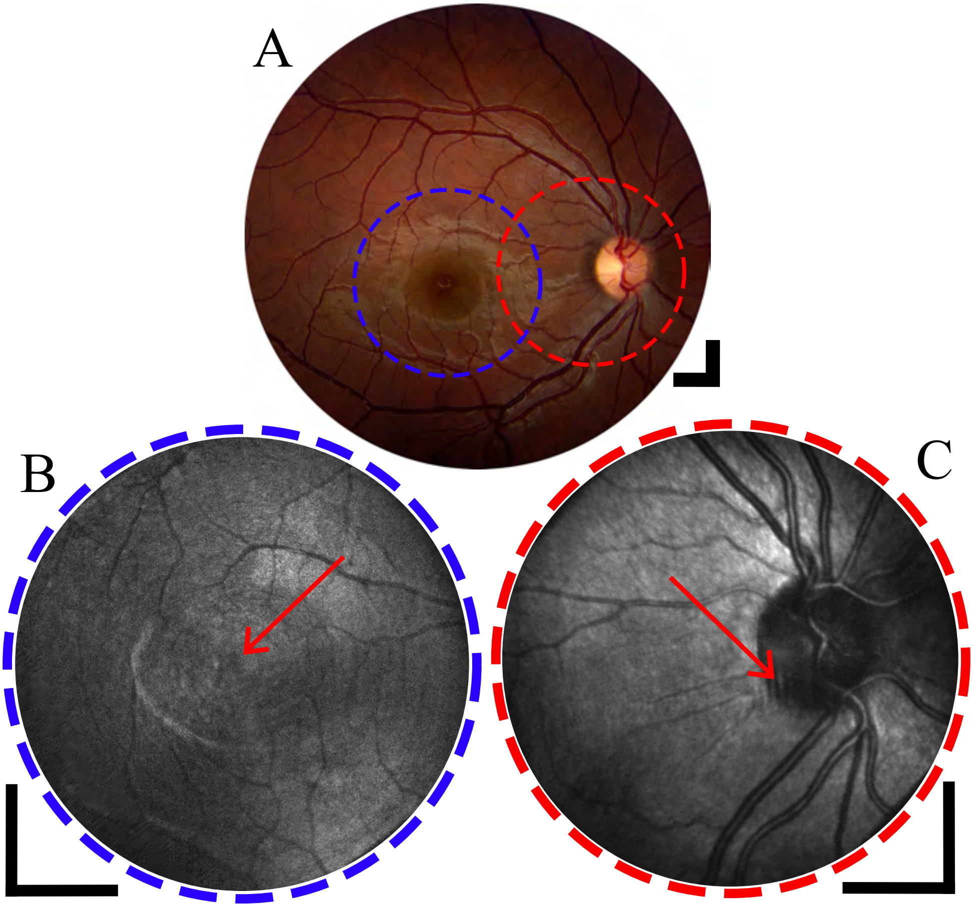

Figure 3.8: A: Fundus photograph of subject 2 showing the macular region (blue dashed circle) and the ONH region (red dashed circle) of the ocular fundus. B: The macular region with fovea indicated by the red arrow. C: The ONH (indicated by red arrow) with blood vessels surrounding it. Scale bar is 5° in the retina.

3.4 Discussion

The presented imaging device replaces scanning mirrors and laser sources that are present in the prevailing retinal scanning systems with a DMD and LEDs, potentially reducing cost and increasing flexibility. The new DMD based ophthalmoscope demonstrates several improvements over our previous method [17]. The background from corneal reflections was decreased significantly with the use of annulus, which increased the SNR by almost a factor of two. Moreover, the reduced corneal background made it possible to use higher fill-factors in the DMD, thus improving the imaging speed of the system from 1.4 Hz to 7 Hz without any loss in SNR. Although the concept of annular illumination has been well known for many years, this paper offers a quantitative analysis of the benefit of such lighting when going from the low fill-factor regime (conventional confocal SLO) towards flood illumination. The images obtained with our system are comparable images captured with a commercial SLO. Shifting the centre of the concentric circles to image different regions is a novel way to provide fixation while imaging different peri and parafoveal regions.

The system is modular with respect to the light source and enables changing the wavelength for imaging. Adding new wavelengths will make the system achieve multi-spectral imaging. Multi-spectral retinal imaging has gained interest in recent years [30, 31] as it helps to gather quantitative information on retinal health. The *in vivo* images sometimes show faint circular artefacts after post-processing. This is attributed to motion artefacts creating a discontinuity in scanning. It could be possible to extract motion information and use this to track the eyes movement. When done fast enough, it will also enable doing eye motion correction in real-time [32, 33] to improve the quality of the images by averaging multiple images at the same location and correct for the minor motion artefacts present in these images. Image registration could potentially be better with the parallel illumination as all the illumination points of a single frame are undistorted.

The primary shortcoming of the system is that the illumination light efficiency is poor. The DMD is operated at low fill-factor resulting in the majority of power not being used. Hence a high power and low divergence LED is needed to provide sufficient power for imaging the retina. Although a low divergence LED was used in our system, this might not be available for all wavelengths, particularly for the wavelengths of interest for multispectral imaging. This is expected to improve in the future with the progress in LED source development. As we currently are a factor of 4 below the maximum permissible exposure according to the IEC standard 60825-1 [21], there is still considerable room for further improvement. The polarization optics to reduce the stray reflections in the system lead to polarisation artefacts in the images due to birefringence of the cornea [34] and retina [29], influencing the images being recorded.

The position of the cornea in the imaging system is critical for the annulus to provide complete rejection of the corneal reflections. If the cornea is not positioned in the optimal imaging plane, the corneal reflections are not blocked, and hence they reach the camera. Although the subjects head is placed on a chin rest, small movement can occur. A pupil camera which tracks the location of the beam on the cornea can be implemented, allowing the re-positioning of the illuminating beam to the centre of the cornea.

3.5 Application: Fixational eye motion detection

As an application of the DMD based ophthalmoscope [35, 36], Retinal motion detection with an accuracy of 0.77 arcmins corresponding to 3.7 µm on the retina was demonstrated. The sub-sampled frames provide 7.7-millisecond snapshots of the retina without motion artefacts between the image points of the subsampled frame, distributed over the full field of view. An ophthalmoscope pattern projection speed of 130 Hz enabled a motion detection bandwidth of 65 Hz. A model eye with a scanning mirror was built to test the performance of the motion detection algorithm. Furthermore, an in vivo motion trace was obtained from a healthy volunteer. The captured eye motion trace clearly shows the three main types of fixational eye movements (FEM). Lastly, the obtained eye motion trace was used to correct for the eye motion in consecutively obtained subsampled frames to produce an averaged confocal image correct for motion artefacts.

In vivo eye motion detection

An example of an in vivo image correlation [35] is shown in Fig. 3.9. The reference, in this case, is a confocal image of the ONH area. The subsampled frame of the same area is then cross-correlated with the reference frame resulting in a 2D correlation matrix seen on the right side of Fig. 3.9. With the 5% fill factor of the DMD, the highest normalized cross-correlation coefficient values reach about 0.3 to 0.35. For the *in vivo* data we did not determine the centre of mass of the cross-correlation, but used the peak location, resulting in a motion resolution determined by the image pixel size (corresponding to 7.9 µm on the retina or 1.6 arcmins).

An *in vivo* eye motion trace is presented in Fig. 3.9, where the red line indicates motion in the horizontal direction and the blue trace shows motion in the vertical

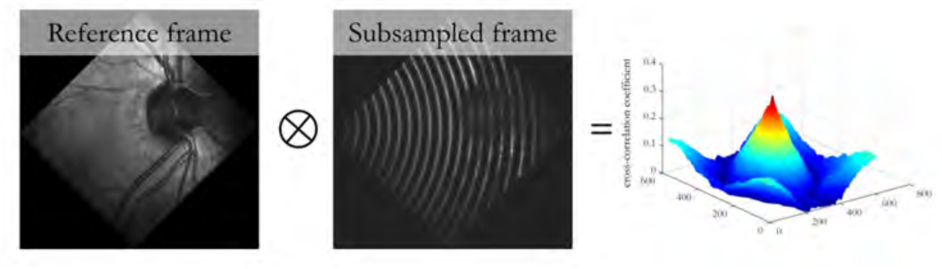

Figure 3.9: An *in vivo* example of the cross-correlation. First, a confocal frame is constructed, which will act as a reference frame. Then the next subsampled frame will be cross-correlated to the reference frame to obtain the shift between these two frames. The peak that occurs in the correlation matrix indicates the offset of the subsampled pattern with respect to the reference. The better the two images match, the higher the peak in the correlation matrix will be.

direction. All three types of FEM can be distinguished from the trace. Two microsaccades occurred during the recording at around 1.1 seconds and 2.9 seconds, having amplitudes of about 17 and 22 arcmins respectively. Slow drift is visible throughout the trace having amplitude values between 5 and 20 arcmins, which is similar to values reported in the literature [37]. And finally, the tremor is superimposed on top of the motion trace as high-frequency, low amplitude jitter.

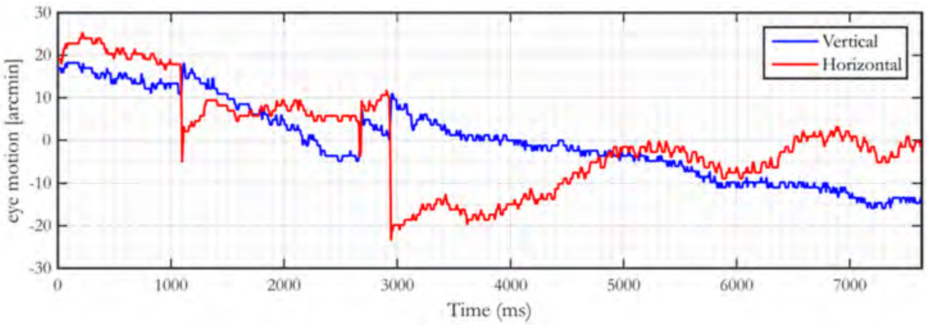

Figure 3.10: Extracted eye motion traces from a healthy subject. All three types of eye movements can be distinguished from the traces, namely micro-saccades (large jumps at 1.1 s and 2.9 s), drift (drifting motion along the trace with small amplitude and frequency) and tremor, high-frequency motion superimposed on top of the eye motion trace

The obtained eye motion trace shows the displacement of each subsampled frame compared to the reference frame. This displacement information can be used to adjust the position of each subsampled frame with respect to the reference frame and generate an averaged confocal image that is corrected for motion. For this specific data set, a total of 1000 subsampled frames were taken. With a DMD fill factor of 0.05, this results in 50 full confocal images (20 patterns per confocal image) over 7.6 seconds with most of them affected by eye movements. Figure 3.11 shows three confocal images. In Fig. 3.11(A), a single confocal image, is shown as a reference. In Fig. 3.11(B) the patterns are not corrected according to the eye motion trace before applying the Heintzmann algorithm, and the resulting confocal image is blurry and distorted by the eye motion. In Fig. 3.11(C), the eye movements during the measurement has been corrected before applying the algorithm. The resulting high-quality image shows good contrast and many anatomical features such as the larger blood vessels that are now sharp and the smaller vessels originating from ONH that are visible.

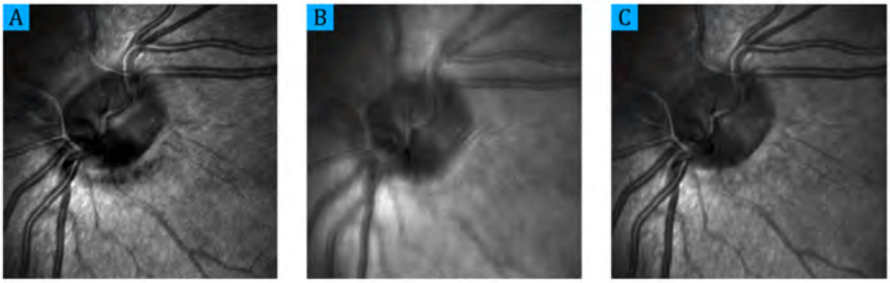

Figure 3.11: Averaging multiple confocal images without and with motion correction. To generate the images, 1000 subsampled frames were taken over 7.6 seconds. As the fill factor of the DMD was 0.05, it took 20 patterns to scan the entire FOV. This then resulted in 50 full confocal images that were averaged. (A) A single confocal image for comparison. (B) When the subsamples images are not corrected for motion, the resulting averaged image is blurry. (C) When each subsampled frame is corrected for the eye movements, the averaged image has high quality, showing good contrast and lots of features typical of the area around the ONH.

3.6 Conclusion

We have developed an SLO using a DMD displaying concentric circle pattern to scan the retina and provide a fixation target to the subject to fixate the eye. By changing the centre of the concentric circle pattern, different regions could be imaged. We used an annulus in the illumination arm to create an annular illumination on the cornea and block most of the corneal reflections using a circular aperture in the detection arm. Using the annulus, there was a 6.6-fold decrease in the background translating to a 1.9-fold increase in the SNR. This translates to a nearly 7-fold increase in speed for $\Gamma = 0.05$ at the same SNR. We demonstrated the experimental implementation of the imaging system by imaging two subjects in vivo with a maximum FOV of 20° diameter at a 140 Hz sub-frame rate and 7 Hz full frame rate. Further, we have demonstrated the feasibility of eye motion detection in our DMD based ophthalmoscope. The motion detection bandwidth was 65 Hz which was enough to detect most of the eye movements in the data set. The motion detection accuracy was better than 0.77 arcmins in vivo corresponding to 3.7 µm on the retina.

References

[1] A. E. Elsner, A. H. Jalkh, and J. J. Weiter, “New devices in retinal imaging and functional evaluation,” *Practical Atlas of Retinal Disease and Therapy*, W. Freeman, ed. pp. 19-35, Raven Press, New York (1993).

[2] F. C. Delori, and K. P. Pflibsen, “Spectral reflectance of the human ocular fundus,” Appl. Opt. **28**(6), 1061-1077 (1989).

[3] M. Hammer, and D. Schweitzer, “Quantitative reflection spectroscopy at the human ocular fundus,” Phys. Med. Biol. **47**(2), 179-191 (2002).

[4] D. A. Atchison and G. Smith, *“Optics of the Human Eye”*, Butterworth-Heinemann, pp. 34-35 Oxford (2000).

[5] R. Klein, B. E. Klein, M. W. Neider, L. D. Hubbard, S. M. Meuer and R. J. Brothers, Diabetic Retinopathy as detected using ophthalmoscopy, a Nonmydriatic camera and a standard fundus camera, Ophthalmology **92**(2), 485-491 (1985) .

[6] R. H. Webb, G. W. Hughes, and O. Pomerantzeff, "Flying spot TV ophthalmoscope," Appl. Opt. **19**(17), 2991-2997 (1980).

[7] M. Rajadhyaksha, R. R. Anderson, and R. H. Webb, “Video-rate confocal scanning laser microscope for imaging human tissues *in vivo*,” Appl. Opt. **38**(10), 2105-2115 (1999).

[8] A. Plesch, U. Klingbeil, and J. Bille, “Digital laser scanning fundus camera,” Appl. Opt. **26**(8), 1480 (1987).

[9] A. Manivannan, P. F. Sharp, R. P. Phillips, and J. V. Forrester, “Digital fundus imaging using a scanning laser ophthalmoscope,” Physiol. Meas. **14**(1), 43-56 (1993).

[10] R. H. Webb, G. W. Hughes, and F. C. Delori, “Confocal scanning laser ophthalmoscope,” Appl. Opt. **26**(8), 1492-1499 (1987).

[11] K. Kobayashi, and T. Asakura, “Imaging techniques and applications of the scanning laser ophthalmoscope,” Opt. Eng. **34**(3), 717-726 (2005).

[12] A. E. Elsner, S. A. Burns, G. W. Hughes, and R. H. Webb, “Reflectometry with a scanning laser ophthalmoscope,” Appl. Opt. **31**(19), 3697-3710 (1992).

[13] D. X. Hammer, R. D. Ferguson, T. E. Ustun, C. E. Bigelow, N. V. Iftimia, and R. H. Webb, “Line-scanning laser ophthalmoscope,” J. Biomed. Opt. **11**(4), 041126 (2006).

[14] Y. He, H. Li, J. Lu, G. Shi, and Y. Zhang, Retina imaging by using compact line scanning quasi-confocal ophthalmoscope, Chin. Opt. Lett. **11**(2), 1113 (2013).

[15] K. Im, S. Han, H. Park, D. Kim, and B. Kim, Simple high-speed confocal line-scanning microscope, Opt. Express **13**(13), 51515156 (2005).

[16] N. V. Iftimia, D. X. Hammer, C. E. Bigelow, T. Ustun, J. F. de Boer, and R. D. Ferguson, Hybrid retinal imager using line-scanning laser ophthalmoscopy and spectral domain optical coherence tomography, Opt. Express **14**(26), 1290912914 (2006).

[17] K. V. Vienola, M. Damodaran, B. Braaf, K. A. Vermeer, and J. F. de Boer, “Parallel line scanning

ophthalmoscope for retinal imaging," Opt. Lett. **40**(22), 5335-5338 (2015).

[18] B. Lochocki, A. Gambin, S. Manzanera, E. Irles, E. Tajahuerce, J. Lancis, and P. Artal, "Single pixel camera ophthalmoscope," Optica **3**(10), 1056-1059 (2016).

[19] M. S. Muller, J. J. Green, K. Baskaran, A. W. Ingling, J. L. Clendenon, T. J. Gast, and A. E. Elsner, "Non-mydriatic confocal retinal imaging using a digital light projector," Proc. SPIE. **9376**, 93760E (2015).

[20] E. DeHoog, and J. Schwiegerling, "Optimal parameters for retinal illumination and imaging in fundus cameras," Appl. Opt. **47**(36), 6769-6777 (2008).

[21] International Electrotechnical Commission, Safety of Laser Products Part 1: Equipment Classification and Requirements, (Geneva, Switzerland), IEC-60825-1 (2014).

[22] Y. C. Huang, and J. W. Pan, "High contrast ratio and compact sized prism for DLP projection system," Opt. Express **22**(14), 1701617029 (2014).

[23] V. N. Mahajan, Uniform versus Gaussian beams a comparison of the effects of diffraction, obscuration, and aberrations, J. Opt. Soc. Am. A **3**(4), 470-485 (1986).

[24] F. P. Martial and N. A. Hartell, "Programmable illumination and high-speed, multi-wavelength, confocal microscopy using a digital micromirror," PLoS One **7**(8), 0043942 (2012).

[25] N. Chakrova, R. Heintzmann, B. Rieger and S. Stallinga, "Studying different illumination patterns for resolution improvement in fluorescence microscopy," Opt. Express **23**(24), 31367-31383 (2015).

[26] R. Heintzmann and P. Benedetti, "High-resolution image reconstruction in fluorescence microscopy with patterned excitation," Appl. Opt. **45**(20), 5037-5045 (2006).

[27] W. N. Charman , "Optics of the human eye," in *Visual Optics and Instrumentation,* J. C Dillon, ed. (CRC press, Boca Raton, 1991), pp. 126.

[28] European Machine Vision Association, Standard for Characterization of Image Sensors and Cameras, EMVA Standard 1288, (2016).

[29] A. Weber, A. E. Elsner, M. Miura, S. Kompa, and M. C. Cheney, "Relationship between foveal birefringence and visual acuity in neovascular age-related macular degeneration," Eye, **21**(3), 130-134 (2012).

[30] J. V. Kristjansdottir, S. H. Hardarson, G. H. Halldorsson, R. A. Karlsson, T. S. Eliasdottir, and E. Stefansson, "Retinal oximetry with a scanning laser ophthalmoscope," Invest. Ophthalmol. Vis. Sci. **55**(5), 31203126 (2014).

[31] H. Li, J. Lu, G. Shi, and Y. Zhang, Measurement of oxygen saturation in small retinal vessels with adaptive optics confocal scanning laser ophthalmoscope," J. Biomed. Opt. **16**(11), 110504 (2011).

[32] K. V. Vienola, B. Braaf, C. K. Sheehy, Q. Yang, P. Tiruveedhula, D. W. Arathorn, J. F. de Boer, and A. Roorda, "Real-time eye motion compensation for OCT imaging with tracking SLO," Biomed. Opt. Express **3**(11), 2950-2963 (2012).

[33] C. K. Sheehy, Q. Yang, D. W. Arathorn, P. Tiruveedhula, J. F. de Boer, and A. Roorda, "High-speed, image based eye tracking with a scanning laser ophthalmoscope," Biomed. Opt. Express **3**(10), 2611-2622 (2012).

[34] R. W. Knighton and X. Huang, Linear Birefringence of the Central Human Cornea, Invest. Ophthalmol. Vis. Sci. **43**(1), 8286 (2016).

[35] K. V. Vienola, M. Damodaran, B. Braaf, K. A. Vermeer, and J. F. De Boer, "In vivo retinal imaging for fixational eye motion detection using a high-speed digital micromirror device (DMD)-based ophthalmoscope," Biomed. Opt. Express **9**, 591602 (2018).

[36] M. Damodaran, K. V Vienola, K. A. Vermeer, and J. F. De Boer, "Dual-wavelength Scanning Light Ophthalmoscope with concentric circle scanning," Invest. Ophthalmol. Vis. Sci. 58, 3132 (2017).

[37] S. Martinez-Conde, S. L. Macknik, and D. H. Hubel, The role of fixational eye movements in visual perception, Nat. Rev. Neurosci. **5**(3), 229240 (2004).

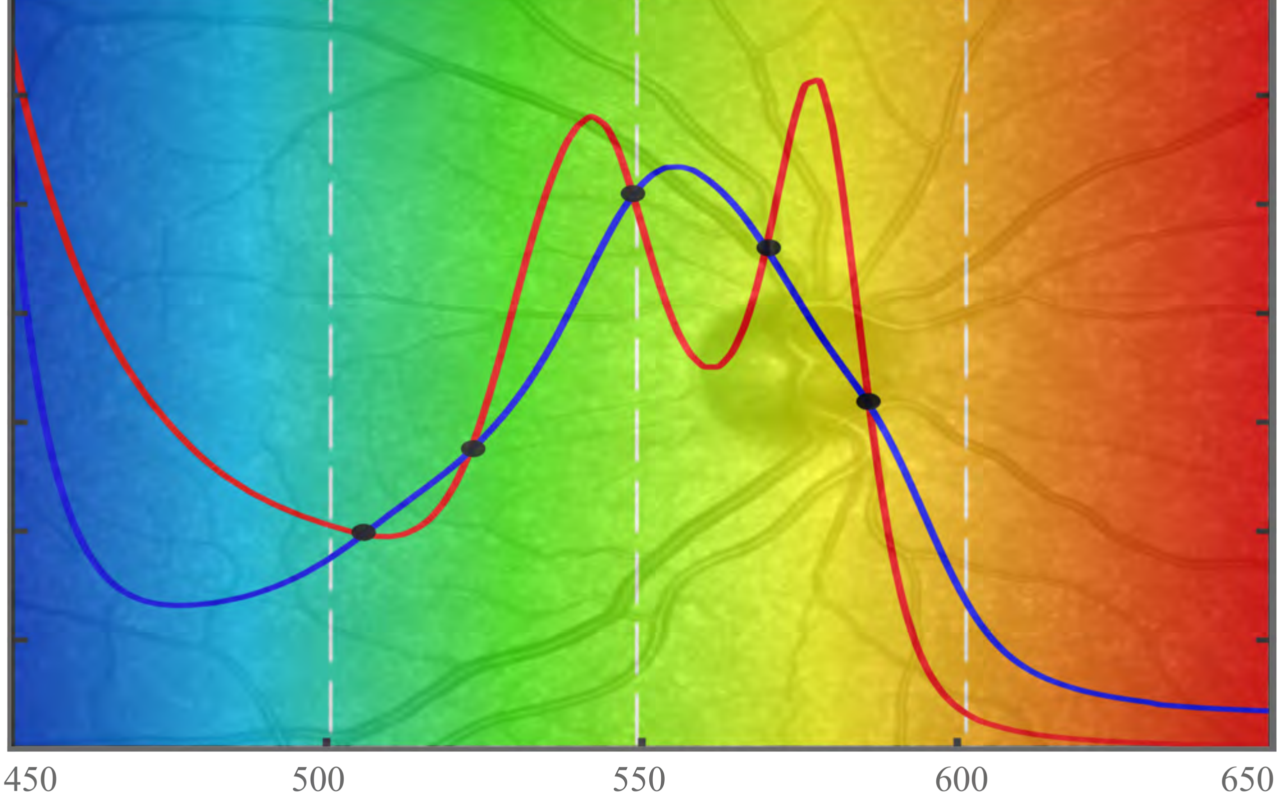
450
500
550
600
650

4

Optimal wavelengths for sub-diffuse scanning laser oximetry

based on :

M. Damodaran, A. Amelink, and J. F. de Boer, "Optimal wavelengths for subdiffuse scanning laser oximetry of the human retina," J. Biomed. Opt. Express **23**, (2018)

Abstract

Retinal blood vessel oxygenation is considered to be an important marker for numerous eye diseases. Oxygenation is typically assessed by imaging the retinal vessels at different wavelengths using multispectral imaging techniques where the choice of wavelengths will affect the achievable measurement accuracy. Here we present a detailed analysis of the error propagation of measurement noise in retinal oximetry, to identify optimal wavelengths which will yield the lowest uncertainty in saturation estimation for a given measurement noise level. In our analysis, we also investigate the effect of haemoglobin packing in discrete blood vessels (pigment packaging) which may result in a non-negligible bias in saturation estimation if unaccounted for under specific geometrical conditions, such as sub-diffuse sampling of smaller blood vessels located deeper within the retina. Our analyses show that by using 470 nm, 506 nm and 592 nm, a fairly accurate estimation of the whole oxygen saturation regime [0 1] can be realised, even in the presence of the pigment packing effect. To validate the analysis, we developed a scanning laser ophthalmoscope to produce high contrast images with a maximum pixel rate of 60 kHz and a maximum 30° imaging field-of-view. Confocal reflectance measurements were then conducted on a tissue-mimicking scattering phantom with optical properties similar to retinal tissue including narrow channels filled with absorbing dyes to mimic blood vessels. By imaging at three optimal wavelengths, the saturation of the dye combination was calculated. The experimental values show good agreement with our theoretical derivations.

4.1 Introduction

Haemoglobin oxygen saturation in the blood flowing through the retinal vasculature is an important physiological parameter involved in the pathophysiology of numerous retinal diseases including diabetic retinopathy [1, 2], glaucoma [3–5], retinitis pigmentosa[6–8], age related macular degeneration[9] and retinal vessel occlusions[10]. Several retinal diseases result in reduced oxygen circulation in the retina causing hypoxia[11], which is one of the key drivers of angiogenesis. As such, measuring the retinal blood oxygen saturation will enable monitoring of the development of hypoxia and thus will allow preventing the loss of retinal tissue due to vasoproliferation through timely therapeutic interventions. Furthermore, although damage occurring to the retina in advanced stages of many retinal diseases associated with hypoxia has been established, oxygenation measurements could also aid in understanding the onset or presence of systemic diseases. For example, a recent study reported that elevated oxygen saturation in retinal blood vessels is an indicator of Alzheimers disease[12, 13].

The earliest attempts to demonstrate retinal vessel oximetry date back several decades[14, 15]. Various imaging modalities such as fundus camera [16–23], hyperspectral imaging [24–26], scanning laser ophthalmoscope (SLO) [27, 28], adaptive optics SLO [29] and Optical Coherence Tomography (OCT) [30, 31] have since then been employed to estimate oxygen saturation in retinal blood vessels. These non-invasive techniques all involve recording light reflected from the fundus and measuring the amount of light absorbed by the blood flowing through the retinal vessels at multiple wavelengths. Retinal oxygen saturation is typically calculated from reflection intensities recorded by a point or array detector, and the error on the measured intensities propagates to a saturation error. Using a detailed error analysis, we here aim to identify optimum wavelengths which will yield minimum uncertainty on the saturation estimation for a given measurement error in the intensities.

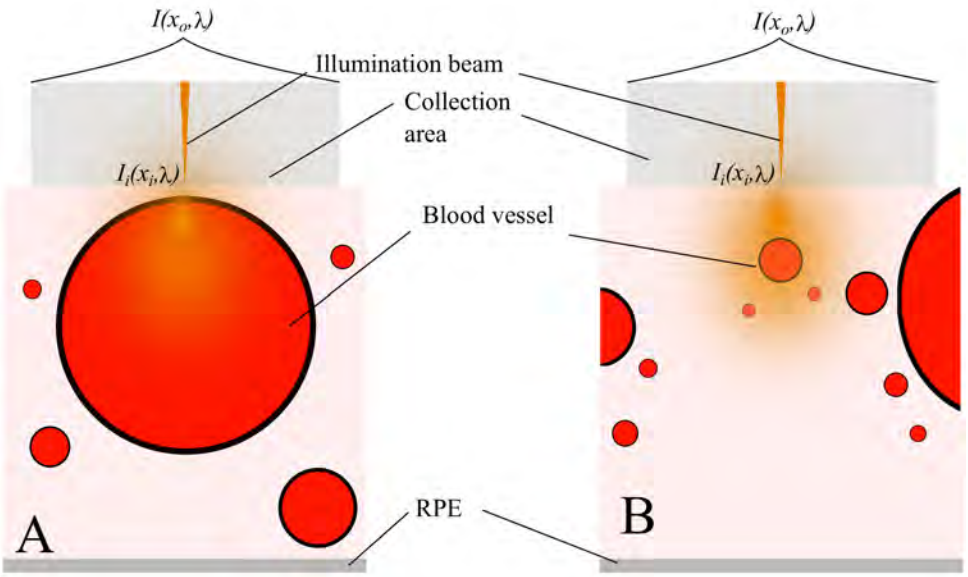

Figure 4.1: Two different vessel geometries in sub-diffuse retinal oximetry: A: A large blood vessel with a diameter comparable to the collection area present superficially in the retina. In this case, the probability that a detected photon has not passed through the blood vessel is negligible, and hence, the pigment packing effect is not observed. B: A small blood vessel embedded in the scattering medium (retinal tissue) is illuminated with a narrow beam, while the collection aperture is much larger than the illumination aperture and the vessel diameter. In this case, the blood vessel occupies only a small portion of the total probed volume and hence the pigment packing effect should be considered.

One factor that has not been considered in retinal oximetry to date is the fact that haemoglobin is not distributed homogeneously in the tissue but confined to discrete blood vessels. This effect is particularly relevant for smaller blood vessels that occupy only a small portion of the total probed volume in a quasi-confocal/ sub-diffuse scheme. As a result, a fraction of the incident photons is reflected from the tissue without ever encountering a blood vessel, causing the apparent absorption coefficient of blood packed in small vessels to be different compared to when the blood would have been homogeneously distributed through the probed tissue. Such an effect is called the pigment packaging effect, and several research studies have experimentally verified this effect [32–34]. We have included this effect in retinal oximetry algorithms to increase the accuracy of the saturation estimation, in particular for small blood vessels located deeper in the retina, probed using a (sub)diffuse measurement technique. Large and superficially located blood vessels, whose diameters are comparable to the detection aperture, are not expected to suffer from this effect, as the probability that the detected photons have not travelled through the blood vessel is negligible. In this paper, we present modified retinal oximetry equations that include the pigment packaging effect and evaluate the effect of pigment packaging on saturation estimation. We then identify optimum wavelengths for retinal oximetry using a detailed error analysis of the oximetry equations including the pigment packaging effect and identify the wavelengths which give minimum saturation error for both discussed geometries (Fig. 4.1A and 4.1B) and minimise the saturation offset in the presence of the pigment packing effect.

To validate our theoretical predictions, we have fabricated a thin, multi-layer retina-mimicking phantom with narrow channels representing the blood vessels in the retina. The reduced scattering coefficient (μ_s') of the scattering medium in the layers was chosen to be similar to the expected values for the retina. The retina-mimicking phantom was placed in a model eye. An SLO using a supercontinuum laser as the light source was used to scan the artificial retina. Two dyes of suitable concentrations were tailored to have absorption coefficients comparable to oxy- and deoxyhaemoglobin with an artificial isosbestic point at 548 nm. The procedure for selecting optimum wavelengths to estimate the saturation within this artificial vessel was applied to this phantom and three optimal wavelengths (488 nm, 548 nm and 612 nm) were selected based on this analysis. Using the resulting wavelengths, the experiments were conducted on the phantom. There was a good agreement between the predicted and real values of saturation of the different dye combinations using these three optimal wavelengths.

4.2 Theory of retinal oximetry and identifying optimum wavelengths

4.2.1 Theory of retinal oximetry

Figure 4.2A shows the absorption spectrum of the oxy- and deoxyhaemoglobin having various isosbestic points, i.e. wavelengths where the absorption of oxy and deoxyhaemoglobin is equal. Figure 4.2B shows a typical fundus image of a healthy human eye obtained with 570 nm illumination. A general method for measuring the absorbance of blood at a particular blood vessel in the retina is shown in the inset of Fig. 4.2B where the intensity profile of the blood vessel (dotted line in Fig. 4.2B) is plotted as a function of the location on the retina. The scattering properties of blood have been reported in *Bosschaart et al.*[35], where it was shown that although blood has a high scattering coefficient, it also has a high scattering anisotropy, resulting in a reduced scattering coefficient of $\approx$ 1-2 mm^{-1}. Further, the reduced scattering coefficient of blood is close to the reduced scattering coefficient of the surrounding tissue [36] and about an order of magnitude smaller than the absorption coefficient of blood in the 450-650 nm wavelength range.

In a retinal imaging experiment, the measured intensity $I(x_o, \lambda)$ (see Fig. 4.1) from a spatial location x_o in the retina for a given illumination wavelength λ depends on the incident illumination intensity distribution $I_i(x_i, \lambda)$ at the point x_i, and the backscattered reflectance function of the retina $R(x_o, x_i, \lambda)$. We consider a quasi-confocal or sub-diffuse scheme where a narrow, focused beam illuminates a point x_i in the retina, and the detection pinhole collects from a larger volume around a point x_o. Let $\overline{x}_o$ be the location of an averaged volume of tissue surrounding x_o that contributes to the collected intensity, $I(x_o, \lambda)$. The extent of volume averaging for any location concerning the spatial distribution of the optical properties at that location is determined by the incident illumination profile $I_i(x_i, \lambda)$ and the detection pinhole. Under these conditions, we write the measured intensity I as,

$$I(x_o, \lambda) = \int I_i(x_i, \lambda) \cdot R(x_o, x_i, \lambda) \cdot dx_i = I_i(x_o, \lambda) \cdot R(\overline{x}_o, \lambda) \tag{4.1}$$

The function $R(\overline{x}_o, \lambda)$ describes the reflectivity of the tissue averaged over a small tissue volume at the location x_o due to scattering and absorption. Let x_b and x_t denote the recorded locations at the centre of a blood vessel and in the adjacent tissue, respectively. Then the light collected from a tissue location x_t is given by,

$$I(x_t, \lambda) \propto I_i(x_t, \lambda) \cdot R(\overline{x}_t, \lambda) = I_i(x_t, \lambda) \cdot R\big(\mu_s(\overline{x}_t, \lambda), p(\overline{x}_t, \theta, \lambda)\big) \tag{4.2}$$

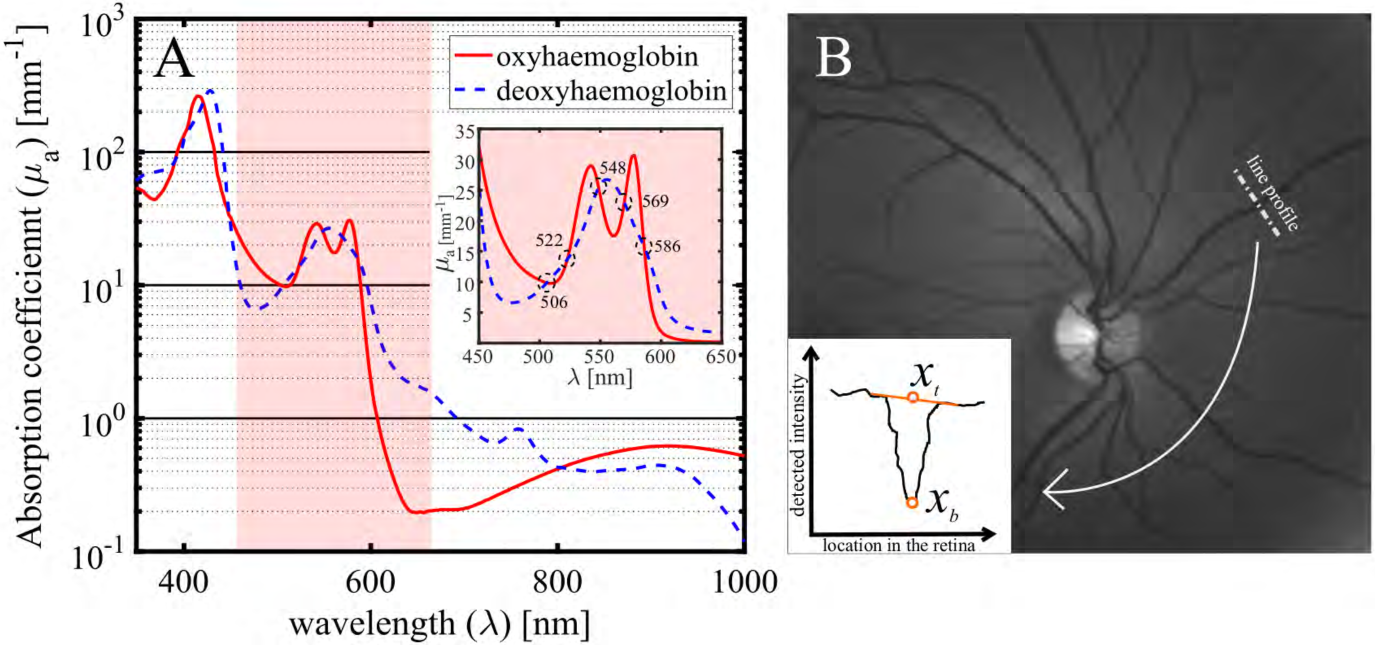

Figure 4.2: A: Absorption spectrum of oxy- and deoxyhaemoglobin from 350 nm to 1000 nm assuming a concentration of 150 mg of haemoglobin in 1 mL of blood[33]. The inset shows the absorption spectrum from 450 nm to 650 nm. The absorption of these two types of haemoglobin is different for most wavelengths except for the isosbestic points (denoted by black dashed circles: 506 nm, 522 nm, 548 nm, 569 nm, and 586 nm in the inset) where the absorption depends on factors other than the oxygen saturation. B: Fundus reflectance of the right eye of a healthy adult male at 570 nm recorded using a Fundus camera (Oxymap T1, Oxymap ehf., Iceland, fitted to a Topcon fundus camera, Topcon TRC 50-DX, Topcon corp., Japan). The inset shows a typical vessel absorption profile across a blood vessel (dotted line) in the fundus photo demonstrating a drop in the detected intensity at the blood vessel location (x_b) compared to the intensity at the tissue location (x_t).

where we have stated that $R(\overline{x}_t, \lambda)$ is a function of the average scattering coefficient ($\mu_s(\overline{x}_t, \lambda)$) of the volume of tissue around x_t (denoted by $\overline{x}_t$) at the wavelength λ and of the scattering phase function ($p(\overline{x}_t, \theta, \lambda)$) of the same tissue volume. We have assumed that there is no blood present in tissue volume $\overline{x}_t$ and that any other absorbing molecules within the tissue volume $\overline{x}_t$ in the neural retina have a negligible contribution to the reflected intensities. Similarly, the light collected from the centre of a blood vessel location x_b is given by,

$$I(\overline{x}_b, \lambda) \propto I_i(x_b, \lambda) \cdot R(\overline{x}_b, \lambda) = I_i(x_b, \lambda) \cdot R\big(\mu_s(\overline{x}_b, \lambda), p(\overline{x}_b, \theta, \lambda), \mu_a(\overline{x}_b, \lambda)\big) \quad (4.3)$$

where we have stated that $R(\overline{x}_b, \lambda)$ is a function of the average scattering coefficient $\mu_s(\overline{x}_b, \lambda)$ of the volume of tissue around x_b (denoted by $\overline{x}_b$) at the wavelength λ, of the scattering phase function $p(\overline{x}_b, \theta, \lambda)$ of the same tissue volume and the effective absorption coefficient of the tissue volume containing the blood vessel $\mu_a(\overline{x}_b, \lambda)$. We can now write the relative optical density OD_λ of the tissue at the blood vessel location compared to the surrounding tissue at a particular wavelength as the logarithm of the ratio of tissue and blood vessel reflectivity at the same wavelength i.e.,

$$OD_\lambda = \ln\left(\frac{I(x_t, \lambda)}{I(x_b, \lambda)}\right) = \ln\left(\frac{R(\overline{x}_t, \lambda)}{R(\overline{x}_b, \lambda)}\right) = \langle L_{eff}(\lambda)\rangle \cdot \mu_a(\overline{x}_b, \lambda) + G(\lambda) \quad (4.4)$$

Here we have assumed that the incident light intensity was the same at both locations and that the attenuation of the reflected light due to the blood within $\overline{x}_b$ is governed by *modified Beer-Lamberts law* [37, 38], with $\langle L_{eff}(\lambda)\rangle$, the effective path length of photons travelling through the probed volume before reaching the detector. The effective path length $\langle L_{eff}(\lambda)\rangle$ depends on the absorption and scattering properties of the probed volume. $G(\lambda)$ is a factor which accounts for any apparent increase or decrease in the ODs purely due to scattering differences within the volumes $\overline{x}_b$ and $\overline{x}_t$, e.g. due to the difference in scattering properties of blood within the blood vessel compared to the surrounding tissue. Since in the wavelength range 450-650 nm the reduced scattering coefficient of blood is similar to that of the surrounding tissue, we do not expect G to be a significant factor, in particular for the case shown in fig. 4.1B, where the blood vessel occupies only a small fraction of the interrogated tissue volume. Equation 6.4 assumes that all additional reflections occurring internally in the system due to optics and the stray reflections from the cornea are accounted for, e.g. by subtracting a reference measurement. The absorption coefficient $\mu_a(\overline{x}_b, \lambda)$ of the blood is a function of saturation (S) of the blood (i.e., the fraction of the oxygenated haemoglobin concentration to the total concentration of haemoglobin) and is given by,

$$\mu_a(\overline{x}_b, \lambda) = \left(S \cdot \mu_a^{HbO_2}(\lambda) + (1 - S) \cdot \mu_a^{Hb}(\lambda)\right) \tag{4.5}$$

The parameters $\mu_a^{HbO_2}(\lambda)$ and $\mu_a^{Hb}(\lambda)$ are the absorption coefficients of oxy- and deoxyhaemoglobin, respectively (assuming a concentration of 150 mg of haemoglobin in 1 mL of blood) and are well-known functions of wavelength. Combining Eq. 6.4 and Eq. 5.5,

$$OD_\lambda = \langle L_{eff}(\lambda)\rangle \cdot \nu \cdot \left(S \cdot \mu_a^{HbO_2}(\lambda) + (1 - S) \cdot \mu_a^{Hb}(\lambda)\right) + G(\lambda) \tag{4.6}$$

where ν is the fraction of interrogated tissue occupied by the blood vessel[33, 34]. We define the ratio $\rho_{\lambda_1|\lambda_2}$ of ODs at 2 wavelengths λ_1 and λ_1 as,

$$\begin{aligned} \rho_{\lambda_1|\lambda_2} &= \frac{OD_{\lambda_1}}{OD_{\lambda_2}} \\ &= \frac{\langle L_{eff}(\lambda_1)\rangle \cdot \Big(S \cdot \mu_a^{HbO_2}(\lambda_1) + (1 - S) \cdot \mu_a^{Hb}(\lambda_1)\Big) + G(\lambda_1)}{\langle L_{eff}(\lambda_2)\rangle \cdot \Big(S \cdot \mu_a^{HbO_2}(\lambda_2) + (1 - S) \cdot \mu_a^{Hb}(\lambda_2)\Big) + G(\lambda_2)} \end{aligned} \tag{4.7}$$

If the scattering and absorption coefficients at the two wavelengths are close to each other, $\langle L_{eff}(\lambda_1)\rangle \simeq \langle L_{eff}(\lambda_2)\rangle$ and $G(\lambda_1) \simeq G(\lambda_2)$. We will later discuss the validity of this assumption. Under this condition, we can write S as a function of $\rho_{\lambda_1|\lambda_2}$ as,

$$S_{\lambda_1|\lambda_2} = \frac{\rho \cdot \mu_a^{Hb}(\lambda_2) - \mu_a^{Hb}(\lambda_1)}{(\mu_a^{Hb}(\lambda_2) - \mu_a^{HbO_2}(\lambda_2)) \cdot \rho + (\mu_a^{HbO_2}(\lambda_1) - \mu_a^{Hb}(\lambda_1))} + \alpha \cdot G \tag{4.8}$$

where $\alpha \cdot G$ [1] is an offset, if any, to the saturation due to scattering. As discussed earlier, for visible wavelenghts we expect $G(\lambda) \to 0$, and in the remainder of the analyses, we only focus on the first term in the right-hand side of Eq.4.8.

Although not mathematically necessary, it is advantageous to choose one of the wavelengths as an isosbestic wavelengths to simplify the calculations, especially for error propagation purposes. If λ_2 is taken to be the isosbestic wavelength, $\lambda_2 = \lambda_i$, $\mu_a^{HbO_2} = \mu_a^{Hb} = \mu_a^i$. In that case, Eq. 4.8 can be written as,

$$S_{\lambda_a|\lambda_i} = \frac{\rho \cdot \mu_a^i(\lambda_i) - \mu_a^{Hb}(\lambda_a)}{\mu_a^{HbO_2}(\lambda_a) - \mu_a^{Hb}(\lambda_a)} \tag{4.9}$$

---

[1] $\alpha = \frac{\rho - 1}{\langle L_{eff}\rangle \cdot ((\mu_a^{HbO_2}(\lambda_2) - (\mu_a^{Hb}(\lambda_2)) \cdot \rho + (\mu_a^{HbO_2}(\lambda_1) - (\mu_a^{Hb}(\lambda_1)))}$

where we have denoted the saturation sensitive 'anisosbestic' wavelength as λ_a. We will now first consider the geometry as described in Fig. 4.1A where the blood vessel where a large, superficial blood vessel occupies the majority of the probed volume.

Optimum wavelengths without pigment packing

If there is a large blood vessel with a diameter close to or greater than the size of the collection aperture directly below the illumination point, as shown in Fig. 4.1A,the assumption that the blood vessel occupies only a portion of the probed volume does not hold. In such geometries, the blood vessel occupies majority of the probed volume. *Monte Carlo* simulations [39, 40] have suggested that in this type of geometry with a quasi-confocal aperture, the photons reaching the detector have predominantly been backscattered from within the blood vessel. In this case, $\langle L_{eff}(\lambda)\rangle$ in Eq. 4.6 becomes the average backscatter path length $\langle L_{bs}(\lambda)\rangle$ from within the blood vessel (and blood volume fraction ν becomes 1):

$$OD_\lambda = \langle L_{bs}(\lambda)\rangle \cdot \big(S \cdot \mu_a^{HbO_2}(\lambda) + (1-S) \cdot \mu_a^{Hb}(\lambda)\big) + G(\lambda) \tag{4.10}$$

Under the condition that scattering coefficient and absorption coefficient of blood is approximately equal at both wavelengths λ_a and λ_i, $\langle L_{bs}(\lambda_a)\rangle \approx \langle L_{bs}(\lambda_i)\rangle$. The saturation in this case is given by Eq. 4.9.

Turning now to the error on the saturation, this error is given by,

$$\Delta S = \frac{dS}{d\rho} \cdot \Delta\rho \tag{4.11}$$

where $\Delta\rho_{\lambda_a|\lambda_i}$ is given by propagating the error on OD_a and OD_i in Eq. 4.7,

$$\Delta\rho_{\lambda_a|\lambda_i} = \frac{OD_a}{OD_i} \cdot \sqrt{\Big(\frac{\Delta OD_a}{OD_a}\Big)^2 + \Big(\frac{\Delta OD_i}{OD_i}\Big)^2} \tag{4.12}$$

The error in the ODs is given by the underlying error of the reflected intensities $I(x_t, \lambda)$ and $I(x_b, \lambda)$ as,

$$\Delta OD_\lambda = \sqrt{\Big(\frac{\Delta I(x_t,\lambda)}{I(x_t,\lambda)}\Big)^2 + \Big(\frac{\Delta I(x_b,\lambda)}{I(x_b,\lambda)}\Big)^2} \tag{4.13}$$

Due to very low absorption at wavelengths $>$ 650 nm, there is a poor contrast between the recorded intensity at the tissue location and the blood vessel location which results in OD → 0. This results in large errors in ρ (following Eq. 4.12) and therefore, in saturation estimation. Absorption is very high in the *Soret band* (430 nm) resulting in most of the light being absorbed by the blood resulting in a very poor signal to noise ratio at the blood vessel locations. Most importantly, the blue light hazard for the wavelengths $<$ 450nm substantially limits the maximum permissible exposure of the retina for light [41] of these wavelengths. Thus, we exclude the wavelengths $<$ 450 nm and $>$ 650 nm for the remainder of the analysis. From Eqs. 4.11, 4.12 and 4.13, it is evident that the standard error of the mean recorded intensities by the detector ($\Delta I/I$ or standard deviation / mean) propagates to an error in the OD's and then to an error in ρ , and thus contributes to the saturation error ΔS. For example, a 1.0 % error in the intensities ($\Delta I/I = 0.01$) propagates to an error in the ODs ($\Delta OD = 0.014$). If $OD_{\lambda_1} = 0.5$ and $OD_{\lambda_2} = 0.7$, this gives 3.4 % error in ρ according to Eq. 4.12, this error in ρ propagates to saturation error in a complex manner ΔS through Equation 4.11.

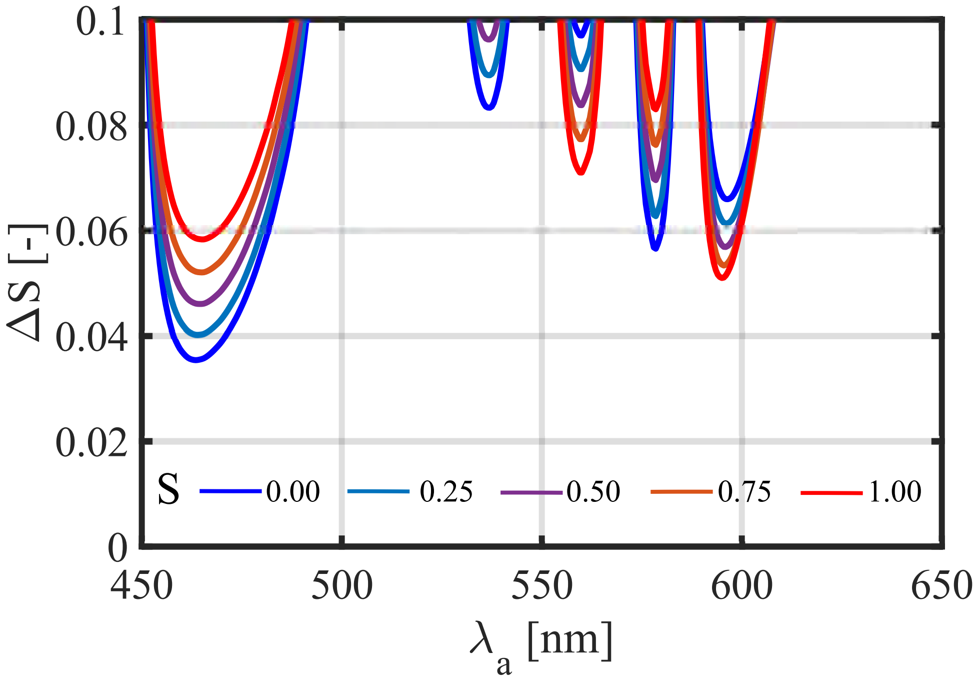

Figure 4.3: Saturation error ΔS as a function of λ_a when estimating different oxygenation levels from 0 to 100 %, with 1 % error on the recorded intensities. 506 nm was chosen as the isosbestic wavelength. This graph holds for geometry described in Fig. 4.1A, where the photons are mostly backscattered from a blood vessel.

Figure 4.3 shows the calculated saturation error for different oxygen saturation levels in the retina when 506 nm was used as the isosbestic wavelength and the anisosbestic wavelength varied over the 450 nm to 650 nm range, assuming a 1 %

measurement error in the intensity. For low saturation values [0.0 0.5], choosing the anisosbestic wavelength in the range 458 nm to 474 nm gives a saturation error less than 5 %, while for high saturation values [0.5 1.0], choosing the anisosbestic wavelength in the range 591 nm to 599 nm gives a saturation error less than 5 %. A similar trend was found for other isosbestic points shown in fig. 4.2A. Note, however, that the condition that the absorption coefficients are similar at $\mu_a(\lambda_a) \approx \mu_a(\lambda_i)$ so that $\langle L_{bs}(\lambda_a)\rangle \approx \langle L_{bs}(\lambda_i)\rangle$ is met best by choosing 506 nm as the isosbestic wavelength (Fig. 4.2A).

Optimum wavelengths including pigment packing

Figure 4.1B describes a geometry where a small blood vessel is embedded in the scattering retina. In this case the blood vessel occupies only a fraction of the total probed volume by the imager. As a result, Eq.4.6 (which assumes a homogeneous distribution of haemoglobin throughout the probed tissue volume) does not hold as the absorbing haemoglobin molecules are not homogeneously distributed but are contained in a discrete package (the blood vessel) that occupies only part of the probed tissue volume. This packaging of absorbing molecules effectively flattens the apparent absorption spectrum for high absorption coefficients, and is called the pigment packaging effect. It has previously been shown that this effect can be modelled through the incorporation of a correction factor to the absorption spectrum[32–34]. Equation 5.5 in this case is modified to,

$$\mu_a(\overline{x}_b, \lambda) = \nu \cdot \big(S \cdot \mu_a^{HbO_2}(\lambda) + (1-S) \cdot \mu_a^{Hb}(\lambda)\big) \cdot C_\lambda \tag{4.14}$$

where the correction factor C_λ[34, 42] is given by,

$$C_\lambda(S, \lambda, D_{ves}) = \frac{1 - \exp\big(-D_{ves} \cdot (S \cdot \mu_a^{HbO_2}(\lambda) + (1-S) \cdot \mu_a^{Hb}(\lambda))\big)}{D_{ves} \cdot (S \cdot \mu_a^{HbO_2}(\lambda) + (1-S) \cdot \mu_a^{Hb}(\lambda))} \tag{4.15}$$

where D_{ves} is the blood vessel diameter. The OD can now be written as,

$$OD_\lambda = \frac{\langle L_{eff}(\lambda)\rangle \cdot \nu}{D_{ves}} \cdot (S \cdot \mu_a^{HbO_2}(\lambda) + (1-S) \cdot \mu_a^{Hb}(\lambda))\big) \cdot C_\lambda + G(\lambda) \tag{4.16}$$

The saturation S can be written as (ignoring the term $\alpha \cdot G^2$ as was done for Eq. 4.9),

$$S_{\lambda_a|\lambda_i} = \frac{(C_{\lambda_i}/C_{\lambda_a}) \cdot \rho \cdot \mu_a^i(\lambda_i) - \mu_a^{Hb}(\lambda_a)}{\mu_a^{HbO_2}(\lambda_a) - \mu_a^{Hb}(\lambda_a)} \tag{4.17}$$

---

[2] $\alpha = \frac{\rho - 1}{\langle L_{eff}\rangle \cdot \nu \cdot ((\mu_a^{HbO_2}(\lambda_a) - \mu_a^{Hb}(\lambda_a))) \cdot C_{\lambda_a}}$

where S is now also a function of the blood vessel diameter D_{ves}, due to the addition of the diameter-dependent correction factor.

A detailed error analysis of Eq. 4.13 is necessary to find the optimal wavelengths. The error propagation formula gives the error in saturation ΔS as,

$$\Delta S = \sqrt{\left(\frac{\partial S}{\partial \rho}\right)^2 \cdot (\Delta\rho)^2 + \left(\frac{\partial S}{\partial D_{ves}}\right)^2 \cdot (\Delta D_{ves})^2} \qquad (4.18)$$

The error ΔS is a function of S, D_{ves} and λ_a for a chosen λ_i. Now we proceed to analyse each term in Eq. 4.18 and its contribution to the saturation error ΔS. For an image based estimation of the blood vessel diameter D_{ves} (explained in section 4.3.3) using an SLO technique, we chose a constant error on the estimation of the diameter (ΔD_{ves}) as 12 µm based on spatial resolution of the system (see Table 1). The error on $\rho_{\lambda_a|\lambda_i}$ is given by error propagation in Eq. 4.12.

Figure 4.4 and Figure 4.5 shows the colour coded graph of the calculated errors in saturation as a function of D_{ves} and λ_a considering a 1% error ($\Delta I/I$) in the intensities when 506 nm (lowest μ_a^i in the 450 nm 650 nm interval) and 548 nm (highest μ_a^i in the 450 nm 650 nm interval) were used as isosbestic points, respectively. For simplicity, all the saturation error values (ΔS) $>$ 0.10 were set to 0.10 to emphasize the combinations with accuracy better than 0.1. From Figure 4.4, we see that when 506 nm is used as an isosbestic wavelength, there are two spectral bands optimal for oximetry. For low saturation values (0.00 - 0.25), either of the bands, 460 nm to 480 nm or 590 nm to 600 nm could be used. But for higher saturation levels (0.75 1.00), only the 589 to 600 nm gives $\Delta S < 0.1$. When 548 nm is used as an isosbestic wavelength (Fig. 4.5), 589 to 600 nm is not ideal for detecting the low saturation values and 460 to 480 nm is not suitable for high saturation values.

Figure 4.6 shows the saturation error for a 50 µm (Fig.4.6A-4.6C) and a 100 µm (Fig.4.6D-4.6F) blood vessel for different saturation levels. From these graphs, we see that that all the five isosbestic wavelengths perform similarly for estimating fully oxygenated blood (S = 1.00) when the 590-600nm wavelength range is used as anisosbestic wavelength. However, for estimating low saturation values, 522 nm, 586 nm and 506 nm perform marginally better than 548 nm and 569 nm when the 460-480nm wavelength range is used as anisosbestic wavelength.

Figure 4.7 shows ΔS values as a function of λ_a (λ_i= 506 nm) for a fully oxygenated 50 µm and 100 µm blood vessel for different levels of the standard error of the mean ($\Delta I/I$). It can be seen in this figure, that to reach saturation accuracy levels better than 5 % for 100 % oxygenation when measuring near 594 nm, the required accuracy level of the mean intensity was 1 % for both the 50 µm and 100 µm

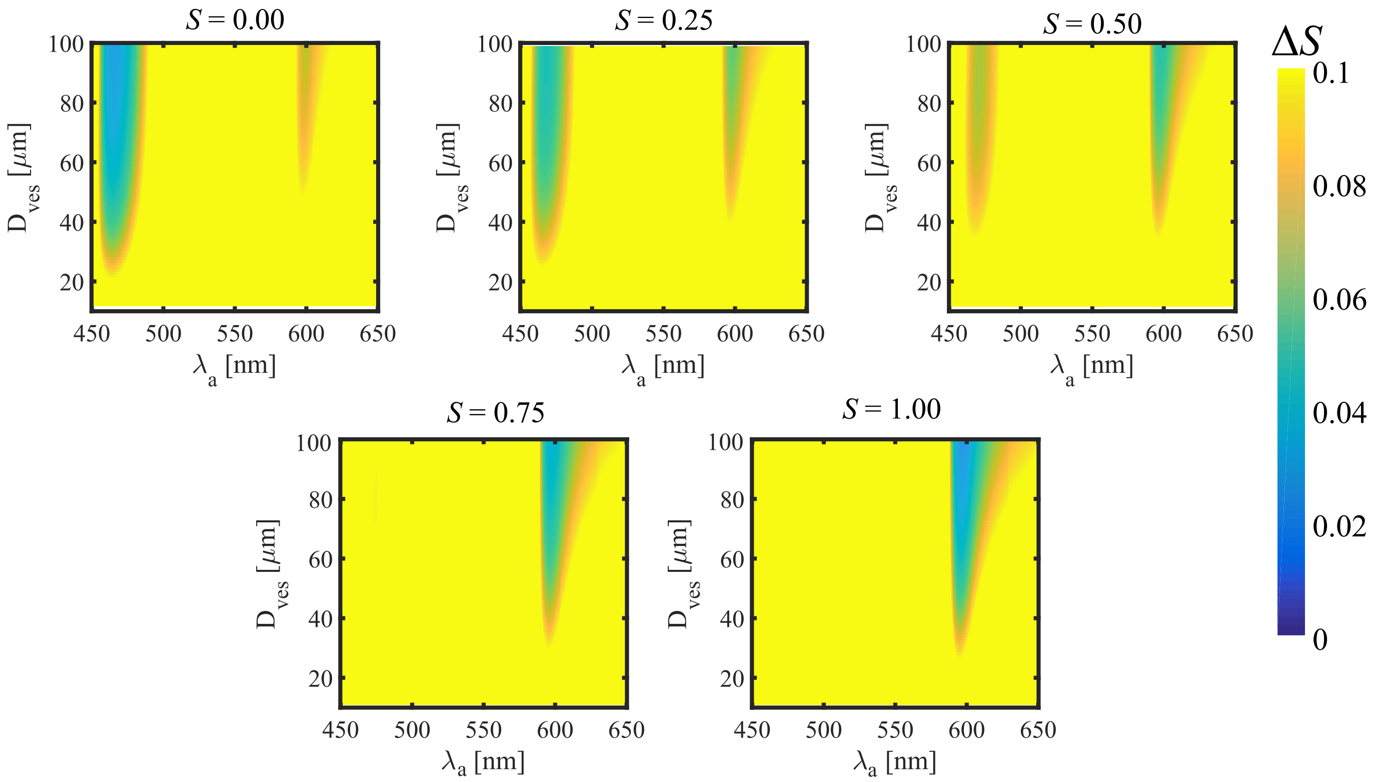

Figure 4.4: Saturation error ΔS for different λ_a when 506 nm is chosen as the isosbestic wavelength. The standard error on the mean recorded intensity values ($\frac{\Delta I}{I}$) was assumed to be 1%. All values of $\Delta S > 0.10$ were made as 0.10.

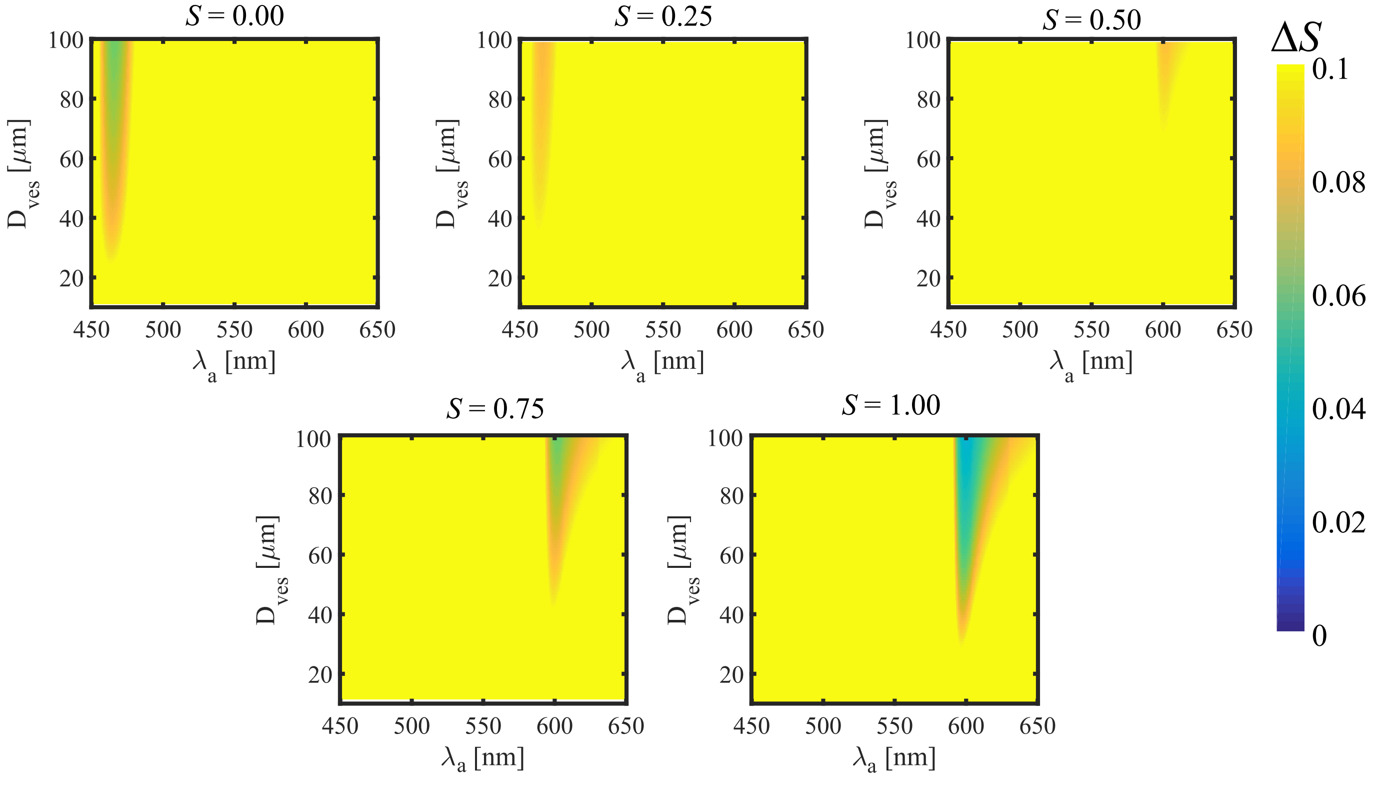

Figure 4.5: Saturation error ΔS for different λ_a when 548 nm is chosen as the isosbestic wavelength. The standard error on the mean recorded intensity values ($\frac{\Delta I}{I}$) was assumed to be 1%. All values of > 0.10 were made as 0.10.

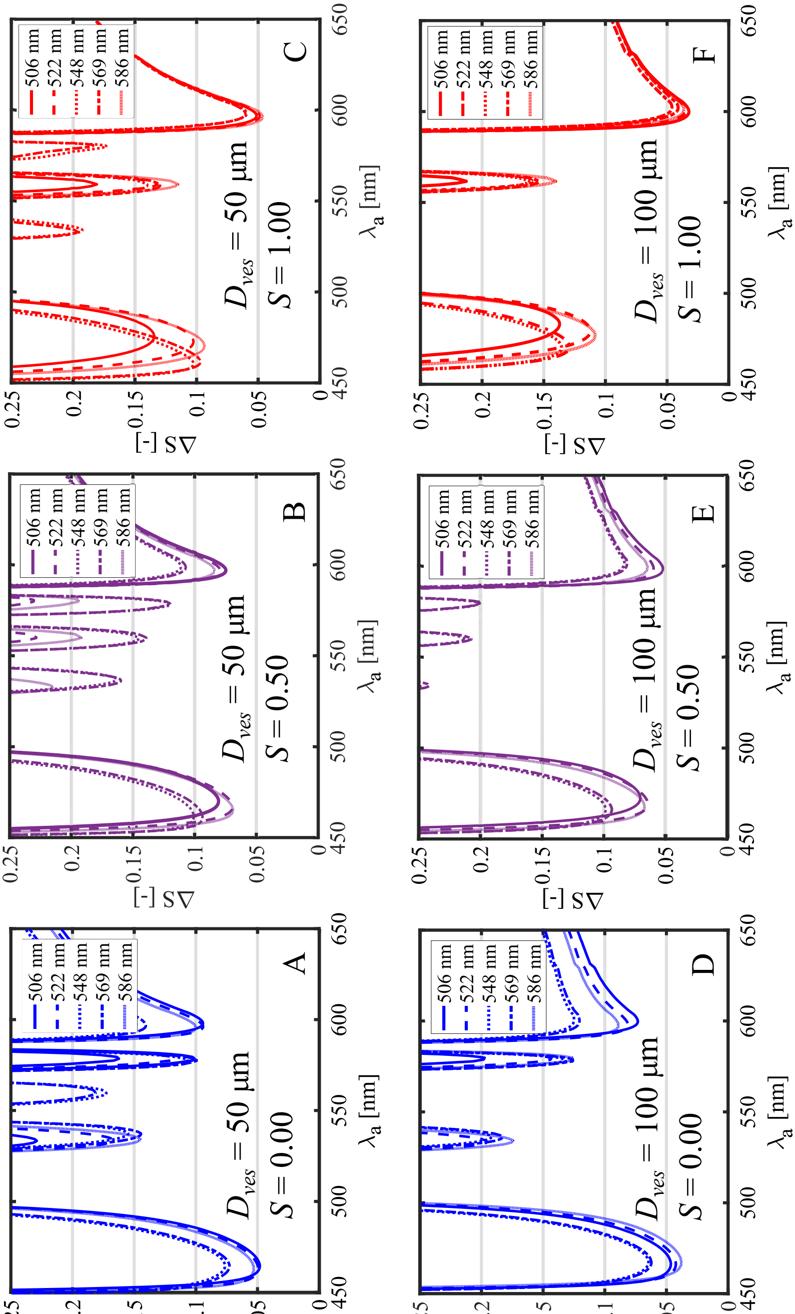

Figure 4.6: Saturation error ΔS as a function of λ_a for different saturation levels (A,D: S=0.00; B,E: S=0.50; C,F=1.00) for a 50 µm (A, B and C) blood vessel and a 100 µm (D, E and F) blood vessel when different isobestic wavelengths in the 500 nm to 600 nm range were chosen as the λ_i.

vessels.

We note that the optimal wavelength bands calculated in the presence, as well as absence of pigment packaging, are very similar. In fact, it is observed that if the ratio of correction factors $C_{\lambda_i}/C_{\lambda_a}$ in Eq. 4.17 is 1, Eq. 4.17 reduces to Eq. 4.9. Thus, choosing wavelengths within the [460 480] and [590 600] band where $C_{506}/C_{\lambda_a} \approx 1$ would serve the purpose of minimising the saturation error independent of the effect of pigment packing. For such wavelength combinations, Eq. 4.9 can be used even in the presence of pigment packing without applying any correction.

Figure 4.8A and 4.8D show the difference in saturation estimated with (Eq. 4.17) and without (Eq. 4.9) pigment packing effect for a 50 µm blood vessel displayed as an offset ($S_{offset} = S_{Eq.17} - S_{Eq.9}$), at isosbestic wavelength $\lambda_i = 506$ nm.

The dark blue region in the colour map in Fig. 4.8A and 4.8D denote the situation when $C_{506}/C_{\lambda_a} \approx 1$, i.e., when pigment packing has no effect. Unfortunately, this condition is satisfied for different wavelengths in the [460 480] and [590 600] wavelength bands for different saturation levels. Figure 4.8B and 4.8E show the saturation error (Eq. 4.11) in the [460 480] and [590 600] wavelength bands, respectively, assuming a 1% measurement error of intensities and when 506 nm was used as an isosbestic wavelength. Figures 4.8C and 4.8F show the combined effect of saturation error from a 1% measurement error and ignoring pigment packing, indicating that by using the 470 nm - 506 nm pair, the combined error is minimized for saturation in the range [0.00 0.55], and by using the 592 nm - 506 nm pair, the combined error is minimized for saturation in the range [0.40 1.00]. Thus, the triad of wavelengths 470, 506 and 592 nm appear to be optimal for retinal oximetry. At these wavelengths, (i) the blood absorption coefficients are approximately equal, and as a consequence, $C_{506}/C_{\lambda_a} \approx 1$, which minimizes the effect of pigment packaging on saturation estimation. Similar absorption and scattering coefficients at these wavelengths satisfies the assumption that $\langle L_{bs}(\lambda_a)\rangle \simeq \langle L_{bs}(\lambda_i)\rangle$ and $\langle L_{eff}(\lambda_a)\rangle \simeq \langle L_{eff}(\lambda_i)\rangle$, which are conditions for our algorithms to hold, ii) the blood absorption coefficients are sufficiently high to yield a good vascular contrast in the images. and finally, (iii) the saturation error is low because the error in measured intensities has a minimized propagation of the error to OD and ρ.

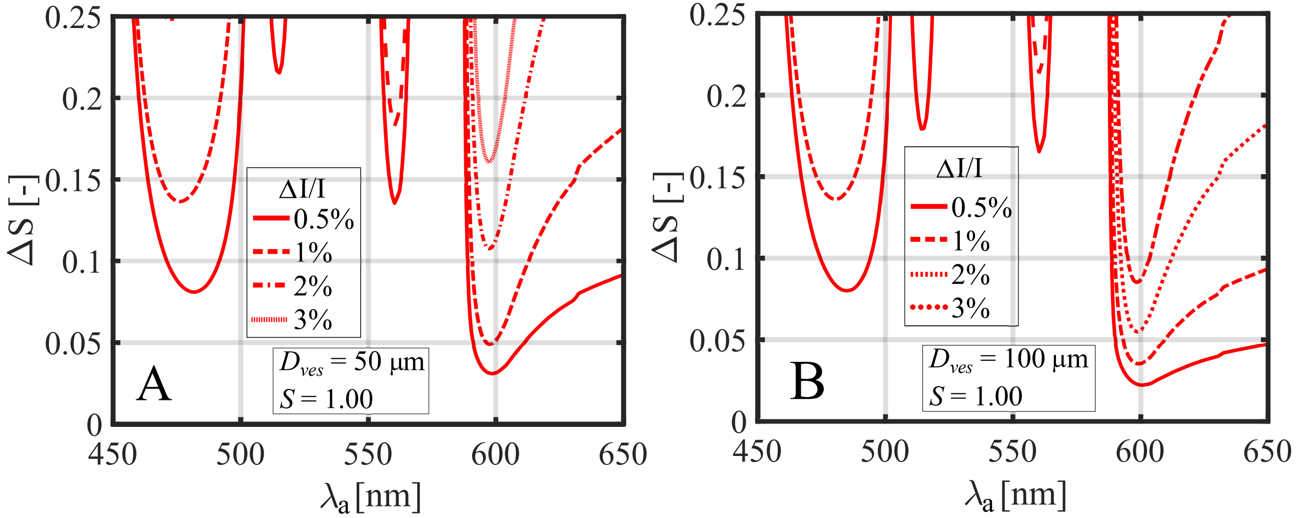

Figure 4.7: Saturation error ΔS as a function of λ_a when estimating full oxygenation (S = 1.00) for a 50 µmblood vessel (A) and 100 µm blood vessel (B) for different levels of % error in the intensities. The isosbestic point chosen was 506 nm.

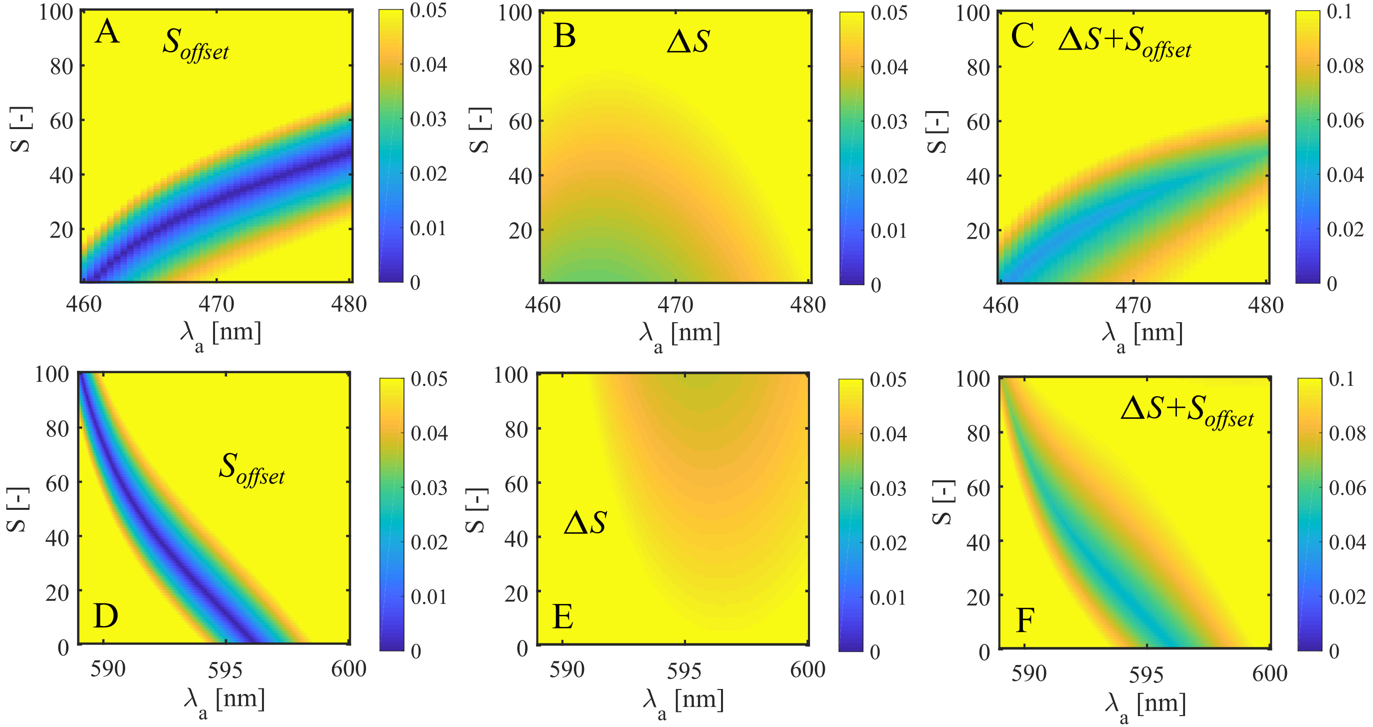

Figure 4.8: A and D: Calculated saturation difference with and without pigment packing effect shown as an offset ($S_{offset} = S_{Eq.17} - S_{Eq.9}$) . B and E: Saturation error calculated from Eq. 4.11 assuming a 1% measurement error of intensities. C and F: Addition of the saturation offset and the saturation error for wavelengths [460 480] and [590 600], respectively

4.3 Experimental validation

To validate our theoretical predictions, we have fabricated a thin, multi-layer retina-mimicking phantom with narrow channels representing blood vessels in the retina. The retina-mimicking phantom was placed in a model eye. An in-house built SLO system using a supercontinuum laser as the light source was used to scan the artificial retina at different wavelengths, to experimentally validate our theory.

4.3.1 Scanning Laser Ophthalmoscope - description of the system

A multiwavelength Scanning Laser Ophthalmoscope (SLO) [43–46] was developed for the continuous acquisition of *en face* images of a phantom retina as shown in Figure 5.3. The pixel rate of the system for imaging the phantoms was 30 kHz, although the maximum pixel rate of the system was 60 kHz. The size of a single image frame was 512 x 512 pixels. Thus, each image took 8.7 seconds to record. The essentially static nature of the phantoms precluded motion artefacts in the recorded image. The key system parameters are detailed in Table 1. Using a relatively large core diameter of 100 µm in the detection compared to single mode core diameter of 2.5 µm in illumination, eliminated the speckle noise in the final image at the expense of spatial resolution due to reduced confocality.

Table 4.1: **System parameters of the SLO**

System parameter	value
Spot size in the retinal plane (at 548 nm)	8.9 µm (Airy disc diameter)
Maximum field of view (FOV)	30° in air
Pixel rate	30 KHz
Digital resolution	11.7 µm

4.3.2 Measurements in model eye using a retina mimicking phantom

Uniformly scattering phantoms were manufactured using a method previously described by de Bruin *et al.* [47]. Using mixtures with different w% of TiO_2, layered phantoms were made in a petri dish, each layer cured in a thermal oven at 80 ^{o}C for 60 minutes. Thin metallic wires of different diameter thickness (90 µm and 140 µm) were embedded in the topmost scattering layer of the phantom while still in the viscous state and then cured. Then a transparent layer of silicone without any TiO_2 particles was poured finally to provide mechanical stability to the phantom. After solidifying completely, the metallic wires were removed from the phantom. For

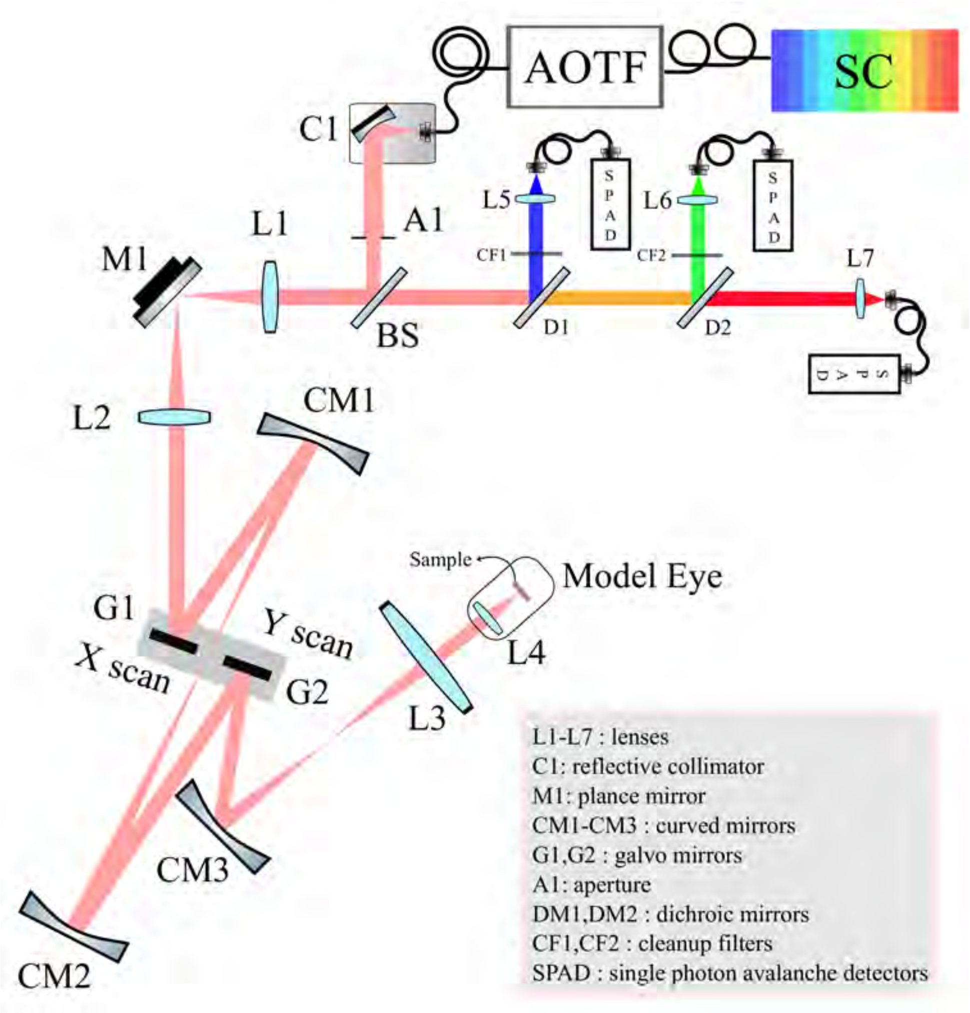
AOTF
SC
C1
L1
A1
M1
BS
L5
CF1
SPAD
D1
L6
CF2
SPAD
D2
L7
SPAD
L2
CM1
G1
Y scan
X scan
G2
Sample
Model Eye
L4
L3
CM3
CM2
L1-L7 : lenses
C1: reflective collimator
M1: plance mirror
CM1-CM3 : curved mirrors
G1,G2 : galvo mirrors
A1: aperture
DM1,DM2 : dichroic mirrors
CF1,CF2 : cleanup filters
SPAD : single photon avalanche detectors

Figure 4.9: Schematic of the multiwavelength SLO used for imaging: Supercontinuum (SC) laser source (NKT Photonics A/S, Denmark) was used as the light source. An acoustic-optic tunable filter, (AOTF) (Select, NKT Photonics A/S, Denmark) coupled to the supercontinuum source provided a spectrally tunable illumination source for the multiple wavelength measurements. The polychromatic light beam from the AOTF was coupled into a single mode fibre with a core diameter of 4ţm and was relayed to a model eye. The model eye was constructed with an uncoated lens L4 (f =15.4 mm) having a curvature very similar to the cornea of the human eye. The sample was placed in the focus of L4. The light was reflected and back-scattered by the sample and 90% of the reflected light passed through the beam splitter in the return path and split using dichroic mirrors into multimode fibres with a core diameter of 100 µm.

our experiments, we used three layer phantoms (Fig. 4.10A) with a transparent top layer, a thin 200 µm layer with $\mu_s^{'}$= 1 mm^{-1} with channels in the middle, and a bottom layer with $\mu_s^{'}$= 5 mm^{-1}.

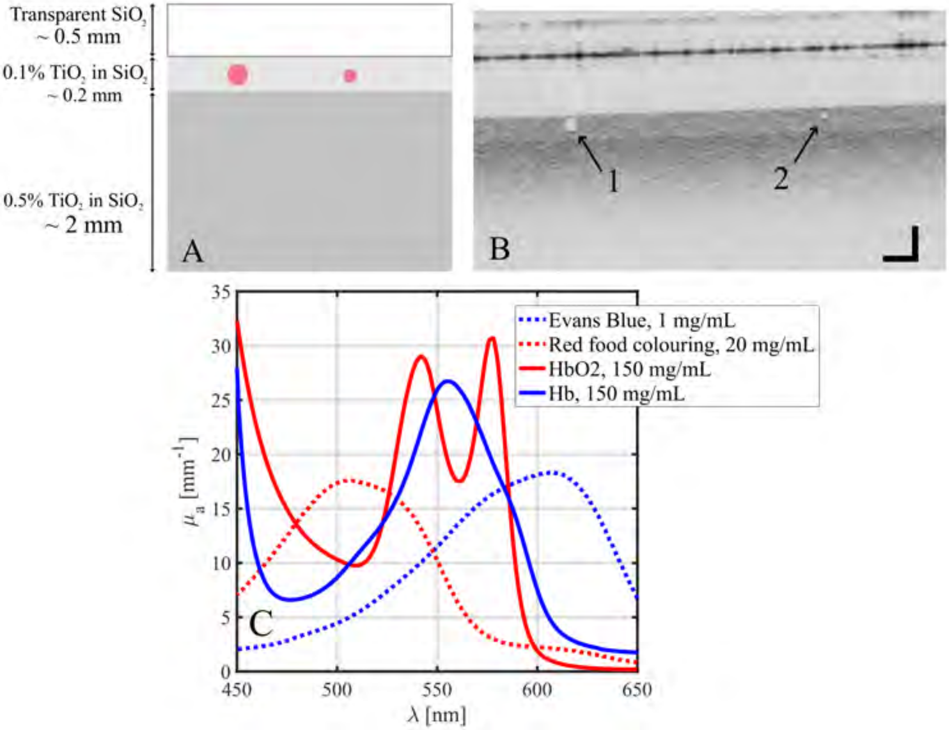

Figure 4.10: A: Layered structure of the phantoms: The phantoms were made to mimic the scattering properties of the retina and two cylindrical channels (red circles) with a diameter of 90 ţm and 140 ţm were embedded in the scattering medium to mimic the blood vessels in the retina. B: OCT B-scan (in house 1310 nm OCT, average of 15 consecutive B scans) of the phantom with the 140 µm hollow (empty) channel (1) and 90 µm hollow (empty) channel (2). Scale bar is 300 ţm in each direction C: Comparison between absorption spectrum of the dyes chosen for phantom measurements and blood.

Figure 4.10B shows an OCT B-scan (cross-section) of the phantom used for the measurements in the model eye. Two water-soluble dyes - Evans Blue (Sigma Aldrich B.V., The Netherlands) and red food colourant (Lebenmittelfarbe, Birkmanns Voedelkleurstof, Germany) were used to mimic the deoxyhaemoglobin and oxyhaemoglobin absorption, respectively. Using a suitable concentration of these dyes, an artificial isosbestic point was created at 548 nm as shown in Fig. 4.10C. Using a syringe, different calibrated proportions of the dyes were injected into the channels. If [EB] is the concentration of Evans Blue and [FC] is the concentration of the red food colourant, we define a parameter ς as, If $[EB]$ is the concentration of Evans Blue and $[FC]$ is the concentration of the red food colourant, we define a parameter ς as,

$$\varsigma = \frac{[FC]}{[FC] + [EB]} \tag{4.19}$$

An analysis similar to the analysis in section 4.2 was performed to find the wavelengths resulting in low errors when estimating the parameter ς. The optimum wavelengths for the dye combination was found to be 500 nm, 548 nm (isosbestic) and 610 nm. Due to the choice of the dichroic mirrors (DM1 and DM2 in Fig. 5.3) in the detection channel, 488 nm and 612 nm were chosen as the two anisosbestic wavelengths to measure the saturation. Using a suitable ratio of [FC] and [EB], solutions with five different ς (0.00, 0.25, 0.50, 0.75 and 1.00) were made and injected into the channels using a syringe. The phantoms were imaged simultaneously using the three different wavelengths, 488 nm (bandwidth, FWHM: 2 nm), 612 nm (bandwidth, FWHM: 3 nm) and 548 nm (isosbestic) (bandwidth, FWHM: 2 nm), and *en face* face images were created for each wavelength. The number of reflected photons from TiO_2 and the dye-filled channel was estimated from the image and the parameter ς was then calculated after estimating the ODs, ρ and D_C (channel diameter) values from the images.

4.3.3 Estimating vessel diameter from the images

Figure 4.11 shows the typical intensity profile of a phantom blood vessel. The phantom blood vessel diameter was determined by the distance (in pixels) between the points with maximum slope magnitude along the blood vessel profile *v1* and *v2*. The intensity at the blood vessel location was directly estimated by the minima of the vessel profile.

The intensity at the tissue location *t* was estimated using the points *t1* and *t2* by a linear approximation. The points *t1* and *t2* represent the locations where the light has not interacted with the blood and are at a fixed number of pixels from *v1* and *v2*, respectively such that the locations *t* and *b* are affected by similar factors except the absorption by haemoglobin. In our analysis, we took the points *t1* and *t2*, at a distance of 2×diameter from on each side from *v1* and *v2*. To increase the accuracy of the estimated intensities (points t and b), the intensities were average along multiple locations in the tissue and in the middle of the blood vessel as shown in Fig. 4.11.

The intensity $I(\overline{x}_b, \lambda)$ was obtained by averaging the intensities of the points *b* along the valley (along with the y dimension — denoted by dotted lines). The point *t* and thereby $I(\overline{x}_t, \lambda)$ is obtained by averaging the points in an area as shown in Fig.

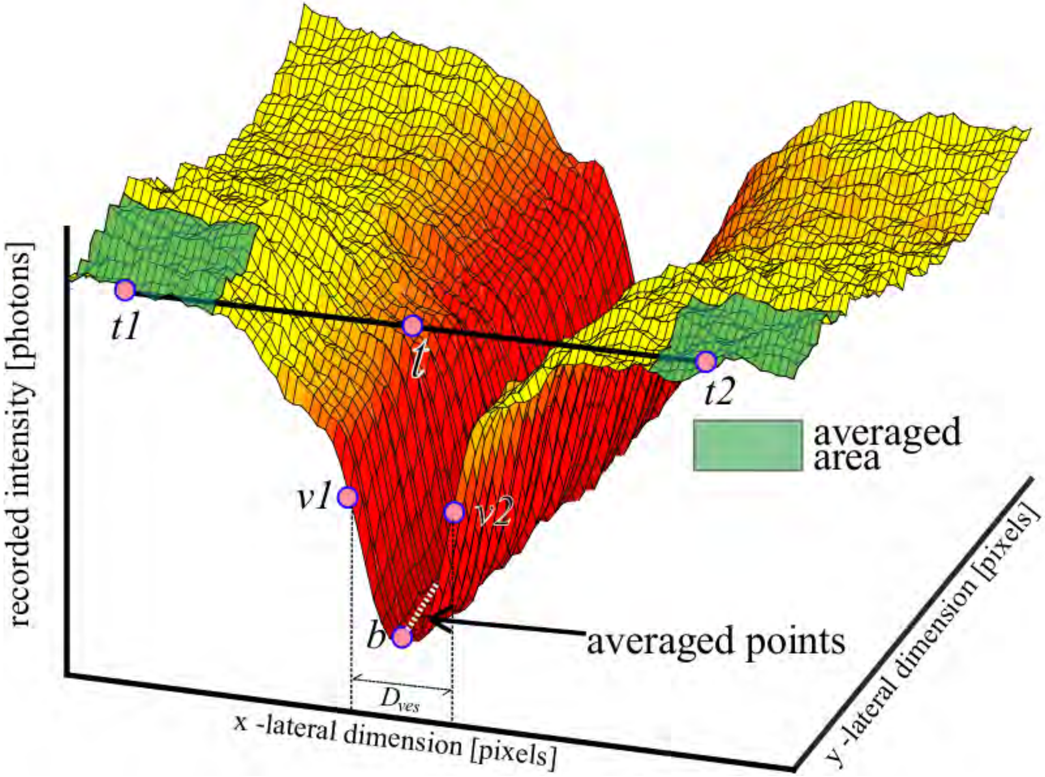

Figure 4.11: Typical phantom blood vessel intensity profile: The blood vessel absorption creates a dip in the intensity profile with a local minimum at point *b*. The OD is calculated as a ratio of the intensity of point *t* (the linear approximation of the tissue intensity in the absence of the blood vessel) and point *b*. The points *v1* and *v2* are the points with a maximum slope along the vessel walls and *t1* and *t2* are the tissue locations used for the linear approximation of the tissue intensities.

4.11.

4.3.4 Experimental Results with retinal phantoms

Figure 4.12A - Fig. 4.12C shows the reflectance measurements for 100 % food coloring (ς= 1.00) showing high absorption at 488 nm (Fig. 4.12A). Figure 4.12D - Fig. 4.12F shows the reflectance measurements for 0 % food colouring (ς= 0.00). Measurement points were chosen along the center of the channel and in the tissue (TiO_2 layer in this case) to estimate the reflected light intensity (I_b and I_t). To bring the standard error on the mean intensity in both the tissue and along the blood vessels to acceptable values of $\leq 1\%$, up to 400 points were averaged in the tissue location and 40 points were averaged in the blood vessel location. The intensity profiles along the lines indicated in Fig. 4.12D - Fig. 4.12F is plotted in Fig. 4.12G. The dip in the intensity profile due to the absorption of blood is obvious in Fig. 4.12G. The channels in the phantom are slightly curved due to the process of manufacturing the phantoms as described in section 3.2. The phantom was slightly angled during measurements to reduce specular reflections. This resulted in a slight change in the non-uniformity of the collected intensities within the imaging field. The bright spots in Fig. 4.12A and 4.12D are due to specular reflections from the surface of the sample and could be caused by dust on the surface.

The comparison between the theoretical (with and without pigment packing correction) and experimentally obtained average ρ values in the phantom channel are shown in Fig. 13, for both the 90 µm and the 140 µm channels used in the phantom. Our phantom geometry resembles the geometry in fig. 4.1A here the pigment packing effect is not expected to play a large role. Indeed, Fig. 13 clearly shows that the estimated values closely follow the theoretical values without correction for pigment packaging. The estimated diameter of the channels from the images for 140 µm and 90 µm were 144 ± 6 µm and 92 ± 7 µm, respectively.

In Fig. 13, both the fitted curves with and without pigment packing describe the measurements reasonably well since the difference between the uncorrected and corrected calculated ρ values are small. This illustrates that by picking optimum wavelengths that fulfill the conditions stated in section 4.2, the deviation between the ρ values with and without pigment packing could be minimised. For non-optimal wavelengths, the difference in ρ values with and without correction is much higher (data not shown) and hence, using the simplified model presented without pigment packing would result in large offsets to the saturation estimation for smaller blood vessels embedded deeper in tissue. Figure 5.14 shows the pseudo colour map of the saturation overlaid on the corresponding reflectance image from

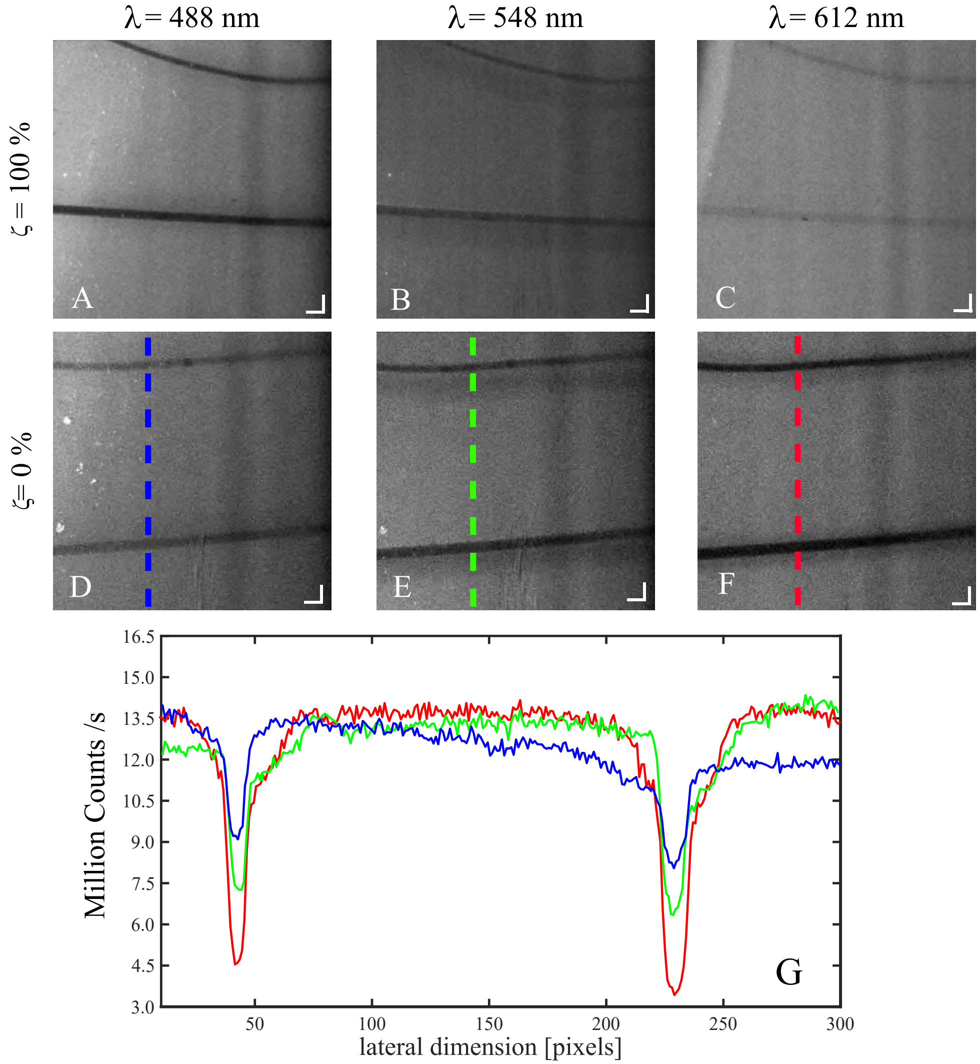

Figure 4.12: A-F : Reflectance measurements of the phantoms in the model eye at three different wavelengths (λ, columns) and two different saturation levels (ς,rows). The intensity profiles along the lines indicated in D - F is plotted in G - 488 nm (blue), 548 nm (green) and 612 nm (red). Scale bar is

300 µm

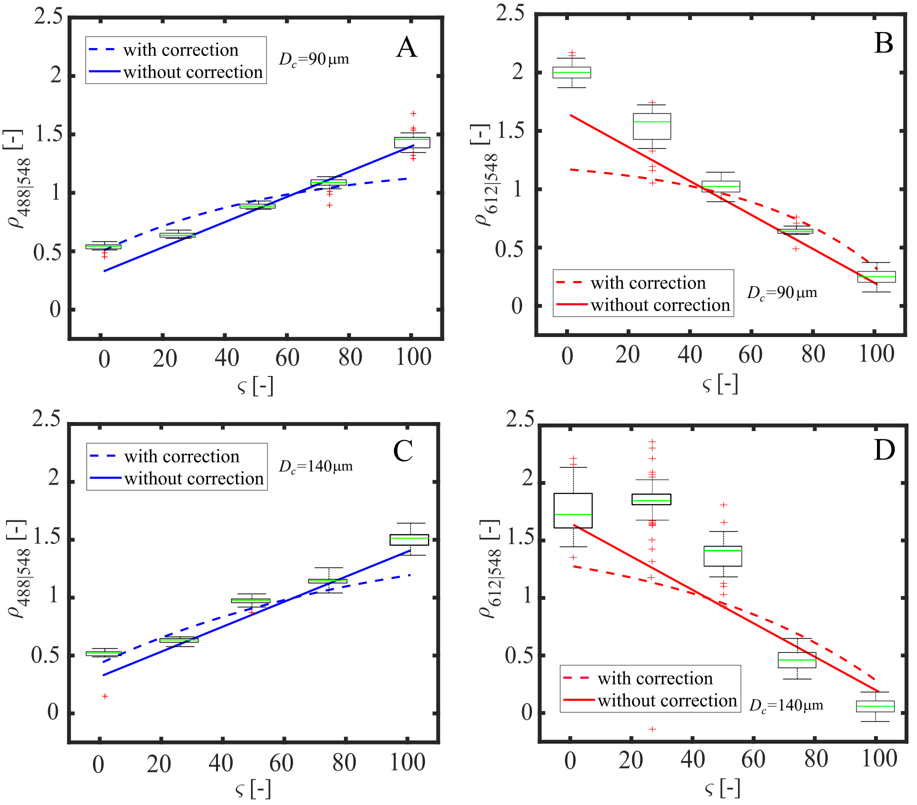

Figure 4.13: Comparison between the theoretical and experimental ρ values for the different ratio of dye concentrations in the 90 µm channel (A and B), 140 µm channel (C and D). The average values in the channels for each value are plotted as a box plot, with '+' values representing the outliers. Left panels (blue lines, panels A and C) use the 488-548 nm wavelength pair for ρ calculations, right panels (red lines, panels B and D) use the 548-612 nm wavelength pair for ρ calculations.

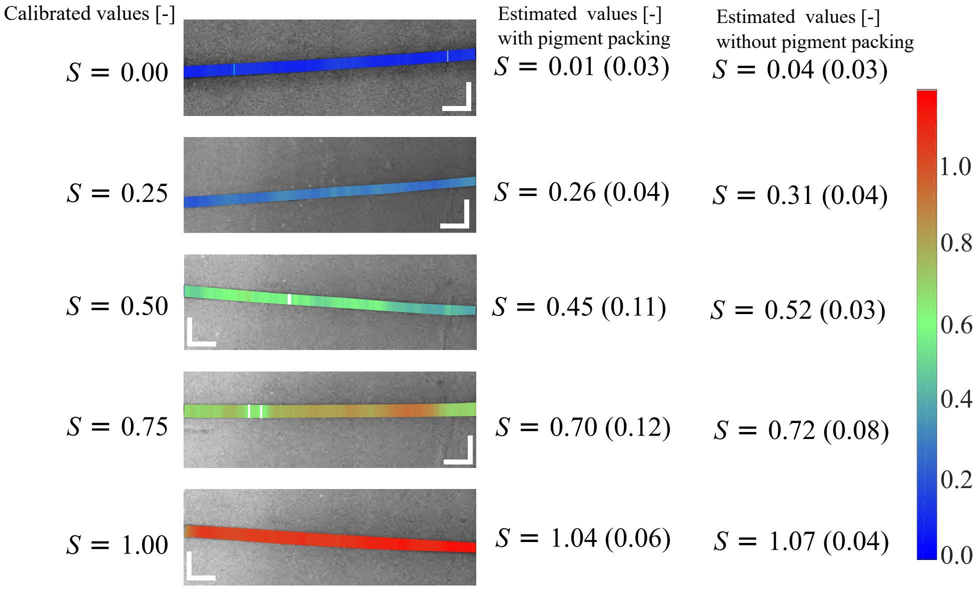
Calibrated values [-]
Estimated values [-] with pigment packing
Estimated values [-] without pigment packing
$S = 0.00$
$S = 0.01\ (0.03)$
$S = 0.04\ (0.03)$
$S = 0.25$
$S = 0.26\ (0.04)$
$S = 0.31\ (0.04)$
$S = 0.50$
$S = 0.45\ (0.11)$
$S = 0.52\ (0.03)$
$S = 0.75$
$S = 0.70\ (0.12)$
$S = 0.72\ (0.08)$
$S = 1.00$
$S = 1.04\ (0.06)$
$S = 1.07\ (0.04)$
1.0
0.8
0.6
0.4
0.2
0.0

Figure 4.14: Pseudocolour images of the saturation ς superimposed on the reflectance image for the 140 µm blood vessel. Scale bar is 300 µm. The estimated values with and without pigment packing are presented as mean (standard deviation) of all values of estimated ς in each channel.

the SLO for the 140 µm blood vessel for 5 different calibrated values. The estimated values show the overall mean and standard deviation of the saturation in the channel. For the estimation of ς, the 488-548 nm pair was used for ς =0.00, 0.25 and 0.50, while the 548-612 nm pair was used for ς = 0.75 and 1.00.

4.4 Discussion

SLO-based retinal oximetry has advantages over conventional fundus camera-based method regarding resolution and contrast. A critical factor for clinically relevant retinal oximetry is to be able to determine blood oxygen saturation in small retinal vessels — capillaries, venules and arterioles. It is in these micro vessels that the oxygen saturation is expected to decrease in response to increased metabolic demand or decreased oxygen delivery capacity. The larger retinal vessels (>100 µm) are expected to be less sensitive to changes in tissue metabolic demand or micro-vascular dysfunction and are therefore not ideal as early hypoxia markers. The clinical value of fundus camera-based oximeters is most likely limited due to the low spatial resolution, even if the oxygen saturation estimates would be accurate and robust taking into account our optimised wavelengths and our proposed algorithms that include pigment packaging. SLO based oximeters have been investigated before, but their performance was limited due to suboptimal choices for the wavelengths used, combined with oximetry algorithms that did not take pigment packaging into account, which is likely a non-negligible factor for smaller blood vessels located deeper in the retina.

In this paper, we have for the first time addressed factors that affect the accuracy of SLO based oximeters, i.e. measurement noise and pigment packaging when measuring small, embedded blood vessels. Although we have used relatively large diameter blood vessels in our validation experiments, this was a limitation of the phantom fabrication technique yielding unstable phantoms at low channel diameters and is not a limitation of the imaging technique as current SLO technology can image blood vessels smaller than 50 µm.

In our SLO design, we used single-mode fibre illumination and multimode fibre detection. Hence the imaging is not truly confocal, but quasi-confocal or sub-diffuse. We believe that quasi-confocal, sub-diffuse detection reduces the central light reflex, a bright specular reflection from the centre of a blood vessel that is common to many fundus imaging modalities that do not use cross polarisers. When the central light reflex is present in an image, the intensity in the centre of the vessel could be extracted by reconstructing the blood vessel profile using analytical models, such as a fourth order polynomial [39, 48]. This adds additional error to the blood vessel OD estimation and thereby, the saturation estimation. Longitudinal chromatic aberration (LCA) is another potential source of error in oximetry due to the dispersion in the human eye [49]. LCA causes the spatial location of each pixel in the multispectral image to be in a slightly different axial plane for different wavelengths. This effect can lead up to a 250 µm longitudinal focal shift between the 470 nm and 592 nm wavelengths. However, this effect can be corrected as has been done previously by others [50, 51] by using an achromatizing lens in the beam path. The Optimum wavelength analysis was made with a 1 nm bandwidth around each central wavelength. The filter bandwidth choice can be incorporated into the oximetry analysis by multiplying the absorption spectrum of haemoglobin and the filter transmission spectrum and obtaining an average absorption coefficient for that spectral band, and then by using this averaged absorption coefficients in Eq. 4.9 and Eq. 4.17 to obtain a saturation estimation, and therefore the saturation error.

As explained previously, the noise in the images propagates into the saturation error. To achieve acceptable levels of saturation error (we aim for <5%, but it depends on the clinical application), a large number of points along the blood vessel and the tissue location have to be averaged. While this is relatively easy in our experiments due to the homogeneous nature of the phantom, an *in vivo* image contains structural information and choosing many points might lead to an incorrect estimation of the intensity in the absence of a blood vessel. A smaller number of points around the blood vessel should be averaged to overcome this problem, and this requires multiple images to be produced within a short amount of time. Fundus cameras are based on snapshot imaging, and it might not always be possible to acquire multiple images continuously without causing discomfort to the subject or exceeding the safety limit for radiant exposure. Although our current SLO images at relatively slow speeds, significant improvements in speed can be achieved by using a resonant scanner, with a reduced signal-to-noise ratio. Inhomogeneities in absorption within a vessel due to the distribution of red blood cells is less relevant in the final saturation estimation due to the required averaging and resulting image acquisition speeds to achieve desired SNR. Current commercial SLO technology has an imaging speed of about 30 Hz, which facilitates the averaging of multiple consecutive images to accomplish noise reduction.

The effective path length ($\langle L_{eff} \rangle$) that photons travel through a tissue volume before being collected depends on the illumination and collection geometry and is also a function of the optical properties of the tissue and is, therefore, wavelength dependent. We have assumed that the effective path length for the two wavelengths used to calculate the factor ρ (Eq. 4.12) is almost the same. In the wavelength range 450-600 nm where absorption remains of the same order and scattering varies slowly with wavelength (roughly as $1/\lambda$). However, if there is a slight mismatch in the path lengths, this results in an offset in the saturation estimation. We have calculated that a 20% mismatch in path lengths ($\langle L_{\lambda_p} \rangle / \langle L_{\lambda_i} \rangle$ =1.2) could lead up to a 30% offset in the saturation estimates. For the phantoms that we fabricated, scattering was a slowly varying function of wavelength, similar to tissue, and the absorption coefficients of the dyes in the channels were of the same order of magnitude as the absorption coefficients of oxy- and deoxyhaemoglobin. For our phantoms, we have shown to accurately recover the saturation in the channels, suggesting that there were no significant changes in the path length due to scattering and absorption in a tissue-mimicking phantom with relevant scattering and absorbing properties. A limiting factor of our phantom was that the dyes that mimic the oxy- and deoxyhemoglobin were non-scattering, which is different from real blood.

Additionally, in a sub diffuse approach, pigments which are present in the retina, especially in the retinal pigment epithelium (RPE) and absorption background due to choroid blood can affect the recorded intensity. The effect of the melanin on backscattered light varies with concentration [52], and an *a priori* knowledge of the pigment concentration in RPE melanin and its contribution to the backscattered light can aid in removing the influence of RPE in the backscattered light. OCT-based oximetry methods might have an advantage here that layers of the retina free from the influence of RPE can be used for extracting the intensities. But, OCT being a coherent detection method suffers from speckles, and a significant amount of averaging has to be performed to improve the image quality and reduce the error on intensity down to 1%. We must emphasise that insufficient removal of the system reflections from the recorded intensities will result in a wrong estimation of the ODs and hence the saturation. Therefore, in our experiments, all the internal system reflections were subtracted by taking a reference measurement without any sample.

There have been several attempts to choose the optimal wavelengths for retinal oximetry but none of them has accounted for the haemoglobin packaging effect. Most of these attempts were aimed at two wavelength oximetry [15, 53, 54] using one isosbestic wavelength and another non-isosbestic wavelength where $|\mu_a^{HbO_2}(\lambda) - \mu_a^{Hb}(\lambda)|$ is maximum, the popular choice being 570 nm (isosbestic) and 600 nm. While this wavelength combination might give sufficiently accurate saturation estimation in arteries, our analysis shows that they are not reliable for low saturation values of $S < 60\%$. *Schweitzer et al.*[55] reported a physiologically relevant retinal oxygenation range of 57 %-92%. However, lower saturations may be expected due to various pathological conditions. *Smith et al.* [56] chose 803 nm (isosbestic) and 670 nm to estimate the saturation. The infra-red wavelengths have weak blood absorption and therefore give a poor estimate of the blood absorption leading to a large error in the saturation estimations according to our calculations. In 1988 *Delori* [14] used three wavelengths — 558 nm, 570 nm (isosbestic) and 548 nm (isosbestic) — to scan a small area of the retina with blood vessel tracking to reduce eye motion artefacts. This wavelength choice, similar to the 570-600 nm wavelength pair, results in poor accuracy for low saturation values, $S < 60\ \%$. Our assessment of the modified oximetry equations suggests that the 470, 506 (isosbestic) and 592 nm triad is the best combination for oximetry. Although this choice spans a relatively broad wavelength range (≈130 nm), the absorption coefficients and scattering coefficients in this wavelength range are similar to those we have used in our phantoms, suggesting that the effective path lengths differences within this wavelength range are of minor importance.

The accuracy of saturation estimation can be potentially improved by including more wavelengths. To this end, hyperspectral imaging [17, 23–25, 57, 58] approaches towards in vivo retinal oximetry have also been undertaken by various groups. However, the challenge of acquiring images with sufficient SNR from multiple wavelengths at high spatial resolution, in a large field of view, with high speed and with low power levels remains.

4.5 Conclusions

We have presented a method to select optimal wavelengths for oximetry measurements in the retina through an error analysis on a modified oximetry equation that includes the effect of pigment packaging. The result of the analysis yielded 470 nm, 506 nm (isosbestic) and 592 nm as three suitable wavelengths for accurate estimation of oxygenation in the retinal blood vessels. We have developed a quasi-confocal, multispectral SLO capable of simultaneously imaging the retina at all these wavelengths and demonstrated the validity of our approach in tissue-mimicking phantoms. *In vivo* human experiments are pending ethical committee approval.

References

[1] E. D. Cole, E. A. Novais, R. N. Louzada, and N. K. Waheed, "Contemporary retinal imaging techniques in diabetic retinopathy: a review," Clin. Exp. Ophthalmol. **44** (2016).

[2] R. Klein, B. E. K. Klein, M. W. Neider, L. D. Hubbard, S. M. Meuer, and R. J. Brothers, "Diabetic Retinopathy as Detected Using Ophthalmoscopy, a Nonmyciriatic Camera and a Standard Fundus Camera," Ophthalmology **92** (1985).

[3] G. Michelson, M. Scibor, and D. Schweizter, "Intravascular oxygen saturation in retinal vessels in glaucoma," Invest. Ophthalmol. Vis. Sci. **43** (2002).

[4] E. Nitta, K. Hirooka, T. Shimazaki, S. Sato, K. Ukegawa, Y. Nakano, and A. Tsujikawa, "Retinal oxygen saturation before and after glaucoma surgery," Acta Ophthalmol. 2017.

[5] O. B. Olafsdottir, S. H. Hardarson, M. S. Gottfredsdottir, A. Harris, and E. Stefánsson, "Retinal oximetry in primary open-angle glaucoma," Investig. Ophthalmol. Vis. Sci. **52**, 6409-6413 (2011).

[6] T. Eysteinsson, S. H. Hardarson, D. Bragason, and E. Stefánsson, "Retinal vessel oxygen saturation and vessel diameter in retinitis pigmentosa," Acta Ophthalmol. **92**, 449-453 (2014).

[7] C. Türksever, C. Valmaggia, S. Orgül, D. Schorderet, J. Flammer, and M. Todorova, "Retinal vessel oxygen saturation and its correlation with structural changes in retinitis pigmentosa.," Acta Ophthalmol **92**, 454-460 (2014).

[8] T. Ueda-Consolvo, C. Fuchizawa, M. Otsuka, T. Nakagawa, and A. Hayashi, "Analysis of retinal vessels in eyes with retinitis pigmentosa by retinal oximeter," Acta Ophthalmol. **93**, e446-e450 (2015).

[9] A. Geirsdottir, S. H. Hardarson, O. B. Olafsdottir, and E. Stefánsson, "Retinal oxygen metabolism in exudative age-related macular degeneration," Acta Ophthalmol. **92**, 27-33 (2014).

[10] S. Yoneya, T. Saito, Y. Nishiyama, T. Deguchi, M. Takasu, T. Gil, and E. Horn, "Retinal oxygen saturation levels in patients with central retinal vein occlusion," Ophthalmology **109**, 1521-1526 (2002).

[11] M. I. Uddin, S. M. Evans, J. R. Craft, M. E. Capozzi, G. W. McCollum, R. Yang, L. J. Marnett, M. J. Uddin, A. Jayagopal, and J. S. Penn, "In Vivo Imaging of Retinal Hypoxia in a Model of Oxygen-Induced Retinopathy.," Sci. Rep. **6**, 310-11 (2016).

[12] A. B. Einarsdottir, S. H. Hardarson, J. V. Kristjansdottir, D. T. Bragason, J. Snaedal, and E. Stefánsson, "Retinal Oximetry Imaging in Alzheimers Disease," J. Alzheimers Dis. **49**, 79-83 (2015).

[13] N. J. Hart, Y. Koronyo, K. L. Black, and M. Koronyo-Hamaoui, "Ocular indicators of Alzheimer's: exploring disease in the retina," Acta Neuropathol. **132**, 767-787 (2016).

[14] F. C. Delori, "Noninvasive technique for oximetry of blood in retinal vessels.," Appl. Opt. **27**, 1113-1125 (1988).

[15] 1. J. B. Hickam, H. O. Sieker, and R. Frayser, "Studies of retinal circulation and A-V oxygen difference in man.," Trans. Am. Clin. Climatol. Assoc. **71**, 34-44 (1959).

[16] E. DeHoog and J. Schwiegerling, "Optimal parameters for retinal illumination and imaging in fun-

dus cameras.," Appl. Opt. **47**, 6769-6777 (2008).

[17] J. C. Ramella-Roman, S. a Mathews, H. Kandimalla, A. Nabili, D. D. Duncan, S. a DAnna, S. M. Shah, and Q. D. Nguyen, "Measurement of oxygen saturation in the retina with a spectroscopic sensitive multi aperture camera.," Opt. Express **16**, 6170-6182 (2008).

[18] M. Hammer and D. Schweitzer, "Quantitative reflection spectroscopy at the human ocular fundus," Phys.Med.Biol. **47**, 179-191 (2002).

[19] M. Hammer, W. Vilser, T. Riemer, and D. Schweitzer, "Retinal vessel oximetry-calibration, compensation for vessel diameter and fundus pigmentation, and reproducibility," J. Biomed. Opt. **13**, (2008).

[20] T. Shiba, K. Maruo, and T. Akahoshi, "Development of a multi-field fundus photographing system using a non-mydriatic camera for diabetic retinopathy," Diabetes Res. Clin. Pract. **45**, 1-8 (1999).

[21] A. Geirsdottir, O. Palsson, S. H. Hardarson, O. B. Olafsdottir, J. V Kristjansdottir, and E. Stefansson, "Retinal Vessel Oxygen Saturation in Healthy Individuals," Investig. Ophthalmol. Vis. Sci. **53**, 5433-5442 (2012).

[22] S. H. Hardarson, A. Harris, R. A. Karlsson, G. H. Halldorsson, L. Kagemann, E. Rechtman, G. M. Zoega, T. Eysteinsson, J. A. Benediktsson, A. Thorsteinsson, P. K. Jensen, J. Beach, and E. Stefánsson, "Automatic retinal oximetry," Investig. Ophthalmol. Vis. Sci. **47**, 5011-5016 (2006).

[23] D. J. Mordant, I. Al-Abboud, G. Muyo, A. Gorman, A. Sallam, P. Ritchie, A. R. Harvey, and A. I. McNaught, "Spectral imaging of the retina," Eye **25**, 309-320 (2011).

[24] W. R. Johnson, D. W. Wilson, W. Fink, M. Humayun, and G. Bearman, "Snapshot hyperspectral imaging in ophthalmology.," J. Biomed. Opt. **12** (2014).

[25] B. Khoobehi, J. M. Beach, and H. Kawano, "Hyperspectral Imaging for Measurement of Oxygen Saturation in the Optic Nerve Head," Invest. Ophthalmol. Vis. Sci. **45**, 1464-72 (2004).

[26] A. H. Kashani, E. Kirkman, G. Martin, and M. S. Humayun, "Hyperspectral computed tomographic imaging spectroscopy of vascular oxygen gradients in the rabbit retina In Vivo," PLoS One **6**, 1-11 (2011).

[27] R. A. Ashman, F. Reinholz, and R. H. Eikelboom, "Oximetry with a multiple wavelength SLO," Int. Ophthalmol. **23**, 343-346 (2001).

[28] J. V. Kristjansdottir, S. H. Hardarson, G. H. Halldorsson, R. A. Karlsson, T. S. Eliasdottir, and E. Stefánsson, "Retinal oximetry with a scanning laser ophthalmoscope," Investig. Ophthalmol. Vis. Sci. **55**, 3120-3126 (2014).

[29] H. Li, J. Lu, G. Shi, and Y. Zhang, "Measurement of oxygen saturation in small retinal vessels with adaptive optics confocal scanning laser ophthalmoscope," J. Biomed. Opt. **16**, 110504 (2011).

[30] S. P. Chong, M. Bernucci, H. Radhakrishnan, and V. J. Srinivasan, "Structural and functional human retinal imaging with a fiber-based visible light OCT ophthalmoscope," Biomed. Opt. Express **8**, 323 (2017).

[31] S. Chen, J. Yi, W. Liu, V. Backman, and H. F. Zhang, "Monte Carlo Investigation of Optical Coherence Tomography Retinal Oximetry," IEEE Trans. Biomed. Eng. **62**, 2308-2315 (2015).

[32] J. C. Finlay and T. H. Foster, "Effect of pigment packaging on diffuse reflectance spectroscopy ofsamples containing red blood cells," Opt. Lett. **29**, 965-967 (2004).

[33] A. Amelink, T. Christiaanse, and H. J. C. M. Sterenborg, "Effect of hemoglobin extinction spectra on optical spectroscopic measurements of blood oxygen saturation," Opt. Lett. **34**, 1525-1527 (2009).

[34] N. Rajaram, A. Gopal, X. Zhang, and J. W. Tunnell, "Experimental validation of the effects of microvasculature pigment packaging on in vivo diffuse reflectance spectroscopy," Lasers Surg. Med. **42**, 680-688 (2010).

[35] N. Bosschaart, G. J. Edelman, M. C. G. Aalders, T. G. van Leeuwen, and D. J. Faber, "A literature review and novel theoretical approach on the optical properties of whole blood," Lasers Med. Sci.

dus cameras.," Appl. Opt. **47**, 6769-6777 (2008).

[17] J. C. Ramella-Roman, S. a Mathews, H. Kandimalla, A. Nabili, D. D. Duncan, S. a DAnna, S. M. Shah, and Q. D. Nguyen, "Measurement of oxygen saturation in the retina with a spectroscopic sensitive multi aperture camera.," Opt. Express **16**, 6170-6182 (2008).

[18] M. Hammer and D. Schweitzer, "Quantitative reflection spectroscopy at the human ocular fundus," Phys.Med.Biol. **47**, 179-191 (2002).

[19] M. Hammer, W. Vilser, T. Riemer, and D. Schweitzer, "Retinal vessel oximetry-calibration, compensation for vessel diameter and fundus pigmentation, and reproducibility," J. Biomed. Opt. **13**, (2008).

[20] T. Shiba, K. Maruo, and T. Akahoshi, "Development of a multi-field fundus photographing system using a non-mydriatic camera for diabetic retinopathy," Diabetes Res. Clin. Pract. **45**, 1-8 (1999).

[21] A. Geirsdottir, O. Palsson, S. H. Hardarson, O. B. Olafsdottir, J. V Kristjansdottir, and E. Stefansson, "Retinal Vessel Oxygen Saturation in Healthy Individuals," Investig. Ophthalmol. Vis. Sci. **53**, 5433-5442 (2012).

[22] S. H. Hardarson, A. Harris, R. A. Karlsson, G. H. Halldorsson, L. Kagemann, E. Rechtman, G. M. Zoega, T. Eysteinsson, J. A. Benediktsson, A. Thorsteinsson, P. K. Jensen, J. Beach, and E. Stefánsson, "Automatic retinal oximetry," Investig. Ophthalmol. Vis. Sci. **47**, 5011-5016 (2006).

[23] D. J. Mordant, I. Al-Abboud, G. Muyo, A. Gorman, A. Sallam, P. Ritchie, A. R. Harvey, and A. I. McNaught, "Spectral imaging of the retina," Eye **25**, 309-320 (2011).

[24] W. R. Johnson, D. W. Wilson, W. Fink, M. Humayun, and G. Bearman, "Snapshot hyperspectral imaging in ophthalmology.," J. Biomed. Opt. **12** (2014).

[25] B. Khoobehi, J. M. Beach, and H. Kawano, "Hyperspectral Imaging for Measurement of Oxygen Saturation in the Optic Nerve Head," Invest. Ophthalmol. Vis. Sci. **45**, 1464-72 (2004).

[26] A. H. Kashani, E. Kirkman, G. Martin, and M. S. Humayun, "Hyperspectral computed tomographic imaging spectroscopy of vascular oxygen gradients in the rabbit retina In Vivo," PLoS One **6**, 1-11 (2011).

[27] R. A. Ashman, F. Reinholz, and R. H. Eikelboom, "Oximetry with a multiple wavelength SLO," Int. Ophthalmol. **23**, 343-346 (2001).

[28] J. V. Kristjansdottir, S. H. Hardarson, G. H. Halldorsson, R. A. Karlsson, T. S. Eliasdottir, and E. Stefánsson, "Retinal oximetry with a scanning laser ophthalmoscope," Investig. Ophthalmol. Vis. Sci. **55**, 3120-3126 (2014).

[29] H. Li, J. Lu, G. Shi, and Y. Zhang, "Measurement of oxygen saturation in small retinal vessels with adaptive optics confocal scanning laser ophthalmoscope," J. Biomed. Opt. **16**, 110504 (2011).

[30] S. P. Chong, M. Bernucci, H. Radhakrishnan, and V. J. Srinivasan, "Structural and functional human retinal imaging with a fiber-based visible light OCT ophthalmoscope," Biomed. Opt. Express **8**, 323 (2017).

[31] S. Chen, J. Yi, W. Liu, V. Backman, and H. F. Zhang, "Monte Carlo Investigation of Optical Coherence Tomography Retinal Oximetry," IEEE Trans. Biomed. Eng. **62**, 2308-2315 (2015).

[32] J. C. Finlay and T. H. Foster, "Effect of pigment packaging on diffuse reflectance spectroscopy of-samples containing red blood cells," Opt. Lett. **29**, 965-967 (2004).

[33] A. Amelink, T. Christiaanse, and H. J. C. M. Sterenborg, "Effect of hemoglobin extinction spectra on optical spectroscopic measurements of blood oxygen saturation," Opt. Lett. **34**, 1525-1527 (2009).

[34] N. Rajaram, A. Gopal, X. Zhang, and J. W. Tunnell, "Experimental validation of the effects of microvasculature pigment packaging on in vivo diffuse reflectance spectroscopy," Lasers Surg. Med. **42**, 680-688 (2010).

[35] N. Bosschaart, G. J. Edelman, M. C. G. Aalders, T. G. van Leeuwen, and D. J. Faber, "A literature review and novel theoretical approach on the optical properties of whole blood," Lasers Med. Sci.

46, 1454-1465 (1999).

[56] M. H. Smith, K. R. Denninghoff, A. Lompado, and L. W. Hillman, "Effect of multiple light paths on retinal vessel oximetry," Appl. Opt. **39**, 1183 (2000).

[57] S. Yoneya, T. Saito, Y. Nishiyama, T. Deguchi, M. Takasu, T. Gil, and E. Horn, "Retinal oxygen saturation levels in patients with central retinal vein occlusion," Ophthalmology **109**, 1521-1526 (2002).

[58] J. Beach, J. Ning, and B. Khoobehi, "Oxygen saturation in optic nerve head structures by hyperspectral image analysis.," Curr. Eye Res. **32**, 161-170 (2007).

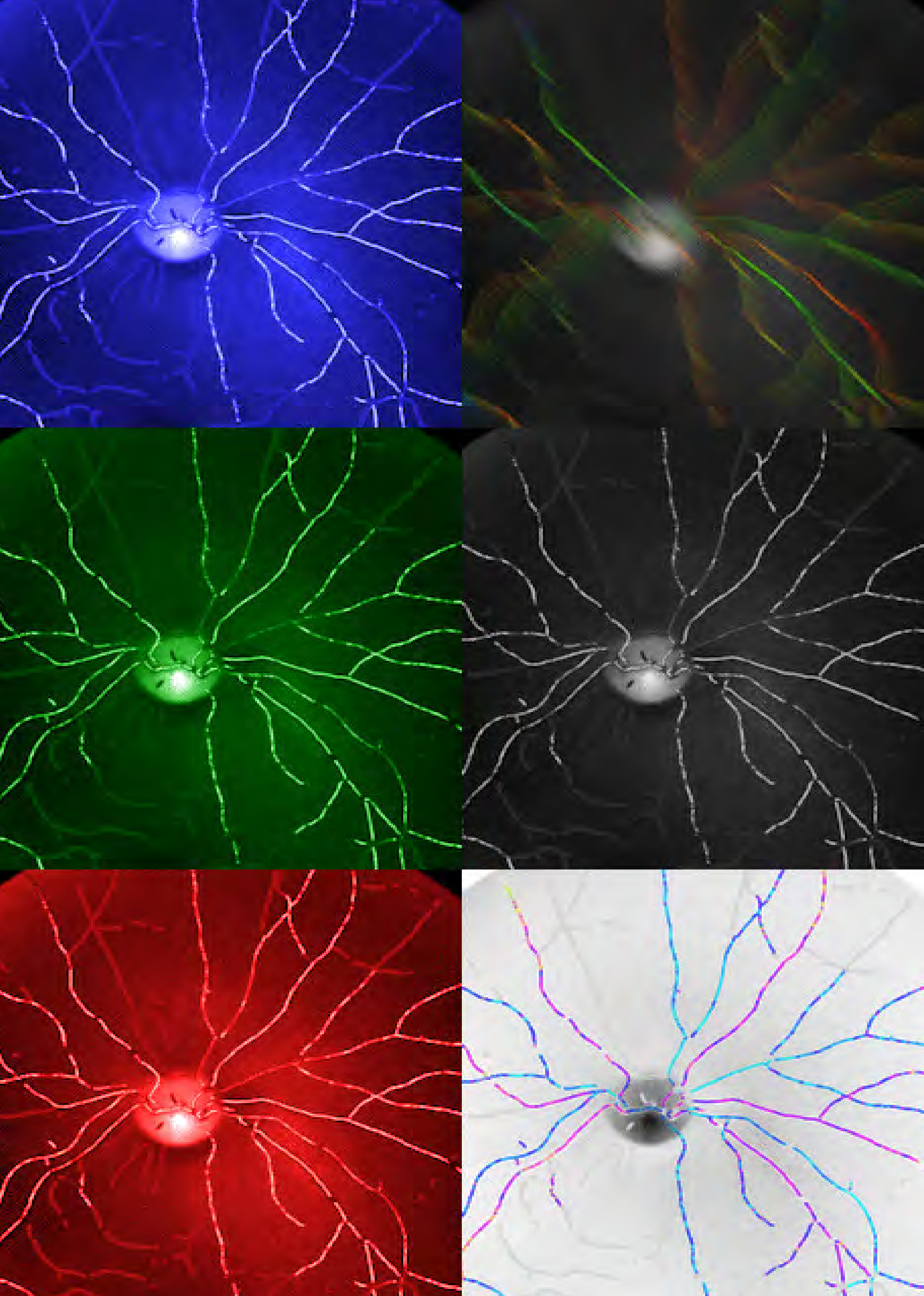

5

sub-diffuse scanning laser oximetry of the human retina *in vivo*

based on :
M. Damodaran, A. Amelink, F. Feroldi, B. Lochocki, V. Davidoiu, and J. F. de Boer, "In vivo subdiffuse scanning laser oximetry of the human retina the human retina," J. Biomed. Opt. **24**, (2019).

Abstract

Scanning laser ophthalmoscopes (SLOs) have the potential to perform high speed, high contrast, functional imaging of the human retina for diagnosis and follow up of retinal diseases. Commercial SLOs typically use a monochromatic laser source or a superluminescent diode for imaging. Multispectral SLOs using an array of laser sources for spectral imaging have been demonstrated in research settings, with applications mainly aiming at retinal oxygenation measurements. Previous SLO based oximetry techniques are predominantly based on wavelengths that depended on laser source availability. In this paper, we describe a novel SLO system based on a supercontinuum source and a double-clad fibre using the single mode core for illumination and the larger inner cladding for quasi-confocal detection to increase throughput and signal to noise. A balanced detection scheme was implemented to suppress the relative intensity noise of the supercontinuum source. The SLO produced dual wavelength, high-quality images at 10 frames per second with a maximum 20^o imaging field of view with any desired combination of wavelengths in the visible spectrum. We demonstrate SLO-based dual wavelength oximetry in vessels down to 50 microns in diameter. Reproducibility was demonstrated by performing 3 different imaging sessions of the same volunteer, 8 minutes apart. Finally, by performing a wavelength sweep between 485 and 608 nm we determined for our SLO geometry an approximately linear relationship between the effective path length of photons through the blood vessels and the vessel diameter.

5.1 Introduction

Measuring the amount of oxygenated and deoxygenated haemoglobin present in the retinal vessels is potentially very valuable to detect and monitor retinal diseases. Oxygen saturation in the retinal vasculature is an important indicator of retinal health [1, 2]. Several studies have investigated and found associations between retinal pathologies and retinal vessel oxygen saturation [3–9]. Moreover, retinal vessel oxygen saturation has also been linked to neurodegenerative diseases [10–12]. Various imaging techniques have been employed in the past to measure retinal oxygen saturation [13–22], while recently emerging techniques have enabled oximetry to be applied in a variety of in vivo applications [23–25]. Nevertheless, the vast majority of retinal oximetry studies use a fundus camera-based approach, which has a limited spatial resolution and provide insufficient contrast to performing oximetry in retinal microvessels smaller than ~100 microns. However, it is in the smaller microvessels that the oxygen saturation is expected to decrease in response to local increased metabolic demand or decreased oxygen delivery capacity. The larger retinal vessels that can be resolved by fundus cameras are expected to be much less sensitive to local changes in tissue metabolic demand or microvascular dysfunction; therefore, the microvasculature provides the most clinically relevant information on local tissue metabolic status. This motivates the development of an SLO-based oximeter, capable of resolving the oxygen saturation in vessels as small as ∼50 micrometres.

We have recently shown that the signal to noise ratio (SNR) of the retinal image strongly influences the accuracy of retinal oximetry [26]. Since the permissible light exposure of the retina is limited in order to prevent injury, it is important to use the allowable light budget efficiently. This implies that imaging should be performed at dedicated wavelength bands, providing the highest SNR for the available light budget. Additionally, averaging of multiple scans of the retina at each wavelength may be necessary to reach a target SNR required to achieve the desired oxygen saturation accuracy.

In this paper, we demonstrate the next-generation SLO-based retinal oximeter with optimised wavelengths and throughput, which can measure retinal oxygenation in vessels down to ∼50 microns diameter. We will first briefly describe the method to select an optimum wavelength for retinal oximetry by taking into account the error on the measured intensities in the retina, the pigment packing effect, the maximum permissible power that can be used for retinal illumination, and the quantum efficiency of the detector. Then we describe the design of an SLO that employs a supercontinuum (SC) source for producing continuous, high contrast images at any desired wavelength from 484 to 700 nm at a speed of 10 frames/second. Balanced detection was implemented to suppress the relative intensity noise (RIN) of the SC source, required to achieve a sufficiently high SNR in the retinal images. Finally, to establish the imaging capabilities of the device, healthy volunteers were imaged. We demonstrate the effect of including an achromatizing lens in the setup to cancel the chromatic aberrations of the eye. Finally, we demonstrate that the extracted oxygen saturation of the smaller retinal vessels is reproducible and within physiological expected ranges.

5.2 Methods

5.2.1 Wavelength selection for dual wavelength retinal oximetry

Oxygenation is typically assessed by imaging the retinal vessels at different wavelengths using multispectral imaging techniques where the choice of wavelengths will affect the achievable measurement accuracy. In an earlier publication, we provided a detailed explanation and calculation of retinal oximetry with and without the pigment packing effect [26]. Here we present a summary of the calculations but now without assuming the use of an isosbestic wavelength for oximetry, as was done in our previous paper. Furthermore, we will account for the maximum permissible power that can be used for retinal illumination and the quantum efficiency of the detector in the calculations.

Let $I(\overline{x}_b, \lambda)$ and $I(\overline{x}_t, \lambda))$ be the recorded intensities in the retinal image at the centre of the blood vessel and adjacent tissue location, respectively, at a wavelength λ and for equal illumination intensity at both locations. The relative optical density OD_λ of the blood vessel location compared to the surrounding tissue can be written as:

$$OD_\lambda = \ln\left(\frac{I(\overline{x}_t, \lambda)}{I(\overline{x}_b, \lambda)}\right) = \langle L_{eff}(\lambda)\rangle \cdot \left(S \cdot \mu_a^{HbO_2}(\lambda) + (1-S) \cdot \mu_a^{Hb}(\lambda)\right) + G(\lambda) \tag{5.1}$$

where the attenuation of the reflected light due to the blood within $\overline{x}_b$ is governed by *modified Beer-Lamberts law* [27, 28], with $\langle L_{eff}(\lambda)\rangle$, the effective path length of photons travelling through the probed volume before reaching the detector. The absorption coefficients [29] of oxy- and deoxy-haemoglobin are given by $\mu_a^{HbO_2}(\lambda)$ and $\mu_a^{Hb}(\lambda)$, respectively, assuming a concentration of haemoglobin of 15 g/dL. $G(\lambda)$ is a factor which accounts for any apparent increase or decrease in the ODs purely due to scattering differences within the volumes $\overline{x}_b$ and $\overline{x}_t$. We define the ratio of ODs at 2 wavelengths λ_1 and λ_1 as:

$$\rho_{\lambda_1|\lambda_2} = \frac{OD_{\lambda_1}}{OD_{\lambda_2}} \tag{5.2}$$

We can then write the saturation (i.e., the fraction of the oxygenated haemoglobin concentration to the total concentration of haemoglobin) as [26],

$$S_{\lambda_1|\lambda_2} = \frac{\rho_{\lambda_1|\lambda_2} \cdot \mu_a^{Hb}(\lambda_2) - \mu_a^{Hb}(\lambda_1)}{(\mu_a^{Hb}(\lambda_2) - \mu_a^{HbO_2}(\lambda_2)) \cdot \rho_{\lambda_1|\lambda_2} + (\mu_a^{HbO_2}(\lambda_1) - \mu_a^{Hb}(\lambda_1))} + \alpha \cdot G \tag{5.3}$$

where the factor $\alpha \cdot G$ [1] is an offset, if any, to the saturation due to scattering. The error on the saturation, ΔS is given by,

---

[1] $\alpha = \frac{\rho - 1}{\langle L_{eff}\rangle \cdot \nu \cdot ((\mu_a^{HbO_2}(\lambda_2) - (\mu_a^{Hb}(\lambda_2)) \cdot \rho + (\mu_a^{HbO_2}(\lambda_1) - (\mu_a^{Hb}(\lambda_1)))}$

$$\Delta S = \frac{\mathrm{d}S}{\mathrm{d}\rho} \cdot \Delta\rho \tag{5.4}$$

where the error in $\rho_{\lambda_1|\lambda_2}$, $\Delta\rho$ is given by the underlying error in the ODs resulting from the error in recorded intensities (please refer to Damodaran *et al.*[26] for mathematical expressions relating ΔS to ΔI). The error in saturation can be calculated using Eq. 6.4. The result is plotted in Fig. 5.1 for different wavelength combinations where $\lambda \in$ [460 650] nm and the standard error on the mean recorded intensity values (ΔI/I) was assumed to be 1%. This figure shows the wavelength combinations that give the smallest saturation errors for a given saturation level. Fig. 5.1 depends on Eq. 6.3, which is correct for a large blood vessel present superficially in the retina with a diameter comparable to the collection area. In case of a small blood vessel embedded in the scattering retinal tissue that is illuminated with a narrow beam, and when the collection aperture is much larger than the illumination aperture and the blood vessel diameter, then the blood vessel occupies only a small portion of the total probed volume and hence the pigment packing effect should be considered and incorporated into the ODs [26, 30, 31]. Equation 6.3 can then be written as,

$$S_{\lambda_1|\lambda_2,pp} = \frac{\rho_{\lambda_1|\lambda_2} \cdot \frac{C_{\lambda_2}}{C_{\lambda_1}} \cdot \mu_a^{Hb}(\lambda_2) - \mu_a^{Hb}(\lambda_1)}{(\mu_a^{Hb}(\lambda_2) - \mu_a^{HbO_2}(\lambda_2)) \cdot \rho_{\lambda_1|\lambda_2} \cdot \frac{C_{\lambda_2}}{C_{\lambda_1}} + (\mu_a^{HbO_2}(\lambda_1) - \mu_a^{Hb}(\lambda_1))} + \alpha \cdot G \tag{5.5}$$

where C_λ is the correction factor to include the pigment packing effect and $\alpha \cdot G$[2] is an offset due to scattering. It can be observed that if the ratio of correction factors $C_{\lambda_2}/C_{\lambda_1}$ in Eq. 5.5 is 1, Eq. 5.5 reduces to Eq. 6.3 i.e., $C_{\lambda_2}/C_{\lambda_1} \simeq 1 \Rightarrow S_{\lambda_1|\lambda_2} \simeq S_{\lambda_1|\lambda_2,pp}$.

Figure 5.2A shows an ensemble ΔS where weights of 0.4, 0.6 , 0.8, 1.0 and 1.0 were applied to the five different saturation graphs S = 0.00, 0.25, 0.50, 0.75 and 1.00 in Fig. 5.1, respectively. The weights were chosen to favour the more physiologically relevant, health range of oxygen saturation [32]. Figure 5.2B shows the difference in calculated saturation with and without the pigment packing effect defined as the saturation offset, S_{offset} ($S_{offset} = S_{\lambda_1|\lambda_2} - S_{\lambda_1|\lambda_2,pp}$) due to the pigment packing effect when the same weights were applied. Figure 5.2C shows addition of the saturation offset and the saturation error for wavelengths $\lambda_1, \lambda_2 \in$ [450 650] respectively. Finally Fig. 5.2D shows Fig. 5.2C corrected for the wavelength dependent maximum permissible exposure (MPE) prescribed for 30000 seconds of continuous single point exposure[33] (see Fig.15 in Appendix), and responsivity of the detector across the wavelengths[34]. The ΔI/I value was 1% for the MPE and responsivity at 600 nm, and increases linearly for decreasing MPE and responsivity as a function of wavelength to get Fig. 5.2D. For example at 460 nm, the MPE normalised on the MPE for $\lambda \geq 500$ nm was 0.1 and the responsivity normalised on the responsivity at 600 nm was 0.7 and hence the ΔI/I was adjusted to 14.3%. Based on Fig. 5.2D, 498 nm and 594 nm wavelengths were chosen for oximetry estimation. Further, this wavelength choice was used as a software setting for central wavelength in the wavelength settings tunable filter of the supercontinuum source. The resulting light spectrum measured with these wavelength settings was convolved with the absorption spectrum values [29] and the following values of the absorption coefficients were obtained and used for calculating the oxygen saturation in the retina : $\mu_a^{Hb}(\lambda_1) = 11.0$, $\mu_a^{HbO_2}(\lambda_1) = 9.5$, $\mu_a^{Hb}(\lambda_2) = 7.3$ and $\mu_a^{HbO_2}(\lambda_2) = 13.1$.

---

[2] $\alpha = \frac{\rho-1}{\langle L_{eff}\rangle \cdot \nu \cdot ((\mu_a^{HbO_2}(\lambda_2) - (\mu_a^{Hb}(\lambda_2)) \cdot \rho \cdot C_{\lambda_2} + (\mu_a^{HbO_2}(\lambda_1) - (\mu_a^{Hb}(\lambda_1)) \cdot \lambda_1)}$

5.2.2 System design

The scanning laser oximeter setup was an adaptation of our previous design [26], with the aim to optimise the SNR of our imaging system. A schematic layout of the system is shown in Fig. 5.3. The light from an SC source (EXU-6, NKT Photonics A/S, Birkerød, Denmark) was filtered using a tunable filter (Select, NKT Photonics A/S, Birkerød, Denmark). A 90:10 fused single-mode 460-HP fibre coupler (TW560R2A2, Thorlabs GmbH, Germany) was used to send 10 % of the light into detection module II for continuous laser power monitoring and balanced detection (see section 2.3). The core of the double clad fibre (DCF) in port S of the DCFC [35, 36] was excited using the 90 % port of the splitter. About 94 % (transmission measured at 550 nm) of this light reached the port A of the DCFC. A reflective fibre collimator (RC02APC-P01, Thorlabs GmbH, Germany) was used to collimate the fibre output from port A into a 2.2 mm beam. This beam size was optimum for two reasons: (i) The beam size was small enough that the beam is not clipped in the pupil of the subject even with the expected pupil constriction due to bright visible radiation. (ii) This beam size was close to the optimum pupil size for lateral resolution [37] A dichroic mirror (D3, long pass cut off 700 nm) was used to prevent any residual pump light of the SC from entering the rest of the system. A custom made dispersion compensating lens (DCL) (Shanghai optics Inc., H-FK61 and K4A, f = 1800 mm) was placed in the common beam path to compensate for the longitudinal focal shift arising from the chromatic aberration of the human eye [38]. A combination of a 2.56 kHz resonant scanner (5.12 kHz line rate by utilising both sides of scanner sweep) (EPOC., Glendale, New York, USA), and a 10 Hz galvanometer

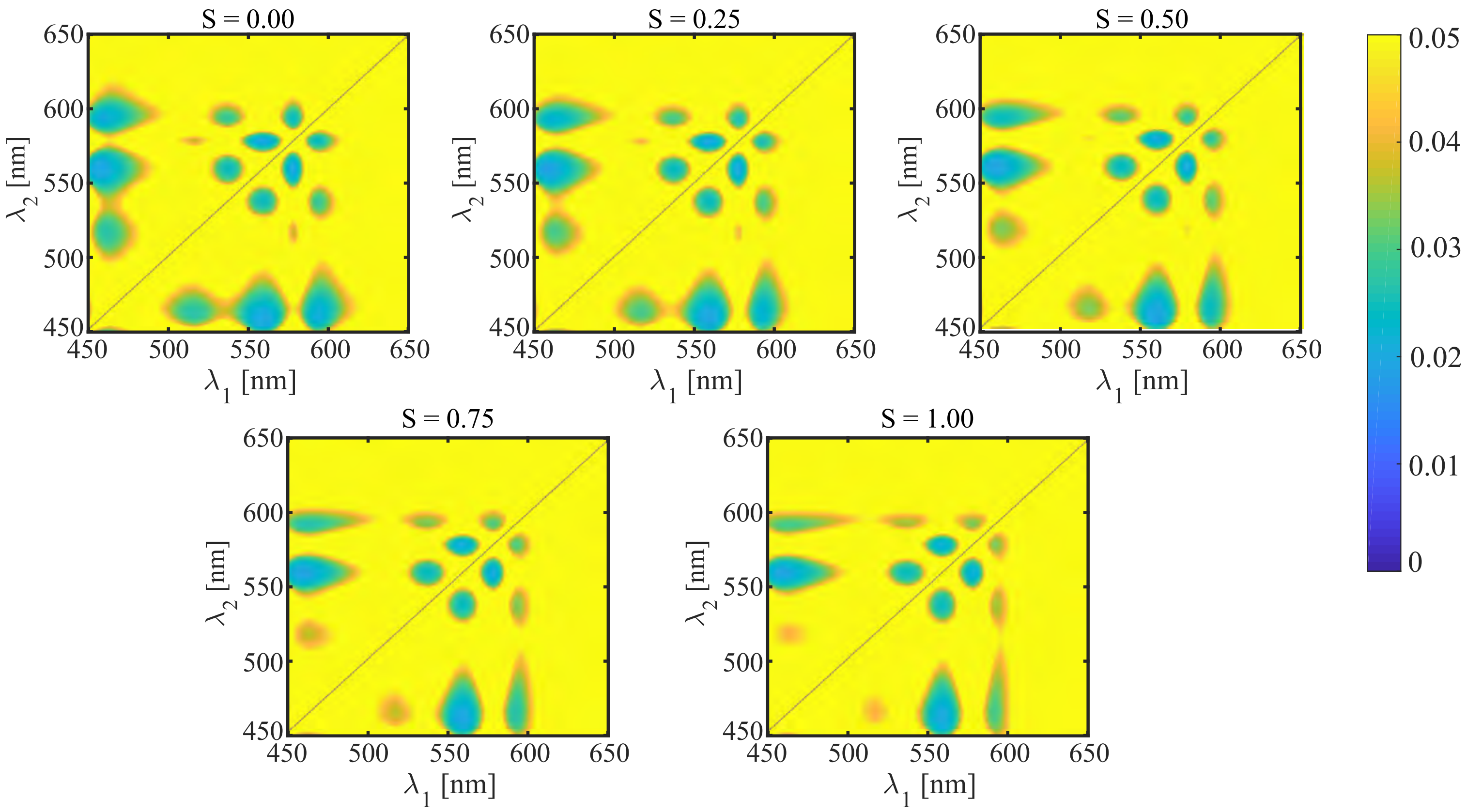

Figure 5.1: *in silico* analysis of saturation error ΔS for different saturation levels and wavelength combinations for $\lambda_1, \lambda_2 \in$ [450 650] nm. The standard error on the mean recorded intensity values ($\Delta I/I$) was assumed to be 1%. All values of $\Delta S > 0.05$ were set to 0.05.

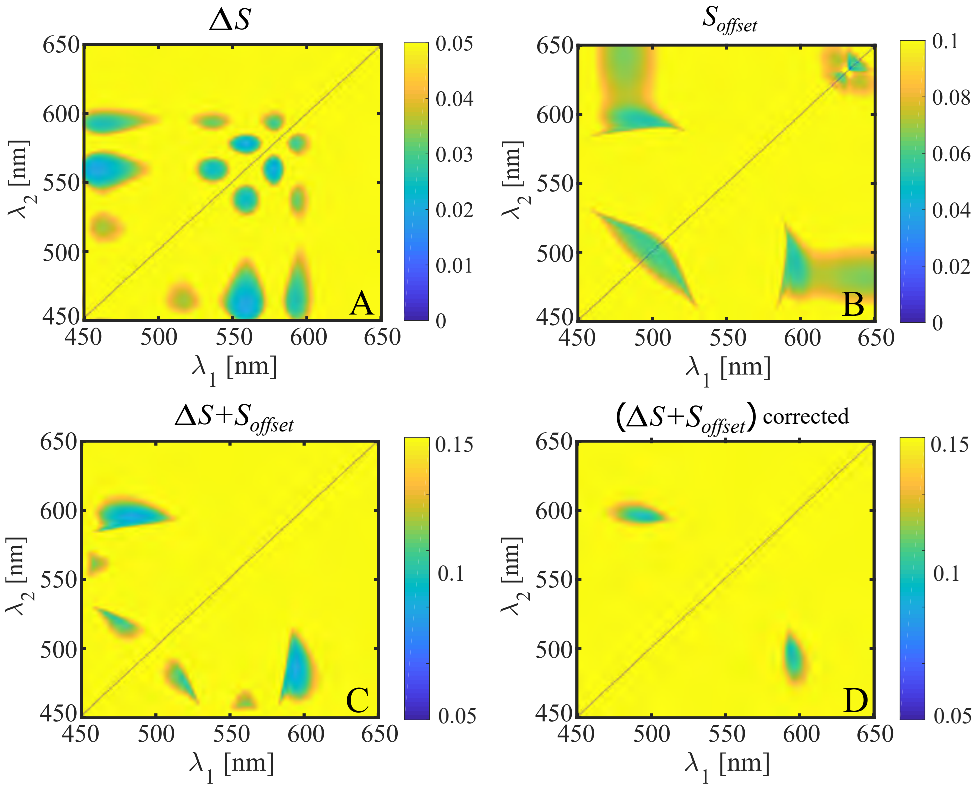

Figure 5.2: *in silico* analysis of saturation error and saturation offset — A: Saturation error ΔS for different wavelength combinations for $\lambda_1, \lambda_2 \in$ [450 650] nm. The standard error on the mean recorded intensity values ($\Delta I/I$) was assumed to be 1%. All values of $\Delta S > 0.05$ are shown as as 0.05. B: Calculated saturation difference with and without pigment packing effect shown as an offset ($S_{offset} = S_{\lambda_1|\lambda_2} - S_{\lambda_1|\lambda_2,pp}$) for a 50 µm diameter blood vessel. Values of $S_{offset} > 0.1$ are shown as 0.1. C: Addition of the saturation offset and the saturation error for different wavelength combinations. The color bar has a range [0.05 0.15]. D: Addition of saturation offset and saturation error corrected for the maximum permissible exposure (MPE) prescribed for 30000 seconds of continuous single point exposure (see Appendix), and quantum efficiency of the detector across the wavelengths.

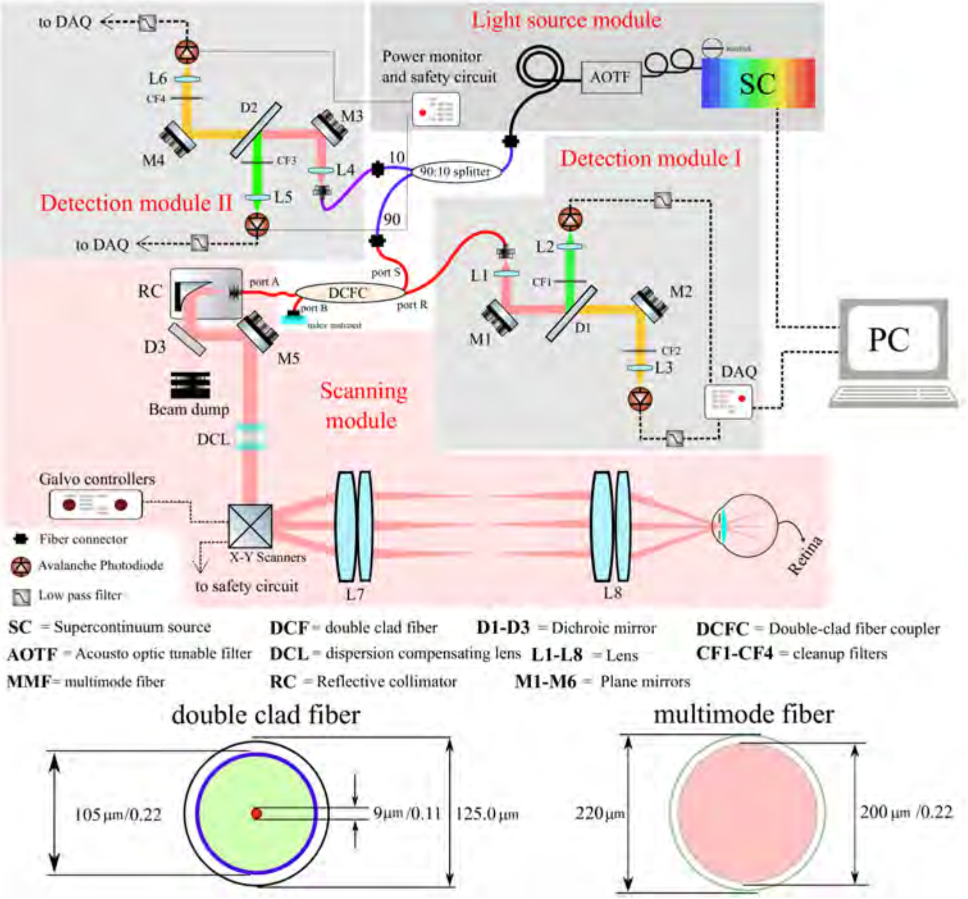
Light source module
Power monitor
and safety circuit
AOTF
SC
to DAQ
L6
CF4
D2
M3
M4
CF3
L4
10
90:10 splitter
L5
Detection module II
90
to DAQ
Detection module I
L2
RC
port A
port S
DCFC
port B
port R
L1
CF1
M2
D3
M5
M1
D1
CF2
L3
DAQ
PC
Beam dump
Scanning
module
DCL
Galvo controllers
Fiber connector
Avalanche Photodiode
Low pass filter
X-Y Scanners
to safety circuit
L7
L8
Retina
SC = Supercontinuum source
AOTF = Acousto optic tunable filter
MMF= multimode fiber
DCF = double clad fiber
DCL = dispersion compensating lens
RC = Reflective collimator
D1-D3 = Dichroic mirror
L1-L8 = Lens
M1-M6 = Plane mirrors
DCFC = Double-clad fiber coupler
CF1-CF4 = cleanup filters
double clad fiber
105 µm/0.22
9µm /0.11
125.0 µm
multimode fiber
220µm
200 µm /0.22

Figure 5.3: A: Schematic sketch of the scanning laser oximeter showing the various components: The abbreviated components are described in the legend. The light from port A of the DCFC was collimated using RC into a 2.2 mm beam. The reflected signal from the retina was collected using the cladding of the DCF with a diameter of 105 µm and a numerical aperture (NA) of 0.22. This light is coupled on to the MMF with a diameter of 200 µm and an NA of 0.22. Thus, the illumination pinhole size is 9 µm and the detection pinhole size is 105 µm. The maximum collection beam diameter of RC was 8 mm. However, the limiting aperture in the optical setup is the pupil of the subject.

mirror (Cambridge tech., Bredford, USA) placed close to each other were used to achieve an imaging throughput of 5.12 million pixels / second (10 frames / second × 512 lines / frame × 1000 pixels / line). A 1:1 telescope consisting of achromatic doublet pairs was used to relay a point approximately in the middle of the two scanning mirrors onto the pupil of the eye. The reflected and scattered light from the retina was then collected using the inner cladding of the double clad fibre in port A. About 63 % (transmission measured at 550 nm) of the collected light is then coupled into the multi-mode fibre (MMF). The fibre cross-section of the DCF and the MMF in the DCF coupler are also shown in Fig. 5.3.

The detection modules consist of a collimating lens (L1 and L4, f = 18 mm), a dichroic mirror (D1 and D2, long pass cutoff 532 nm), two focusing lenses (L2, L3, L5 and L6, f = 25 mm) focusing the spectrally separated light on the active area of avalanche photodiodes (APD) (APD410A2, Thorlabs GmbH, Germany). Two clean-up filters (CF1, CF3: bandpass 470 ± 50 nm, CF2, CF4: long pass 532 nm) were placed just before the focusing lenses to avoid any contribution of light from an unintended wavelength. The detectors in both the detection modules were connected to a 12-bit digitizer (NI-PCI6115, 10 million samples /second /channel, National Instruments, Austin, Texas). The signals from the four detection modules were sampled using four parallel channels of this digitizer running on a single clock. Port B of the DCF coupler was placed in a medium whose index was matching the core index of the MMF to suppress the back reflection from the exit surface of the fibre faucet from entering the detection module I.

5.2.3 Balanced detection to increase the signal-to-noise ratio

Spectrally filtering an SC light source provides an excellent wavelength-flexible alternative to the existing approaches of multispectral imaging. However, in an SC light source such as the EXU-6 used in the setup shown in Fig. 5.3, the generation of a large optical bandwidth through non-linear processes [39, 40] results in high relative intensity noise (RIN) compared to traditional sources such as LEDs, lasers, and superluminescent diodes. The fundamental noise limitation of an SC source is described well by Corwin *et al.* [41]. The pulse-to-pulse intensity variations in the SC source amounts to the RIN. In principle, RIN can be suppressed by averaging more pulses within the integration time of the detector. The EXU-6 has a repetition rate of 78 MHz, and given the short integration times of our SLO, (∼380 ns) only 30 pulses were averaged within an integration time resulting in a significant RIN component in the total noise figure. The total noise power of the system can be written as,

$$\sigma_I^2 = \sigma_{shot}^2 + \sigma_{thermal}^2 + \sigma_{RIN}^2 + \sigma_{DAQ}^2 \tag{5.6}$$

where σ_{shot}^2 is the signal dependent shot noise power, which is the limiting noise component in an ideal heterodyne system, $\sigma_{thermal}^2$ is the signal independent thermal noise power that is inherent to the photodetector, σ_{DAQ}^2 is the noise due to digitization of the signals, and σ_{RIN}^2 is the excess noise due to the RIN of the SC. The signal to noise ratio (SNR) of the detected signal in the APD can be written as,

$$SNR\,[dB] = 10 \cdot \log\left[\frac{\mu_I}{\sigma_I}\right] \tag{5.7}$$

where μ_I is the mean of the signal and σ_I is the standard deviation of the signal. The noise performance of the EXU-6 SC light source is shown in Fig. 4. The number of detected photons within an integration time was controlled using a fibre attenuator. The thermal noise was measured in the absence of any incident photons, and gradually the number of photons was increased until the detectors reached 90% saturation. By including a 1 MHz low-pass filter with a very sharp cut-off, high frequency noise is eliminated. At each moment, the mean and variance of the photocurrent measured by the detector was determined, and plotted. Figure 5.4 shows that the unbalanced detection suffers from significant RIN contribution (dashed green and red lines). In our balanced detection scheme, The signals of detection module 1 were divided by the respective reference signals of detection module 2 to yield RIN corrected signals for each wavelength. Since OD was calculated as a ratio of two RIN corrected intensities at the same wavelength at different locations, the actual magnitude of the module 2 signals is divided out, so the OD does not depend on the actual magnitude of the module 2 signals. This method resulted in an additional SNR improvement due to RIN suppression. Around 5 dB improvement in signal to noise ratio (SNR) was achieved by using balanced detection and a 1 MHz low-pass filter. Figure 5.4 shows the improvement in SNR achieved by balanced detection for 500 nm and 600 nm wavelengths (dotted green and red lines).

5.2.4 Wavelength sweep hyperspectral imaging

The acousto-optic tunable filter (Select, NKT Photonics A/S, Birkerød, Denmark) used in the system (Fig. 5.3) allows to perform a wavelength sweep for the desired wavelength ranges between 450 and 650 nm and in desired steps (minimum step size 0.1 nm, maximum sweep speed of 10 wavelengths/s). We performed a wavelength sweep from 485 to 608 nm with the SLO with a step size in wave-

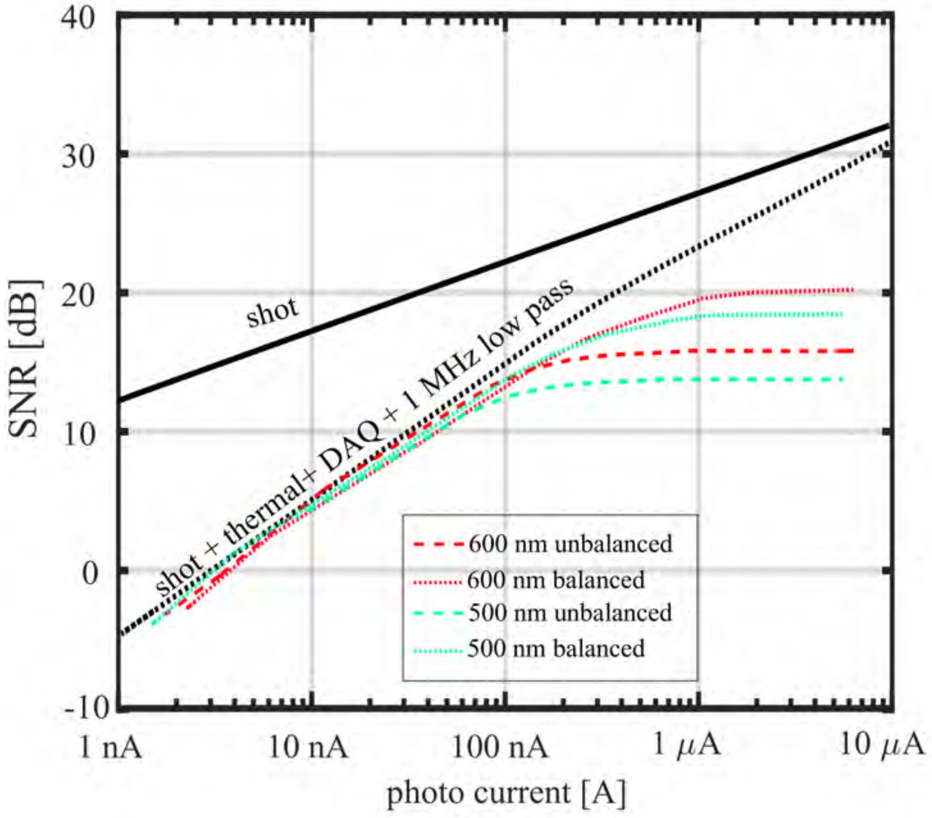

Figure 5.4: Noise performance of the SC source shown by plotting the SNR for different levels of mean signal in the photodetector for two wavelengths, 500nm and 600 nm. The graph shows the theoretical shot noise limited SNR (solid black line), and the expected SNR due to the additional contribution of thermal and quantization noise to the shot noise (dotted black line). The measured SNR for two different wavelengths 500 nm and 600 nm is also shown (dashed green and red line, respectively). The SNR deteriorates for higher photocurrents because RIN noise scales as the square of detected photons in the photodetector. By using balanced detection, an improvement in SNR of approximately 5 dB was achieved for these wavelengths (dotted green and red lines).

length of 3 nm and sweep speed of 1 step/s. Given that the imaging speed of our SLO is 10 fps, this enabled acquiring high-quality retinal images at a rate of 10 images/wavelength within 42 seconds of imaging. For these measurements, the dichroic filters D1, D2 and the clean-up filters CF2 and CF4 (see Fig. 5.3) were removed and only one channel was used in each detection unit.

5.2.5 in vivo human measurements

The clinical pilot study obeyed the principles of the Declaration of Helsinki and was approved for human use by the medical ethical review board at the Amsterdam Universitair Medische Centra (VUmc location), Amsterdam. Tropicamide 0.5 % w./v. drops were administered for pupil dilation during imaging. The optical power used for measuring human subjects was in agreement with the maximum permissible exposure established by the latest IEC standard 60825-1 [33]. The laser safety considerations are detailed in Appendix A. Different FOVs could be implemented by changing the voltages provided to the scanners. Background measurements were taken prior to each imaging session and were subtracted from SLO images to remove artefacts such as lens reflections. In order to utilize the full dynamic range of the detector, strong lens reflections from the last ophthalmic lens in the system were allowed to saturate the detector. All other stray reflections which did not saturate the detector were removed using the background measurements.

5.2.6 Retinal vessel segmentation and oxygenation map

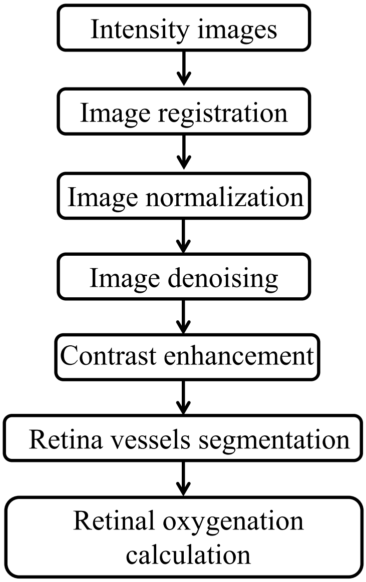
Intensity images
Image registration
Image normalization
Image denoising
Contrast enhancement
Retina vessels segmentation
Retinal oxygenation calculation

Figure 5.5: Pipeline for vessel segmentation and oxyenation extraction from retinal images.

The SLO images were background corrected by performing a reference measurement before imaging *in vivo*. The background subtracted images were corrected for the sinusoidal scanning of the resonant scanner into a single image. The retinal oxygenation was constructed using the flow diagram shown in Fig. 5.5. First, several linear intensity images were registered using the scale-invariant feature transform method (SIFT) [42]. After correcting the images for translation, rotation and affine transformations, an averaged image was constructed from the registered data. In order to segment and extract the vessels in the retinal image, the averaged image $Im(x,y)$ was normalized as $Im_N(x,y)=\frac{Im(x,y)-min[Im(x,y)]}{max[Im(x,y)]-min[Im(x,y)]}$, where min and max are defining the minimum and the maximum values in the registered and averaged image. Under the assumption that the SLO images have an approximate piecewise constant structure, the images were denoised using a total variation (TV) algorithm in order to preserve the vessel edges. Subsequently, contrast enhancement was applied to determine the blood vessel boundaries correctly. As has been shown by Davidoiu *et al.*[43], a regularization TV model using a specialized fixed-point algorithm and isotropic total variation (ITV) norm improved the 2D vasculature network segmentation for ex-vivo heart data. In our case, the regularization parameter in the total variation algorithm has been fixed and chosen to be equal to the standard deviation of the normalized image and the convergence stopping parameter value has been set to 0.01. The contrast enhancement of the denoised image was performed using a method called contrast-limited adaptive histogram equalization (CLAHE) [44]. Finally, the blood vessels detection and diameter calculation was performed using wavelets and edge location refinement (ARIA) [45]. The extracted vessel boundary coordinates were exported to Matlab, and were applied to the averaged image Im(x,y). The extraction of the blood and tissue intensity values was done using the method described by Damodaran *et al.* [26].

5.3 Results and discussion

5.3.1 Technical aspects regarding multispectral SLO with an SC source

SNR improvement by balanced detection

Figure 5.6 shows the comparison between in vivo retinal images with and without balanced detection in three different volunteers with three different wavelengths. These images clearly show the improvement in image quality due to balanced detection. As described in section 2.3, the RIN of the supercontinuum source was mitigated by using a balanced detection scheme. This resulted in an SNR improvement of 5 dB.

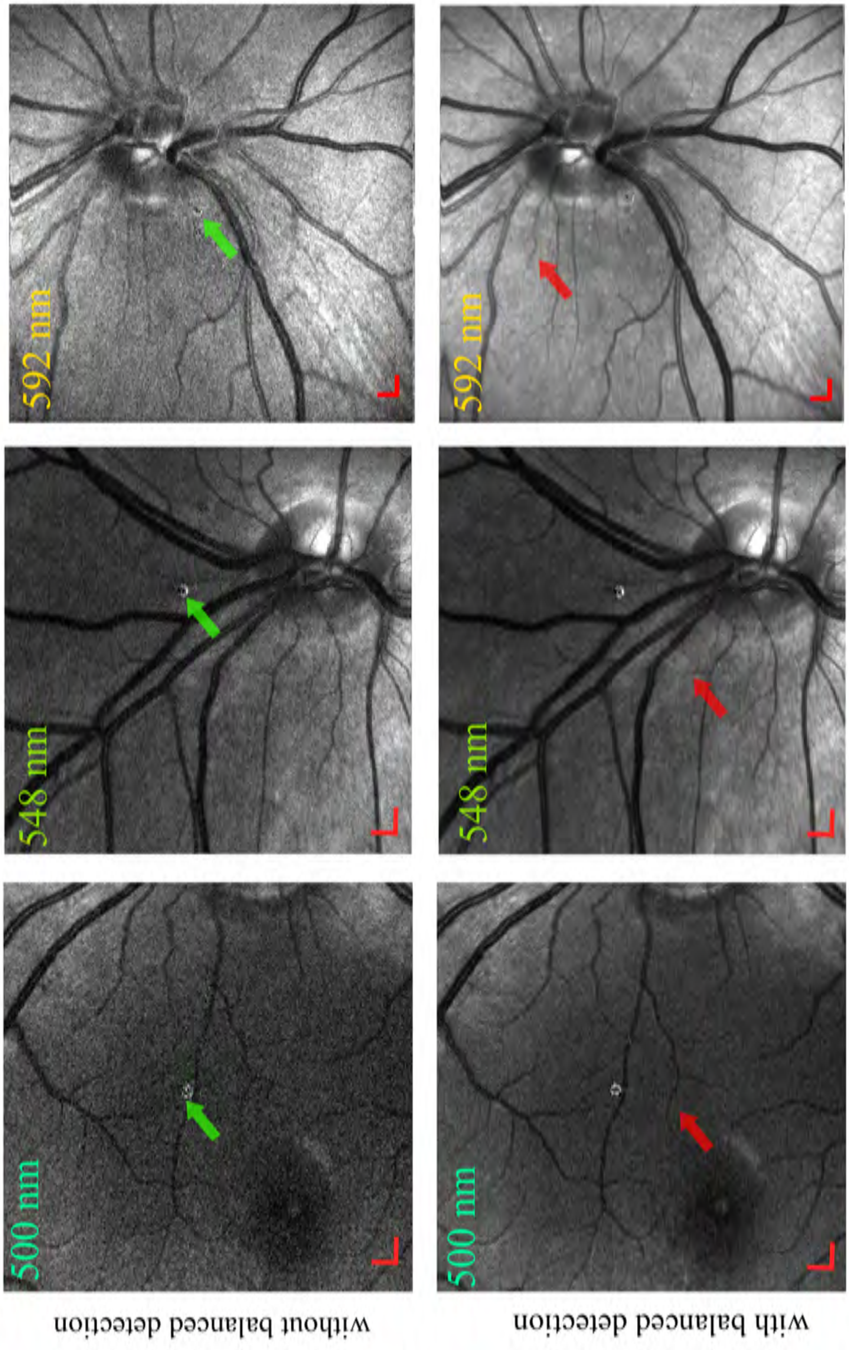
without balanced detection
with balanced detection
500 nm
548 nm
592 nm
500 nm
548 nm
592 nm

Figure 5.6: Comparison of images with and without balanced detection — unaveraged retinal images from three different volunteers show the improvement in image quality due to balanced detection. The red arrows show the blood vessels that become visible only due to balanced detection. The green arrows point to the lens reflection artefact that saturated the detector, and was not removed due to background subtraction. Scale bar represents 300 µm in the retina.

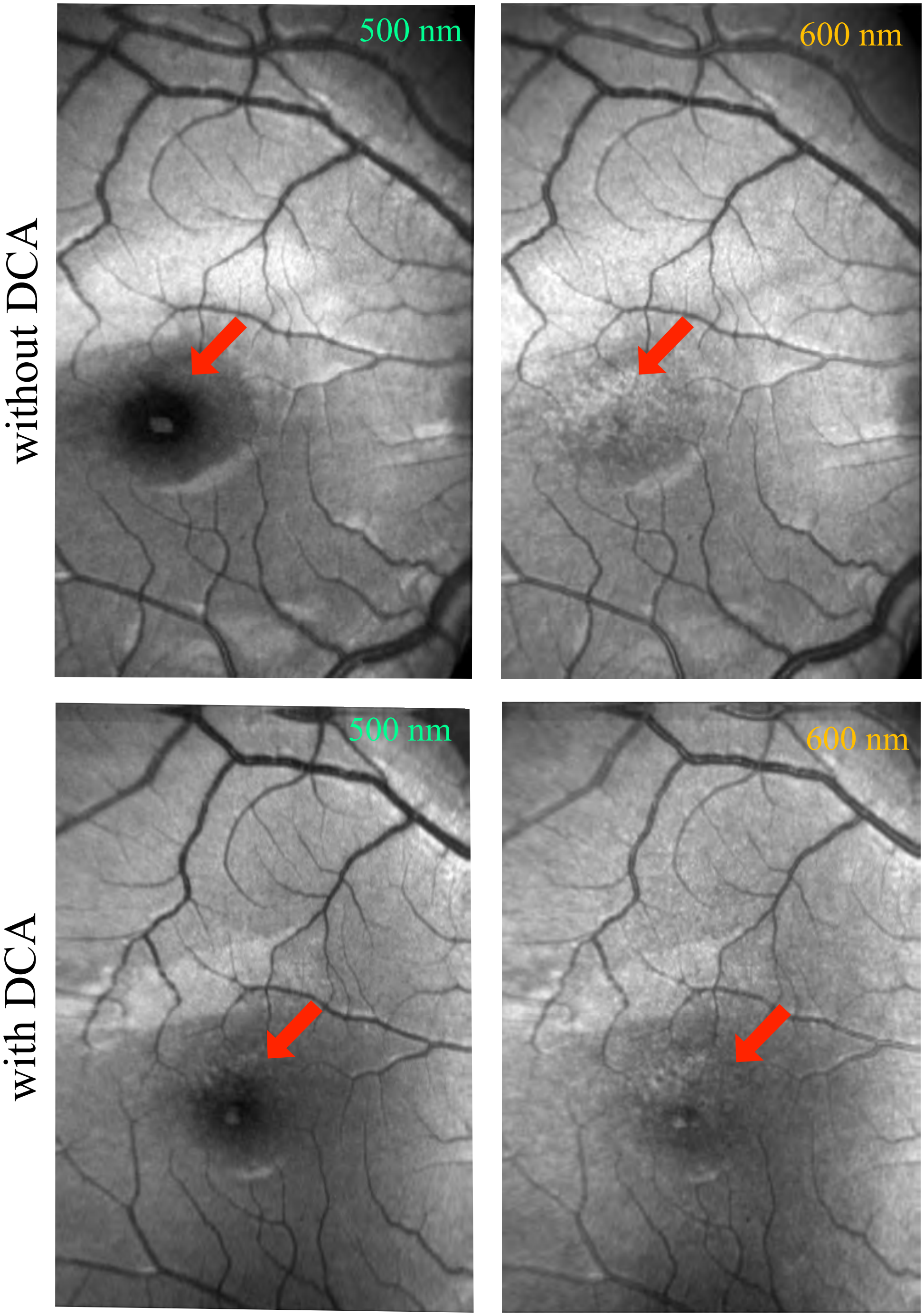

Figure 5.7: Images from right eye of a human volunteer shows the effect of LCA in the absence or presence of a dispersion compensation lens. The foveal pit (red arrows) appear more uniform in the images with dispersion compensation (below) compared to the images without dispersion compensation (top). Scale bar represents 300 µm in the retina.

Compensation for chromatic aberrations of the eye

Chromatic aberrations in the human eye have been studied previously [46, 47]. The longitudinal chromatic aberration (LCA) is a potential source of error in oximetry due to the dispersion in the human eye [38]. LCA causes the spatial location of each pixel in the multispectral image to be in a slightly different axial plane for different wavelengths. This effect can lead up to a 220 µm longitudinal focal shift between the 498 nm and 594 nm wavelengths [48]. This effect can be corrected, as has been shown previously by others [49, 50], by using a dispersion compensating lens in the beam path.

Images acquired at 500 nm and 600 nm without the dispersion compensation lens (Fig. 5.7) in the right eye of a healthy human volunteer demonstrate that chromatic aberrations affect the multiwavelength SLO images; note the difference in the appearance of the foveal pit in the 500 nm and 600 nm images. This can be explained by a focal position that is at the depth of the foveal pit for the 600 nm image, while the 500 nm image has a shallower focus as evidenced by the dark appearance of the foveal pit due to confocal gating. This focal separation between the different wavelengths was compensated by a dispersion compensation lens (Fig. 5.3) that resulted in the images (Fig. 5.7 (bottom)) having a more uniform appearance of the foveal pit between the 500 nm and 600 nm channels. These images are similar to LCA-compensated images published by Larocca *et al.* [50].

The transverse chromatic aberrations (TCA) between the wavelengths was compensated in post-processing of the images by applying a transformation metric which aligns the images of different wavelengths to a chosen wavelength.

Effect of the size of the illumination and collection apertures of the DCF coupler

We determined the effect of using a double clad fibre with different core and inner cladding diameters on throughput and sharpness of the image. Double clad fibre couplers with the same multimode fibres, but different DCFs (different core and inner cladding diameters) were used. Figure 5.8A shows an unaveraged SLO image of right eye of a healthy male volunteer imaged with a DCF having a core diameter of 2.3 µm (single mode at 430 nm) and an inner cladding of 15 µm compared with a DCF having a core diameter of 9 µm and inner cladding diameter of 105 µm (figure 5.8B). The figs show that while the 2.3 µm/15 µm DCF gives images with sharper appearance, this comes at the cost of throughput as indicated by the intensity scale bars. For sub diffuse measurements with higher throughput requirements for fast quantitative imaging, the 9 µm/105 µm DCF is better suited since the amount of averaging required to achieve an SNR of 20 dB is smaller than for the 2.3 µm/15 µm

DCF.

5.3.2 *in vivo* two wavelength oximetry

Retinal oximetry was demonstrated in two healthy volunteers using the optimal two wavelengths, 498 nm and 594 nm. Figure 9A and 9B show the retinal images at 498 nm and 594 nm, respectively. After vessel segmentation and analysis as described section 2.6, an oxygen saturation map of the blood vessels was created and overlaid on the 594 nm image as shown in Fig. 5.14C. Figure 5.14D shows an image taken with the Oxymap Tx for comparison. Similar measurements were made in volunteer 2, as shown in Fig. 5.9. The smallest vessels for which oxygen values are provided are 40 micrometres in diameter.

To analyse the repeatability of the oxygenation measurements, volunteer 1 was imaged three times with 8 minutes intervals in between the measurements. The average oxygenation in 4 vessels (vessel 1-3: arteries; vessel 4: vein) are shown in Fig. 5.10. The calculated oxygenation values in these vessels reproduce very well, despite the difference in positioning of the eye between the 3 imaging sessions, resulting in different overall intensity levels and differences in focus depth, as evidenced by the different appearance of the foveal pit across the 3 sessions.

5.3.3 Wavelength sweep hyperspectral imaging

Similar to other SLO systems, the system described in Fig. 5.3 can image different sections of the retina at high frame rates, but the SC source used in our system also has the advantage of imaging at any desired wavelength and to sweep wavelengths in selected ranges and steps in the 484 to 700 nm range. Figure 5.11 shows the in vivo result of a wavelength sweep from 485 to 608 nm performed in Volunteer 2. The measurement took 42 seconds to complete, and each wavelength image shown in the figure was registered to the first frame of that wavelength and averaged in post-processing. As a result of the balanced detection and well-fixated eye of the volunteer, the images exhibit good contrast.

Six blood vessels providing a wide range of vessel diameters were selected from the spectral cube and the OD values were obtained for these vessels after performing the vessel segmentation in individual images. The weighted mean and the standard deviation (weights = 1/standard error) were obtained for these vessels and Equation 5.1 (where G was assumed to be 0 and the blood haemoglobin concentration was assumed to be 15 g/dL) was used as the model to perform a weighted fit the OD values in order to extract the $\langle L_{eff} \rangle$ and S values as shown in Fig. 5.12.

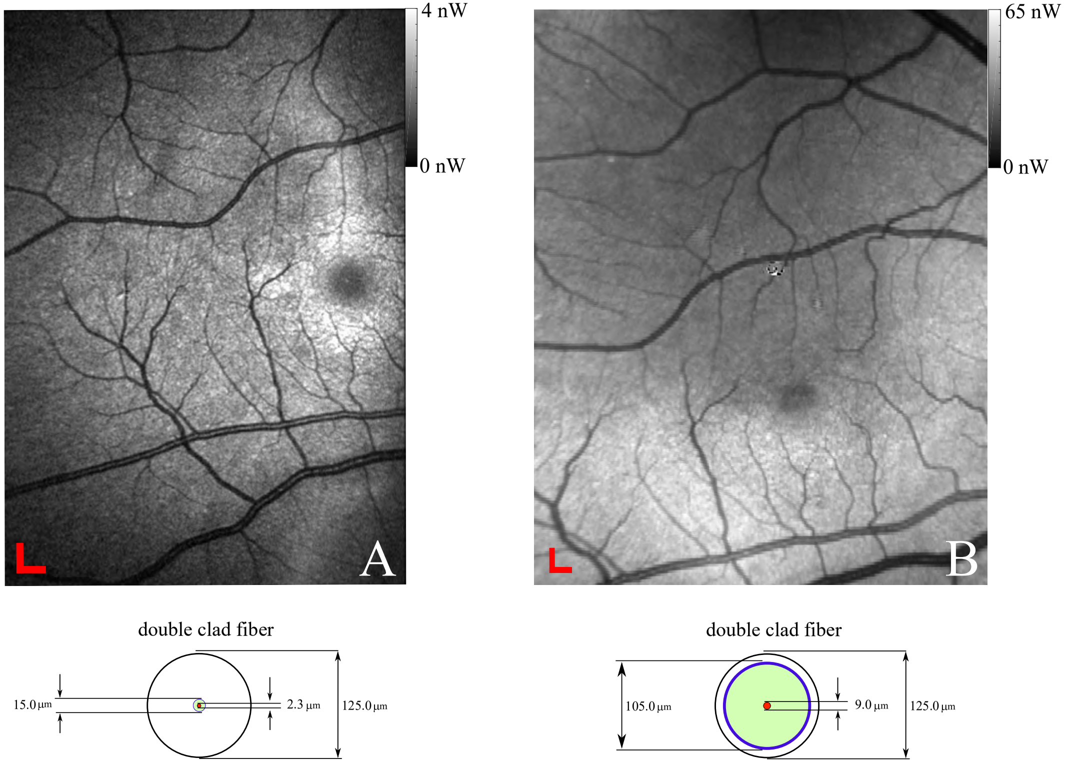
4 nW
0 nW
A
65 nW
0 nW
B
double clad fiber
15.0 µm
2.3 µm
125.0 µm
double clad fiber
105.0 µm
9.0 µm
125.0 µm

Figure 5.8: Unaveraged retinal SLO images (single frame each) from the described design in section 2.2 with different double clad fibers: A – DCF with a core 2.3 µm diameter and an inner cladding of 15 µm. B — DCF with a core 9 µm diameter and an inner cladding of 105 µm. The cross section of the DCF is shown in the bottom diagrams. Scale bar is 300 µm in the retina.

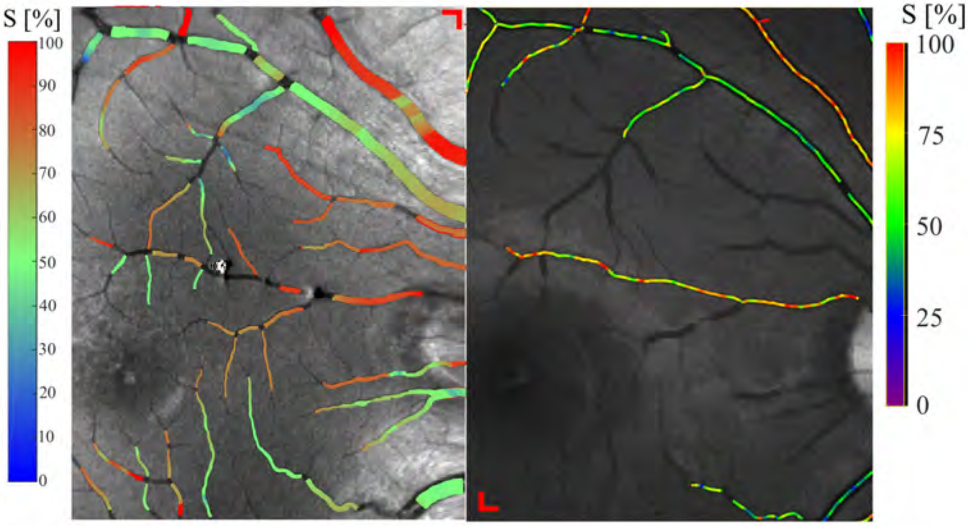
S [%]
100
90
80
70
60
50
40
30
20
10
0
S [%]
100
75
50
25
0

Figure 5.9: A: Estimated oxygenation values in volunteer 2; B: Corresponding image by Oxymap Tx. Scale bar represents 300 µm in the retina.

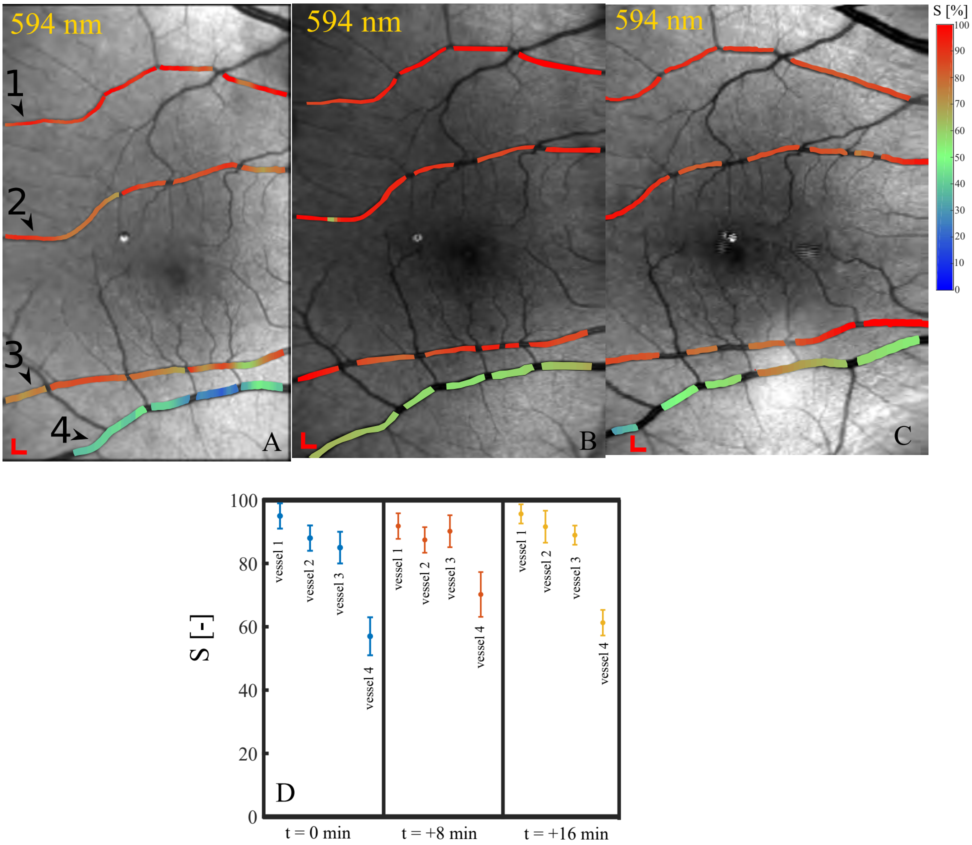
594 nm
594 nm
594 nm
1
2
3
4
A
B
C
S [%]
100
90
80
70
60
50
40
30
20
10
0
S [-]
100
80
60
40
20
0
vessel 1
vessel 2
vessel 3
vessel 4
vessel 1
vessel 2
vessel 3
vessel 4
vessel 1
vessel 2
vessel 3
vessel 4
D
t = 0 min
t = +8 min
t = +16 min

Figure 5.10: Retinal imaging was performed in Volunteer 1 with an interval of 8 minutes to study the repeatability of the measurements. A-C: Measurements made at 0, 8 and 16 minutes in Volunteer 1 with the calculated oximetry for 3 large arteries and a vein. Scale bar represents 300 µm The numerical valued are plotted in D.

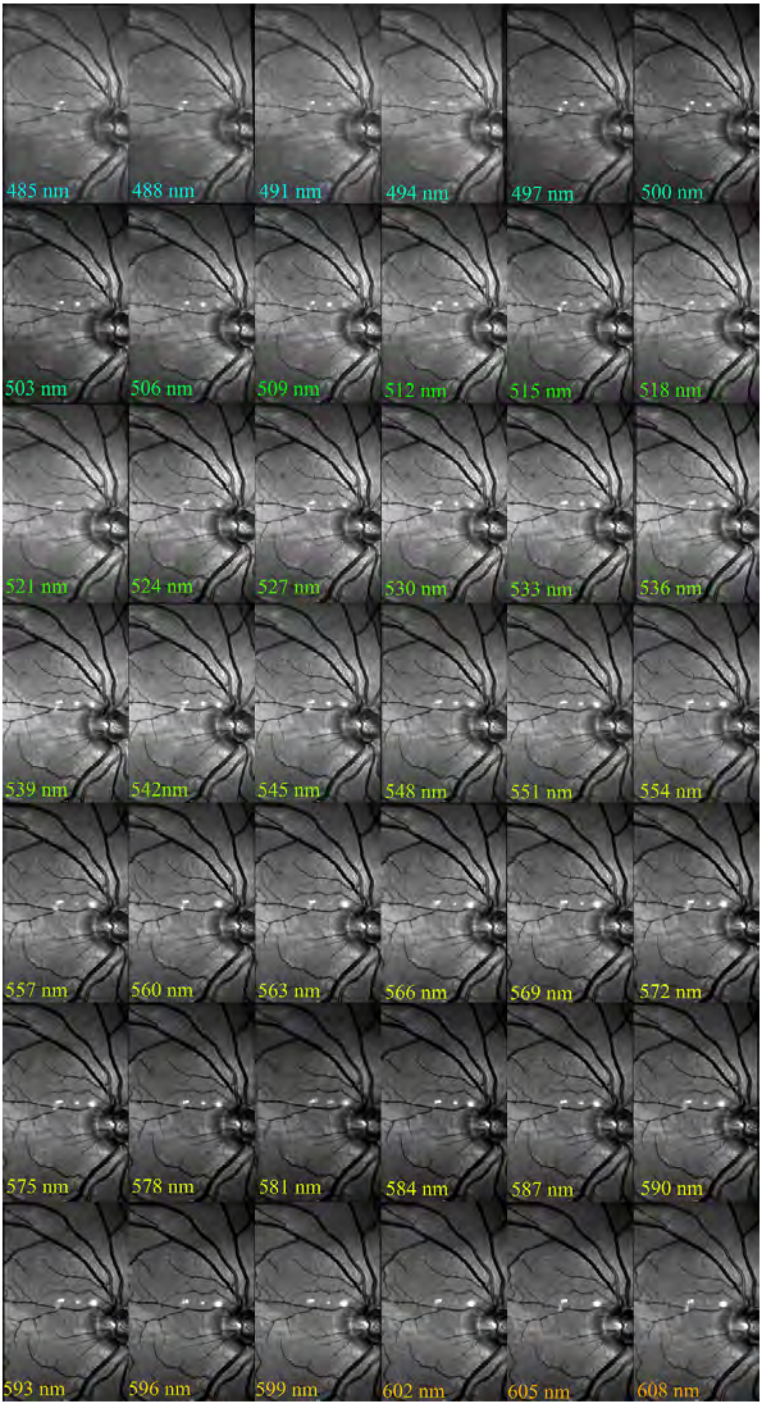
485 nm
488 nm
491 nm
494 nm
497 nm
500 nm
503 nm
506 nm
509 nm
512 nm
515 nm
518 nm
521 nm
524 nm
527 nm
530 nm
533 nm
536 nm
539 nm
542nm
545 nm
548 nm
551 nm
554 nm
557 nm
560 nm
563 nm
566 nm
569 nm
572 nm
575 nm
578 nm
581 nm
584 nm
587 nm
590 nm
593 nm
596 nm
599 nm
602 nm
605 nm
608 nm

Figure 5.11: Wavelength sweep from 485 nm to 608 nm

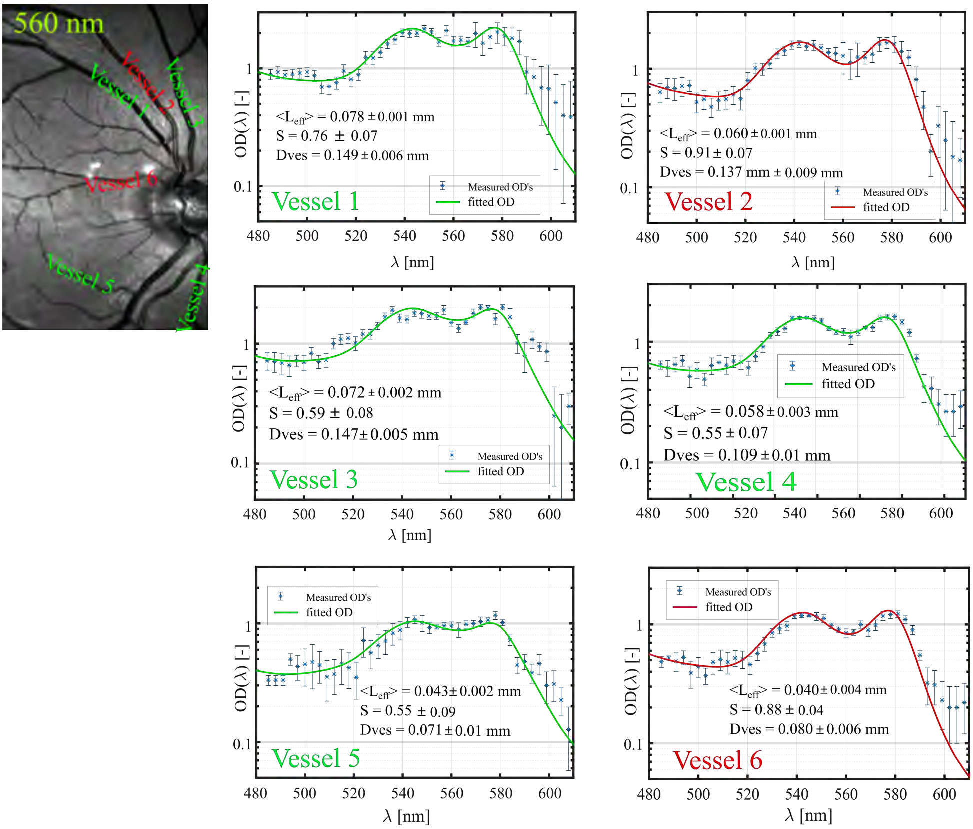

Figure 5.12: Plot of OD as a function of wavelength for six blood vessels in the right eye of a healthy volunteer.

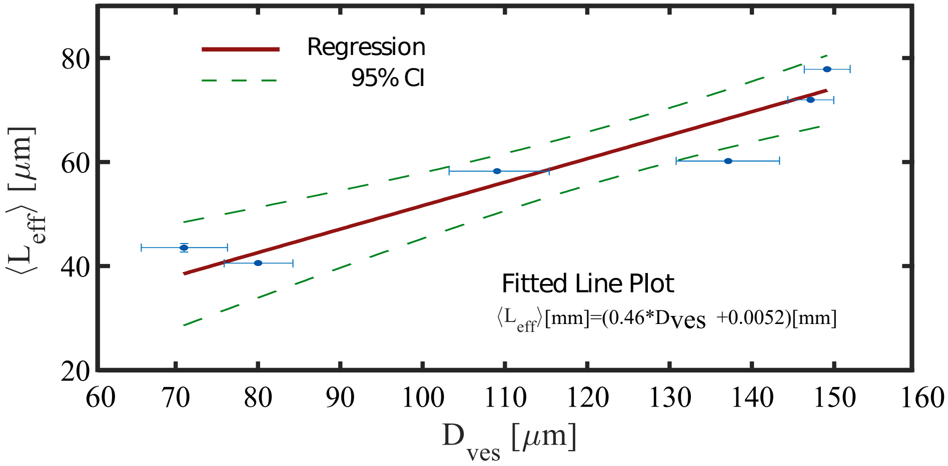

Figure 5.13: Linear regression fit of the effective path length $\langle L_{eff} \rangle$ as a function of the blood vessel diameter D_{ves}

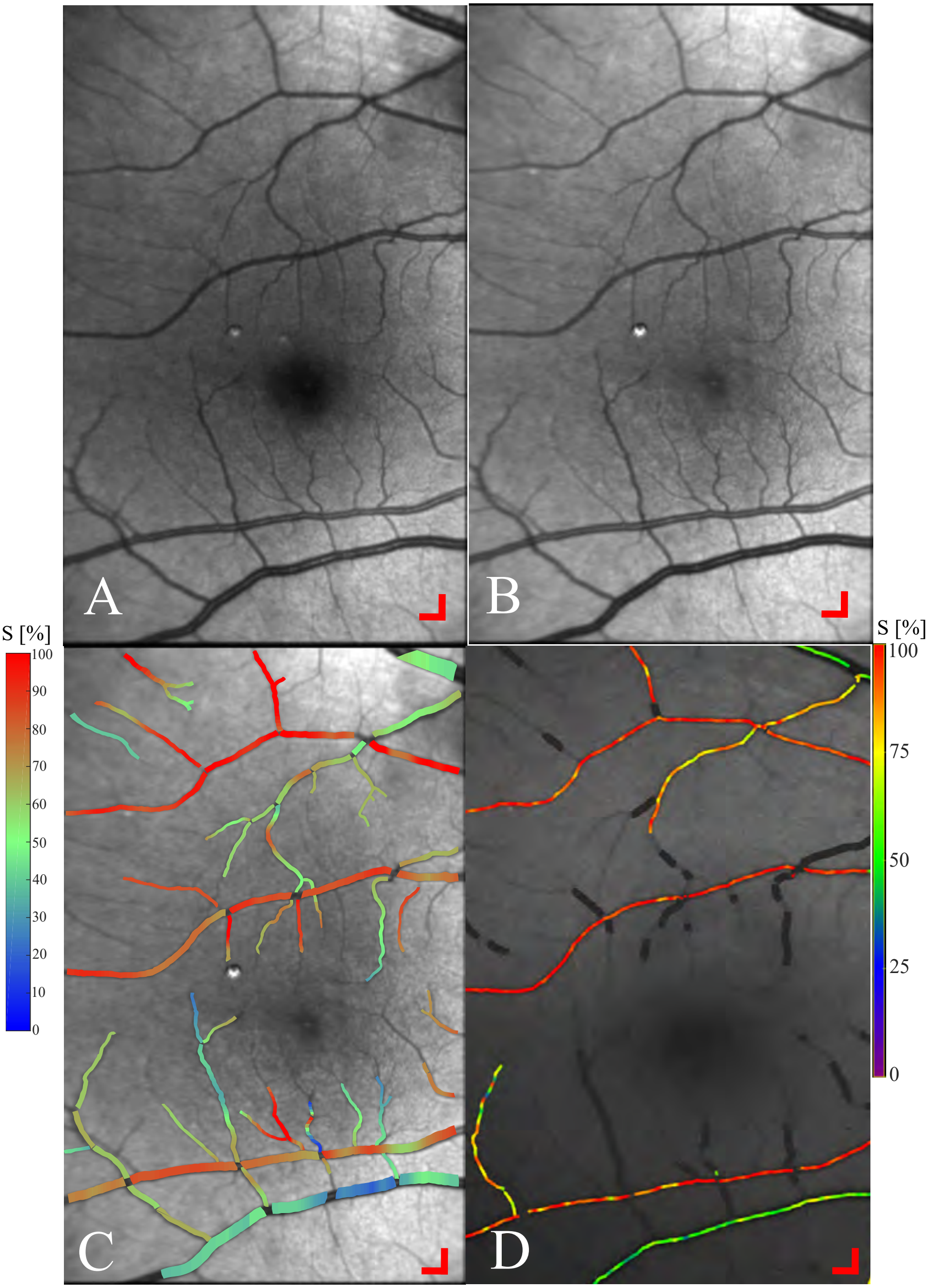
A
B
C
D
S [%]
100
90
80
70
60
50
40
30
20
10
0
S [%]
100
75
50
25
0

Figure 5.14: SLO images taken from a healthy human volunteer at two wavelengths 498 nm (A) and 594 nm (B). 10 frames were registered and averaged to improve the SNR of the images. The estimated oximetry results are shown in C. D shows the image acquired using Oxymap Tx ehf. for comparison. Scale bar represents 300 µm in the retina.

The S values of these vessels are similar to the values obtained by dual-wavelength imaging of the same volunteer (Fig. 5.9) and oxygen saturation maps obtained with Oxymap Tx e.h.f. The errors on the fitted parameters were calculated from the diagonals of the covariance matrix [51]. From the fitted values of $\langle L_{eff} \rangle$, the relationship between $\langle L_{eff} \rangle$ and D_{ves} for these vessels ($D_{ves} \geq 70\,\mu\text{m}$) could be established, and this relationship is plotted in Figure 5.13. The relation between $\langle L_{eff} \rangle$ and Dves was found to be fitted well by a linear function, $\langle L_{eff} \rangle$[µm]=(0.46 $\cdot D_{ves}$+ 5.2) ± 6.0 [µm] where $\langle L_{eff} \rangle$ and D_{ves} are given in micrometres. From this relationship we conclude that our sub-diffuse SLO imaging scheme, where a small illumination spot is used in combination with a large collection aperture, works in a light transport regime between a fundus camera (where $\langle L_{eff} \rangle = D_{ves}$) and a truly confocal SLO (where $\langle L_{eff} \rangle = \langle L_{bs} \rangle$ with $\langle L_{bs} \rangle$ the backscatter path length which is not expected to have a linear dependence on D_{ves}. We expect that the exact relation between $\langle L_{eff} \rangle$ and D_{ves} depends on the details of the measurement geometry, and will, for example, be different for different DCF cladding sizes or, equivalently, for different confocal aperture sizes. Furthermore, we have here in our fits assumed $\langle L_{eff} \rangle$ to be wavelength independent, whereas it is expected that $\langle L_{eff} \rangle$ depends on the scattering and absorption coefficients of blood and is therefore in reality wavelength dependent. This is a topic for future investigations.

One notable advantage of the wavelength sweep using the SLO is the availability of the spectral properties of the entire retina for multiple wavelengths. This will in the future permit expansion of the diagnostic capabilities of an SLO by providing spectral fingerprints of additional chromophores such as carotenoids. However, the imaging speed of the wavelength sweep should be dramatically improved before the clinical implementation of wavelength sweeping would become feasible.

5.4 Conclusion

In conclusion, we have demonstrated *in vivo* human retinal imaging with a novel SLO based on a supercontinuum source. The RIN noise of the illumination source has been addressed by implementing balanced detection. The balanced detection increased the SNR, and therefore improved the image quality and accuracy of oximetry calculations. The implementation of an achromatizing lens reduced the effect of chromatic aberrations introduced by the human eye, although this did not have a large effect on saturation estimation. The use of a double clad fibre with large inner cladding provided the best trade-off between image contrast and SNR. This allowed for high-resolution in vivo visualization of the oxygenation of retinal blood vessels in healthy volunteers. The oxygen saturation of the larger vessels of the retinas of two human volunteers were in agreement with the Oxymap derived saturations; in addition, our SLO system was able to provide oxygen saturation in much smaller vessels. The saturation measured in 3 different imaging sessions of the same volunteer (8 minutes apart) demonstrated the reproducibility of our measurements. Finally, by performing a wavelength sweep between 485 and 608 nm we determined an approximately linear relationship between the effective path length of photons through the blood vessels and vessel diameter for our SLO geometry that employs a DCF with a large inner cladding. It is expected that our SLO will be a valuable tool to study the effect of degenerative retinal diseases on the oxygenation in the retinal microvasculature.

References

[1] N. D. Wangsa-wirawan and R. Linsenmeier, "Retinal Oxygen," Arch Ophthalmol. **121**, 547557 (2003).

[2] T. Bek, E. Stefansson and S. H. Hardarson, Retinal oxygen saturation is an independent contributor to the severity of retinopathy in diabetic patients, Br. J. Ophthalmol., 103 (**8**), 1167 1172 (2018).

[3] E. D. Cole, E. A. Novais, R. N. Louzada, and N. K. Waheed, "Contemporary retinal imaging techniques in diabetic retinopathy: a review," Clin. Exp. Ophthalmol. **44**, 289299 (2016).

[4] R. Klein, B. E. K. Klein, M. W. Neider, L. D. Hubbard, S. M. Meuer, and R. J. Brothers, "Diabetic Retinopathy as Detected Using Ophthalmoscopy, a Nonmyciriatic Camera and a Standard Fundus Camera," Ophthalmology **92**, 485491 (1985).

[5] G. Michelson, M. Scibor, and D. Schweizter, "Intravascular oxygen saturation in retinal vessels in glaucoma," Invest. Ophthalmol. Vis. Sci. **43**, U445U445 (2002).

[6] A. Geirsdottir, S. H. Hardarson, O. B. Olafsdottir, and E. Stefansson, "Retinal oxygen metabolism in exudative age-related macular degeneration," Acta Ophthalmol. **92**, 2733 (2014).

[7] O. B. Olafsdottir, S. H. Hardarson, M. S. Gottfredsdottir, A. Harris, and E. Stefansson, "Retinal oximetry in primary open-angle glaucoma," Investig. Ophthalmol. Vis. Sci. **52**, 64096413 (2011).

[8] E. Nitta, K. Hirooka, T. Shimazaki, S. Sato, K. Ukegawa, Y. Nakano, and A. Tsujikawa, "Retinal oxygen saturation before and after glaucoma surgery," Acta Ophthalmol. 20152018 (2016).

[9] S. Rilven, T. L. Torp, and J. Grauslund, "Retinal oximetry in patients with ischaemic retinal diseases," Acta Ophthalmol. **95**, 119127 (2017).

[10] A. B.Einarsdottiret et al., Retinal oximetry imaging in Alzheimers disease, J. Alzheimers Dis., **49** (1), 79 83 (2015).

[11] N. J. Hart, Y. Koronyo, K. L. Black, and M. Koronyo-Hamaoui, "Ocular indicators of Alzheimer’s: exploring disease in the retina," Acta Neuropathol. **132**, 767787 (2016).

[12] A. B. Einarsdottir, O. B. Olafsdottir, H. Hjaltason, and S. H. Hardarson, "Retinal oximetry is affected in multiple sclerosis," Acta Ophthalmol. **96**, 528530 (2018).

[13] T. Shiba, K. Maruo, and T. Akahoshi, "Development of a multi-field fundus photographing system using a non-mydriatic camera for diabetic retinopathy," Diabetes Res. Clin. Pract. **45**, 18 (1999).

[14] E. DeHoog and J. Schwiegerling, "Optimal parameters for retinal illumination and imaging in fundus cameras.," Appl. Opt. **47**, 67696777 (2008).

[15] A. Geirsdottir, S. H. Hardarson, O. B. Olafsdottir, and E. Stefánsson, "Retinal oxygen metabolism in exudative age-related macular degeneration," Acta Ophthalmol. **92**, 2733 (2014).

[16] J. C. Ramella-Roman, S. a Mathews, H. Kandimalla, A. Nabili, D. D. Duncan, S. a DAnna, S. M. Shah, and Q. D. Nguyen, "Measurement of oxygen saturation in the retina with a spectroscopic sensitive multi aperture camera.," Opt. Express **16**, 61706182 (2008).

[17] D. J. Mordant, I. Al-Abboud, G. Muyo, A. Gorman, A. Sallam, P. Ritchie, A. R. Harvey, and A. I. McNaught, "Spectral imaging of the retina," Eye **25**, 309320 (2011).

[18] B. Khoobehi, J. M. Beach, and H. Kawano, "Hyperspectral Imaging for Measurement of Oxygen Saturation in the Optic Nerve Head," Invest. Ophthalmol. Vis. Sci. **45**, 146472 (2004).

[19] W. R. Johnson, D. W. Wilson, W. Fink, M. Humayun, and G. Bearman, "Snapshot hyperspectral imaging in ophthalmology.," J. Biomed. Opt. **12**, 014036 (2014).

[20] R. A. Ashman, F. Reinholz, and R. H. Eikelboom, "Oximetry with a multiple wavelength SLO," Int. Ophthalmol. **23**, 343346 (2001).

[21] H. Li, J. Lu, G. Shi, and Y. Zhang, "Measurement of oxygen saturation in small retinal vessels with adaptive optics confocal scanning laser ophthalmoscope," J. Biomed. Opt. **16**, 110504 (2011).

[22] S. P. Chong, M. Bernucci, H. Radhakrishnan, and V. J. Srinivasan, "Structural and functional human retinal imaging with a fiber-based visible light OCT ophthalmoscope," Biomed. Opt. Express **8**, 323 (2017).

[23] L. E. MacKenzie, T. R. Choudhary, A. I. McNaught, and A. R. Harvey, "In vivo oximetry of human bulbar conjunctival and episcleral microvasculature using snapshot multispectral imaging," Exp. Eye Res. **149**, 4858 (2016).

[24] J. P. Campbell, M. Zhang, T. S. Hwang, S. T. Bailey, D. J. Wilson, Y. Jia, and D. Huang, "Detailed Vascular Anatomy of the Human Retina by Projection-Resolved Optical Coherence Tomography Angiography," Sci. Rep. **7**, 111 (2017).

[25] S. Pi, A. Camino, X. Wei, J. Simonett, W. Cepurna, D. Huang, J. C. Morrison, and Y. Jia, "Rodent retinal circulation organization and oxygen metabolism revealed by visible-light optical coherence tomography," Biomed. Opt. Express **9**, 58515862 (2018).

[26] M. Damodaran, A. Amelink, and J. F. de Boer, "Optimal wavelengths for subdiffuse scanning laser oximetry of the human retina," J. Biomed. Opt. **23**, 1 (2018).

[27] A. Sassaroli and S. Fantini, "Comment on the modified Beer-Lambert law for scattering media," Phys. Med. Biol. **49**, (2004).

[28] L. Kocsis, P. Herman, and A. Eke, "The modified Beer-Lambert law revisited," Phys. Med. Biol. **51**, (2006).

[29] N. Bosschaart, G. J. Edelman, M. C. G. Aalders, T. G. van Leeuwen, and D. J. Faber, "A literature review and novel theoretical approach on the optical properties of whole blood," Lasers Med. Sci. **29**, 453479 (2014).

[30] N. Rajaram, A. Gopal, X. Zhang, and J. W. Tunnell, "Experimental validation of the effects of microvasculature pigment packaging on in vivo diffuse reflectance spectroscopy," Lasers Surg. Med. **42**, 680688 (2010).

[31] J. C. Finlay and T. H. Foster, "Effect of pigment packaging on diffuse reflectance spectroscopy of-samples containing red blood cells," Opt. Lett. **29**, 965967 (2004).

[32] D. Schweitzer, M. Hammer, J. Kraft, E. Thamm, E. Königsdörffer, and J. Strobel, "In vivo measurement of the oxygen saturation of retinal vessels in healthy volunteers.," IEEE Trans. Biomed. Eng. **46**, 14541465 (1999).

[33] "International Electrotechnical Commission, Safety of Laser Products Part 1: Equipment Classification and Requirements", (Geneva, Switzerland), IEC-60825-1 (2014),

[34] APD410x Operation Manual, Thorlabs GmbH, Germany (2015).

[35] S. Lemire-Renaud, M. Rivard, M. Strupler, D. Morneau, F. Verpillat, X. Daxhelet, N. Godbout, and C. Boudoux, "Double-clad fiber coupler for endoscopy.," Opt. Express **18**, 975564 (2010).

[36] E. De Montigny, W.-J. Madore, O. Ouellette, G. Bernard, M. Leduc, M. Strupler, C. Boudoux, and N. Godbout, "Double-clad fiber coupler for partially coherent detection," Opt. Express **23**, 90409051 (2015).

[37] W. J. Donnelly and A. Roorda, "Optimal pupil size in the human eye for axial resolution.," J. Opt. Soc. Am. A. Opt. Image Sci. Vis. **20**, 20102015 (2003).

[38] M. Vinas, C. Dorronsoro, D. Cortes, D. Pascual, and S. Marcos, "Longitudinal chromatic aberration of the human eye in the visible and near infrared from wavefront sensing , double-pass and psychophysics," Biomed. Opt. Express **23**, 513522 (2015).

[39] I. B. Gonzalo, R. D. Engelsholm, and O. Bang, "Noise study of all-normal dispersion supercontinuum sources for potential application in optical coherence tomography," Prog. Biomed. Opt. Imaging - Proc. SPIE 10591, (2018).

[40] G. McConnell, "Noise analysis of a white-light supercontinuum light source for multiple wavelength confocal laser scanning fluorescence microscopy," J. Phys. D. Appl. Phys. **38**, 26202624 (2005).

[41] J. M. Dudley, S. Coen, K. L. Corwin, N. R. Newbury, B. R. Washburn, S. A. Diddams, and R. S. Windeier, "Fundamental noise limitations on supercontinuum generation in microstructure fiber," Phys. Rev. Lett. **90**, 113904 (2003).

[42] D. G. Lowe, "Distinctive Image Features from Scale-Invariant Keypoints," Int. J. Comput. Vis. **50**, 91110 (2004).

[43] V. Davidoiu, L. Hadjilucas, I. Teh, N. P. Smith, J. E. Schneider, and J. Lee, "Evaluation of noise removal algorithms for imaging and reconstruction of vascular networks using micro-CT," Biomed. Phys. Eng. Express **2**, 45015 (2016).

[44] K. Zuiderveld, "Contrast Limited Adaptive Histograph Equalization," in Graphics Gems IV, P. S. Heckbert, ed. (Academic Press Professional, Inc., 1994), pp. 474485.

[45] P. Bankhead, C. N. Scholfield, J. G. McGeown, and T. M. Curtis, "Fast retinal vessel detection and measurement using wavelets and edge location refinement," PLoS One **7**, 112 (2012).

[46] D. A. Atchison and G. Smith, Optics of the Human Eye, Butterworth-Heinemann, Oxford (2000).

[47] E. J. Fernández, A. Unterhuber, B. Povaay, and B. Hermann, "Chromatic aberration correction of the human eye for retinal imaging in the near infrared," **14**, 16731680 (2006).

[48] R. J. Zawadzki, B. Cense, Y. Zhang, S. S. Choi, D. T. Miller, and J. S. Werner, "Ultrahigh-resolution optical coherence tomography with monochromatic and chromatic aberration correction," Opt. Express **16**, 17341746 (2008).

[49] S. P. Chong, T. Zhang, A. Kho, M. T. Bernucci, A. Dubra, and V. J. Srinivasan, "Ultrahigh resolution retinal imaging by visible light OCT with longitudinal achromatization," Biomed. Opt. Express **9**, 1477 (2018).

[50] F. LaRocca, D. Nankivil, S. Farsiu, and J. A. Izatt, "True color scanning laser ophthalmoscopy and optical coherence tomography handheld probe," Biomed. Opt. Express **5**, 3204 (2014).

[51] A. Amelink, D. J. Robinson, and H. J. C. M. Sterenborg, "Confidence intervals on fit parameters derived from optical reflectance spectroscopy measurements," J. Biomed. Opt. **13**, 114 (2008).

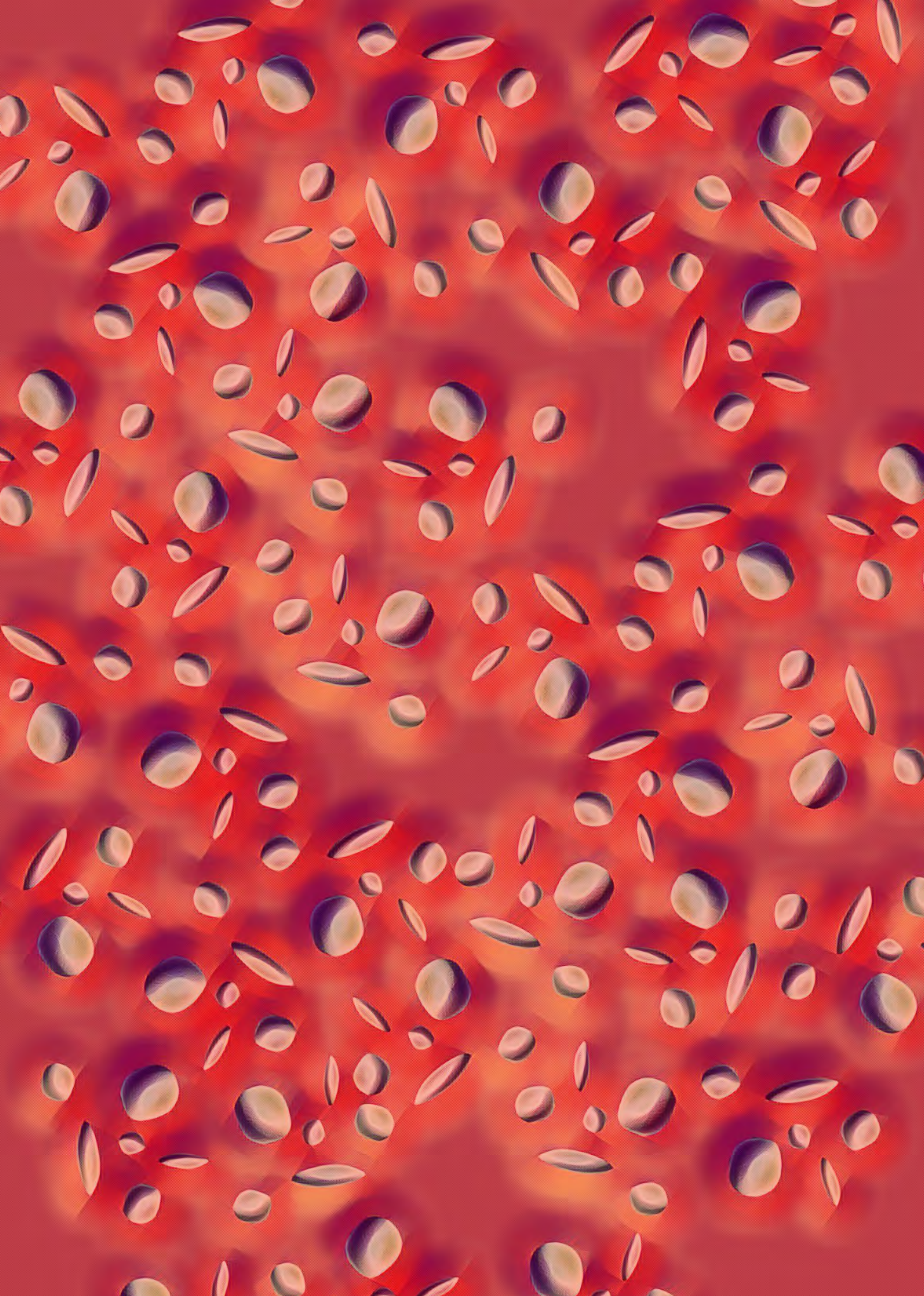

6

Non-invasive optical measurement of haemoglobin concentration in the posterior eye of adult humans

based on:

M. Damodaran, A. Amelink, and J. F. de Boer, "Non-invasive optical measure-ment of haemoglobin concentration in the posterior eye of adult humans" (manuscript in preparation).

Abstract

Haemoglobin concentration in blood is an important biomarker. Current methods to measure blood haemoglobin concentration involves the invasive procedure of drawing blood from a vein or through a finger prick. In this letter, a non-invasive spectrophotometric method to image the retina simultaneously at two isosbestic wavelengths and to extract the haemoglobin concentration values from the two images is presented. We have measured the haemoglobin concentration in human retinas using a dual-wavelength scanning laser ophthalmoscope that uses a supercontinuum light source, and a balanced detection scheme. The optimum wavelength combination (522 nm and 548 nm) for the measurement was chosen based on an error propagation analysis.

6.1 Introduction

Haemoglobin (Hb) concentration in blood is used for many applications in the medical field, e.g. for anaemia diagnosis [1], to screen blood donors, and in transfusion guidance. The need to draw blood for Hb concentration for analysis is undesirable for several reasons, including discomfort to the patient, the time required of medical personnel to draw and handle the samples, and the potential risk of spreading blood-borne diseases through punctures of the skin. Repeated drawing of blood samples and *in vitro* analysis is especially undesirable in infants, in situations with blood loss, and low resource settings in developing countries. Several methods attempting non-invasive Hb concentration quantification have been investigated previously [2]. These methods are mostly based on measurements in skin extremities such as the fingertip or earlobe [3, 4] and require extensive calibration due to the lack of direct visual access to blood vessels. Further, studies assessing the accuracy of point-of-care tests [5] have found high variability in Hb concentration obtained from successive drops of fingerpick blood. Both Hb concentration and haematocrit are used for the diagnosis of anaemia. They are related through the mean corpuscular haemoglobin concentration, which is assumed to be 32 to 36 [g/dL] for human blood [6]. Thus, Hb concentration in g/dL can be approximately converted to haematocrit in % by multiplying Hb concentration by 3. However, the Hb concentration is more stable to plasma volume changes such as dehydration, which makes it more reliable for the assessment of anaemia [7]. The eye provides a unique location in the human body with visual access to blood vessels. The blood vessels in the retina are located very superficially, are optically well accessible, and thus provide a unique access point for Hb concentration estimation due to the lack of thick overlying tissues present elsewhere in the body [8]. The ophthalmic artery, which supplies blood to the eye, is the first branch of the internal carotid artery and any global variation in Hb concentration in the body is expected to be measurable in the retinal vessels close to the optic nerve head (ONH). In the retina, haematocrit quantification by performing in vivo imaging was previously explored using optical coherence interferometry (OCT) methods either by fitting the attenuation slope of the OCT signal [9] centred at 830 nm or by fitting Visible OCT angiogram signals [10]. A direct spectrophotometric method to measure haematocrit has been conceptualised [11] but has not yet been demonstrated. In this letter, we demonstrate Hb concentration estimation using a novel scanning laser ophthalmoscope (SLO) design which uses a supercontinuum light source for imaging the retina simultaneously at two wavelength bands.

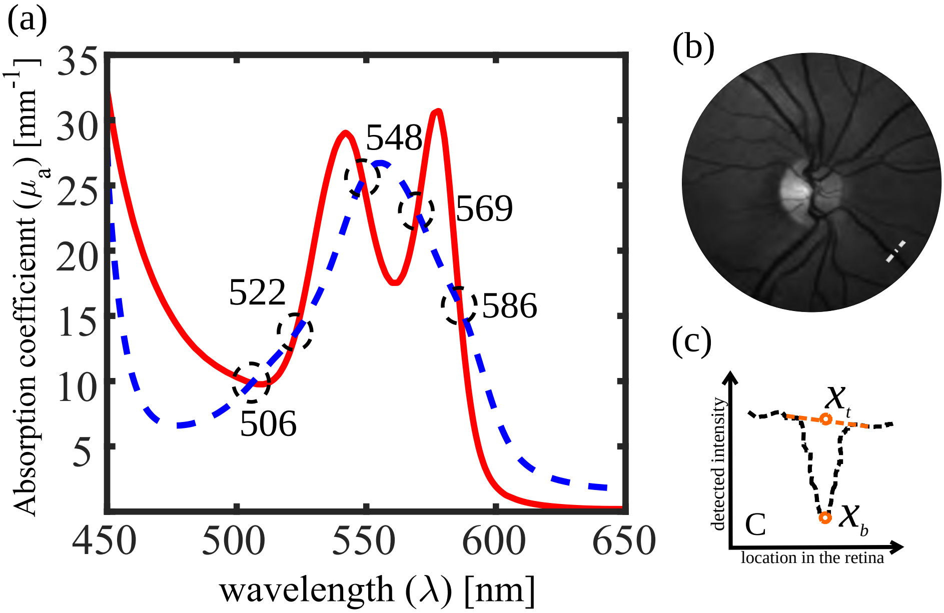

Figure 6.1: (a): Absorption spectrum of oxy- and deoxy- Hb in the [450 650] nm range showing the various isosbestic points where the absorption is independent of the oxygenation of the Hb molecule. (b): in vivo retinal image at (λ = 570 ± 30 nm) obtained using a fundus camera. (c): A line profile along a blood vessel to extract the reflectance value at tissue and blood vessel locations.

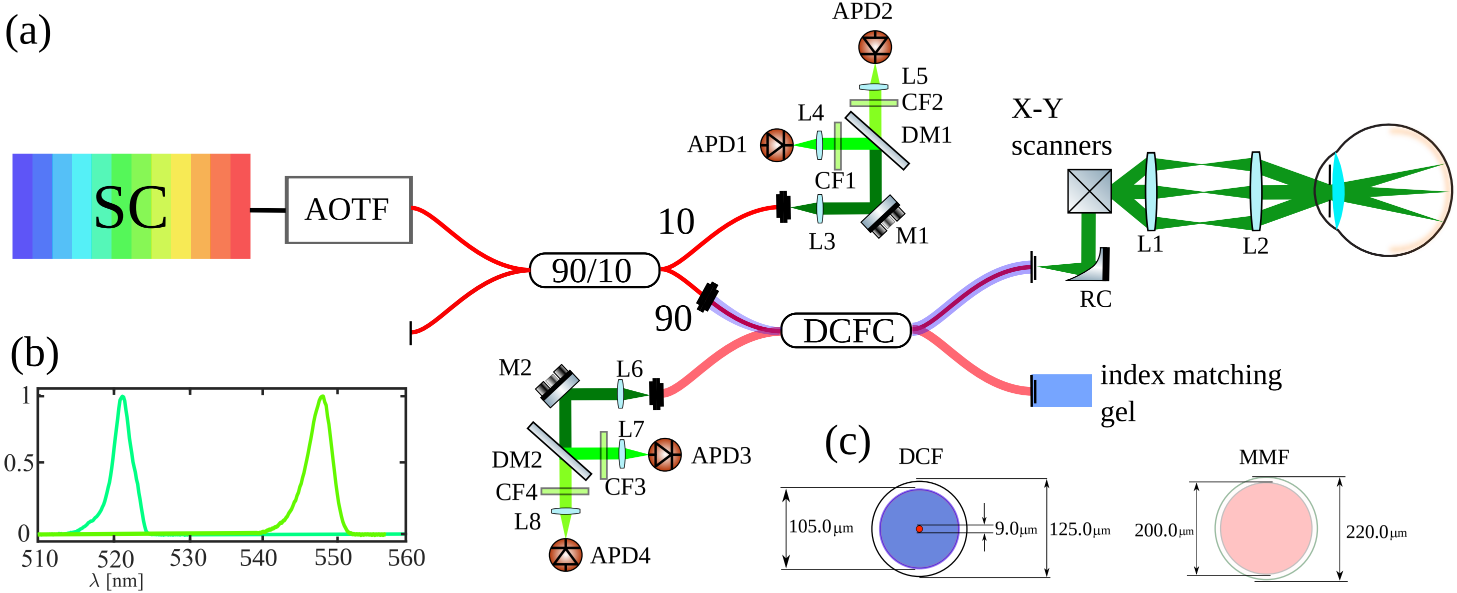
(a)
SC
AOTF
90/10
10
90
APD2
L5
CF2
L4
APD1
DM1
CF1
L3
M1
X-Y
scanners
L1
L2
RC
DCFC
M2
L6
L7
APD3
DM2
CF4
CF3
L8
APD4
index matching
gel
(b)
normalized intensity [A.U]
1
0.5
0
510
520
530
540
550
560
λ [nm]
(c)
DCF
105.0µm
9.0µm
125.0µm
MMF
200.0µm
220.0µm

Figure 6.2: (a): Schematic of the setup: Light from a supercontinuum source (SC) (EXU-6, NKT Photonics A/S, Birkerød, Denmark) was filtered using an acousto optic tunable filter (AOTF) (Select, NKT Photonics A/S, Birkerød, Denmark). A 90:10 coupler (TW560R2A2, Thorlabs GmbH, Germany) was used to split off 10 % of the light for balanced detection. The 90 % port of the splitter was coupled to the core of a double-clad fibre (DCF) in the DCF coupler (DCFC). About 94 % (transmission measured at 550 nm) of this light reached the pupil plane. L1-L8: Lenses, M1-M2: Mirrors, CF1, CF3: bandpass clean-up filters, CF2, CF4: 532 nm long pass clean-up filters, APD1-APD4: Avalanche photodiodes (APD410A2, Thorlabs GmbH, Germany). D1, D2: Dichroic beam splitters (long pass 532 nm), RC: Reflective collimator (RC02APC-P01, Thorlabs GmbH, Germany). (b): Illumination spectrum of the wavelengths 522nm (FWHM: 2.2 nm) and 548 nm (FWHM: 3.7 nm) used for imaging. (c): Configuration of the DCF and multimode fibre (MMF) used in the setup. The DCF had a core numerical aperture (NA) of 0.11. The NA of the inner cladding was 0.22, and the inner cladding of the DCF was coupled to an MMF with NA of 0.22.

6.2 Methods

Figure 6.1a shows the Hb absorption spectrum, which varies for most wavelengths based on the oxygenation of Hb except for isosbestic wavelengths [12]. The effect of optical absorption of Hb on image formation is visible in Fig. 6.1b where the blood vessels look significantly darker compared to the surrounding tissue. The attenuation of light due to the presence of Hb can be used to determine the concentration of Hb within the vessel using a non-invasive reflectance measurement at two isosbestic wavelengths. A typical method for measuring the absorbance of blood at a particular blood vessel in the retina is shown in the inset of Fig. 6.1c where the intensity profile of the blood vessel (dotted line) is plotted as a function of the location on the retina. If $I(\overline{x}_b, \lambda)$ and $I(\overline{x}_t, \lambda)$ are the recorded intensities in the retinal image at the centre of the blood vessel and adjacent tissue location respectively at a wavelength λ, and the incident light intensity was the same at both locations, the relative optical density OD_λ of blood vessel location compared to the surrounding tissue at a particular wavelength can be written as [13],

$$OD_\lambda = \ln\Big(\frac{I(x_t, \lambda)}{I(x_b, \lambda)}\Big) = \langle L_{eff}(\lambda)\rangle \cdot \big(S \cdot \mu_a^{HbO_2}(\lambda) + (1-S) \cdot \mu_a^{Hb}(\lambda)\big) + G(\lambda) \quad (6.1)$$

where the attenuation of the reflected light due to the blood within $\overline{x}_b$ is governed by *modified Beer-Lamberts law* [14] with $\langle L_{eff}(\lambda)\rangle$, the effective path length of photons travelling through the probed volume before reaching the detector. S is the oxygen saturation of blood defined as the ratio of amount of oxy-haemoglobin to the total haemoglobin. The absorption coefficients of oxy- and deoxy-Hb are given by $\mu_a^{HbO_2}(\lambda)$ and $\mu_a^{Hb}(\lambda)$, respectively, and the oxy and deoxy absorption coefficients are the product of the respective molar extinction coefficients, ($\epsilon_{HbO_2}(\lambda)$, $\epsilon_{Hb}(\lambda)$) and the concentration of Hb (c_{Hb}). $G(\lambda)$ is a factor which accounts for any apparent increase or decrease in the ODs purely due to scattering differences within the volumes $\overline{x}_b$ and $\overline{x}_t$. If λ_1 and λ_2 are isosbestic wavelengths (see Fig.6.1a) i.e., $\mu_a^{HbO_2}(\lambda) = \mu_a^{Hb}(\lambda) = \mu_a^{i}(\lambda)$, Eq. 6.1 can be written as,

$$OD_{\lambda_i} = \langle L_{eff}(\lambda_i)\rangle \cdot \mu_a(\lambda_i) + G(\lambda_i) \quad (6.2)$$

We have previously described a novel multi-color scanning laser ophthalmoscope (mcSLO) that uses a supercontinuum source and variable line pass filter to perform retinal oximetry [15]. We here use the same system to perform the first proof of principle measurements of haemoglobin concentration in human retinas. In this double clad fiber (DCF) coupler based SLO shown in Fig. 6.2, only

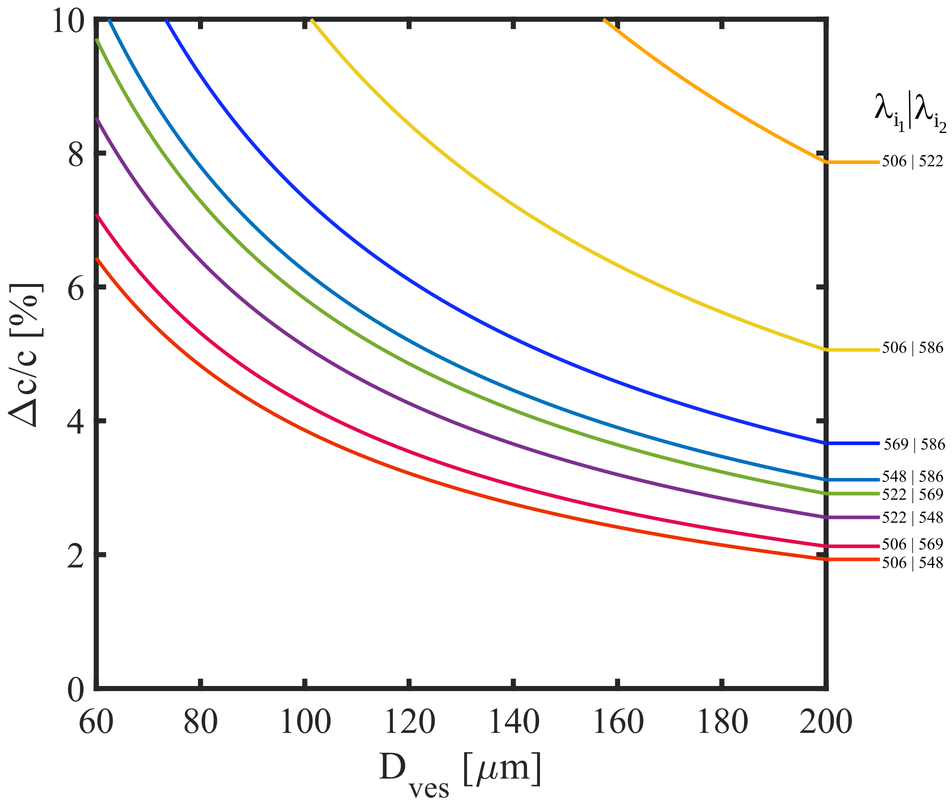

Figure 6.3: The percentage error (0 to 10%) in Hb concentration estimation for different wavelength combinations of isosbestic points assuming an SNR of 20 dB in the retinal images and a standard error in estimating the blood vessel diameter to be 10 µm. The most optimum wavelength combination is 506, 548 nm where the difference in absorption of Hb among these wavelengths is the highest (see Fig. 6.1a).

the light from the cladding is coupled to the multimode fiber, and the direct back scattered light from the retina, which travels through the core, does not reach the detector [16]. We demonstrated that the effective path length $\langle L_{eff}\rangle$ of the detected photons have the following linear relationship with the blood vessel diameter for 70 µm $\leq D_{ves} \leq$ 150 µm : $\langle L_{eff}\rangle$[mm] = (0.46$\cdot D_{ves}$+0.0052)[mm] [15]. Since $\mu_a = \ln 10 \cdot \epsilon(\lambda) \cdot c_{Hb}$, and the molecular weight of Hb is 64500 g/mol we can write the Hb concentration (c_{Hb}) as,

$$c_{Hb}\,[\mathrm{g/L}] = \frac{(OD_{\lambda_{i1}} - OD_{\lambda_{i2}})[-] \times 64500[\mathrm{g/mol}]}{\ln(10) \cdot (0.46 \cdot D_{ves} + 0.0052)[\mathrm{mm}] \cdot \left(\epsilon_a^i(\lambda_{i1}) - \epsilon_a^i(\lambda_{i2})\right)[\mathrm{L/mol/mm}]} \tag{6.3}$$

We can further determine optimum 'isosbestic' wavelength combination for estimating c_{Hb} from the ten combinations possible in [500 600] nm range by performing an error propagation analysis on Eq. 6.3. Figure 6.3 shows the results of this error analysis assuming an SNR of 20 dB in the intensities of the images (corresponding to 1% measurement noise) and uncertainty in vessel diameter estimation of 10 µm. Based on the analysis, 506 nm and 548 nm (largest absorption contrast) are the best wavelength combination for accurate c_{Hb} estimation. Nevertheless, we prefer the 522 and 548 nm combination since the wavelengths are closer (26 nm vs 42 nm separation). Therefore, the difference in wavelength-dependent scattering properties will be smaller, i.e., the difference in the factor $G(\lambda)$ will be smaller, and as a consequence, the wavelength dependence is expected to cancel out better when taking a difference of ODs in Eq. 6.1. The error analysis demonstrates that for the 522 and 548 nm combination the error in C_{Hb} measured in large blood vessels is only slightly higher than for the 506-548 pair and still within 5% for $D_{ves} \geq 100$ µm. For 522-548 nm combination, The c_{Hb} concentration (from Eq. 6.3) becomes

$$c_{Hb}\,[\mathrm{g/dL}] = \frac{1.3[] \times (OD_{\lambda_{i1}} - OD_{\lambda_{i2}})}{(0.46 \cdot D_{ves} + 0.0052)[\mathrm{mm}]} \tag{6.4}$$

The mcSLO (Fig. 6.2) is capable of simultaneous imaging at two different wavelengths. A combination of a 2.56 kHz resonant scanner (5.12 kHz line rate by utilising both directions of scanner sweep) (EPOC., Glendale, New York, USA), and a 10 Hz galvanometer mirror (Cambridge tech., Bredford, USA) placed close to each other were used to achieve an imaging throughput of 10 frames/second. The field of view (FOV) of the images was controlled by the voltage (amplitude) supplied to the scanning mirrors. The reflected and scattered light from the retina was then collected using the inner cladding of the double-clad fibre in port A. About 63 % (transmission measured at 550 nm) of the collected light is then coupled on to the multimode fibre (MMF) which is detected using two APDs and suitable filters to separate the 522 nm and 548 nm channels. The SC source results in noise in the images dominated by relative intensity noise (RIN). To reduce the RIN noise, balanced detection was implemented by simultaneously detecting the illumination signal, as shown in Fig. 6.2. As shown in 6.4, balanced detection resulted in a 6 dB and 7 dB signal to noise ratio improvement for 522 nm and 548 nm images, respectively [15].

The *in vivo* study obeyed the principles of the Declaration of Helsinki and was approved by the Institutional review board at the VU Medical Centre, Amsterdam. Tropicamide 0.5 % w/v. eye drops were administered before imaging the volunteers to obtain better collection efficiency through the pupil of the eye. This was essential because of the involuntary response of the pupil that constricts due to a bright light reflex. Dual-wavelength images were acquired from healthy volunteers. The optical power used for measuring human subjects was 150 µW per wavelength, and this was in agreement with the maximum permissible power prescribed by the IEC standard 60825-1 [17] for 8 hours of continuous exposure. Before recording the images, a reference measurement of the internal system reflections and background was recorded. Each background-subtracted frame containing both the forward and backward direction of the sweep of the resonant scanner was deinterleaved and dewarped. The images showed negligible corneal reflections and were artefact-free except for a strong lens reflection (L2 in Fig. 6.2), which saturated the detector. Consecutive frames were registered and averaged to improve the SNR and image contrast further. Given the improvement in SNR of the images with balanced detection, averaging 10 frames was sufficient to achieve an SNR 20 dB in the blood vessel and tissue locations. The vessel segmentation was done using retinal segmentation package (ARIA) based on wavelets and edge location refinement [18].

The Hb concentration was analysed in blood vessels with diameters $\geq$ 70 µm. The I($\overline{x}_b$,λ) and I($\overline{x}_t$,λ) were acquired for each location in the centre of the blood vessel and surrounding tissue as described previously [13]. The corresponding ODs were estimated, and the Hb concentration was calculated from Eq. 6.4. The *in vivo* imaging results from the right eyes of three healthy human volunteers is shown in Fig. 6.6. The left panel of Fig 6.6 shows the 522 nm image, and the middle panel shows the 548 nm image overlaid with blood vessel segmentation and the Hb estimation. The right panel of Fig. 6.6 shows the Hb concentration (mean value with error bar) estimated for each labelled blood vessel in the middle panel. The Hb concentration was shown only for parts of some vessels for the following reasons: (i) The automated vessel segmentation package (ARIA) [18] was found to be unreliable for vessel crossings, as well as in the edges of the image. (ii) For vessels, which are close to each other, there is not enough 'vessel-free tissue' to average the tissue intensity $I(x_t, \lambda)$ values in Eq. 6.1 to obtain proper estimates of the ODs of the tissue locations adjacent to the vessels.

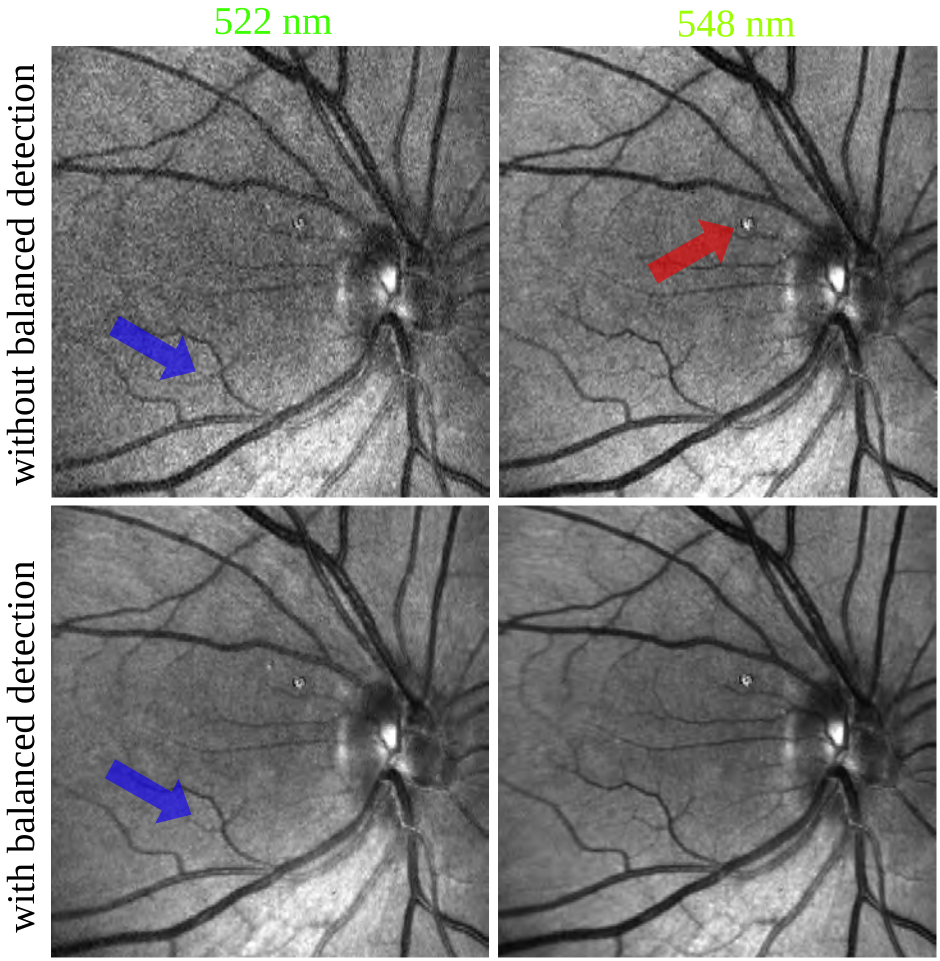

Figure 6.4: Single-frame balanced and unbalanced images from the 522 nm and 548 nm channels clearly show the improvement in image quality achieved by implementing balanced detection. Specific example is the small blood vessel (blue arrow) in the 522 nm channel visible only with balanced detection. The bright central reflection (red arrow) from the lens L1 (see Fig. 2a) was let to saturate the detector so as not to compromise the dynamic range of the image.

6.3 Results and discussion

The estimated mean Hb concentration in the right eye of a healthy volunteer (male, 45 years) was 15.5 ± 0.7 [g/dL].

These extracted values of Hb concentration agree with the physiologically expected values as reported in the literature. These values were derived using an effective path length $\langle L_{eff} \rangle$ that was extracted from a hyperspectral measurement

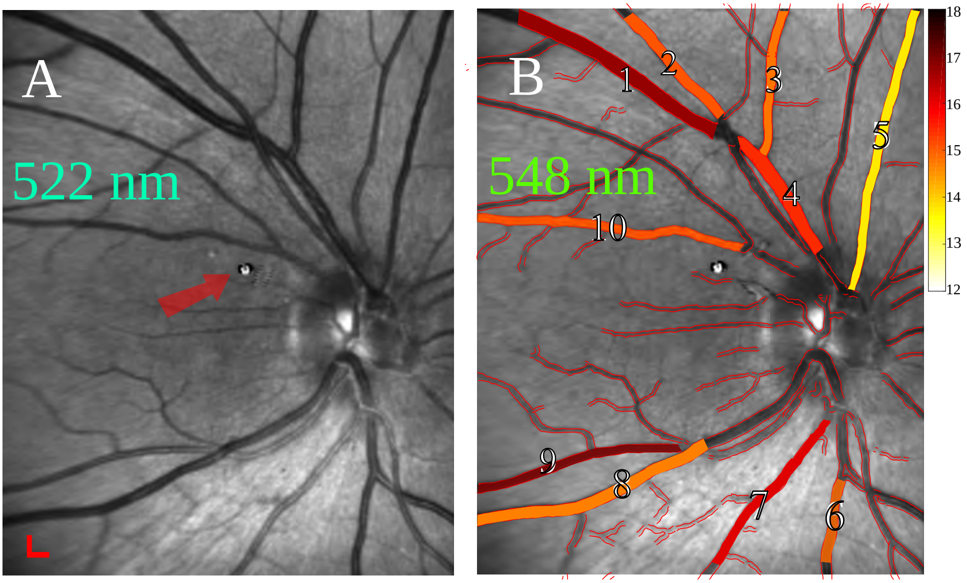

Figure 6.5: Hb concentration estimation in adult human volunteer — The 522 nm (A) and 548 nm (B) retinal image is shown for each volunteer. The vessels with diameters $\geq 65\,\mu$m near the ONH was analysed, and an image overlay showing the Hb concentration estimates as a colormap on the *in vivo* image is shown (B). The value for each individual vessel is also plotted, with the overall mean and standard deviation shown in red. Scale bar represents 300 µm in each direction.

over 484 to 608 nm in a single volunteer where a haemoglobin concentration of c = 15 g/dL was assumed, and $\langle L_{eff} \rangle$ and oxygen saturation S were fitted to the hyperspectral data [15]. However, the exact relation between $\langle L_{eff} \rangle$ and blood vessel diameter and its wavelength dependence deserves further investigation.

We observe intra-retinal variations in Hb concentration within the retina of the volunteer. Although it is hard to find literature that suggests how Hb concentration varies with vessel diameter, we had expected to find a relatively homogeneous distribution of Hb concentration throughout all the (large) vessels in the retina. The observed variations in Hb concentration estimation between different vessels and vessel segments may be caused, e.g. by variations in the depths and angles of the vessels with respect to the tissue surface, or by the presence of a central light reflex, which makes it difficult to estimate the OD in the centre of the vessel. These issues deserve further investigation. Despite the observed variations within each image, averaging the results of all the vessels gives a reasonable estimate of the systemic Hb concentration, which is the parameter of interest.

The error in the overall Hb concentration was around 0.7 [g/dL] when averaged over 10 blood vessels. This is better than the error on previously reported

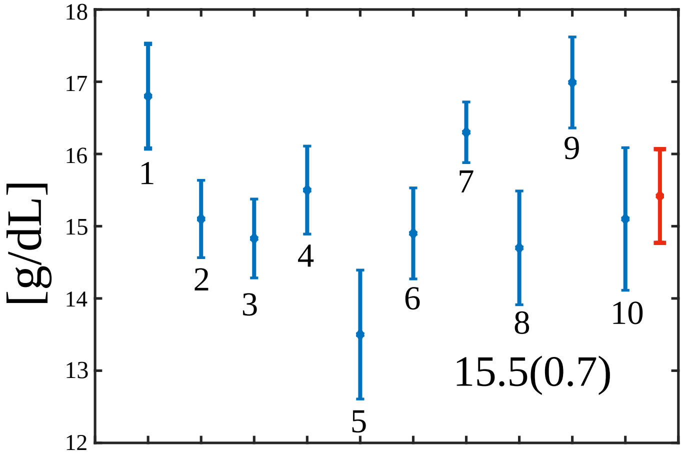

Figure 6.6: Hb concentration estimation in adult human volunteer — The 522 nm (A) and 548 nm (B) retinal image is shown for each volunteer. The vessels with diameters $\geq 65\,\mu\text{m}$ near the ONH was analysed, and an image overlay showing the Hb concentration estimates as a colormap on the *in vivo* image is shown (B). The value for each individual vessel is also plotted, with the overall mean and standard deviation shown in red. Scale bar represents 300 µm in each direction.

values [9, 10] on Hb concentration in the retina. Since the Hb concentration estimation was performed in large, superficial blood vessels in the retina, the pigment packaging effect [19, 20] is not expected to play a significant role in the effective blood vessel absorption. Although the method of haemoglobin concentration estimation from retinal images has been demonstrated with a complex, expensive mcSLO setup, the method could be translated into an application setting using a simpler and compact prototype. For example, a fundus camera employing low-cost hardware [21] and LEDs or filters with transmission windows corresponding to the optimum wavelengths could be implemented. This would not only bring a cost and device simplicity advantage but also remove the complex dependence of $\langle L_{eff} \rangle$ on blood vessel diameter and wavelength as found for our sub-diffuse SLO imaging scheme. Instead, for a fundus camera the relation $\langle L_{eff} \rangle = D_{ves}$ [22] holds, which could simplify the analysis of haemoglobin concentration compared to the SLO implementation.

6.4 Conclusion

In summary, the first results are shown from an experimental SLO system that uses an SC light source to produce multiple high contrast reflectance images of the retina simultaneously at two wavelengths at a speed of 10 fps. The SLO based on an SC source is very promising for spectral visualisation of the posterior part of the eye at high acquisition speeds with good resolution and contrast. Though the SC source has RIN noise, the acquired quasi-confocal images show superior contrast and quality thanks to the balanced detection scheme, which significantly reduced the RIN noise and improved the SNR. Since the SC source can be used to output any wavelength(s) of choice between 450 nm and 2400 nm, it offers numerous possibilities for obtaining spectral signatures of the retina including retinal oximetry, autofluorescence imaging and RPE melanin absorption characterisation. This might be very helpful for the detection of new pathological structural and functional changes in the retina. Although the demonstration of the method has been done with the sophisticated setup in Fig. 2, the method can be translated to clinics, and for field applications using a simpler and compact prototype. For example, a fundus camera employing low-cost hardware [21], and filters with transmission windows corresponding to the optimum wavelengths could be implemented for clinical applications. Fundus cameras also satisfy the requirement of the photon path lengths being approximately equal to the diameter of the blood vessels [22].

References

[1] R. D. Tyler and R. L. Cowell, "Classification and Diagnosis of Anaemia," Comp. Haematol. Int. 6, 116 (1996).

[2] J. W. Mcmurdy, G. D. Jay, S. Suner, and G. Crawford, "Noninvasive Optical, Electrical, and Acoustic Methods of Total Hemoglobin Determination," Clin. Chem. 54, 264272 (2008).

[3] S. Kim and J. Kim, "Noninvasive total hemoglobin measurement," J. Biomed. Opt. 7, 4550 (2002).

[4] A. Sakudo, Y. Hakariya, H. Kuratsune, and K. Ikuta, "Non-invasive prediction of hematocrit levels by portable visible and near-infrared spectrophotometer," Clin. Chim. Acta 408, 123127 (2009).

[5] M. M. Bond and R. R. Richards-Kortum, "Drop-to-drop variation in the cellular components of fingerprick blood: Implications for point-of-care diagnostic development," Am. J. Clin. Pathol. 144, 885894 (2015).

[6] RBC indices: MedlinePlus Medical Encyclopedia, (2019).

[7] L. Quintó, J. J. Aponte, C. Menéndez, J. Sacarlal, P. Aide, M. Espasa, I. Mandomando, C. Guinovart, E. Macete, R. Hirt, H. Urassa, M. M. Navia, R. Thompson, and P. L. Alonso, "Relationship between haemoglobin and haematocrit in the definition of anaemia," Trop. Med. Int. Heal. 11, 12951302 (2006).

[8] J. Mcmurdy, G. Jay, S. Suner, and G. Crawford, "Photonics-based In Vivo total hemoglobin monitoring and clinical relevance," J. Biophotonics 287, 277287 (2009).

[9] N. V. Iftimia, D. X. Hammer, C. E. Bigelow, D. I. Rosen, T. Ustun, A. A. Ferrante, D. Vu, and R. D. Ferguson, "Toward noninvasive measurement of blood hematocrit using spectral domain low coherence interferometry and retinal tracking," Opt. Express 14, 3377 (2006).

[10] S. P. Chong, M. Bernucci, H. Radhakrishnan, and V. J. Srinivasan, "Structural and functional human retinal imaging with a fiber-based visible light OCT ophthalmoscope," Biomed. Opt. Express 8, 323 (2017).

[11] M. J. Rice, R. H. Sweat, W. T. William, and W. Routt, "Non-invasive measurement of blood component using retinal imaging," United States Pat. US6305804B1 (2001).

[12] N. Bosschaart, G. J. Edelman, M. C. G. Aalders, T. G. van Leeuwen, and D. J. Faber, "A literature review and novel theoretical approach on the optical properties of whole blood," Lasers Med. Sci. 29, 453479 (2014).

[13] M. Damodaran, A. Amelink, and J. F. de Boer, "Optimal wavelengths for subdiffuse scanning laser oximetry of the human retina," J. Biomed. Opt. 23, 1 (2018).

[14] A. Sassaroli and S. Fantini, "Comment on the modified Beer-Lambert law for scattering media," Phys. Med. Biol. 49, (2004).

[15] M. Damodaran, A. Amelink, F. Feroldi, B. Lochocki, V. Davidoiu, and J. F. de Boer, "In vivo subdiffuse scanning laser oximetry of the human retina," J. Biomed. Opt. 24, 1 (2019).

[16] E. De Montigny, W.-J. Madore, O. Ouellette, G. Bernard, M. Leduc, M. Strupler, C. Boudoux, and N. Godbout, "Double-clad fiber coupler for partially coherent detection," Opt. Express 23, 90409051

(2015).

[17] International Electrotechnical Commission, "International Electrotechnical Commission, Safety of Laser Products Part 1: Equipment Classification and Requirements, (Geneva, Switzerland), IEC-60825-1 (2014)," 122 (2014).

[18] P. Bankhead, C. N. Scholfield, J. G. McGeown, and T. M. Curtis, "Fast retinal vessel detection and measurement using wavelets and edge location refinement," PLoS One 7, 112 (2012).

[19] N. Rajaram, A. Gopal, X. Zhang, and J. W. Tunnell, "Experimental validation of the effects of microvasculature pigment packaging on in vivo diffuse reflectance spectroscopy," Lasers Surg. Med. 42, 680688 (2010).

[20] J. C. Finlay and T. H. Foster, "Effect of pigment packaging on diffuse reflectance spectroscopy ofsamples containing red blood cells," Opt. Lett. 29, 965967 (2004).

[21] M. Damodaran, K. V. Vienola, B. Braaf, K. A. Vermeer, and J. F. de Boer, "Digital micromirror device based ophthalmoscope with concentric circle scanning," Biomed. Opt. Express 8, (2017).

[22] P. I. Rodmell, J. A. Crowe, A. Gorman, A. R. Harvey, G. Muyo, D. J. Mordant, A. I. McNaught, and S. P. Morgan, "Light path-length distributions within the retina," J. Biomed. Opt. 19, 036008 (2014).

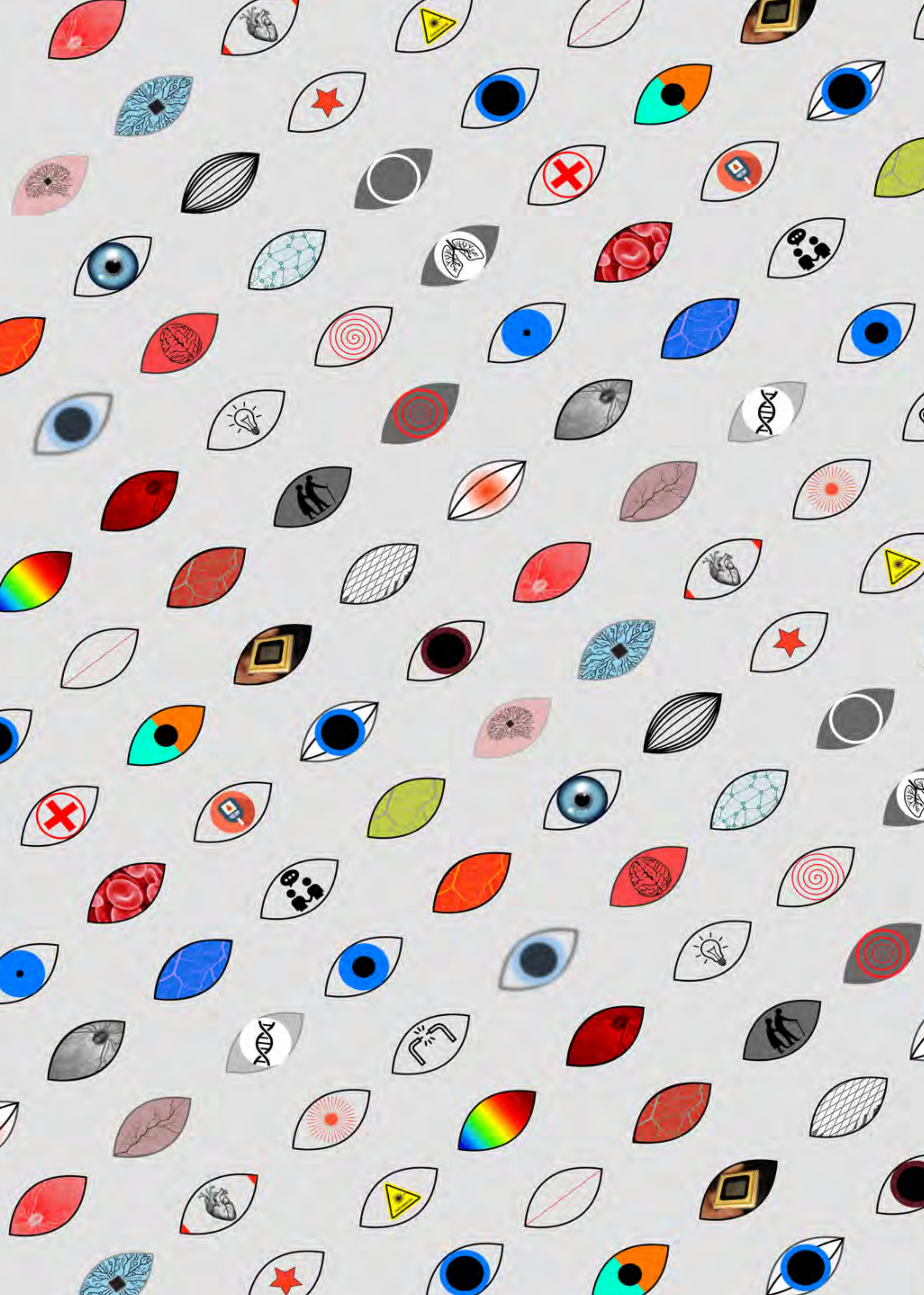

7

Discussion and outlook

7.1 Background

Assessment of retinal health for diagnosis and monitoring of retinal pathologies is predominantly based on its appearance and is visualised by various imaging techniques such as scanning laser ophthalmoscopy (SLO). To this end, a compact, low-cost experimental SLO based on a digital micromirror device (DMD) as described in **Chapter 3** was designed and implemented. Almost all retinal diseases affect the optical properties of the retina. Quantitatively determining these optical properties or changes thereof is of primary interest to our understanding of these diseases and for effective clinical evaluation, follow-up and treatment. Spectral signatures in the retina are related to the chemical composition of the retina and can be used to assess important physiological parameters such as the oxygenation of retinal blood. This was the main motivation in constructing the multispectral SLO. A multi-spectral SLO based on a supercontinuum source was constructed as described in **Chapters 4-6**. Both these *en face* techniques mentioned above show the result of the interaction of a light source with the retinal tissue and were developed to translate them to clinical use for diagnostic and research purposes. **Chapters 3-6** were introduced with a detailed discussion focusing on the research question addressed in those chapters. In this chapter, a short description of key technical aspects is presented, followed by a discussion of its advantages and limitations. Additionally, technologies that can aid in retinal disease diagnostics in the future is presented. Finally, the conclusion of the thesis is given.

7.2 Digital micromirror based SLO

In this thesis, an extension to the line of work on DMD based ophthalmic scanners is presented to demonstrate the value of using the compact ophthalmoscope for imaging at higher speeds while not compromising the signal to noise ratio. In this work, a stand-alone DMD was used to, in contrast to the DLP projector used by others [1, 2]. Concentric circle illumination was used to provide fixation for the subject during measurement. As shown in **Chapter 3**, the ophthalmoscope can produce high contrast images at a 7 Hz imaging speed. The DMD based SLO potentially reduces cost and increases flexibility. Shifting the centre of the concentric circles to visualise different regions is a novel way to provide fixation while imaging different peri- and para-foveal regions. The system is modular with respect to the light source and enables changing the wavelength for imaging. This is advantageous, especially in achieving multispectral imaging.

The main limitation of the DMD based SLO is that the illumination light efficiency is reduced. The DMD is operated at low fill-factor resulting in the majority of power is unused. Hence a high power and low divergence LED is needed to provide sufficient power for imaging the retina. Although a low divergence LED was used in our system, this might not be available for all wavelengths, particularly for the wavelengths of interest for multispectral applications. This is expected to improve in the future with the progress in LED source development. As we currently are a factor of 4 below the maximum permissible exposure according to the IEC standard 60825-1 [3], there is still room for further improvement. The near-infrared (NIR) illumination of the SLO provides a significant gain in the detected signal to noise ratio for structural imaging compared to visible light illuminations. The laser safety standards typically limit the visible illumination power. This, combined with the lack of low étendue sources, results in a lower signal to noise ratios compared with the NIR imaging. The polarization optics to reduce the stray reflections in the system lead to polarisation artefacts in the images due to birefringence of the cornea [4] and retina [5], influencing the images being recorded. Further, for extending the system to a multispectral retinal oximeter faced challenges due to the lack of high power, low divergence LED's in the suitable wavelengths for accurate estimation of retinal oxygenation. It was possible to extract motion information and use this to track the eyes movement using the DMD based SLO. When done fast enough, it will also enable doing eye motion correction in real-time [6–8] to improve the quality of the images by averaging multiple images at the same location and correct for the minor motion artefacts present in these images. Image registration could potentially be better with the parallel illumination as all the illumination points of a single frame are undistorted.

Multispectral retinal imaging has gained interest in recent years as it helps to gather quantitative information on retinal health. Multispectral imaging is more sensitive to subtle variations in the retina, compared to structural imaging. Using the DMD based technique, multispectral imaging can be extended to spatial frequency domain imaging (SFDI) [9] of the retina by projecting spatially confined sinusoidal patterns of different spatial frequencies to extract the absorption and scattering properties of the retina. SFDI can spatially resolve optical absorption and scattering properties and thus allows wide-field quantitative mapping of tissue optical properties. By separating and quantifying the multispectral absorption and scattering optical properties. SFDI provides a more direct assessment of tissue state and aids in measuring physiologically relevant parameters. SFDI can spatially resolve local properties in the retina such as oxygen saturation, total blood volume, and water abundance. It involves projecting sinusoidal illumination patterns of multiple spatial frequencies over a large area of the retina. The reflected image is modified from the illumination pattern due to the specific retinal optical properties. These spatially-modulated waves are demodulated to calculate the retinal modulation transfer function. Using model-based analysis, the diffuse reflectance, and subsequently the tissue optical properties, specifically, the quantitative absorption (μ_a) and reduced scattering ($\mu_s^{'}$) parameters can be extracted by this technique.

7.3 Quantitative retinal imaging

The potential range of applications for multispectral retinal imaging includes diseases that show abnormal colouring on routine ophthalmoscopy. Besides, spectral signatures are related to the chemical composition of the retina can be used to assess the oxygenation of retinal blood. This was the main motivation in constructing the multispectral SLO based on a supercontinuum source.

7.3.1 Retinal oximetry

Chapter 4 presents the *in silico* analysis of the error propagation of measurement noise in retinal oximetry, to identify optimal wavelengths which will yield the lowest uncertainty in saturation estimation for a given measurement noise level. In these analyses, the effect of haemoglobin packing in discrete blood vessels, the so-called ′pigment packing effect′ was also incorporated. This effect may result in a non-negligible bias in saturation estimation if unaccounted for under specific geometrical conditions such as sub-diffuse sampling of smaller blood vessels located deeper within the retina. The Optimal wavelength combination for retinal oximetry was identified based on these analyses. To validate the simulations, an SLO was constructed. Confocal reflectance measurements were then conducted on a tissue-mimicking scattering phantom with optical properties similar to retinal tissue. Narrow channels filled with absorbing dyes to mimic blood vessels were fabricated. By imaging at three optimal wavelengths, the ′saturation′ of the dye combination was calculated. The experimental values showed good agreement with our theoretical derivations. As a follow-up, *in vivo* oxygenation measurements were performed in two healthy volunteers as presented in **Chapter 5**.

From a technical standpoint, **Chapter 5** describes an SLO system based on a supercontinuum source and high-quality passive double-clad fibres (DCFs) and of DCF couplers which improved the collection efficiency by approximately 2.5 times. The larger inner cladding for DCF was used for quasi-confocal detection to increase throughput and signal to noise. A balanced detection scheme was implemented to suppress the relative intensity noise of the supercontinuum source. Finally, by performing a wavelength sweep between 485 and 608 nm, we determined an approximately linear relationship between the effective path length of photons through the blood vessels and the vessel diameter for our SLO geometry.

A demanding factor for clinically relevant retinal oximetry is to be able to determine blood oxygen saturation in small retinal vessels — capillaries, venules and arterioles. SLO based retinal oximetry has benefits over traditional fundus camera-based oximetry methods especially in terms of : resolution and contrast. It is in these microvessels that the oxygen saturation is expected to vary the most in response to increased metabolic demand or decreased oxygen delivery capacity. The larger retinal vessels ($>100\,\mu m$) are suspected to be less sensitive to variations in tissue metabolic requirement or microvascular dysfunction and are hence not ideal as early hypoxia markers. The clinical value of fundus camera-based oximeters is most likely limited due to the low spatial resolution. Even if the oxygen saturation estimates would be robust with such systems and more accurate taking into account our optimised wavelengths and our proposed algorithms that include pigment packaging (**Chapters 4 and 5**).

SLO based oximeters are not new to ophthalmic imaging, but their performance was limited due to sub-optimal choices for the wavelengths used due to lack of lasers at optimum wavelengths. Further pigment packaging, which is likely a non-negligible factor for smaller blood vessels located deeper in the retina, was not taken into account. The effective path length that photons travel through a tissue volume before being collected depends on the illumination and collection geometry and is also a function of the optical properties of the tissue and is, therefore, wavelength-dependent. We have assumed that the effective path length for the two optimum wavelengths in **Chapters 4 and 5** to calculate the ODs is almost the same. In the 450-600 nm wavelength range absorption remains of the same order and scattering varies slowly with wavelength (roughly as $1/\lambda$). However, a slight mismatch in the path lengths results in an offset in the saturation estimation. Additionally, in a diffuse sub approach, pigments which are present in the retina, especially in the retinal pigment epithelium (RPE), and absorption due to choroid blood can affect the recorded intensity. The effect of melanin on backscattered light varies with concentration [10], and a *a priori* knowledge of the pigment concentration in RPE melanin and its contribution to the backscattered light can aid in removing the influence of RPE in the backscattered light.

Saturation error and reproducibility are the major factors which contribute to the 'total cost of quality' of an oximetry system. To achieve acceptable levels of saturation error, a large number of points along the blood vessel and the tissue location had to be averaged (as explained in **Chapter 4**). This is a challenge for all the three techniques mentioned in section 2.3.3, namely the fundus photography, SLO and visible-light optical coherence tomography (OCT). A *in vivo* image contains structural information and choosing many points might lead to an incorrect estimation of the intensity in the absence of a blood vessel. A smaller number of points around the blood vessel should be averaged to overcome this problem (as was demonstrated in **Chapter 5**), and this requires multiple images to be produced within a short amount of time, as is done with an SLO. Fundus cameras are based on snapshot imaging, and it might not always be possible to acquire multiple images continuously without causing discomfort to the subject or exceeding the safety limit for radiant exposure. Visible light OCT offers the possibility of functional retinal imaging, as most retinal chromophores possess clear absorption signatures in the visible spectrum. In OCT-based oximetry methods, layers of the retina free from the influence of RPE can be used for extracting the intensities. Nevertheless, OCT being a coherent detection method suffers from speckles, and a significant amount of averaging has to be performed to improve the image quality and reduce the error on the mean intensity down to 1%. The SLO can be easily integrated with the 1050 nm ophthalmic OCT to get the overall metabolism of the retina (oxygenation and flow) combined with the blood flow in the choroid. By performing a wavelength-sweep hyperspectral imaging (**Chapter 5**), spectral unmixing can be achieved by decomposing the mixed spectral signature of different chromophores into a set of chromophores and their corresponding abundances [11].

As a side note, the system described in **Chapter 5** can be combined with endoscopic scanners to extract blood oxygenation of the pulmonary and gastrointestinal tracts in a minimally invasive manner. In combination with the flow and immuno-NIRF [12], this would give useful information, for instance, on tumour development.

7.3.2 Retinal haemoglobin concentration

In **Chapter 6**, the first results are shown from the same experimental SLO system to measure the haemoglobin content in the retina. Although the demonstration of the method has been done with the sophisticated setup using a supercontinuum source, the method can be translated to clinics, and for field applications using a simpler and compact prototype. For example, a fundus camera employing low-cost hardware, and filters with transmission windows corresponding to the optimum wavelengths could be implemented for clinical applications.

7.4 Future directions

Systemic diseases and retinal imaging

Various systemic diseases affect the retina. There are multiple reports of retinal imaging findings in systemic diseases ranging from neurological [13] to blood infections [14]. The retinal vessel network is optimised for efficient flow [15], and malfunctions that are revealed in abnormal geometric parameters measured on fundus images can give indications of pathologies. These parameters include, but are not limited to vessel diameters fluctuations within a vessel, changes in vessel bifurcation geometry, blood vessel tortuosity and global complexity of the visible network. Such abnormal vessel patterning increases metabolic energy costs and reduces the efficiency of nutrient transport. Retinal microvascular health is indicated by both adequate vessel diameters and optimal branching architecture [16]. A few examples of the potential of fundus imaging in diagnosing and monitoring systemic diseases are described as follows:

Diabetes is a disease due to inadequate production of insulin or owing to cells becoming resistant to insulin. Diabetes has a profound effect on the body's microvasculature. Consequently, retinal vascular changes are also evident on fundus images with a widening of venular diameters found to be associated with subsequent incidence and progression of diabetes. Diabetes can have serious long-term complications, such as diabetic retinopathy (DR). Using retinal imaging to identify the early signs of DR in the eye can help in preventing vision loss and blindness from this disease, and for early intervention. Also, identification of worsening DR signals unstable systemic control of diabetes, prompting a re-evaluation of treatment and other risk factors.

Fundus imaging has been proposed as a screening and monitoring tool for **Alzheimer's disease** (AD) [17]. Frost *et al.* [18] demonstrated altered vessel geometry such as reduced vessel diameters, and less tortuous venules etc. in patients with AD compared to healthy controls. Furthermore, evidence from the *Rotterdam study* on retinal vascular abnormalities in 655 dementia patients [19] underscore the potential role of fundus imaging in distinguishing different forms of dementia. Einarsdottir *et al.* [20] showed that oxygen saturation in moderate Alzheimer's disease was statistically significantly increased compared to healthy individuals.

Retinal oxygenation measurements in subjects with chronic **cardiac or pulmonary disease** [21] has shown reliable results in identifying hypoxia. *Oxymap* and *Imedos* retinal oximetry findings show a good statistical correlation with peripheral finger oximetry. Blood from radial artery of pulmonary disease patients corresponds to retinal oximetry measurements [22], there by showing a potential direction in exploring retinal imaging and retinal oximetry for cardiac and pulmonary ailments.

Artificial intelligence in ophthalmology:

Artificial intelligence (AI) has been used in recent years in ophthalmology for the automatic classification of eye diseases. There has been a paradigm shift in image interpretation and analysis due to the use of AI and specifically, deep learning. Deep learning is a collection of AI techniques that permit an algorithm to determine the relevant predictive features by models from a large set of examples rather than requiring features to be specifically predefined. Deep convolutional neural networks (CNV) has been employed for highly accurate classification and diagnosis of retinal pathologies [23] with accuracy comparable to that of experts.

Ophthalmic imaging is well suited for the implementation of AI-assisted automatic screening and investigation because of the wide-spread use of ophthalmic images which provide large amounts of data. The limited availability of retina specialists and trained human graders to diagnose these diseases is a major challenge in many countries. Hence, unmanned automatic applications and AI can be employed as a potential alternative to ophthalmologists and retina experts for detection and follow up of retinal pathologies.

For example, compact fundus cameras or phone add-on applications [24] can be used to collect retinal data. These devices not only make retinal imaging less expensive and accessible to various populations but also facilitate collection of large amounts of data which can be used to develop algorithms for classification, diagnosis and providing treatment options and advice. The major criticism of these portable fundus camera devices [25] is the inferior image quality. However, identifying good quality images in field conditions using automated image quality assessment is also gathering interest [26]. There can be two main approaches to achieve clinical diagnosis using such a portable or mobile device. In isolated areas where connectivity and access are poor, all the analysis needs to be performed on the device itself. On the other hand, in a setting with data connectivity, the images can be collected and analysed in a central cloud-based architecture for more advanced image processing and diagnostic analysis.

Combining retinal image classifications and diagnostic algorithms at the camera level can be beneficial for solving the need for high computation power. This will provide a paradigm shift in the way retinal imaging is viewed as a diagnostic tool and perhaps will provide a push towards ’point-of-care’ and personal care retinal imaging devices.

'smart camera architectures' [27] which uses AI, for example, the deep-lens camera by Amazon web services which embeds advanced deep learning and image processing algorithms at camera level can be adapted for fundus imaging [28].

7.5 Thesis conclusion

This thesis presents imaging systems whose purpose is visualising the structure and function of the retina *in vivo*. The systems have been designed and implemented to demonstrate the technical capabilities and usefulness of the techniques. First, an *in vivo* ophthalmoscope based on a digital micromirror device was implemented. Annulus illumination was implemented to block most of the corneal reflections using a circular aperture in the detection arm.

Secondly, we have demonstrated *in vivo* human retinal imaging with a novel SLO based on a supercontinuum source. The RIN noise of the illumination source has been addressed by implementing balanced detection. The balanced detection increased the SNR, and therefore improved the image quality and accuracy of oximetry calculations. The implementation of an achromatizing lens reduced the effect of chromatic aberrations introduced by the human eye, although this did not have a large effect on saturation estimation. The use of a double-clad fibre with large inner cladding provided the best trade-off between image contrast and SNR. This allowed for high-resolution *in vivo* visualization of the oxygenation of retinal blood vessels in healthy volunteers. The oxygen saturation of the larger vessels of the retinas of two human volunteers was in agreement with the *Oxymap* derived saturation; besides, our SLO system was able to provide oxygen saturation in much smaller vessels. The saturation measured in 3 different imaging sessions of the same volunteer (8 minutes apart) demonstrated the reproducibility of our measurements. Several innovative methods to extract information from the retina are described. A novel vessel segmentation algorithm that delineates the blood vessels and tissue was described to facilitate the segmentation of small blood vessels for oximetry estimation. It is expected that the SLO will be a valuable tool to study the effect of degenerative retinal diseases on the oxygenation in the retinal microvasculature. Finally, by performing a wavelength sweep between 485 and 608 nm we determined an approximately linear relationship between the effective path length of photons through the blood vessels and vessel diameter for our SLO geometry that employs a DCF with a large inner cladding. Using this relationship, first results on the haemoglobin content in the retinal blood vessels was calculated using two isosbestic wavelengths.

References

[1] 1. M. S. Muller, J. J. Green, K. Baskaran, A. W. Ingling, J. L. Clendenon, T. J. Gast, and A. E. Elsner, "Non-mydriatic confocal retinal imaging using a digital light projector," 9376, 93760 (2015).

[2] K. Vienola, M. Damodaran, B. Braaf, K. Vermeer, and J. F. de Boer, "Parallel line scanning ophthalmoscope for retinal imaging," Opt. Lett. **40**, 5335-5338 (2015).

[3] International Electrotechnical Commission, Safety of Laser Products Part 1: Equipment Classification and Requirements, (Geneva, Switzerland), IEC-60825-1 (2014).

[4] R. W. Knighton and X. Huang, Linear Birefringence of the Central Human Cornea, Invest. Ophthalmol. Vis. Sci. **43**(1), 8286 (2016).

[5] A. Weber, A. E. Elsner, M. Miura, S. Kompa, and M. C. Cheney, “Relationship between foveal birefringence and visual acuity in neovascular age-related macular degeneration,” Eye, **21**(3), 130-134 (2012).

[6] K. V. Vienola, B. Braaf, C. K. Sheehy, Q. Yang, P. Tiruveedhula, D. W. Arathorn, J. F. de Boer, and A. Roorda, “Real-time eye motion compensation for OCT imaging with tracking SLO,” Biomed. Opt. Express **3**(11), 2950-2963 (2012).

[7] C. K. Sheehy, Q. Yang, D. W. Arathorn, P. Tiruveedhula, J. F. de Boer, and A. Roorda, “High-speed, image based eye tracking with a scanning laser ophthalmoscope,” Biomed. Opt. Express **3**(10), 2611-2622 (2012).

[8] K. V. Vienola, M. Damodaran, B. Braaf, K. A. Vermeer, and J. F. De Boer, "In vivo retinal imaging for fixational eye motion detection using a high-speed digital micromirror device (DMD)-based ophthalmoscope," Biomed. Opt. Express **9**, 591-602 (2018).

[9] D. J. Cuccia, F. Bevilacqua, A. J. Durkin, F. R. Ayers, and B. J. Tromberg, "Quantitation and mapping of tissue optical properties using modulated imaging," J. Biomed. Opt. **14**, 024012-024012-13 (2009).

[10] G. Liew, J. J. Wang, P. Mitchell, and T. Y. Wong, "Retinal vascular imaging: a new tool in microvascular disease research.," Circ. Cardiovasc. Imaging **1**, 156-61 (2008).

[11] Mikael Marois, S. L. Jacques, Keith D. Paulsen, "Optimal wavelength selection for optical spectroscopy of hemoglobin and water within a simulated light-scattering tissue," J. Biomed. Opt. **23**, 1 (2018).

[12] F. Feroldi, M. Verlaan, H. Knaus, V. Davidoiu, D. J. Vugts, G. A. M. S. van Dongen, C. F. M. Molthoff, and J. F. de Boer, "High resolution combined molecular and structural optical imaging of colorectal cancer in a xenograft mouse model.," Biomed. Opt. Express **9**, 6186-6204 (2018).

[13] P. P. Chhablani et al., Retinal Findings on OCT in Systemic Conditions, Semin. Ophthalmol. 33(**4**), 525-546, Taylor and Francis (2018).

[14] Pirani et al., The Eye as a Window to Systemic Infectious Diseases: Old Enemies, New Imaging, J. Clin. Med. 8(**9**), 1392 (2019).

[15] G. Liew et al., Retinal vascular imaging: a new tool in microvascular disease research., Circ. Cardiovasc. Imaging 1(**2**), 156-161 (2008).

[16] G. Liew, P. Mitchell, E. Rochtchina, T. Y. Wong, W. Hsu, M. L. Lee, A. Wainwright, and J. J. Wang, "Fractal analysis of retinal microvasculature and coronary heart disease mortality," Eur. Heart J. **32**, 422-429 (2011).

[17] M. K. Ikram, C. Y. Cheung, T. Y. Wong, and C. P. L. H. Chen, "Retinal pathology as biomarker for cognitive impairment and Alzheimers disease.," J. Neurol. Neurosurg. Psychiatry **83**, 917-22 (2012).

[18] S. Frost, Y. Kanagasingam, H. Sohrabi, J. Vignarajan, P. Bourgeat, O. Salvado, V. Villemagne, C. C. Rowe, S. Lance MacAulay, C. Szoeke, K. A. Ellis, D. Ames, C. L. Masters, S. Rainey-Smith, and R. N. Martins, "Retinal vascular biomarkers for early detection and monitoring of Alzheimer's disease," Transl. Psychiatry **3**, (2013).

[19] F. J. De Jong, E. M. C. Schrijvers, M. K. Ikram, P. J. Koudstaal, P. T. V. M. De Jong, A. Hofman, J. R. Vingerling, and M. M. B. Breteler, "Retinal vascular caliber and risk of dementia: The Rotterdam Study," Neurology **76**, 816-821 (2011).

[20] A. B. Einarsdottir, S. H. Hardarson, J. V. Kristjansdottir, D. T. Bragason, J. Snaedal, and E. Stefánsson, "Retinal Oximetry Imaging in Alzheimers Disease," J. Alzheimers Dis. **49**, 7983 (2015).

[21] S. Traustason, A. S. Jensen, H. S. Arvidsson, I. C. Munch, L. Sondergaard, and M. Larsen, "Retinal oxygen saturation in patients with systemic hypoxemia," Investig. Ophthalmol. Vis. Sci. **52**, 5064-5067 (2011).

[22] T. S. Eliasdottir, "Retinal oximetry and systemic arterial oxygen levels," Acta Ophthalmol. **96**, 144 (2018).

[23] V. Gulshan, L. Peng, M. Coram, M. C. Stumpe, D. Wu, A. Narayanaswamy, S. Venugopalan, K. Widner, T. Madams, J. Cuadros, R. Kim, R. Raman, P. C. Nelson, J. L. Mega, and D. R. Webster, "Development and Validation of a Deep Learning Algorithm for Detection of Diabetic Retinopathy in Retinal Fundus Photographs," 94043, 1-9 (2016).

[24] T. N. Kim, F. Myers, C. Reber, P. J. Loury, P. Loumou, C. Echanique, P. Li, J. R. Davila, R. N. Maamari, A. Neil, J. Keenan, M. A. Woodward, Y. M. Paulus, T. Margolis, and D. A. Fletcher, "A Smartphone-Based Tool for Rapid , Portable , and Automated Wide-Field Retinal Imaging," Transl. Vis. Sci. Technol. **7**, 1-15 (2018).

[25] G. L. Monroy, D. R. Spillman, S. A. Boppart, G. L. Monroy, J. Won, D. R. Spillman, J. R. Dsouza, and S. A. Boppart, "Clinical translation of handheld optical coherence tomography : practical considerations and recent advancements Clinical translation of handheld optical coherence tomography : practical considerations and recent," Biomed. Opt. Express **22**, (2017).

[26] G. J. Kutuwal et al., "Automated fundus image field detection and quality assessment", US patent US9905008 (2018).

[27] D. Ginhac, F. Berry, and R. Kleihorst, "Special issue on advances on smart camera architectures for real-time image processing," J. Real-Time Image Process. 14, 635-636 (2018).

[28] P. Teikari, R. P. Najjar, L. Schmetterer, and D. Milea, "Embedded deep learning in ophthalmology : making ophthalmic imaging smarter," Therapeutic Advances in Ophthalmology, 1 -21 (2019).

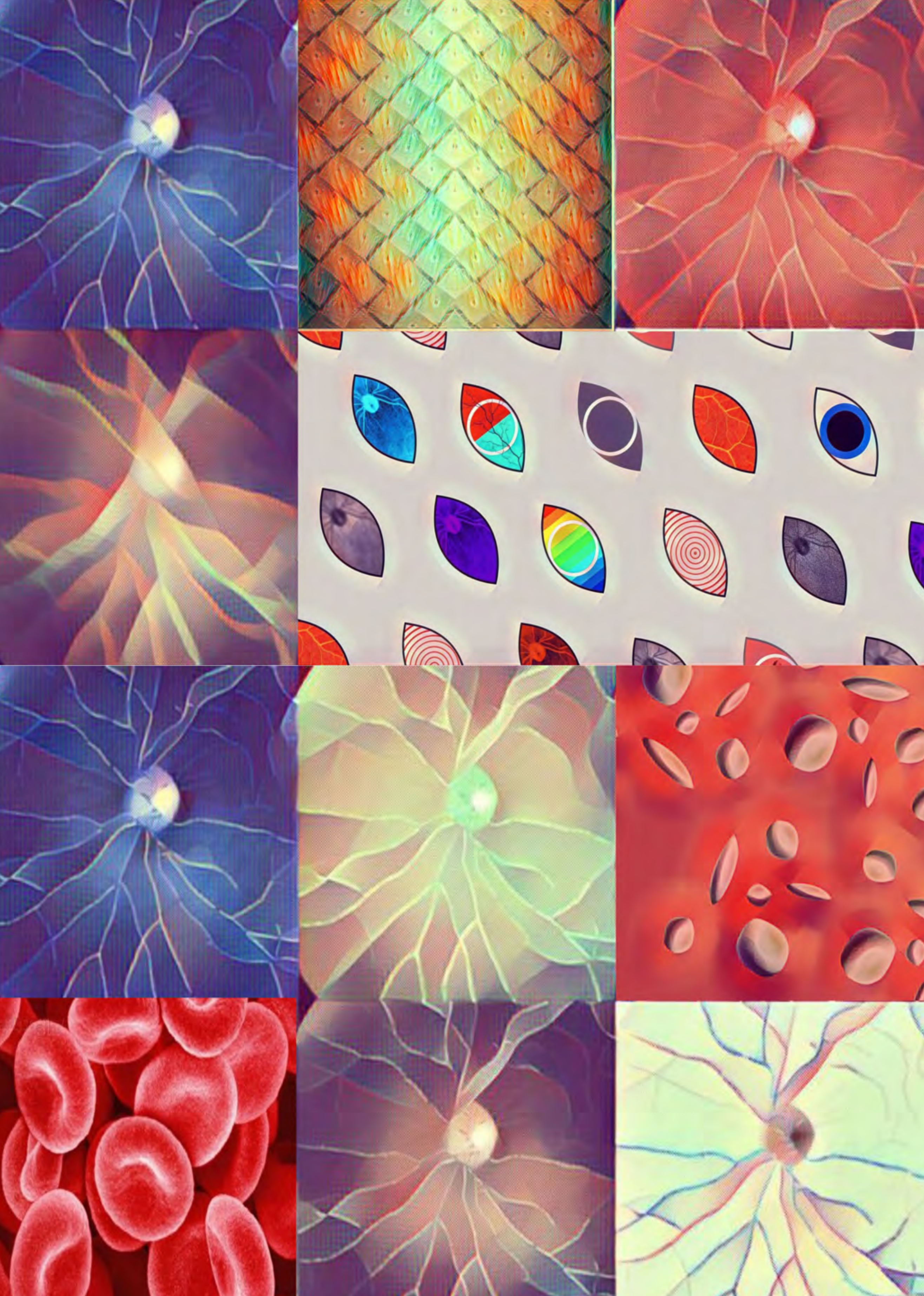

8

Summary

Ophthalmic imaging has been an active area of clinical investigation that has been expanding steadily, providing scientists and doctors with valuable information. New diagnostic and therapeutic methods have been established in this field, driven by an overall need to advance clinical care in ophthalmology. New scanning and imaging technologies have had a significant impact on ophthalmology. Structural imaging techniques help in visualising the retina in great detail and helps in assessing retinal health. However, the structure does not always provide information on the tissue health, and thus techniques which can provide a quantitative, functional aspect of living tissue is required in many cases. The work presented in this thesis aims to develop new devices and techniques which can perform imaging of the retina and to apply them for non-invasive imaging of structure and function in the *in vivo* human retina.

To extract structural and functional information from the retina using an SLO, it is essential to understand it's design, construction, and working. For this purpose, **chapter 2** of this thesis discusses the principle of scanning based ophthalmic imaging systems, gives a brief explanation of various design considerations for constructing an SLO, and introduces the retinal oximetry and its importance in diagnosing various retinal diseases. Laser safety considerations for intentional exposure of the retina to the laser light is also described in detail. The knowledge from this chapter forms the basis of the scientific work presented in chapters 3 to 6.

In **Chapter 3**, a novel digital micromirror device (DMD) based SLO is presented. Concentric circle patterns were implemented as a scanning scheme to image the retina and provide fixation at the same time. The DMD was used *in lieu* of traditional scanning mirrors and offered flexibility in terms of speed and confocality. The concentric circles improved the fixation and reduced motion artefacts compared to previously implemented parallel line scanning design. An annulus was used to reduce the corneal reflections from the retina and thereby to increase the signal to noise ratio. *in vivo* imaging was demonstrated by performing non-mydriatic imaging on two subjects at a speed of 7 frames per second with a maximum 20° (diameter) field of view. The images were shot noise limited and clearly show various anatomical features of the retina with high contrast. The images were comparable to images from a commercial SLOs but at a fraction of the cost.

Chapter 4 describes a detailed analysis of the error propagation of measurement noise in retinal oximetry, to identify optimal wavelengths which will yield the lowest uncertainty in saturation estimation for a given measurement noise level. The effect of haemoglobin packing in discrete blood vessels (pigment packing) is also introduced in this chapter. Pigment packing may result in a non-negligible bias in saturation estimation if unaccounted for under specific geometrical conditions, such as sub-diffuse sampling of smaller blood vessels located deeper within the retina. To validate the analysis, an SLO was developed to produce high contrast images. Confocal reflectance measurements were then conducted on a tissue-mimicking scattering phantom with optical properties similar to retinal tissue, including narrow channels filled with absorbing dyes to mimic blood vessels. By imaging at three optimal wavelengths, the ′saturation′ of the dye combination was calculated.

In **Chapter 5**, construction of an SLO based on a double-clad fibre coupler and a supercontinuum source is described in detail. Implementation of a balanced detection scheme to suppress the relative intensity noise of the supercontinuum source is also described with experiments validating the improvements in the signal to noise ratio with the use of balanced detection. The optimum wavelengths for accurate *in vivo* oximetry estimation using two wavelengths are established with an *in silico* analysis. The SLO produced dual-wavelength, high-quality images at 10 frames / second with a 20° imaging field of view. The blood oxygen saturation in retinal blood vessels was mapped from the images.

The eye provides a unique location in the human body with visual access to blood vessels. The blood vessels in the eye are regarded as highly superficial and thus is a desirable access point for Hb concentration estimation due to the lack of thick overlying tissues present elsewhere in the body. In **Chapter 6**, a non-invasive spectrophotometric method to image the retina simultaneously at two ′isosbestic′ wavelengths, and then to extract the haemoglobin concentration values from the two images is described.

Finally, in **Chapter 7**, the discussion on the results obtained from the scientific work in chapters 3-6 is presented with an outlook for future research. The concluding remarks of the thesis are also given in this chapter.

Nederlandse Samenvetting

Oogheelkundige beeldvorming is een actief gebied van klinisch onderzoek dat gestaag uitbreidt en dat wetenschappers en artsen waardevolle informatie biedt. Nieuwe diagnostische en therapeutische methoden zijn op dit gebied vastgesteld vanuit een algemene behoefte om klinische zorg in de oogheelkunde te verbeteren.

Nieuwe scan- en beeld technologieen hebben een significante invloed op de oogheelkunde. Beeldvormingstechnieken die de structuur weergeven helpen bij het gedetailleerd visualiseren van het netvlies en daarmee het beoordelen van de gezondheid van het netvlies. Weefstelstructuur geeft echter niet altijd informatie over de gezondheid van het weefsel en daarom zijn in veel gevallen technieken nodig die een kwantitatief, functioneel aspect van levend weefsel kunnen weergeven. Het doel van het werk dat gepresenteerd wordt in dit proefschrift is om nieuwe apparaten en technieken te ontwikkelen die beeldvorming van het netvlies kunnen uitvoeren, en deze toe te passen voor niet-invasieve beeldvorming van structuur en functie in het *in vivo* menselijk netvlies.

Om structurele en functionele informatie uit het netvlies te halen met behulp van een SLO, is het belangrijk om het ontwerp, de constructie en de werking ervan te begrijpen. Met dit doel bespreekt **Hoofdstuk 2** van dit proefschrift het principe van oogheelkundige beeldvormingssystemen die gebruik maken van scannen. Tevens geeft dit hoofdstuk een korte uitleg over verschillende ontwerpoverwegingen voor het construeren van een SLO en introduceert het retinale oximetrie en het belang ervan bij de diagnose van verschillende retinale ziekten. Laserveiligheidsoverwegingen voor het opzettelijke blootstelling van het netvlies aan het laserlicht worden ook in detail beschreven. De kennis uit dit hoofdstuk vormt de basis van het wetenschappelijke werk dat in de hoofdstukken 3 tot en met 6 wordt gepresenteerd.

In **Hoofdstuk 3** wordt een nieuwe SLO op basis van een digital micromirror device (DMD) gepresenteerd. Concentrische cirkelpatronen werden geïmplementeerd als een scanschema om het netvlies af te beelden en tegelijkertijd een fixatie te verschaffen. De DMD werd gebruikt in plaats van traditionele scan-spiegels en biedt flexibiliteit met betrekking tot snelheid en confocaliteit. De concentrische cirkels verbeterden de fixatie en verminderden bewegingsartefacten in vergelijking met het eerder geïmplementeerde ontwerp dat scande met een parallelle lijn. Een annulus werd gebruikt om de cornea-reflecties van het netvlies te verminderen en daarmee de signaal-ruisverhouding te vergroten. *In vivo* beeldvorming werd aangetoond door niet-mydriatische beeldvorming op twee participanten uit te voeren met een snelheid van 7 beelden per seconde en een maximum gezichtsveld van 20° (diameter). De beelden waren shotnoise gelimiteerd en tonen met een hoog contrast duidelijk de verschillende anatomische kenmerken van het netvlies. De afbeeldingen waren vergelijkbaar met afbeeldingen van commerciële SLO's, maar slechts voor een fractie van de kosten.

Hoofdstuk 4 beschrijft een gedetailleerde analyse van de foutpropagatie van meetruis in retinale oximetrie, om zo optimale golflengten te identificeren die de kleinste onzekerheid opleveren in de verzadigingsschatting voor een bepaald meetruisniveau. Het effect van hemoglobineclustering in afzonderlijke bloedvaten (pigmentclustering) wordt ook in dit hoofdstuk geïntroduceerd. Pigmentclustering kan resulteren in een niet-verwaarloosbare bias bij het schatten van de verzadiging indien geen rekening gehouden wordt met de specifieke geometrische omstandigheden, zoals sub-diffuse bemonstering van kleinere bloedvaten dieper in het netvlies. Om de analyse te valideren werd een SLO ontwikkeld die beelden met een hoog contrast kon produceren. Confocale reflectiemetingen werden vervolgens uitgevoerd op een verstrooiend fantoom dat weefsel nabootst. Dit fantoom had optische eigenschappen vergelijkbaar met netvliesweefsel, inclusief smalle kanalen gevuld met absorberende kleurstoffen om bloedvaten na te bootsen. Door beeldvorming bij drie optimale golflengten werd de 'verzadiging' van de kleurstofcombinatie berekend.

In **Hoofdstuk 5** wordt de constructie van een SLO op basis van een double clad fiber coupler en een supercontinuümbron in detail beschreven. De implementatie van een gebalanceerd detectieschema, om de relatieve intensiteitruis van de supercontinuümbron te onderdrukken, wordt beschreven aan de hand van experimenten die de verbeteringen in de signaal / ruisverhouding valideren met behulp van gebalanceerde detectie. De optimale golflengten voor nauwkeurige *in vivo* oximetrieschatting met behulp van twee golflengten worden bepaald aan de hand van een *in silico* analyse. De SLO produceerde beelden van hoge kwaliteit met dubbele golflengte met 10 beelden per seconde en een gezichtsveld van 20°. De bloedzuurstofsaturatie in retinale bloedvaten werd in kaart gebracht aan de hand van de gemaakte afbeeldingen.

Het oog biedt een unieke locatie in het menselijk lichaam waar visuele toegang is tot de bloedvaten. De bloedvaten in het oog worden als zeer oppervlakkig beschouwd en zijn dus een gewenst toegangspunt voor schatting van de hemoglobine concentratie, wegens het ontbreken van dikke bovenliggende weefsels die elders in het lichaam aanwezig zijn. In **Hoofdstuk 6** wordt een niet-invasieve spectrofotometrische methode beschreven om het netvlies tegelijkertijd op twee isosbestische golflengten af te beelden en vervolgens hoe de hemoglobine concentratiewaarden uit de twee afbeeldingen te extraheren is.

Ten slotte wordt in **hoofdstuk 7** de discussie over de resultaten van het in hoofdstuk 3-6 gepresenteerde wetenschappelijke werk besproken, met vooruitzichten voor toekomstig onderzoek. De slotopmerkingen van het proefschrift worden ook in dit hoofdstuk gegeven.

ஆய்வுச்சுருக்கம்

கண் என்பது நம் உடலின் முக்கியமான உறுப்பாகும். கண் நமக்குப் பார்வை உணர்வைத் தருவது மட்டுமல்லாமல், சுற்றியுள்ள உலகத்தை அவதானிக்கவும் அனுமதிக்கிறது. நாம் செய்யும் ஒவ்வொரு செயலிலும் நாம் நம் கண்களைப் பயன்படுத்துகிறோம். எனவே பார்வையைப் பாதிக்கும் எந்த ஒரு நோயும் ஒரு நபரின் வாழ்க்கைத் தரத்தில் எதிர்மறையான தாக்கத்தை ஏற்படுத்துகிறது.

வயது தொடர்பான நோய்கள் ஒரு குறிப்பிடத்தக்க பொது சுகாதார பிரச்சினையாக மாறியுள்ளன. குறிப்பாக, விழித்திரையில் (retina) ஏற்படும் நோய்கள் பார்வை செயல்பாட்டுக் குறைபாட்டையும் மற்றவர்களைச் சார்ந்திருக்கும் சூழ்நிலையையும் ஏற்படுத்தும். மிகவும் மோசமான நிலையில், ஒருவர் ஊனமுற்றவராக மாறுகிறார். உலக சுகாதார அமைப்பின் (WHO) கூற்றுப்படி, சுமார் 1.3 பில்லியன் (130 கோடி) மக்கள் ஏதேனும் ஒரு பார்வைக் குறைபாட்டுடன் வாழ்கின்றனர். அவர்களில் 270 மில்லியன் (27 கோடி) மக்கள் மிதமான அல்லது கடுமையான பார்வைக் குறைபாட்டைக் கொண்டுள்ளனர். உலகளவில் 80% பார்வைக் குறைபாடுகள் தவிர்க்கக்கூடிய குறைபாடுகளாகக் கருதப்படுகின்றன.

விழித்திரை என்பது கண்ணின் தலையாய பகுதியாகும். விழித்திரை நோய்கள் விழித்திரையில் கட்டமைப்பு (structural) மற்றும் செயல்பாட்டு (functional) மாற்றங்களை வெளிப்படுத்துகின்றன. விழித்திரை உருவமாக்கம் (retinal imaging) நுட்பங்களைப் பயன்படுத்தி அவை மதிப்பிடப்படுகின்றன. விழித்திரை நோய்களைப் பற்றிய நமது புரிதலுக்கும், பயனுள்ள மருத்துவ மதிப்பீடு, பின்தொடர்தல் மற்றும் சிகிச்சையிலும் விழித்திரை உருவமாக்கம் மிகவும் முக்கியமானது. இந்நுட்பங்கள் விஞ்ஞானிகளுக்கும் மருத்துவர்களுக்கும் மதிப்புமிக்க தகவல்களை வழங்குகின்றன. நவீன ஸ்கேனிங் மற்றும் இமேஜிங் தொழில்நுட்பங்கள் கண் மருத்துவத்தில் குறிப்பிடத்தக்க தாக்கத்தை ஏற்படுத்தியுள்ளன.

கட்டமைப்பு இமேஜிங் நுட்பங்கள் விழித்திரையை மிக விரிவாகக் காட்சிப்படுத்த உதவுகின்றன. விழித்திரை ஆரோக்கியத்தை மதிப்பிடுவதற்கும் இது உதவுகிறது. இருப்பினும், கட்டமைப்பு எப்போதும் விழித்திரை ஆரோக்கியம் குறித்த தகவல்களை வழங்குவதில்லை. இதனால் விழித்திரை அளவு மற்றும் செயல்பாட்டு அம்சத்தைக் கணக்கிட்டு வழங்கக்கூடிய நுட்பங்கள் பல்வேறு சந்தர்ப்பங்களிலும் பல்வேறு கண் நோய்களிலும் தேவைப்படுகின்றன.

விழித்திரை உருவமைப்பு முறைகளில் ஏற்பட்ட பல்வேறு முன்னேற்றங்களால் கடந்த இருபது வருடங்களில் கண் சிகிச்சை தரம் வெகுவாக மேம்பட்டுள்ளது. விழித்திரை நோய்களுக்கும் ஒளி பண்புகளுக்கும் (optical properties) இடையேயுள்ள தொடர்பைக் கண்டயறியக்கூடிய புதிய தொழில்நுட்பங்கள் உருவாக்கப்படவேண்டும். விழித்திரையின் உருவமாக்கம் செய்யக்கூடிய புதிய சாதனங்கள் மற்றும் நுட்பங்களை உருவாக்குவதும், மனித விழித்திரையில் கட்டமைப்பு மற்றும் செயல்பாட்டின் இமேஜிங்கிற்கு அவற்றைப் பயன்படுத்துவதும் இந்த ஆய்வின் முக்கிய நோக்கம் ஆகும். இவ்வாய்வு விழித்திரை இமேஜிங்கிற்கான இரண்டு முக்கிய அணுகுமுறைகளில் கவனம் செலுத்துகிறது:

1. குறைந்த விலை டிஜிட்டல் நுண்-கண்ணாடிகள் (digital micro mirror) அடிப்படையிலான ‘வருடும் கிளர்கதிர் கண்சோதனைக்கருவியை’ (scanning laser ophthalmoscope/SLO) வடிவமைத்தல், அக்கருவியைக் கொண்டு விழித்திரையின் கட்டமைப்பை உருவமாக்குவது (அத்தியாயம் 3).

2. பன்னிற வருடும் கிளர்கதிர் கண்சோதனைக்கருவியை (multispectral SLO) வடிவமைத்தல் (அத்தியாயம் 3 மற்றும் 4), அக்கருவியைக் கொண்டு விழித்திரையைப் பலநிற கிளர்க்கதிர்களைக் கொண்டு உருவமாக்குதல் (அத்தியாயம் 4). மேலும் இப்பலநிற கிளர்கதிர் உருவங்களைக் கொண்டு விழித்திரையின் ஆக்சிஜனூட்டம் (அத்தியாயம் 4) மற்றும் ஹீமோகுளோபின் செறிவை (அத்தியாயம் 5) கண்டறிதல்.

அத்தியாயங்கள் 1 மற்றும் 2, இந்த ஆய்வறிக்கையின் நோக்கத்தையும் பயன்படுத்தப்பட்ட முறைகளையும் விளக்குகின்றன. அத்தியாயம் 7 இந்த ஆய்வறிக்கையின் நிறைவுரையையும் எதிர்கால கண்ணோட்டத்தையும் அளிக்கிறது.

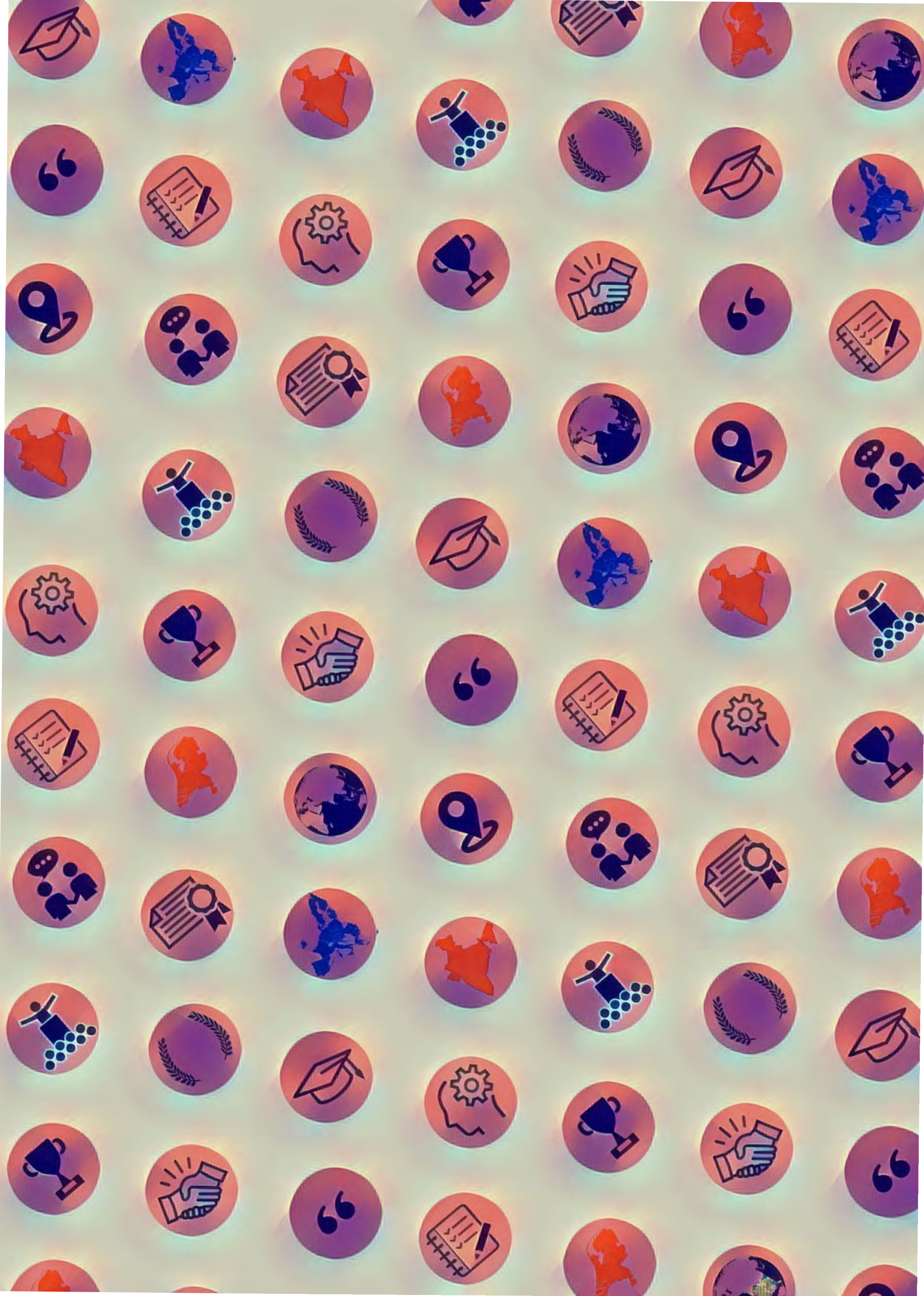

9

Curriculum Vitae

Mathivanan (Mathi) Damodaran was born on October 9th, 1989 in Dharmapuri, Tamil Nadu, India. He obtained his Bachelor of Engineering degree in Electronics and Communication Engineering (ECE) in 2011 from Anna University, Chennai. For his Bachelor's degree, he did an internship at the Indian Institute of Technology (IIT, Madras) on 'fibre lasers'. He joined the Erasmus Mundus MSc. in Photonics program and did his masters course in three different universities namely, Universiteit Gent (Gent, *Belgium*), Kungliga tekniska högskolan (Stockholm, *Sweden*) and University of St.Andrews (St.Andrews, *Scotland*). He completed the master's degree in 2013. As part of his master's degree, he did an internship on optics design for a compact hand-held probe for fluorescence lifetime imaging in Advanced Quantum Architecture Lab (AQUA) (Ecole Polytechnique fédérale de Lausanne, *Switzerland*). The master's thesis was done in the Synthetic Optics group at the School of Physics and Astronomy, (St.Andrews Scotland) on 'All-optical manipulation of 2D polymeric membranes'. In October 2013, Mathi started as a PhD candidate at the imaging group of the Rotterdam Ophthalmic Institute and in June 2014, he moved to the Biophotonics and Imaging group in the Department of Physics and Astronomy, Vrije Universiteit Amsterdam to finish his research which culminated in this thesis. In December 2018, He took the position as a scientist in Philips Research (Eindhoven, *The Netherlands*).

Awards and Honours

- Erasmus Mundus scholarship for 2 years of Msc. study
- Poster Award at the BIGSS Graduate Summer School 2014
- International Travel Grant, ARVO Annual meeting 2017

Patents

- Retinal oximetry with improved accuracy (pending, 2019)

Conference presentations

- **Confocal imaging of the retina using DMD based ophthalmoscope** *Biophotonics and imaging graduate summer school* 2014, Galway, *Ireland*.
- ***In vivo* confocal imaging of the retina using patterned illumination**, oral presentation, *Emerging Digital Micromirror Device Based Systems and Applications VII*, SPIE photonics west, February 2015, San Francisco, *USA*.

- **Digital micromirror device based multispectral retinal imaging using optimized illumination schemes**, oral presentation, *Emerging Digital Micromirror Device Based Systems and Applications VIII*, SPIE photonics west, February 2016, San Francisco, *USA*.

- **Multispectral Scanning Light Ophthalmoscope (MSLO) using optimized illumination schemes**, poster presentation, *ARVO Annual Meeting* May 2016, Seattle, *USA*.

- **Dual wavelength scanning light ophthalmoscope using digital micromirror device**, oral presentation, *Ophthalmic Technologies XXVII*, SPIE photonics west, January 2017, San Francisco, *USA*.

- **Dual wavelength Scanning Light Ophthalmoscope with concentric circle scanning**, poster presentation, *ARVO Annual Meeting* May 2017, Baltimore, *USA*.

- **Choosing optimum wavelength combination for retinal vessel oximetry: Effect of haemoglobin packaging**, oral presentation, *Imaging, Manipulation, and Analysis of Biomolecules, Cells, and Tissues XVI*, SPIE photonics west, January 2018, San Francisco, *USA*.

- **DMD based ophthalmoscope with concentric circle scanning for fixation**, oral presentation, *Emerging Digital Micromirror Device Based Systems and Applications X*, SPIE photonics west, January 2018, San Francisco, *USA*.

- **Sub-diffuse scanning laser oximetry in the retina using optimum wavelengths**, poster presentation, *ARVO Annual Meeting*, May 2018, Honolulu, *USA*.

Publications list

Publications (partly) included in the thesis:

- **M. Damodaran**, K. V. Vienola, B. Braaf, K. A. Vermeer, and J. F. de Boer, "Digital micromirror device based ophthalmoscope with concentric circle scanning," Biomed. Opt. Express 8, (2017).

- K. V. Vienola, **M. Damodaran**, B. Braaf, K. A. Vermeer, and J. F. De Boer, "In vivo retinal imaging for fixational eye motion detection using a high-speed digital micromirror device (DMD)-based ophthalmoscope," Biomed. Opt. Express 9, 591-602 (2018).

- **M. Damodaran**, A. Amelink, and J. F. de Boer, "Optimal wavelengths for subdiffuse scanning laser oximetry of the human retina," J. Biomed. Opt. 23, 1 (2018).

- **M. Damodaran**, A. Amelink, and J. F. de Boer, "Non-invasive optical measurement of haematocrit in the posterior eye of adult humans," *manuscript in preparation*.

- **M. Damodaran**, A. Amelink, F. Feroldi, B. Lochocki, V. Davidoiu, and J. F. de Boer, "In vivo subdiffuse scanning laser oximetry of the human retina," J. Biomed. Opt. 24, 1 (2019).

- K. V. Vienola, **M. Damodaran**, B. Braaf, K. A. Vermeer, and J. F. de Boer, "Parallel line scanning ophthalmoscope for retinal imaging," Opt. Lett. 40, 5335-5338 (2015).

Publications outside the thesis:

- **M. Damodaran**, K. V. Vienola, B. Braaf, K. Vermeer, and J. F. De Boer, "Multispectral Scanning Light Ophthalmoscope (MSLO) using optimized illumination schemes," Invest. Ophthalmol. Vis. Sci. 57, 1697 (2016).

- **M. Damodaran**, K. V Vienola, K. A. Vermeer, and J. F. De Boer, "Dual wavelength Scanning Light Ophthalmoscope with concentric circle scanning," Invest. Ophthalmol. Vis. Sci. 58, 3132 (2017).

- **M. Damodaran**, A. Amelink, and J. F. De boer, "Sub-diffuse scanning laser oximetry in the retina using optimum wavelengths," Invest. Ophthalmol. Vis. Sci. 59, 4656 (2018).

- A. Bekal, **M. Damodaran**, D. Venkitesh, and B. Srinivasan, "Optimization of cavity configuration of a Q-switched fibre LASER," Proc. SPIE - Int. Soc. Opt. Eng. 8173, 17 (2011).

Acknowledgments were not published with the web version of this thesis